Fall 11-7-2016

Understanding the Behavior of Embankment Dams Under Blast Loading

Courtney L. Busch
University of New Mexico

Courtney L. Busch

Candidate

Civil Engineering

Department

This dissertation is approved, and it is acceptable in quality and form for publication:

Approved by the Dissertation Committee:

Dr. Rafiqul A. Tarefder , Chairperson

Dr. Catherine Aimone-Martin

Dr. Arup K. Maji

Dr. Tang-Tat Ng

Dr. Yu-Lin Shen

UNDERSTANDING THE BEHAVIOR OF EMBANKMENT DAMS UNDER BLAST LOADING

by

COURTNEY L. BUSCH

B.S., MINERAL ENGINEERING, 2004
M.S., MINERAL ENGINEERING, 2006
NEW MEXICO INSTITUTE OF MINING AND TECHNOLOGY

DISSERTATION

Submitted in Partial Fulfillment of the
Requirements for the Degree of
Doctor of Philosophy

Engineering

The University of New Mexico
Albuquerque, New Mexico

November 2016

DEDICATION

For my children.

I see endless possibility when I look in your eyes.

ACKNOWLEDGEMENTS

This endeavor has been both challenging and rewarding through the years and I have many people to thank for their help along the way. I'd like to start by thanking my advisor for the opportunity to work on this research; many doors have opened to me because of this work and have led me down the path to a career that I love. Thank you also to my committee members, especially Dr. Catherine Aimone-Martin, who has been a mentor since the start of my academic career and has donated many hours of her personal time to advise me.

I'd like to thank my work colleagues for graciously accommodating and encouraging my studies while being a working engineer. I've been very fortunate to work with a group that values higher education and supported me in all that it entailed. My division manager, Mr. Robert Couch, made being a working student possible. I'd like to especially thank Mr. Daniel Chitty for his tireless support during this process and the many hours of brainstorming that we did together. I'd also like to thank Mr. Craig Sheffield and Dr. Robert Bocchieri for their assistance with the challenging world of numerical modeling. Thank you also to Dr. Len Schwer for the ideas and dialogue.

Thank you a million times over to my family for their unconditional love and support during my studies. A marriage and two beautiful children have occurred during the course of this work and my family has tirelessly helped me to juggle the responsibilities that this entailed. My husband Joel has been my biggest supporter. I love you, Dear. My best friend and sister, Meghan, a talented engineer in her own right, has always been there for me. I couldn't have done it without you. Thank you to my loving and strong-

willed mother Nancy, who raised me with a love of learning and never doubted that I would pursue a higher education.

Lastly I would like to acknowledge the Divine Creator for guiding me down this path. How beautiful His world is when studied through the lens of engineering.

UNDERSTANDING THE BEHAVIOR OF EMBANKMENT DAMS UNDER BLAST LOADING

by

Courtney L. Busch

B.S., Mineral Engineering, New Mexico Institute of Mining and Technology, 2004

M.S., Mineral Engineering, New Mexico Institute of Mining and Technology, 2006

Ph.D., Engineering, University of New Mexico, 2016

ABSTRACT

This purpose of this study is to investigate the deformation-induced stability of earthen embankment dams to explosive airblast loading. This study specifically investigated the effects of close-in explosive airblast loads on the downstream toe of a homogeneous earthen embankment dam composed of cohesive soils. Small-scale explosive airblast experiments were performed on cohesive soils to obtain an experimental data set with which to compare numerical analyses. Experimental measurements included crater geometry, ground vibration energy, and air overpressure from the blast events. Laboratory tests were conducted on the experiment soils to obtain engineering properties including shear strength and compressibility indices. Finite element simulations of airblast loading on a cohesive soil embankment dam were performed using Multi-Material Arbitrary Lagrangian Eulerian (MM-ALE) methods in LS-DYNA and compared to experimental results. Blast effects on varying reservoir levels and engineered drainage were investigated to determine the impact on dam stability.

The airblast simulations created craters on the downstream slope and reduced the toe length. While larger explosive masses removed more material, crater dimensions did not significantly increase with explosive mass due to energy loss in air. Circular slip surfaces intersected the crater and reduced stability for dams with no engineered drainage. A horizontal toe drain effectively lowered the phreatic surface away from the blast crater and increased structural stability.

Failure (as defined by a factor of safety less than unity) was induced in dams with no engineered drainage at reservoir levels of 80 percent reservoir capacity or greater. Dams with lower reservoir levels did not experience failure from an explosive airblast event. In addition, failure could not be induced in dams with engineered drainage. It was concluded that explosive airblasts posed a possibility of slope failure only for dams with no engineered drainage that were close to full reservoir capacity.

TABLE OF CONTENTS

LIST OF FIGURES

LIST OF TABLES

1 INTRODUCTION

1.1 PROBLEM STATEMENT

Understanding the vulnerability of embankment dams to blast loading is a key requirement for the protection of national infrastructure and studies in this area can provide important understanding for the construction or retrofitting of embankment dams to withstand blast loading as well as earthquake loading. An embankment dam is a dam constructed of materials such as soils, clay, sand, gravel, boulders or fragmented rock and built across a stream to retain water. Approximately 85 percent of the total 70,000 dams in the United States are embankment dams (Billington and Jackson 2006) and were constructed from the 1930s to the 1970s (U.S. Bureau of Reclamation 1986). Many of these dams were not designed to withstand high-stress loading, from earthquake or blast loading, and may be susceptible to failure under dynamic forces.

The response of soil material to blast loading is an important aspect of embankment dam safety based on complex structure geometries, material heterogeneities, and variable saturation states within the dam. The response of an embankment dam subjected to blast loading involves understanding the constitutive behavior of earthen materials under the high stress loading during an explosive event. In addition, the deformation mechanisms of an earthen embankment dam resulting from explosive blast loading must be understood to determine the risk of stability failures.

The majority of studies of explosive airblast loading on structures involve the response of building structures to blast loading. Previous studies of explosive blast loading on soils

have generally included empirically derived relationships to relate explosive quantity to the dimensions of craters formed by the detonation. In addition, studies that involve blast loading of soil structures have generally been performed by government organizations and the results are not open source information. Data for elevated explosive blasts on soils are sparse. Studies typically group results from many different soil types without extensive laboratory tests to characterize the soils.

Due to the number of embankment dam structures in the United States and their range of accessibility, it is possible that an earthen embankment dam could be subjected to blast loading through terrorist activity. Dams could be subjected to ground shock and airblast loading from the close-in detonation of an explosive-filled vehicle could induce large scale deformation and potentially result in structural failure. It is therefore of interest to investigate the effects of blast loading on earthen dam structures.

1.2 OBJECTIVES

The primary objective of this study is to investigate the effects of explosive airblasts on the deformation (crater) induced stability of a homogeneous earthen embankment dam of cohesive soils. To achieve this objective the study is divided into four parts:

1. Laboratory testing to characterize the cohesive soils used in field experiments.

2. Small-scale explosive airblast tests on clay soils to obtain an experimental data set of ground displacement and vibration with which to compare numerical analyses.

3. Finite element simulations of the small-scale blasts to simulate airblast events on cohesive soils.

4. Finite element simulations of explosive airblasts on the downstream toe of an earthen embankment dam composed of cohesive soils. Evaluation of seepage and stability.

Specific tasks performed in this study include the following:

- Laboratory testing to obtain engineering properties including shear strength and compressibility indices.
- Small-scale field experiments of explosive airblast tests on clay soils to obtain ground response data in terms of crater dimensions and ground vibrations.

- Incorporating the results from the laboratory and field tests into constitutive material models for use in numerical finite element simulations.

- Comparing ground response data of experimental explosive airblasts on clay soils to numerical finite element simulations. Evaluation of the numerical model to simulate explosively-induced airblast loads on cohesive soils. Selection of a material model that best characterizes the response of a cohesive soil to airblast loading.

- Investigating the effects of explosive airblasts on a homogeneous earthen embankment dam through the use of finite element simulations. Simulate explosive airblast events located on the downstream toe of an embankment dam through the use of finite element analysis.

- Characterizing the interaction of blast-induced pressures with embankment soils to quantify the deformation to the dam surface by determining crater geometry from the airblast events.

- Evaluating the effects of the explosive airblasts on an earthen embankment dam through seepage and slope stability analyses. Determining seepage conditions and factor of safety (FOS) for each blast event.

- Performing a parametric study to investigate the effects of varying reservoir levels and engineered drainage on dam stability.

2 BACKGROUND

An airblast event occurs when unconfined explosives are detonated in air. Airblast events from explosive detonations near earthen materials result in high-stress, dynamic loading that may make many earthen structures, such as slopes and walls, susceptible to failure. Such a situation may occur with the detonation of explosives contained within a vehicle. A high yield blast event of this nature may induce large scale ground surface deformations and potentially result in structural failure. This chapter describes the background behind an explosive airblast and the response of soils and earthen structures subjected to explosive loading.

2.1 High Explosive Detonation

An explosive is categorized as a low explosive or a high explosive based on its rate of decomposition, or the velocity of the explosive reaction zone. Low explosives deflagrate or burn rapidly, with a reaction zone spreading slower than the speed of sound. High explosives detonate with a reaction zone propagating much faster than the speed of sound. High explosives generally detonate at rates of 6.5 to 8.5 kilometers per second (U.S. Army 1990). The detonation wave is characterized by strong shock energy and can have pressures as high as 40 GPa, which breaks the atomic bonds of the explosive molecules as the detonation wave propagates through the explosive (U.S. Naval Academy 2010).

The explosive energy created during an airblast is often characterized by a TNT equivalency, which compares the energy released during an explosion to the equivalent

mass of TNT required to produce the same amount of energy (Cooper 1996). The TNT mass equivalence of a particular explosive can be described by comparing the heat of explosion of a particular explosive to the heat of explosion of TNT. The TNT mass equivalence is calculated with Equation 2.1

$$TNT\ \ Equivalency = \left(Mass_{Explosive}\right)\left(\frac{HE_{Explosive}}{HE_{TNT}}\right) \qquad \text{Equation 2.1}$$

where $Mass_{Explosive}$ = mass of the explosive in use, $HE_{Explosive}$ = heat of explosion of the explosive in use, and HE_{TNT} = heat of explosion of TNT equal to $4.52(10^6)$ J.

2.2 Shock Wave Propagation

Shock waves occur when a material is stressed beyond the elastic limit by a pressure disturbance. At stresses beyond the elastic limit, the shock wave velocity increases with increasing pressure. In addition, the particle velocity, or the speed at which the shocked material has been accelerated, also increases. Blast waves can typically be modeled as an impulse load due to the almost instantaneous increase in stress following a detonation. The first effect of a blast detonation is an immediate shock wave created by the detonation that quickly decays to a stress followed by a pressure force caused by expanding gases.

Figure 2.1 depicts shock wave formation over distance or time. The velocity at any point along the wave is expressed as the sum of the sound wave velocity and particle velocity

as given by Equation 2.2. At point *A* in Figure 2.1 (a), the pressure, particle velocity and corresponding wave velocity are low. Since wave velocity increases with increasing pressure, the wave velocity at point *B* is higher than at point *A*. Also, the wave velocity at point *C* is higher than that at points *A* and *B*. This results in a steeper wave profile as shown in Figure 2.1 (b) and (c). Eventually the wave profile becomes steeper until points *B* and *C* reach a vertical front aligned with point *A* and the wave becomes a shock wave as shown in Figure 2.1 (d). The vertical wave profile of the shock wave causes the material in front of the shock wave to undergo an abrupt transition from a non-shocked to a shocked state.

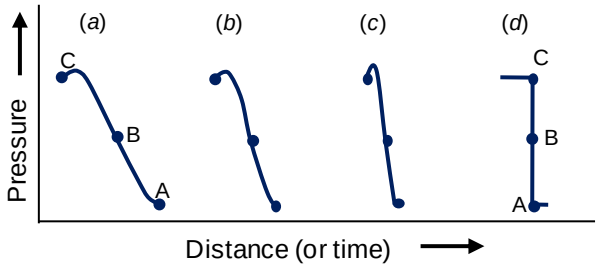

Figure 2.1. Pressure and shock wave profile vs. distance or time (Cooper 1996)

$$U = C + u \qquad \text{Equation 2.2}$$

where U = wave velocity at any point of a pressure wave, C = sound wave velocity, and u = particle velocity.

Figure 2.2 depicts the post-detonation propagation of a square-pulse shock wave over time. The front of the wave shown in Figure 2.2 (*a*) depicts the vertical front of the shock wave. The expansion wave, which is the trailing edge of the shock wave, is represented

by points *A*, *B* and *C*. Point *A* of the pressure wave in Figure 2.2 (*a*) moves into a region of higher density and particle velocity due to the effects of the vertical shock wave front. As a result, point *A* moves with a higher velocity and rapidly catches up to the vertical front as shown in Figure 2.2 (*b*). Point *C* in Figure 2.2 is at zero pressure and therefore has a lower velocity than point *A* and the shock front, causing this portion of the wave to trail behind the rest of the wave as shown in Figure 2.2 (*c*). Attenuation of the shock wave occurs when the trailing edge of the shock wave eventually reduces the pressure and velocity of the leading wave as the wave propagates through a material (Figure 2.2 *d*). The amplitude of the stress wave decreases and the wave changes shape due to energy dissipation. The stress is eventually reduced to the region of elastic behavior and the shock wave decays into a sound wave as shown in Figure 2.2 (*e*).

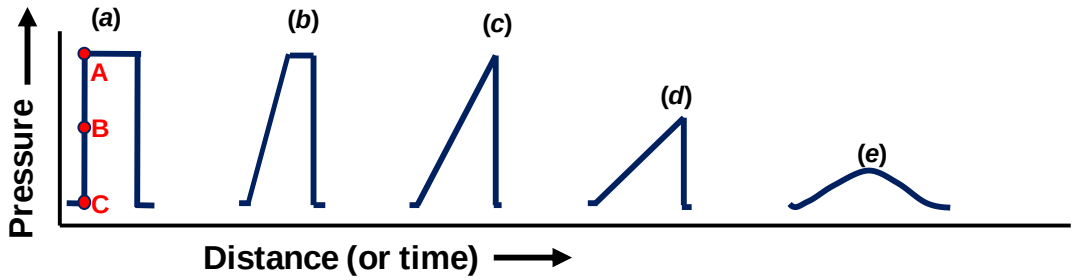

Figure 2.2. Attenuation of a square shock wave (Cooper 1996)

2.3 Explosive Airblasts

An airblast is a term used to describe air pressure waves that are generated by the detonation of an explosive (Dowding 2000). An example of a typical stress time history generated by an explosive airblast on a point in free air space is shown in Figure 2.3 (Baker 1973). An explosive detonation results in a rapid expansion of gases and causes

an abrupt increase in temperature, pressure, density and velocity in the surrounding materials. As shown in Figure 2.3, the pressure (P) increases very rapidly at the arrival time (t_a) of the shock wave with an approximately vertical waveform. The maximum pressure of the shock wave is designated as P_s in the figure. The peak air pressure above ambient air pressure (P_a) is referred to as the peak overpressure and is shown as P_s in Figure 2.3. The peak overpressure is reached almost instantaneously during an airblast event.

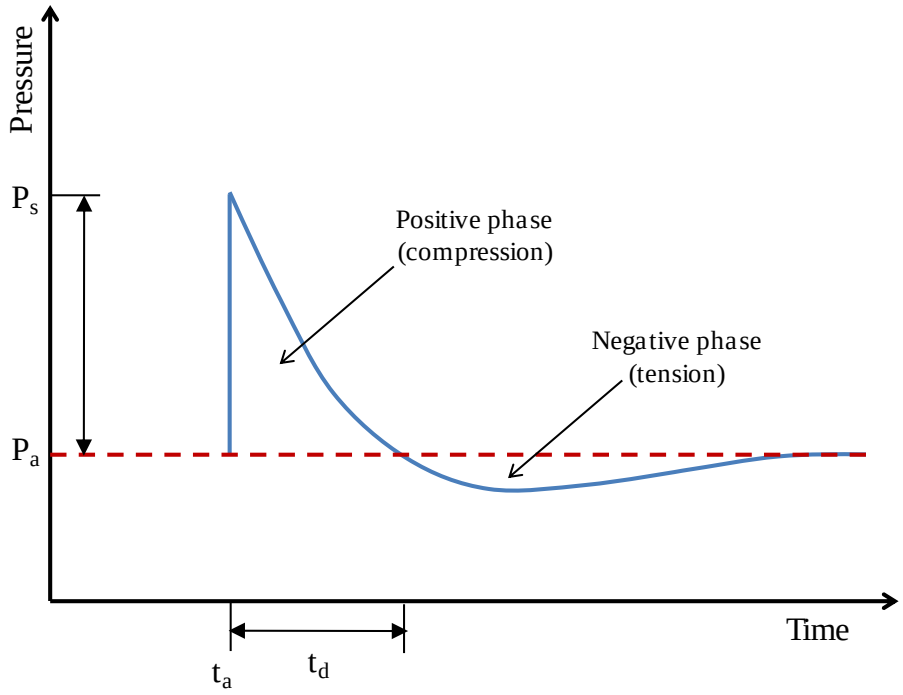

Figure 2.3. Time history of an explosive airblast

After the peak overpressure is reached, the pressure generated by the shock wave decreases in a much slower fashion (few hundredths of a second) until it reaches ambient air pressure at time (t_a + t_d) in Figure 2.3. The pressure then drops below ambient air

pressure after time (t_a + t_d). The duration where pressure is greater than ambient air pressure is referred to as the *positive phase*. The duration where pressure is lower than ambient air pressure is referred to as the *negative phase*.

The explosive airblast creates a stress wave that propagates outward from the explosive source into the air and through the ground surface. Once the stress wave, referred to as the *incident wave*, encounters the ground surface it is transmitted and referred to as the *transmitted wave*. The remainder of the incident wave is reflected back from the surface in the opposite direction as a *reflected wave*. The effects of reflection can vary based on the geometry of the interface and the angle of the detonation point to a surface (Larcher 2007).

2.4 General Material Stress-Strain Response

Constitutive material response can be utilized to describe shock phenomena. Shock behavior is generally described considering uniaxial compressive stress and strain, or the effects along a single axis of the material, with an infinite dimension of the material perpendicular to the strain axis.

Figure 2.4 shows that at low stresses most materials exhibit linear behavior, where the strain produced in a material is directly proportional to the stress that is placed on it. As the stress increases to σ_1, the elastic limit is reached, at which plastic deformation occurs and the material does not return to its original shape after the stress is released. At stress levels between σ_1 and σ_2, a combination of plastic and elastic behavior generally occurs. Elastic-plastic behavior typically occurs at stress levels around ten times the elastic limit.

At stress levels above σ_2, the material exhibits plastic behavior and behaves similar to a fluid. This region is generally studied for blast shock waves due to the high stress levels induced by blast loading.

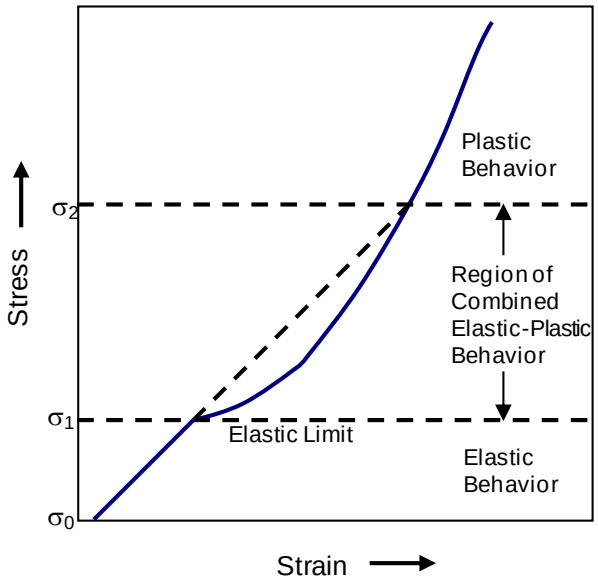

Figure 2.4. Compressive stress-strain curve for varying stress levels

2.5 Soil Response to Airblast Loading

2.5.1 Response of Soil Structure to Airblast Loading

Soil can be defined as a porous, three-phased medium consisting of the solid skeleton, voids within the soil matrix, and void infilling of air or water as shown in Figure 2.5. The three phases of the soil affect the response of the material to blast loading. During explosive airblast events near geologic or soil materials, the soil remains in an undrained condition because loading takes place very rapidly and soil pore pressures cannot dissipate. The soil response in this high intensity, dynamic loading environment cannot

generally be described by conventional soil mechanics, in which loading takes place gradually (such as during construction activities). The compressibility of the solid mineral grains, soil skeleton, and the pore water must be accounted for to adequately describe soil behavior.

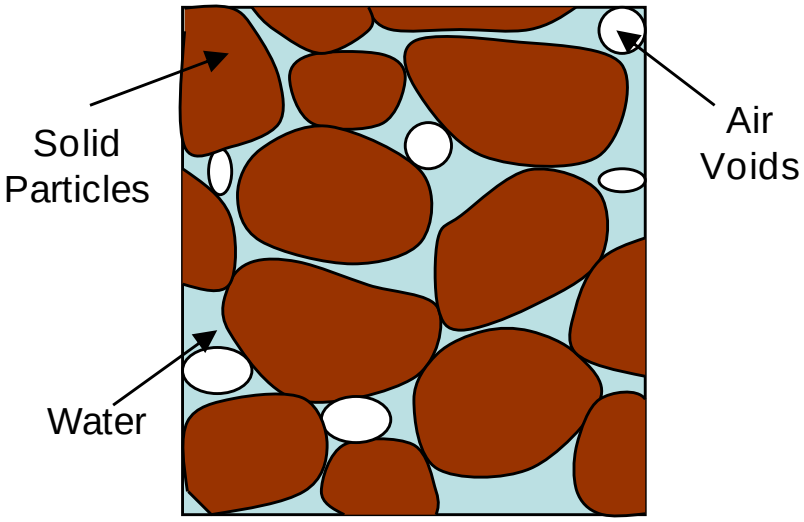

Figure 2.5. Phases of a soil

The compressibility of soils subjected to blast loading depends on the saturation level of the soil. At low pressures, dry soils exhibit elastic deformation along the contact surfaces of the soil skeleton mineral grains. As pressure increases, the grains are further displaced and the soil is compacted. Deformation of saturated soils during rapid dynamic loading is controlled by volumetric compression of the three phases, particularly of the mineral grains and water, as opposed to compression of the soil skeleton (Wang et al. 2004).

Saturated or nearly-saturated cohesive soils are commonly present in an earthen embankment to prevent seepage through the structure. A typical compressibility curve for

a nearly saturated soil (which contains air voids) is shown in Figure 2.6. . At low mean stresses the air voids compress, because of low stiffness and low bulk modulus. This response continues until all air voids are crushed, at which point the compressibility response of the water and solid mineral phases result in a high stiffness and resulting high bulk modulus. For an earthen embankment dam that is newly constructed, air voids will still be present in the material and a two-phase compressibility response such as the curve shown in Figure 2.6 should be anticipated. If the earthen structure has been in place long enough for consolidation to occur and air voids to be crushed out, a single phase, high stiffness soil response should be anticipated.

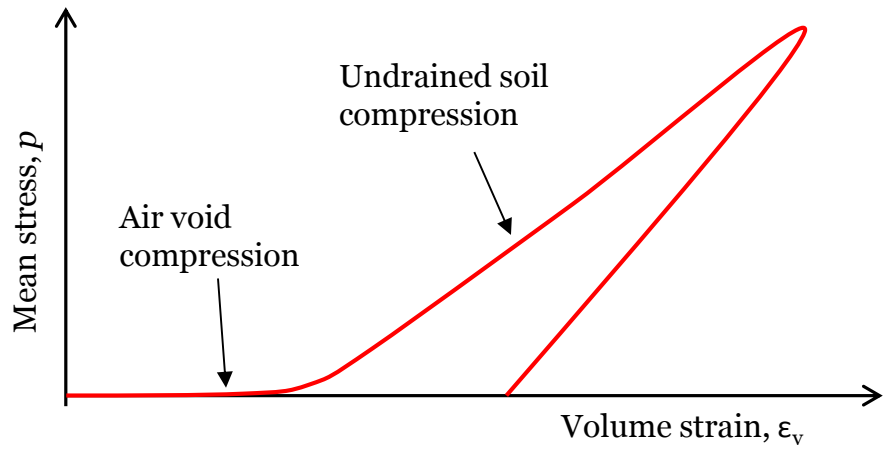

Figure 2.6. Typical compressibility response of a partially saturated soil

2.5.2 Cratering Processes

Soils exposed to explosive airblast loading are subjected to air-induced ground shock that compresses the ground surface and sends a pressure pulse into the material, resulting in the formation of a crater. A schematic of the crater geometry from an explosive event is shown in Figure 2.7. An explosion generates a large amount of energy (in the form of a

shock wave and generation of gaseous products) in a very short period of time (Helwany and Chowdhury 2004). The explosion first generates an initial shock that scours and compacts the soil, resulting in plastic flow and the formation of an initial, "true", crater (Zimmie et al. 2010). Detonation gases are infused into the ground and eject soil (termed "ejecta") into the air as they expand. The direction of the soil particle velocity reverses as a rarefaction wave travels into the compressed material and forms more ejecta (Cooper 1996). Some of the ejecta are deposited back into the true crater as fallback, and the resulting crater geometry after this event is termed the "apparent" crater (Zimmie et al. 2010).

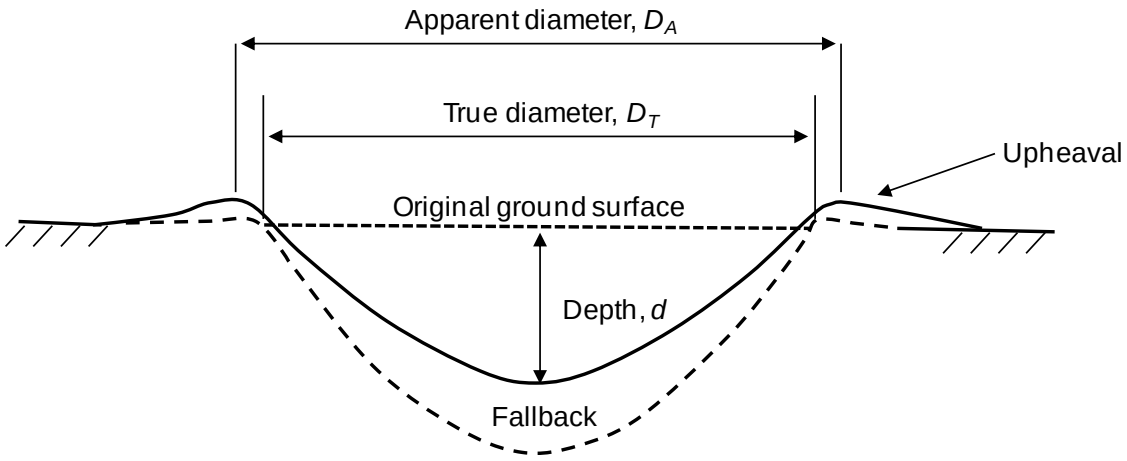

Figure 2.7. Crater geometry from an explosive event (Zimmie et al. 2010)

The location of the explosive in relation to the ground surface has a large effect on the resulting crater formation as shown in Figure 2.8 (Defense Nuclear Agency 1979). Craters formed from airblast events, labeled "near ground bursts" in Figure 2.8, typically generate shallower craters with large diameters. Blasts located on the ground surface or with a shallow depth of burial (DOB) generate deeper craters that are hemispherical in

shape. The explosive DOB can be optimized to generate maximum crater volume and induce significant damage in an earthen structure. Once the DOB becomes greater than this optimal level, the resulting crater volumes decreases until only subsurface craters that have no expression on the ground surface are created.

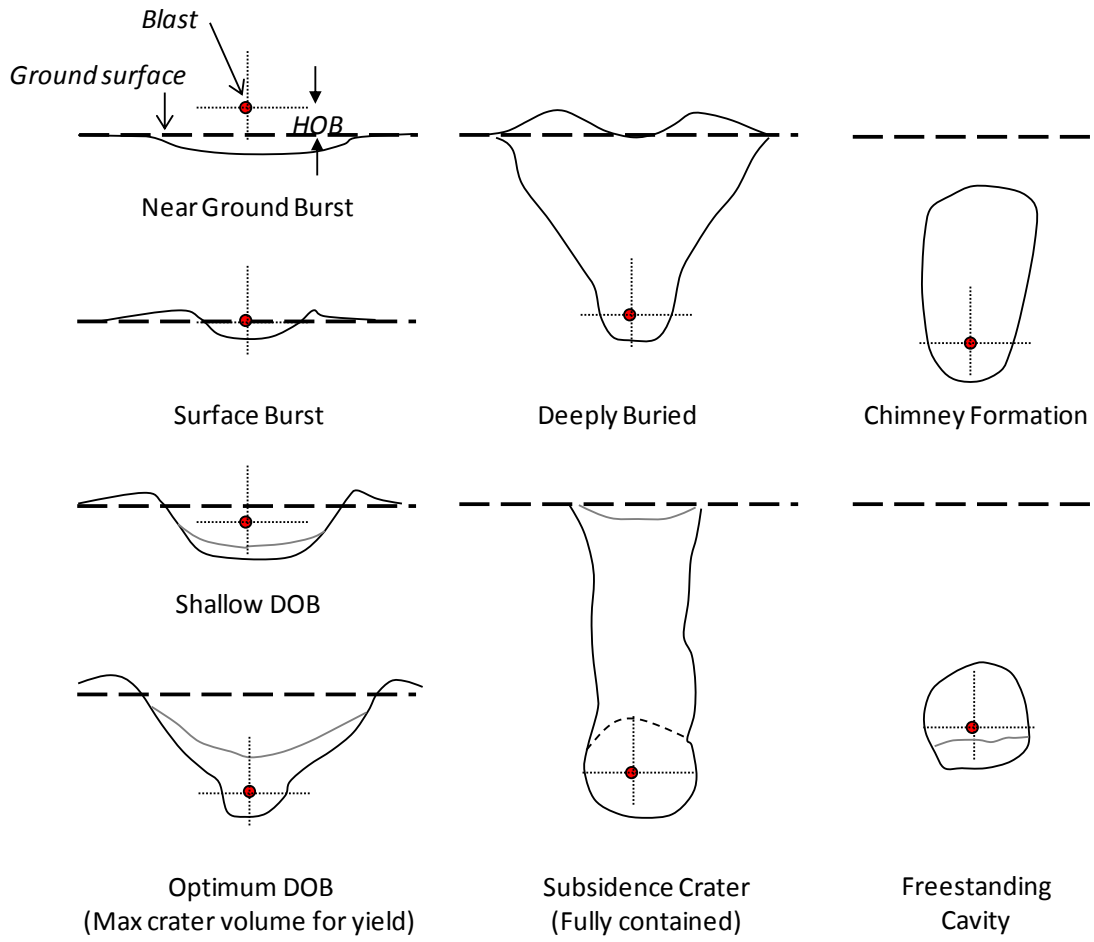

Figure 2.8. Crater types resulting from a variety of burst positions (Defense Nuclear Agency 1979)

While explosive airblast events may not optimize the crater volume in a structure, these events are still of interest to study because a high yield airblast event could be a quick and efficient method to deploy in a terrorist event through the detonation of an explosive-

filled vehicle on an earthen structure. It is of interest to determine if a large enough payload could induce large scale deformations that could lead to the failure of the earth structure.

Numerous historical explosive tests conducted have been conducted in varying geology by government organizations to study cratering efficiency as a function of geology type (Defense Nuclear Agency 1979). Average craters were compared for near-surface bursts in materials ranging from hard rock to soft sand and clay. Geologic properties greatly affected the resulting craters formed after the explosive events. The properties that had the greatest effect on cratering behavior were moisture content, shear strength, dry porosity and compressibility. The soil moisture content had the most significant effect on crater volume for a given explosion. Increased moisture content decreased the shear strength of the material, which in turn resulted in larger craters. Saturated soils resulted in the largest observable craters for a given explosive detonation. Porosity and compressibility of the soil greatly affected the amount of energy that was coupled into the medium. Soils with high air-filled porosity and compressibility allowed more energy to be imparted into the soil and created larger craters.

A well-known study of airblast explosions on soils was performed by Kinney and Graham (1985), who compiled the results of 200 accidental, large magnitude surface explosions on soils and developed an empirically derived equation that estimated the apparent crater diameter to be equal to eighty percent of the cubed root of the explosive charge mass. Kinney and Graham also developed empirical relationships based on this

data that estimated crater depth to be approximately one quarter of the diameter. Vortman (1977) compiled results from high explosive surface blasts in soils and showed that the ratio of apparent crater radius to depth increased with increasing explosive energy and varied based on site soil conditions. Ambrosini et al. (2002) performed numerous small scale, elevated explosive tests on in-situ, fine grained soils and developed an empirical relationship that showed an increase in crater dimensions with increasing explosive mass and decreasing blast height. Numerical studies were also performed by Ambrosini and Luccioni (2006) and relationships were developed to estimate crater dimensions from spherical surface blasts.

2.5.3 Energy and Attenuation Measurement Methods

A common method of analyzing data from open air detonations is in terms of scaled distance, which scales the airblast effects through the Hopkinson-Cranz scaling relationship (Kinney and Graham 1985) as shown in Equation 2.3. The relationship states that a similar explosive energy is generated when two different explosive masses with identical geometry are detonated in the same atmospheric conditions. This allows the distance from an explosive charge mass to be expressed in terms of a scaled distance and is a useful way to compare blast energy from explosive events with varying charge mass and distance.

$$SD_h = h/W^{1/3} \qquad \text{Equation 2.3}$$

where SD = scaled distance above the ground surface (m/kg$^{1/3}$), h = blast height above the ground surface (m), and W = equivalent mass of Trinitrotoluene (TNT) (kg).

During an airblast event, soils are subjected to air-induced ground shock, which compresses the ground surface and sends a pressure pulse into the subsurface soils which results in ground motion. Ground motions generated during a blast event are a function of the explosive mass and the distance from to the blast source and are generally recorded through a time history of acceleration or velocity. A predictive relationship between the charge mass and distance was developed by the U.S. Bureau of Mines based on extensive empirical site studies performed for mining applications (Nicholls 1971). The studies plotted vibration data versus scaled distance on log-log plots and determined an attenuation data fit by least squares methods as shown in Equation 2.4. The maximum ground motion for numerous blast events was described through the peak particle velocity (*PPV*) in the vertical direction, which is the maximum vertical ground motion perpendicular to the horizontal ground surface. *PPV* values are commonly used in construction vibration standards to prevent damage to structures by specifying allowable blast and construction-induced vibration limits (Ozcan et al. 2012). The attenuation of air overpressures is similarly described by Equation 2.4.

$$PPV = K(SD)^{-b} \qquad \text{Equation 2.4}$$

where *PPV* = peak particle velocity in the vertical direction (cm/s), *SD* = scaled distance from blast ($m/kg^{1/3}$), *K* = K-factor, and *b* = attenuation exponent.

The K-factor describes the relative magnitude of explosive energy coupled into the ground and is defined as the intercept of the attenuation trendline at a *SD* value of one.

The K-factor is highly dependent on site geology and generally must be experimentally derived for a specific site through the measurement of blast-induced ground vibrations to obtain the most representative value (Nicholls 1971). However Kumar et al. (2014) developed empirical predictions of the K-factor based on soil properties when site-specific investigations aren't possible. The slope term, *b*, describes the rate of decay in *PPV* with distance from the blast. Large values of *b* result in a steep slope and indicate that the energy from the blast is absorbed quickly and that blast vibrations do not attenuate to far distances. A slope approaching zero indicates far-attenuating blast energy.

2.6 Constitutive Modeling of Soils Subjected to Dynamic Loading

Numerical modeling of soil behavior under blast loading has been studied by numerous authors. The soil response is difficult to capture due to the abrupt increase in pressures within the material during blast loading. Various numerical constitutive models have been developed to attempt to capture the behavior of soils under rapid dynamic loading. A discussion of some of these models is provided in the sections below.

2.6.1 Mohr-Coulomb Plasticity Model

Constitutive soil modeling can begin with a review of the classical Mohr-Coulomb plasticity model. This model is commonly used to describe soil behavior with the well-known shear strength criteria given in Equation 2.5.

$$\sigma_y = \tau - (c - \sigma \tan\phi) = 0 \qquad \text{Equation 2.5}$$

where σ_y = yield function, τ = shear stress on the failure plane, σ = normal effective stress on the failure plane, c = cohesion, and φ = angle of internal friction.

The Mohr-Coulomb yield criterion is described in terms of maximum and minimum principal stresses, which is computationally simple but does not account for the effects of intermediate principal stresses. The yield surface becomes more complicated in three dimensions and is shown by Equation 2.6 (Abbo and Sloan 1995). The surface is described in a pressure versus stress deviator space and incorporates a lode angle function, $K(\theta)$. The lode angle describes the magnitude of the intermediate principal stress, σ_2 to the minimum principal stress, σ_3 and the maximum principal stress, σ_1. The lode angle has values of +30° for triaxial compression, where $\sigma_2 = \sigma_3$ and -30° for triaxial extension, where $\sigma_2 = \sigma_1$ (Mellegard et al. 2005).

$$\sigma_y = -P\sin\phi + K(\theta)\sqrt{J_2} - c\cos\phi = 0 \qquad \text{Equation 2.6}$$

where σ_y = yield function, P = pressure (mean stress), φ = angle of internal friction, c = cohesion, J_2 = second invariant of the stress deviator, $K(\theta)$ = function of angle θ in the deviatoric plane:

$$K(\theta) = \cos\theta - \frac{1}{\sqrt{3}}\sin\phi\sin\theta,$$

θ = Lode angle: $\theta = \frac{1}{3}\sin^{-1}\left(\frac{-3\sqrt{3}J_3}{2J_2^{3/2}}\right)$,

and J_3 = third invariant of the stress deviator.

The standard Mohr-Coulomb surface forms a hexagonal pyramid in principal stress space. This shape is deficient for numerical calculations because the surface creates a singularity at the crossing of the pressure axis at zero shear strength. This area of the pressure axis is important to capture the effects of surface explosions in soils where there is no confinement, and having a singularity in the yield surface at this point can create numerical instabilities and inefficiencies. The standard Mohr-Coulomb surface also has sharp vertices in the octahedral plane as shown in Figure 2.9 which can result in numerical instabilities.

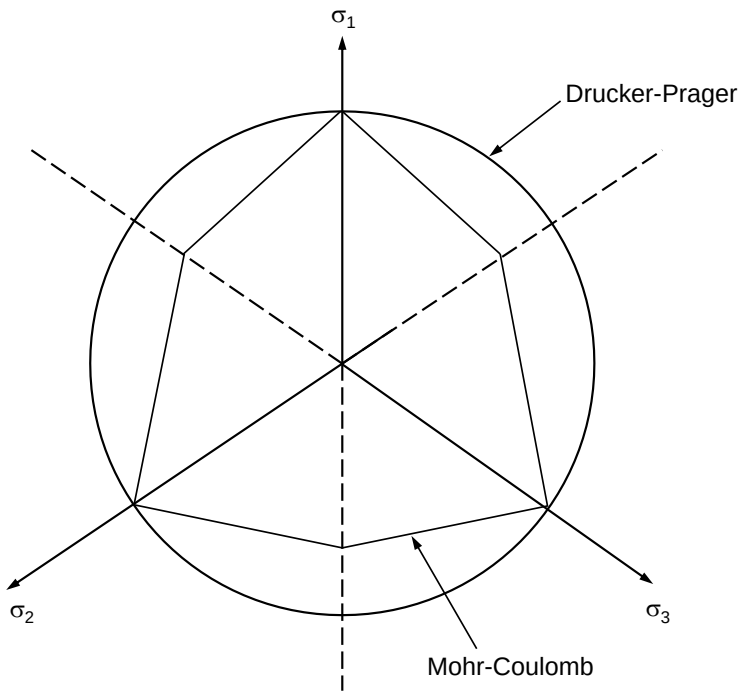

Figure 2.9. Mohr-Coulomb and Drucker-Prager yield surface on the π plane

2.6.2 Drucker-Prager Plasticity Model

The Drucker-Prager model is a smooth generalization of the Mohr-Coulomb model and accounts for the effects of all principal stresses through the use of stress invariants (Desai and Siriwardane 1984). This model is computationally efficient and provides a good first approximation of soil failure (Chen and Baladi 1985). The model can capture elastic soil response, failure and elastic unloading after yielding. The Drucker-Prager yield surface is defined by Equation 2.7 and plots as a straight line in $\sqrt{J_2}$ vs J_1 stress space as shown in Figure 2.10. The surface plots as a circular cone in three dimensional principal stress space and as a circle in the π plane as shown in Figure 2.9. While this consistent surface is computationally efficient for numerical algorithms, a circular failure surface in the π plane does not accurately represent some materials such as cohesionless soils (Chen and Baladi 1985).

$$\sigma_y = \sqrt{J_2} - \alpha J_1 - k \qquad \text{Equation 2.7}$$

where σ_y = yield function; α, k = slope and intercept of yield surface in vs J_1 stress space, respectively; J_1 = first invariant of the stress tensor; and $\sqrt{J_2}$ = square root of the second invariant of the stress deviator tensor.

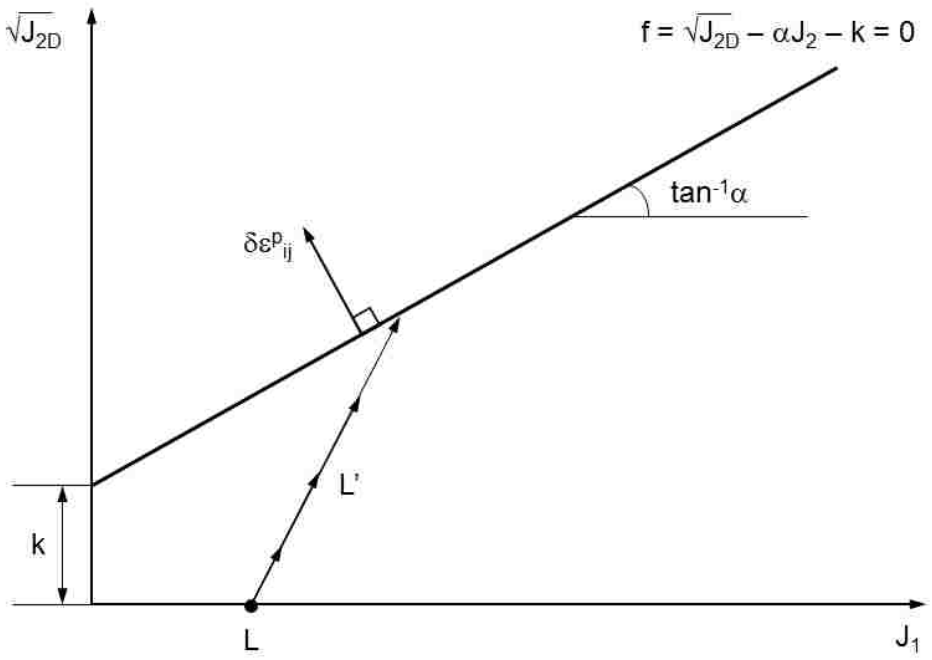

Figure 2.10. Drucker-Prager yield surface (Desai and Siriwardane 1984)

Elastic deformation occurs when the stress state in the material remains below the yield surface, and plastic deformation occurs when the stress state reaches the yield surface. Stress states located above the yield surface are not permitted. The total strain is separated into elastic and plastic components with incremental plastic strain described through an associated flow rule that is normal to the yield surface. The incremental plastic strain has a negative volumetric component which allows dilation to occur at failure (Desai and Siriwardane 1984). This is a drawback to the Drucker-Prager model since most soils primarily undergo compaction during shear loading. Unrealistic dilation occurs in both the Drucker-Prager and Mohr-Coulomb models that can lead to an unrealistic response to shear loading (Hallquist 2006).

2.6.3 Modified Drucker-Prager Plasticity Model

An example of a Drucker-Prager model adapted for numerical simulations is the Federal Highway Administration (FHWA) soil model developed by Lewis (2004). The model is a modified Drucker-Prager plasticity model and was developed to simulate soil-structure interaction of road base soils and safety structures. Advantages to this model are that it attempts to capture the effects of varying saturation levels, strain hardening, strain softening and pore water pressure. A major drawback of the model is that it requires more than twenty input parameters, not all of which can be derived from physical soil testing and must be determined through parametric testing.

The yield surface of the FHWA model follows a modified Mohr-Coulomb yield surface based on the work of Abbo and Sloan (1995). The modified yield surface of the model is presented in Equation 2.8 and shown in Figure 2.11. The surface addresses the deficiencies discussed in Section 2.6.2 with a modified hyperbola fit to the standard Mohr-Coulomb surface. The modified function eliminates the singularity found at the crossing of the pressure axis at zero shear strength by introducing a parameter (*AHYP*) that creates a smooth surface at this intersection. If *AHYP* is set to zero then the standard Mohr-Coulomb surface is retained. The shape of the yield surface in the octahedral plane is corrected through the modification of the *K(θ)* parameter with a function developed by Klisinski (1985) as described by Equation 2.9.

$$\sigma_y = -P\sin\phi + \sqrt{J_2 K(\theta)^2 + (AHYP)^2 \sin^2\phi} - c\cos\phi = 0 \qquad \text{Equation 2.8}$$

$$K(\theta) = \frac{4\left(1-e^2\right)\cos^2\theta + \left(2e-1\right)^2}{2\left(1-e^2\right)\cos\theta + \left(2e-1\right)\left[4\left(1-e^2\right)\cos^2\theta + 5e^2 - 4e\right]^{1/2}}$$ Equation 2.9

where e = eccentricity parameter describing the ratio of triaxial extension to triaxial compression strength, and $AHYP$ = fit coefficient to determine how closely the modified surface is fit to the standard Mohr-Coulomb surface.

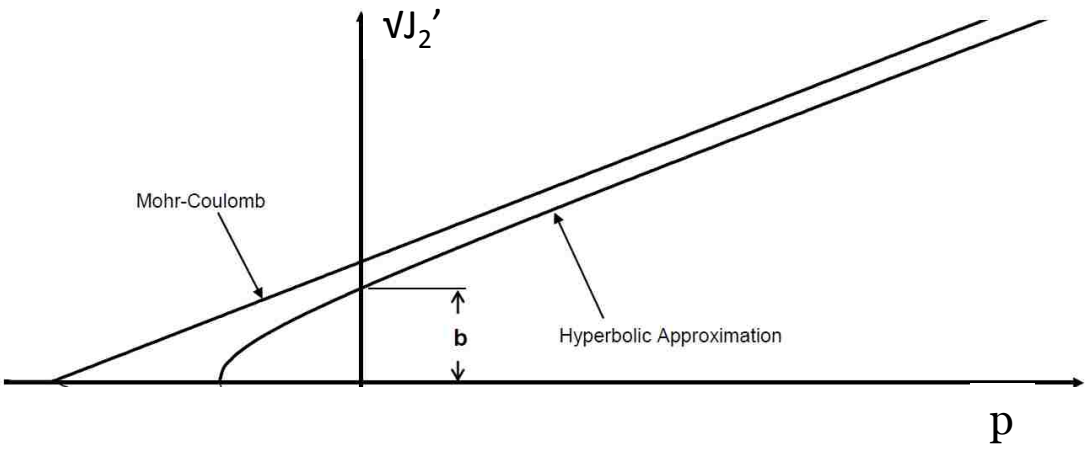

Figure 2.11. FHWA yield surface (Reid et al. 2004)

The FHWA material model accounts for the effects of moisture content and air voids in partially saturated soils by modifying the bulk modulus with a constant, D_1, that controls the stiffness of the soil before air voids are collapsed as shown in Equation 2.10 (Reid et al. 2004). A D_1 value of zero results in standard linear elastic bulk modulus behavior.

$$K = \frac{K_{sk}}{1 + K_{sk} D_1 n_{cur}}$$ Equation 2.10

where K = bulk modulus modified for moisture content and air voids, K_{sk} = skeleton bulk modulus, D_1 = parameter that controls the stiffness of the soil before air voids are collapsed, and n_{cur} = current porosity.

The FHWA material model also simulates the effects of excess pore water pressure by Equation 2.11. The total pressure is reduced by the excess pore water pressure to obtain an effective pressure, which decreases the shear strength of the soil.

$$u = \frac{K_{sk}}{1 + K_{sk} D_2 n_{cur}} \varepsilon_v \qquad \text{Equation 2.11}$$

where u = Pore water pressure, K_{sk} = skeleton bulk modulus, n_{cur} = current porosity, ε_v = total volumetric strain, and D_2 = parameter for pore-water pressure before air voids are collapsed

Lee (2006) conducted experiments of soil liquefaction in saturated sands induced by consecutive blasts of buried, cylindrical charges and performed simulations of the blasts using the FHWA Soil material model. Extensive parametric studies were performed to calibrate and verify the input parameters for the material model. Data from the experimental tests utilized to validate model results included pore water pressure, volumetric strain, shear strain, and particle acceleration.

2.6.4 Simplified Mean Stress Dependent Strength Models

Mean stress dependent strength models can be used to capture the constitutive response of soils due to the dependency of the soil strength on mean stress. Strength models of this

type are also commonly used to capture the response of foam materials. While the models are simplified, they are very robust and have been used for a considerable amount of time, thereby benefitting and improving from user experience and feedback (Thomas et al. 2008). Examples of mean stress dependent strength models are the Soil and Foam model and the next generation of Pseudo tensor model discussed in Hallquist (2014). These models simulate crushing of soil materials through volumetric deformations.

The Soil and Foam model is defined by inputs for mass density, shear modulus, and unloading bulk modulus. The model is also defined by three coefficients that define the shear failure surface of the material and a stress-strain curve that describes the compressibility. In addition, a maximum pressure cutoff in tension, which represents tensile fracture, is required for the model. Tension is no longer allowed in the element if the pressure in an element reaches the specified value.

The shear failure surface for this material model is described by the second deviatoric stress invariant, J_2 as a function of the mean stress, p. The failure surface for the material can be obtained through triaxial compression laboratory testing and is defined using the pressure-dependent, perfectly plastic yield function shown in Equation 2.12, (Hallquist 2014). The yield surface coefficients a_0, a_1 and a_2, are the coefficients of the quadratic fit of the J_2 versus p yield surface curve. The a_0 term is the y-intercept of the yield curve with the J_2 axis, a_1 is the initial slope of the yield curve and a_2 is the curvature coefficient of the yield curve (Thomas et al. 2008).

$$\sigma_y = J_2 - \left(a_0 + a_1 p + a_2 p^2\right) \qquad \text{Equation 2.12}$$

where σ_y = plastic yield function, J_2 = second deviatoric stress invariant, a_0, a_1, a_2 = yield surface coefficients, and p = pressure (equal to mean stress, positive in compression).

Volumetric deformation of the Soil and Foam model is described by a material-specific curve of mean stress versus volumetric strain. The model requires the stress-strain curve to be defined by the natural logarithm of volumetric strain as shown in Equation 2.13.

$$\varepsilon_{\log} = \ln\left(\frac{V}{V_0}\right) \qquad \text{Equation 2.13}$$

where ε_{log} = logarithmic strain, V = current volume, and V_0 = initial volume before loading.

The next generation of the Soil and Foam model is the Pseudo Tensor model (Hallquist 2014), which is another model that is commonly used to simulate earthen materials subjected to high strain, dynamic loading. The model is capable of running in two different modes to define the shear failure surface: a simplified pressure-dependent failure surface and a more complex mode that utilizes two failure surface functions to describe intact and damaged material. Mode one is generally more suitable to capture the response of soils, while the second mode is typically used to describe the response of rigid materials such as concrete or rock.

Mode one of the Pseudo Tensor model can be used to define a Mohr-Coulomb yield surface with an optional Tresca limit as shown in Figure 2.12. The shear failure surface is defined as a curve of stress difference, $(\sigma_1 - \sigma_3)/2$ versus mean stress, p. Mode one of the Pseudo Tensor model is defined by inputs for mass density, shear modulus, tensile cutoff to define tensile failure, and tabulated values that define the shear failure surface.

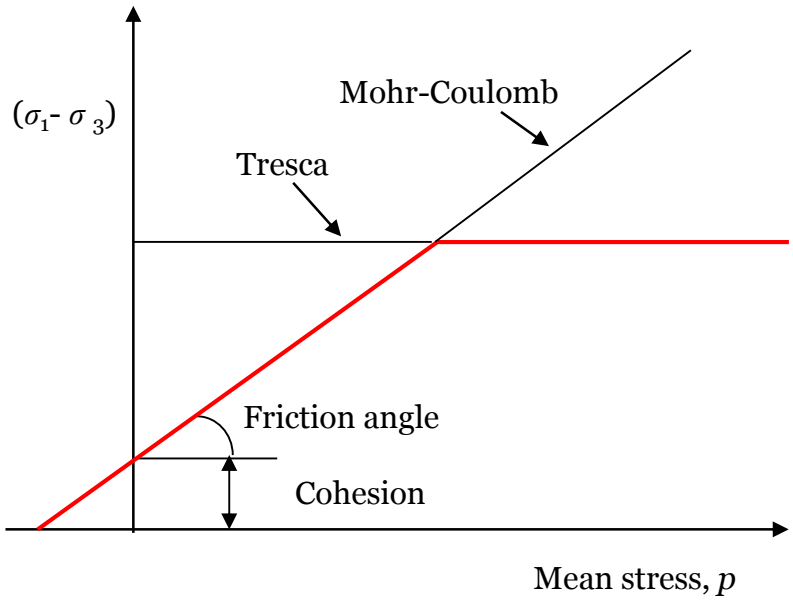

Figure 2.12. Pseudo Tensor model yield surface (Hallquist 2014)

The Pseudo Tensor model must be coupled with an equation of state to describe the compaction of the soil. This generally takes the form of material-specific, tabulated values of mean stress versus true volumetric strain. The model requires the stress-strain curve to be defined by the natural logarithm of true volumetric strain as shown in Equation 2.13. A bulk unloading modulus, K_{Unload}, must also be defined for the compressibility curve to describe the unloading path of the material.

2.6.5 Cap Plasticity Models

Advances in soil modeling include two-invariant cap plasticity models initially proposed by Drucker et al. (1957). These models treat the soil as an elastic-plastic, work-hardening material. Advantages to cap models are that they control the predicted plastic dilatency of the soil and account for hysteresis during hydrostatic loading and unloading (Chen and Baladi 1985).

The cap model accounts for the plastic deformation that is observed almost immediately after a soil is loaded. As loading continues the soil continuously yields until the stress state reaches the ultimate yield state. Cap models account for this behavior by defining successive yield surfaces prior to the final, ultimate yield surface. The yield surface intersects the J_1 axis to account for plastic behavior under hydrostatic loading, forming a convex end cap as shown in Figure 2.13. As the soil continues to yield it exhibits work hardening and a new yield surface is defined when the stress state moves beyond the current yield surface. An advantage of the cap model is that it allows for control of the amount of dilatency caused during shear loading, which can reach unrealistic values in Drucker-Prager or Mohr-Coulomb models that do not allow for the control of this response (Hallquist 2006). The cap surface contracts through a hardening law and controls the dilatency of the material.

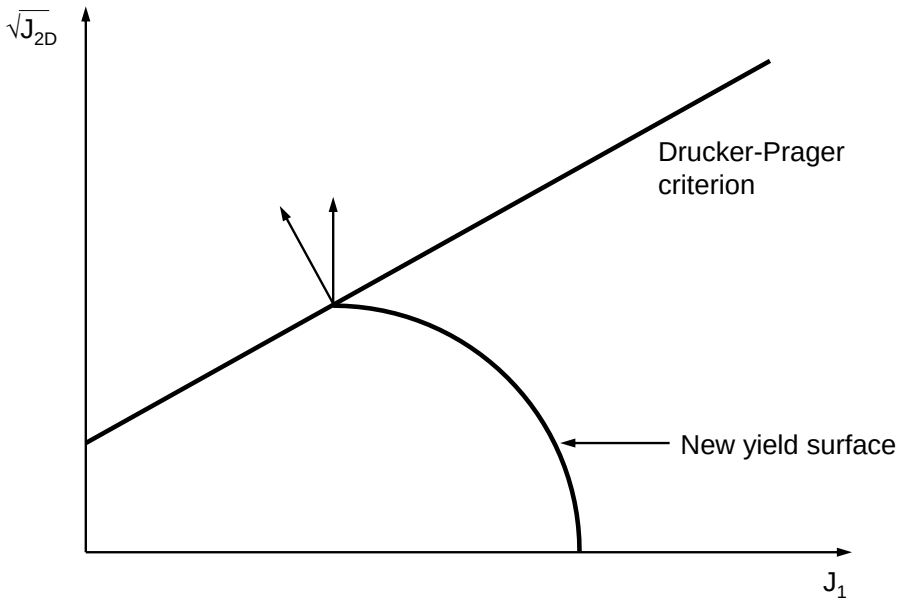

Figure 2.13. Geologic cap model yield surface (Desai and Siriwardane 1984)

Further improvements to the cap plasticity model included nonlinear kinematic hardening models developed by Isenberg et al. (1978). This model was developed to capture the effects of blast loads on geologic materials. The inviscid cap plasticity model is an example of a two-invariant cap model with kinematic hardening developed for numerical analyses. The model is based on the nonlinear kinematic hardening models and the formulations of Simo et al. (1988, 1990) and Sandler and Rubin (1979). The failure surface and the cap are defined by Equation 2.14. The total volume strain is separated into elastic and plastic components. The hardening function is related to the plastic volume strain by Equation 2.15. More recent advances of this type of model include the incorporation of the third stress invariant, strain rate effects and damage modeling (Schwer and Murray 1994).

$$\sqrt{J_2} = \alpha - \gamma \exp(-\beta J_1) + \theta J_1 \qquad \text{Equation 2.14}$$

where $\sqrt{J_2}$ = square root of the second invariant of the stress deviator tensor; J_1 = first invariant of the stress tensor; and α, β, θ, and γ = failure envelope coefficients

$$\varepsilon_v^p = W\{1 - \exp[D(X(\kappa) - X_0)]\} \qquad \text{Equation 2.15}$$

where ε_v^p = plastic volume strain, W = hardening law coefficient (generally assumed equivalent to air-filled porosity), D = hardening law exponent, X_0 = hardening law exponent (generally assumed zero for soil), κ = J_1 coordinate of the intersection of cap surface and failure surface.

Other forms of the cap model include a viscoplastic cap model (Tong and Tuan 2007) developed to capture the response of soils under high strain rate loading. The model incorporates the increase in soil stiffness and strength observed during high strain rate loading through the use of an associative flow rule. This allows for higher transmitted pressures and faster shock wave propagation through the material. The viscoplastic cap model was improved by An et al. (2011) by treating the soil material as three different phases (air, water and solid skeleton) and developing an equation of state for each phase to capture the response of the individual phases. A major advantage of this approach is that the model can simulate the behavior of soils with variable saturation levels.

2.6.6 Disturbed State Concept Damage Model

More recent advances in constitutive modeling of soils include the Disturbed State Concept (DSC) developed by Desai (2001). The DSC is a constitutive model that predicts damage in a material using both classical damage and fracture failure techniques. An initially intact material experiences microstructural changes, such as particle reorientation and microcracking as loading is applied. Portions of the material accumulate damage and transition to the "fully adjusted" (damaged) state as loading continues to be applied. Stiff materials, such as granular soil and rock, deform and may become discontinuous during this applied loading. Softer materials, such as saturated clay, may degrade during loading but will generally remain continuous (Katti and Desai 1995). It is for this reason that the DSC method refers to a damaged material as "fully adjusted". The fully adjusted state can be described as void or crack formation in brittle materials or as a critical state in soft, cohesive materials. The critical state is the state in which no volume change occurs during further shearing. In the DSC model, the cumulative response of the material is an interaction between the intact response and the fully adjusted response that is described through a disturbance function.

The DSC can be applied to cohesive soils for both drained and undrained conditions (Katti and Desai 1995). The response of the material can be described through an elastic or plasticity model, while the fully adjusted response can be described through a critical state. The yield surface for the DSC is shown in Figure 2.14. In the figure, point A represents the initial state with no disturbance. Point D represents the fully adjusted or critical state. The general form of the yield surface for the fully adjusted state is described

by Equation 2.16. Point C represents the intermediate state with the average response of the material.

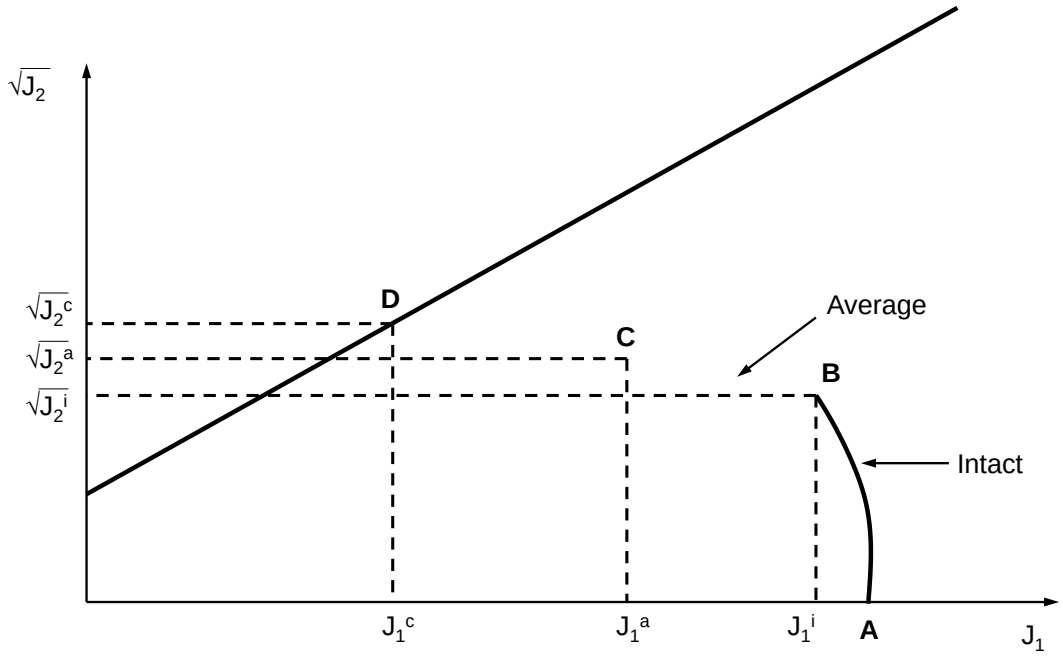

Figure 2.14. Disturbed state concept yield surface (Katti and Desai 1995)

$$\sqrt{J_2^c} = m' J_1^c \qquad \text{Equation 2.16}$$

where $\sqrt{J_2^c}$ = square root of the second invariant of the stress deviator tensor in the critical state, J_1^c = first invariant of the stress tensor in the critical state, and m' = critical state parameters.

The benefits of the DSC concept for constitutive soil modeling are that the method couples the response of the intact and fully adjusted behavior within the material. Thus, the collective, observed response of the material is provided. The incorporation of the

disturbance function also allows for frictional effects from plastic strain increments that are not normal to the yield surface without the use of non-associative plasticity, which can result in an unrealistic response. The DSC has been successfully applied to predict the behavior of cohesive soils subjected to cyclic loading (Katti and Desai 1995).

2.7 Stability of Embankment Dams Subjected to Airblast Loading

Earthen embankment dams are the most common type of dam used worldwide to impound and divert water (Stephens 2010). The following sections describe the evaluation of earthen dam stability and the structural response to explosive events.

Earth embankment dams retain water by relying on their mass to resist sliding and overturning. Key factors that influence stability include dam geometry, soil strength, pore water pressure conditions, and imposed loading on the structure. Key factors that influence stability include dam geometry, soil shear strength, seepage forces, and imposed loading on the structure.

The most common way to assess slope stability is through classic limit equilibrium methods in which a potential sliding mass is discretized into vertical slices with a circular slip surface. Equations of statics that satisfy moment and force equilibrium are used to calculate a single, constant factor of safety as shown in the following equations (GEO-SLOPE International Ltd. 2015b).

$$F_m = \frac{\sum \left(c' \beta R + \left(N - u\beta \right) R \tan \phi' \right)}{\sum Wx - \sum Nf \pm \sum Dd}$$ Equation 2.17

$$F_f = \frac{\sum \left(c' \beta \cos\alpha + \left(N - u\beta \right) \tan\phi' \cos\alpha \right)}{\sum N \sin\alpha - \sum D \cos\omega}$$ Equation 2.18

$$N = \frac{W + \left(X_R - X_L \right) - \frac{\left(c' \beta \sin\alpha + u\beta \sin\alpha \tan\phi' \right)}{F}}{\cos\alpha + \frac{\sin\alpha \tan\phi'}{F}}$$ Equation 2.19

where F_m = factor of safety with respect to moment equilibrium; F_h = factor of safety with respect to horizontal force equilibrium; N = slice base normal force; c' = effective cohesion; φ' = effective friction angle; u = pore water pressure; W = slice weight; D = concentrated point load; β, R, x, f, d, ω = geometric parameters; α = inclination of slice base; and X_R, X_L= interslice shear forces on either side of the slice.

Interslice shear forces are described by a formulation developed by Morgenstern and Price (1965) as shown in Equation 2.20. The shear forces are defined by a half-sine shear function.

$$X = E\lambda f(x)$$ Equation 2.20

where X = interslice shear force, $f(x)$ = shear force function, λ = percentage (in decimal form) of the shear force function, and E = interslice normal force.

A disadvantage of limit equilibrium methods is that they do not satisfy stress-strain constitutive relationships (GEO-SLOPE International Ltd. 2015b). Constitutive relationships may be incorporated into a stability analysis through the use of finite element methods, which calculate stress distributions within the potential sliding mass. Stability analyses can then be performed using the calculated stress conditions.

Explosions on an embankment dam may reduce the stability of the structure. Figure 2.15 depicts an embankment dam subjected to blast loading at the crest and includes a schematic of blast-induced pressure versus time. Region 1 shows the immediate blast region in which the soils exhibit hydrodynamic behavior and move as a fluid. Craters are created in this region as a result of the high-magnitude stresses applied to the dam surface. Region 2 is located deeper into the dam where blast-induced stresses exhibit attenuation and damping. Crater formation in Region 1 may result in slope failure due to reduction of the structure mass or alteration of the phreatic surface location, which can increase interslice forces within the sliding mass.

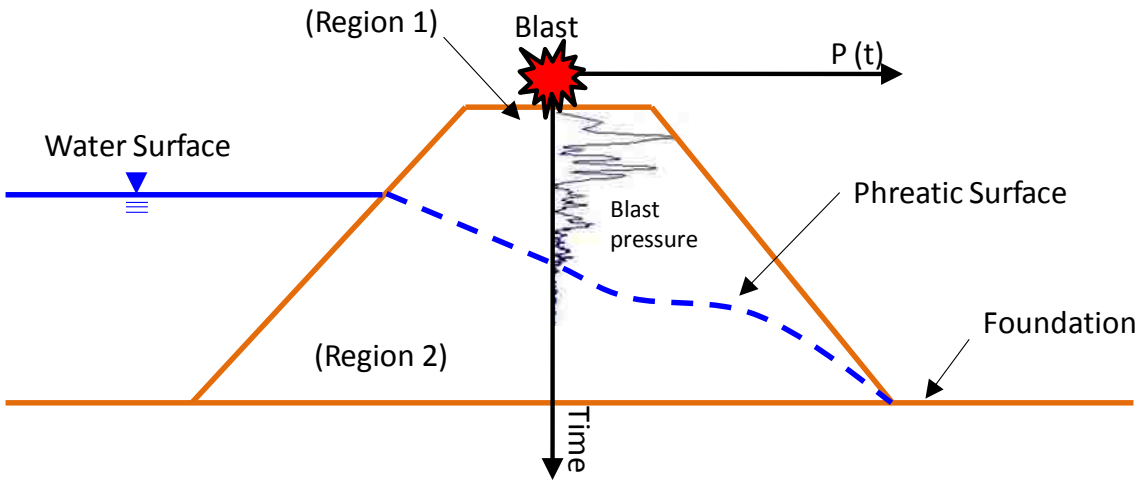

Figure 2.15. Earthen embankment dam subjected to blast loading

Stability analyses of earthen dams subjected to blast loading must therefore account for the effects of craters formed on the structure. Since the September 11, 2011 terrorist attacks there have been interest regarding the effects of explosions on embankment dam

stability. Open source government research has been performed by numerous agencies including the U.S. Army Corps of Engineers (USACE), the U.S. Department of Homeland Security (DHS), and the U.S. Army Engineer Research and Development Center (ERDC) (Sharp et al. 2011). Some experimental research has been performed by the academic community pertaining to explosive loading of granular embankment dams (Charlie et al. 2001, Hatzor et al. 2009, De et al. 2013, Ha 2013).

Li et al. (2007) constructed a small scale dam in in-situ, dry, granular soils and performed surface blasts on the dam crest. The experiments were performed on without retained water (dry conditions). Relationships were obtained for crater diameter and depth versus explosive mass. Afriyie (2014) utilized the results of Li (2007) to validate finite element simulations of explosions on the crest of a granular embankment dam. A parametric study was performed to assess the effects of slope angle and reservoir level on resulting crater size. It was determined that crater dimensions increased with increasing explosive mass, reservoir level, and downstream slope angle.

To the authors' knowledge there have been no studies performed to assess the stability of an earthen embankment dam composed of cohesive soils subjected to explosive blast loading. In addition, the studies previously described have studied the effects of explosive blasts located on the dam crest. Vehicle access to the crest of major dam structures is generally restricted due to security concerns since the events of 2011. Hoover Dam for example no longer allows uninspected vehicles to travel along the highway located on the dam crest, while large box trucks are prohibited (USBR 2016). It is therefore of interest

to study an explosive detonation at locations other than the dam crest (such as the toe) that a commercial vehicle may access.

3 LABORATORY TESTING

Geotechnical characterization tests and strength tests were performed for the clay and sandy soils used in this study to characterize the soils used in the field experiments. A description of the testing is provided in the following sections.

3.1 Clay Soil Testing

The clay soil used in the experiments was a commercial clay manufactured from claystone brick dust mixed with a small amount of fine sand. The clay was manufactured as relatively homogeneous blocks with a consistent density, moisture and fine sand content.

Laboratory tests consisted of geotechnical characterization tests and triaxial compression tests performed in accordance with ASTM standards. Geotechnical characterization test results (performed in accordance to ASTM D1140, D2216, D4318, D6913, and D7263) corresponding to average values for the clay soils are shown in Table 3.1. The laboratory tests indicated that the tested soil was classified as low-plasticity clay based on the Standard Practice for Classification of Soils for Engineering Purposes (ASTM D2487).

Geotechnical characterization tests included unit weight, moisture content, Atterberg Limits, and particle size distribution. A plot of the Atterberg Limits results is shown in Figure 3.1. The results plot as a low-plasticity clay (CL).

Table 3.1. Geotechnical properties of clayey soils used in experiment

Parameter	ASTM standard	Result
Dry density	D2487	1.52 g/cm^3
Saturation	D2487	96.0%
Moisture content, A and C blast series	D2216	28.8%
Moisture content, B blast series	D2216	36.6%
Liquid limit (LL)	D4318	35
Plasticity index (PI)	D4318	15
$C_{0.075\ mm}$ (% passing 0.075 mm)	D1140	92%

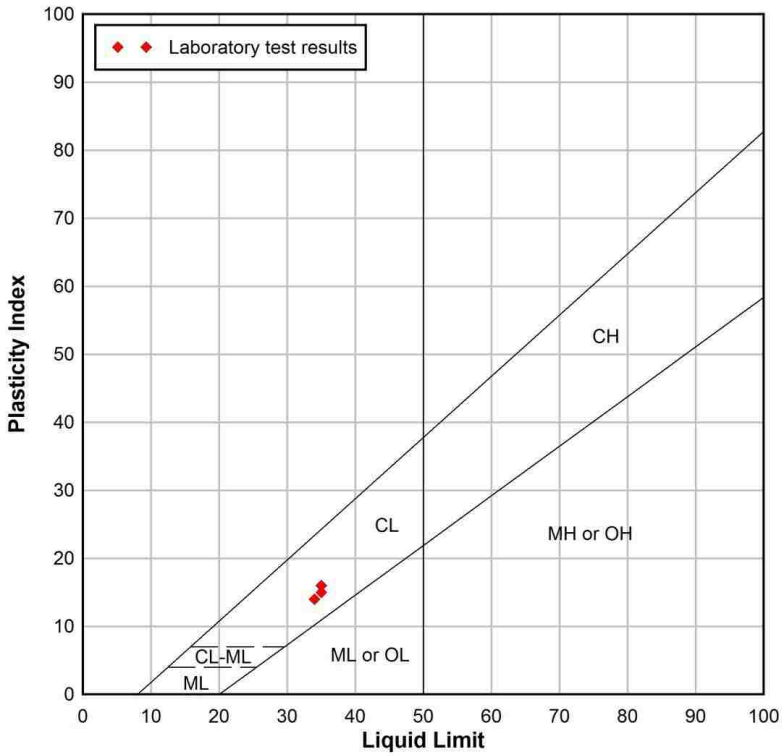

Figure 3.1. Atterberg Limits results from laboratory testing

Unconsolidated, undrained (UU) triaxial compression tests were performed on the clay soils in accordance with ASTM D2850. A photo of the triaxial compression test device is shown in Figure 3.2. In UU triaxial tests, pore pressures do not dissipate and consolidation of the soil does not occur. Undrained tests were selected to represent the conditions of the clay soils utilized in the explosive blast testing, which were in an undrained condition. UU tests were also selected to represent the soil response during blast loading, as the loading takes place very rapidly and pore pressures cannot dissipate.

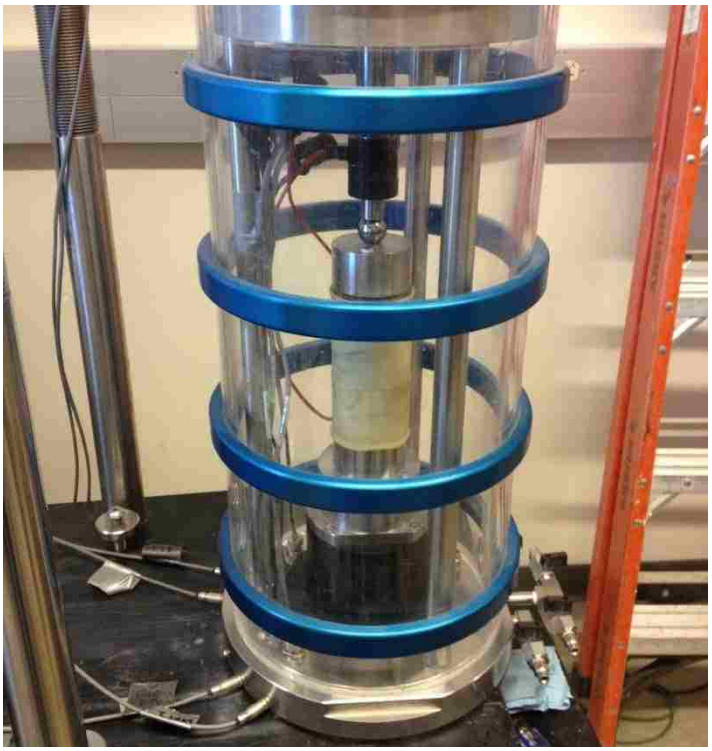

Figure 3.2. Triaxial compression test device

The triaxial tests were performed on three soil samples just below 100% saturation. Confining pressures of 11.7, 23.5 and 28.7 kPa were utilized to represent the range of

overburden stress on the clay soils during the experiments. An axial strain rate of 1% per minute was used, and the failure of the soil was defined as the maximum stress difference observed during testing or the deviator stress at 15% axial strain, whichever was obtained first, based on ASTM D2850. The Mohr-Coulomb shear strength envelope obtained from the test results is shown in Figure 3.3. The results of the triaxial compression tests are summarized in Table 3.2.

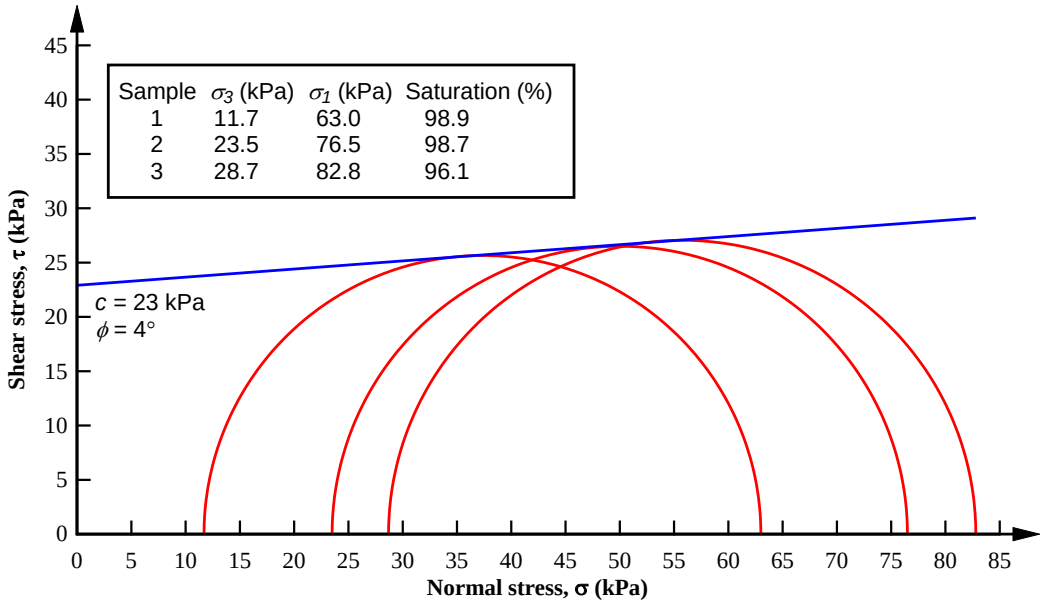

Figure 3.3. Shear strength envelope obtained from triaxial compression testing

Table 3.2. Triaxial compression testing average results

Parameter	Result
Cohesion, c	23 kPa
Friction angle, φ	4°
Elastic modulus, E	7.6 MPa

Unconfined compressive strength (UCS) tests were performed on clay specimens to estimate soil parameters for slow displacement rates and confirm elastic calculations. Cylindrical clay samples were placed in a loading frame on a metal plate as shown in Figure 3.4. The equipment was instrumented with a vertical load cell and linear variable displacement transducer (LVDT) position sensors placed in both the vertical and radial directions to measure vertical and radial displacement.

Figure 3.4. Unconfined compressive strength (UCS) testing

A displacement platen was lowered onto the upper surface of the soil sample at a constant strain rate of 2 percent per minute. The axial stress on the specimen was recorded until failure of the sample was reached (the unconfined compressive strength) as defined by a maximum vertical strain limit of 15 percent. The Poisson's ratio, v was estimated by

plotting radial strain versus axial strain and measuring the slope from the elastic portion of the curve. Similarly, the shear modulus, *G* was estimated by plotting axial stress versus strain difference and measuring the slope from the elastic portion of the curve. Average results from the UCS tests are given in Table 3.3.

Table 3.3. Triaxial compression testing average results for clayey soils

Parameter	Result
Unconfined compressive strength, *UCS*	60 kPa
Poisson's ratio, *v*	0.42
Shear modulus, *G*	2.9 MPa

The shear modulus value from lab testing was checked against elastic calculations using Equation 3.1 with the Poisson's ratio from the UCS test results and the elastic modulus obtained from triaxial compression testing (given in Table 3.2). This resulted in a shear modulus value, *G* of 2.7 MPa, which was consistent with the UCS test results; this shear modulus value was therefore recommended to characterize the clay soils to remain consistent with elastic relationships.

$$G = \frac{E}{2(1+\upsilon)} \qquad \text{Equation 3.1}$$

where *G* = shear modulus (MPa), *E* = elastic modulus (MPa), and *v* = Poisson's ratio

The compressive ultrasonic wave velocity of the clay was determined through laboratory ultrasonic velocity testing performed on 5 cm by 10 cm blocks of clay soil. Piezoelectric

transducers were affixed to each end of the soil block using a clamp as shown in Figure 4.1. A variable frequency signal generator was connected to the transducers and transmitted an ultrasonic source through the soil sample. The signal generator's transmitting source channel and the transducer output were connected to an oscilloscope that measured the applied voltage and displayed both the source wave and compressive wave transmitted through the soil. The difference between the source wave and the arrival time of the transmitted wave was recorded from the oscilloscope screen. The ultrasonic velocity of the longitudinal wave transmitted through the specimen was calculated by dividing the length of the specimen by the arrival time of the compressive wave. Test results are summarized in Table 3.4.

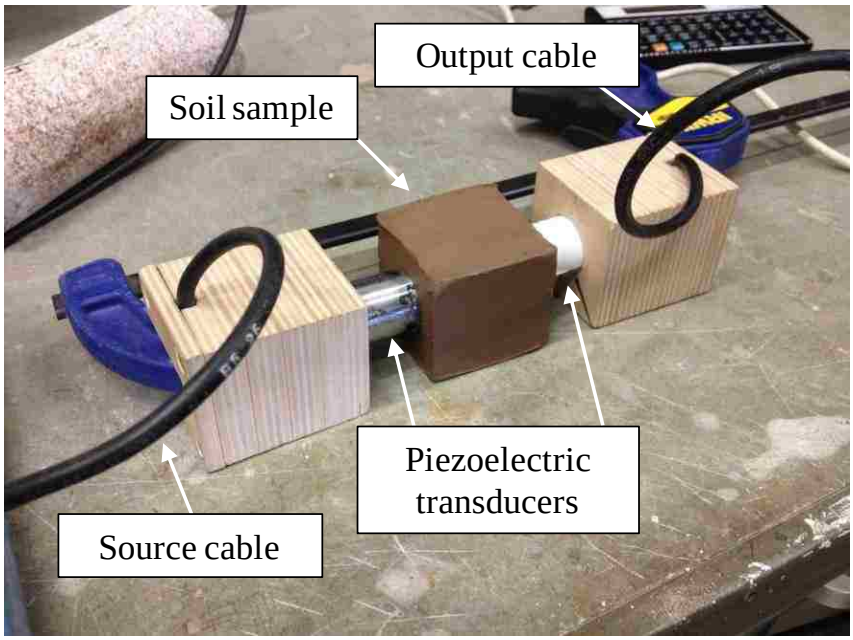

Figure 3.5. Ultrasonic wave speed testing of clay soil

The Poisson's ratio of the clay for undrained conditions was calculated from the compressional velocity using Equation 3.2. This resulted in a Poisson's ratio value close to 0.5, which is consistent with the anticipated value for saturated clay (Hunt 2005). The high Poisson's ratio value from the ultrasonic wave velocity testing indicates that the undrained, dynamic response of the saturated clay soil was exercised.

$$v_p = \sqrt{M/\rho} \qquad \text{Equation 3.2}$$

where v_p = compressional wave (P-wave) velocity (m/s), M = P-wave modulus (Pa), and ρ = mass density (kg/m^3).

Table 3.4. Ultrasonic velocity testing average results for clayey soils

Parameter	Result
Ultrasonic velocity, v_p	1,543 m/s
Poisson's ratio, v	0.4997

3.1.1 Recommended Properties for Use in Analysis

The following paragraphs summarize the recommended clay properties for use in analyses based on the results of the laboratory tests performed in this study. Table 3.5 provides a summary of recommended geotechnical and strength properties for use in analysis.

Based on the results of the laboratory testing, the clayey soils used in the experiment were close to fully saturated with a 96% saturation level. The compressibility curve for

the soil should consist of a two-part curve similar to Figure 2.6, with a low stiffness response to describe the crushing of the air voids until the air porosity value is reached. At this point the compressibility curve should transition to a stiffer response corresponding to undrained compressibility. To determine this transition point, the air porosity of the clay soils was calculated with Equation 3.3 through Equation 3.5 using the laboratory test results from Table 3.1 and an assumed grain density of 2.8 g/cm^3. This resulted in an air porosity of approximately 3%. Based on this result, the compressibility curve for the clay material should transition to a stiffer response at a volume strain value corresponding to an air porosity value of 3%.

Table 3.5. Recommended geotechnical and strength properties for clay soils

Parameter	**Value**
Dry density	1.522 g/cm^3
Moisture content	29.0%
Mohr-Coulomb cohesion, *C*	23.0 kPa
Mohr-Coulomb friction angle, φ	4.0°
Elastic modulus, *E*	7.6 MPa
Shear modulus, *G*	2.7 MPa

$$n_{air} = e - \left(w \cdot \rho_g\right) \qquad \text{Equation 3.3}$$

$$e = n/\left(1-n\right) \qquad \text{Equation 3.4}$$

$$n = 1 - \left(\rho_d / \rho_g\right) \qquad \text{Equation 3.5}$$

where n_{air} = air porosity, e = void ratio, n = soil porosity, w = moisture content (from Table 3.1), ρ_d = dry bulk density (g/cm^3) (from Table 3.1), and ρ_g = grain density (g/cm^3) (Assumed as 2.8 g/cm^3).

The stiffness values (bulk moduli) for the clay compressibility curve were calculated based on laboratory test results using the elastic relationship provided in Equation 3.6. Poisson's ratio inputs used in the equation are summarized in Table 3.6. The elastic modulus value from the triaxial test results (given in Table 3.5) was used in the calculation.

$$K = \frac{E}{3(1-2\upsilon)} \qquad \text{Equation 3.6}$$

where K = bulk modulus (MPa), E = elastic modulus (MPa), and υ = Poisson's ratio .

Two Poisson's ratio values were used: the lower ratio computed from UCS testing was used to describe the soil response prior to crushing of air voids, while the higher ratio obtained from the ultrasonic wave velocity testing, which exercised the undrained, dynamic response of the soil was used to describe the undrained soil stiffness. This approach provided bulk moduli values for the two-part compressibility curve of the clay soils used in the experiment. The recommended compressibility properties for the clay soils are summarized in Table 3.6

The recommended compressibility curve for the clay soil is shown in Figure 3.6. The curve illustrates the low stiffness response prior to the crushing of air voids. After a volume strain of 3 percent (which corresponds to the air-filled porosity) the air voids are crushed and the undrained response characterizes the soil behavior.

Table 3.6. Recommended compressibility properties for clay soils

Parameter	Result
Soil porosity, n	0.457
Poisson's ratio prior to air void crushing, v_1	0.42
Poisson's ratio for undrained response, v_2	0.4997
Bulk modulus prior to air void crushing, K_1	15.8 MPa
Bulk modulus for undrained response, K_2	4,680 MPa

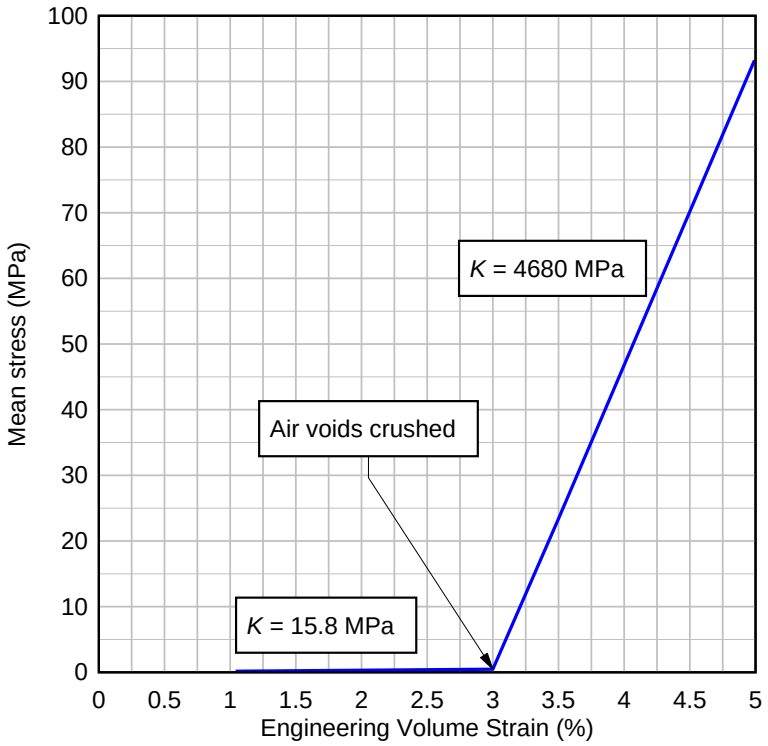

Figure 3.6. Recommended two-part compressibility model for clay soils

To evaluate the accuracy of the undrained bulk modulus used in the model, the modulus obtained from lab testing was compared to equations for bulk and constrained compressibility of undrained, saturated soils developed by Blouin and Kim (1984). The study proposed equations that accounted for the compressibility of each soil phase of air, skeleton, water, and mineral grains. The equations for a fully coupled bulk modulus, which accounts for the effects of different soil phases and effective stress on volume strain in the soil-water mixture, is given in Equation 3.7 through Equation 3.10

$$K_f = K_p + K_m K_s \left[\frac{K_m + K_s - \frac{K_m K_s}{K_g} - K_g}{K_g^2 - K_m K_s} \right] \qquad \text{Equation 3.7}$$

$$K_p = K_d - \frac{K_m K_s}{K_g} \qquad \text{Equation 3.8}$$

$$K_m = \frac{K_g K_w}{K_w + n(K_g - K_w)} \qquad \text{Equation 3.9}$$

$$K_d = K_m + K_s \qquad \text{Equation 3.10}$$

where K_f, K_p, K_d, K_m = fully coupled, partially coupled, decoupled, and mixture model undrained bulk modulus; K_s = bulk modulus of soil skeleton; K_g =bulk modulus of solid grains, K_w = bulk modulus of water; and n = porosity.

Inputs used in the above equations are given in Table 3.7. Based on the equations above, the parameters that most affect the fully coupled, undrained modulus, K_f, are the bulk modulus of the solid mineral grains, K_g and the bulk modulus of water, K_w. The mineral grain modulus was estimated for kaolinite based on a study from the literature on elastic properties of clay minerals (Wang et al. 2001). The bulk modulus of the soil skeleton, K_s has a minimal contribution to the undrained modulus of the soil and was estimated as approximately ten percent of the undrained bulk modulus value obtained from ultrasonic velocity testing. Based on these results, a fully coupled bulk modulus for undrained soil, K_f, was calculated as shown in Table 3.7. The calculated value agrees well with the modulus obtained from ultrasonic velocity testing.

Table 3.7. Inputs and results for calculation of fully-coupled bulk modulus for undrained soil based on Blouin and Kim (1984)

Parameter	**Result**
Bulk modulus of solid grains, K_g	52,000 MPa (7,500 ksi)
Bulk modulus of water, K_w	2,068 MPa (300 ksi)
Bulk modulus of soil skeleton, K_s	400 MPa (60 ksi)
Porosity, n	0.457
Fully coupled bulk modulus, K_f	4,660 MPa (680 ksi)

3.2 Sand Soil Testing

The results of geotechnical characterization tests performed on the sandy soils used as backfill in the field experiments are presented in Table 3.8. The particle distribution curves for the sand material are shown in Figure 3.7.

Table 3.8. Geotechnical properties of sandy soils used in experiment

Parameter	ASTM standard	Result
Dry density	D7263	1.63 g/cm^3
Saturation	D7263	15.4%
Moisture content	D2216	3.5%
Liquid limit (LL)	D4318	Nonplastic
Plasticity index (PI)	D4318	Nonplastic
$C_{4.75\ mm}$ (% passing 4.75 mm)	D6913	78%
$C_{0.075\ mm}$ (% passing 0.075 mm)	D1140	16%

Due to the dry, loose nature of the sandy soil, direct shear tests were performed on the backfill sand rather than triaxial tests to characterize the shear strength of the soil. These tests were simpler to perform due to the loose nature of the sands and provided adequate information to obtain general modeling parameters for the backfill soil that was used to contain the clay experimental soils.

A photo of the direct shear testing apparatus is shown in Figure 3.8. The direct shear tests were performed in accordance with ASTM D3080 at in-situ moisture content. Normal stresses of 4.8, 9.6 and 19.2 kPa were applied to the soil to conduct three-point tests within the stress range of interest based on the overburden pressures on the backfill soils.

Samples were horizontally sheared at a rate of 0.127 mm/min to a final displacement of 12.7 mm. Maximum and residual soil strength parameters were obtained from the direct shear tests as shown in Figure 3.9. The direct shear results are summarized in Table 3.9.

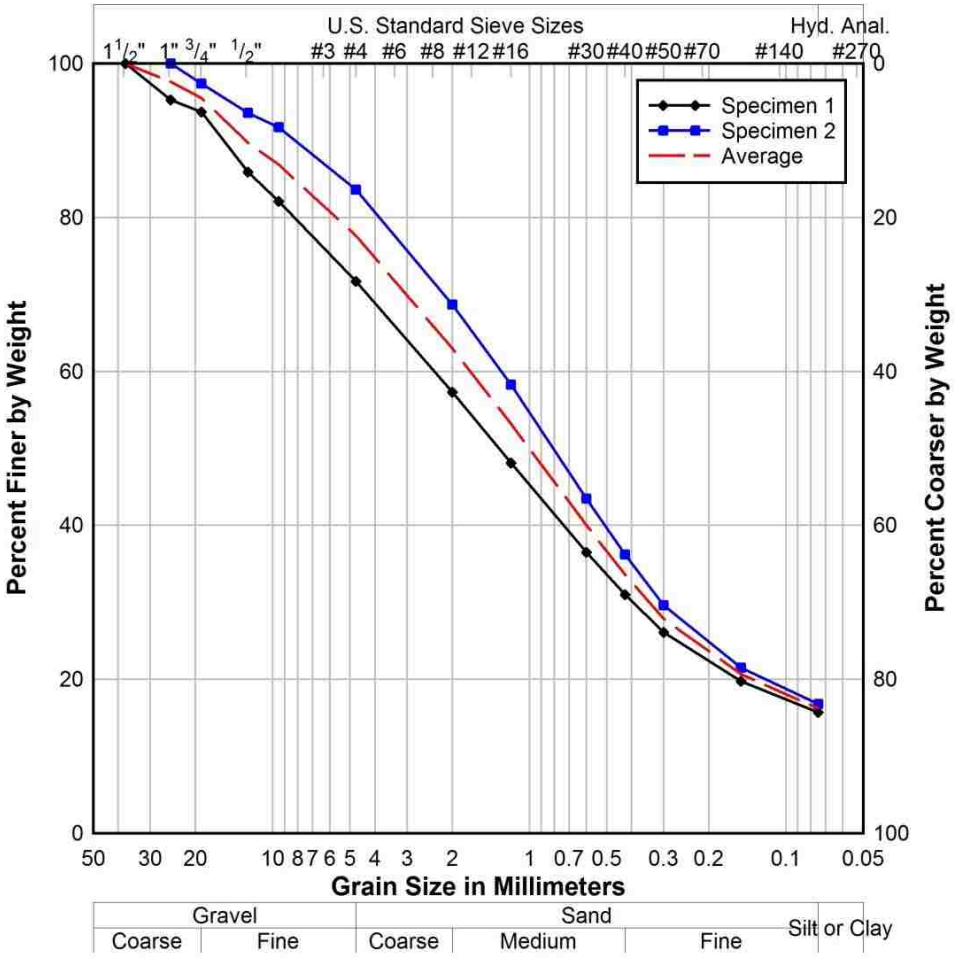

Figure 3.7. Particle size distribution curve for sandy soils

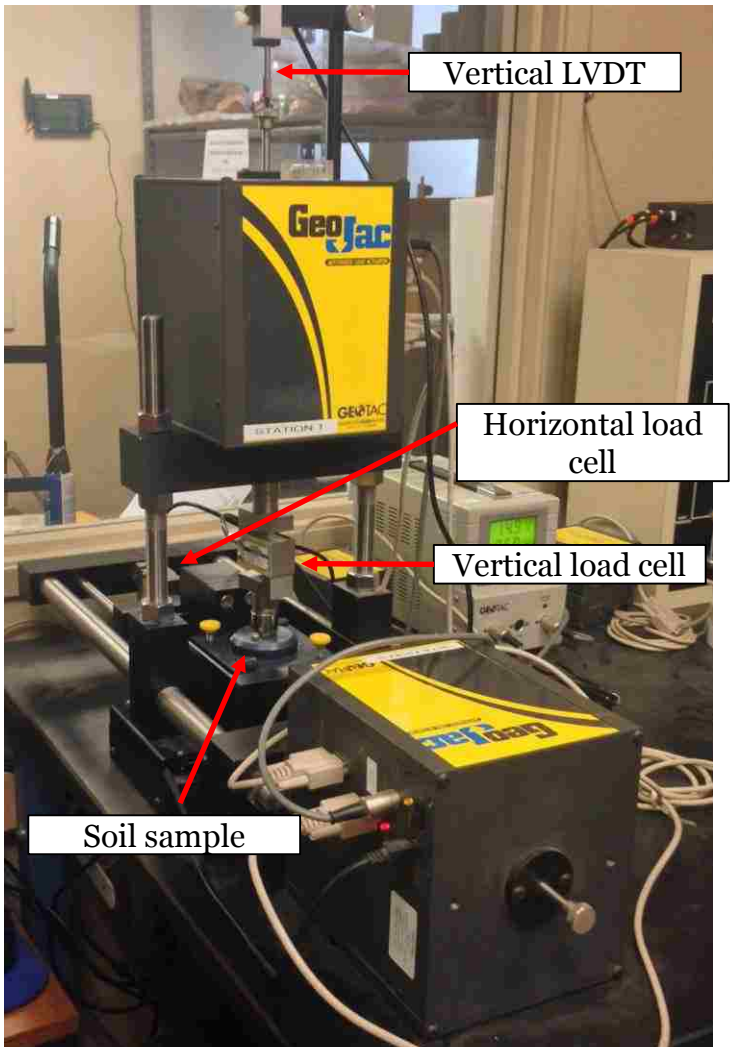

Figure 3.8. Direct shear testing apparatus

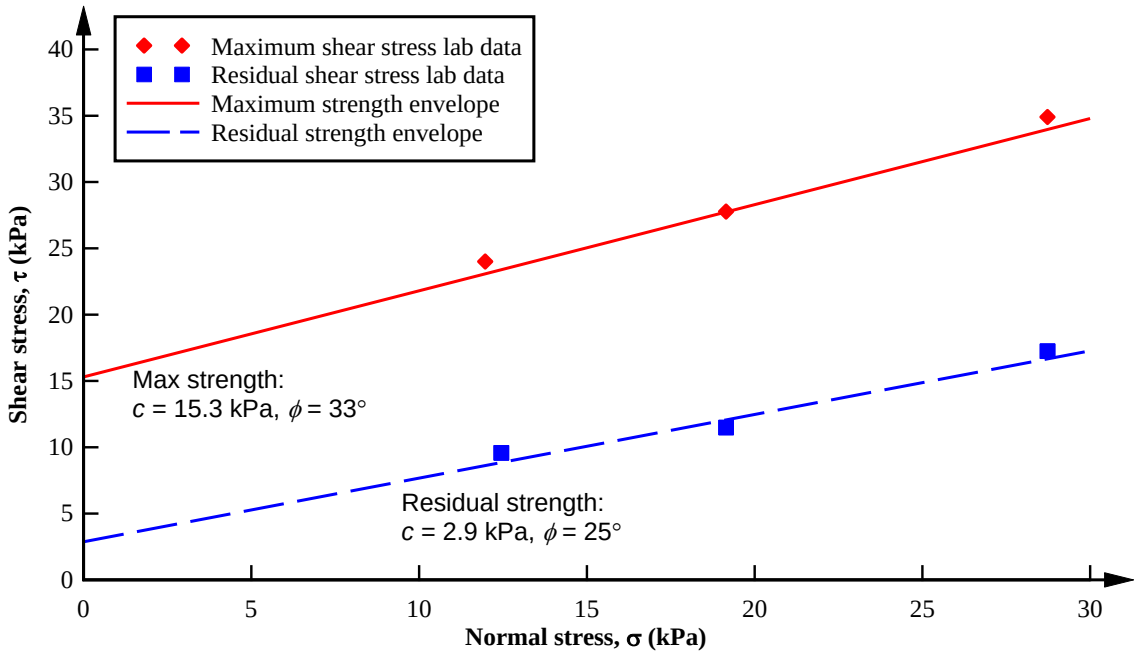

Figure 3.9. Shear strength envelope of sandy soils obtained from direct shear testing

Table 3.9. Direct shear testing average results for sandy soils

Parameter	Result
Maximum friction angle, φ	33.0°
Residual friction angle, φ_{res}	25.0°
Maximum cohesion, c	15.3 kPa
Residual cohesion, c_{res}	2.9 kPa

4 EXPLOSIVE AIRBLAST TESTING

Small-scale explosive airblast tests were conducted on clay soils to obtain an experimental data set with which to compare numerical analyses. The experiment methodology and results are discussed in the following sections.

4.1 Test Methodology

A total of thirty-three explosive airblasts were conducted on the homogeneous and low-plasticity clayey soil previously characterized. Of these, twenty-four tests in three series were performed to measure ground motions and record crater dimensions. The remaining nine tests were performed to obtain airblast data only. The clay soils used in the field experiments were in an equivalent condition (in terms of density and moisture content) as the laboratory testing soils. The test bed is illustrated in Figure 4.1 and was constructed by excavating a pit in in-situ, sandy soils. The pit was excavated to a depth of 1.5 m below the ground surface (bgs) and filled with 15 cm of loosely compacted site soil.

A clay column was constructed within the excavation using a cylindrical cardboard form with a 30 cm diameter and length of 1.2 m backfilled with homogeneous clay soil. The form was lined with plastic sheeting to avoid moisture loss in the clay. The clay was backfilled in small lifts and gently tamped with a tamping rod to mold to the shape of the form and maintain a consistent density. This process was continued until the form was entirely filled with clay. The form was left in the ground during the experiments and was not removed due to the impracticality of extraction after it was filled with clay. It was

assumed that the cardboard form would have a minimum impact on the experiment results from vibration reflections due to its low density.

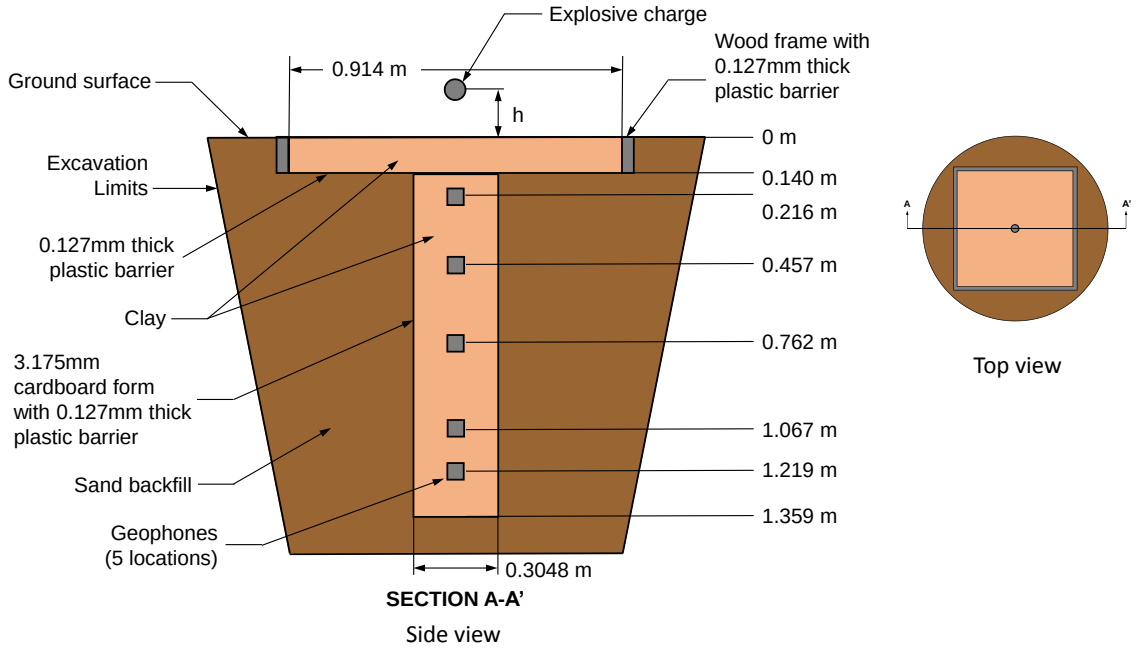

Figure 4.1. Experimental configuration of explosive blast tests

Five triaxial geophones (Figure 4.2) were placed in a vertical array within the clay column during the backfill process at depths of 0.2 m, 0.5 m, 0.8 m, 1.1 m, and 1.2 m bgs. The geophones had a frequency response between 2 to 250 Hertz (Hz). A horizontal surface array of airblast sensors (Figure 4.3) were arranged on the ground surface at distances of 1.6 to 7.8 m to measure air overpressure from the blasts. Seismographs were connected to the geophones and airblast sensors to record ground vibration and air overpressure.

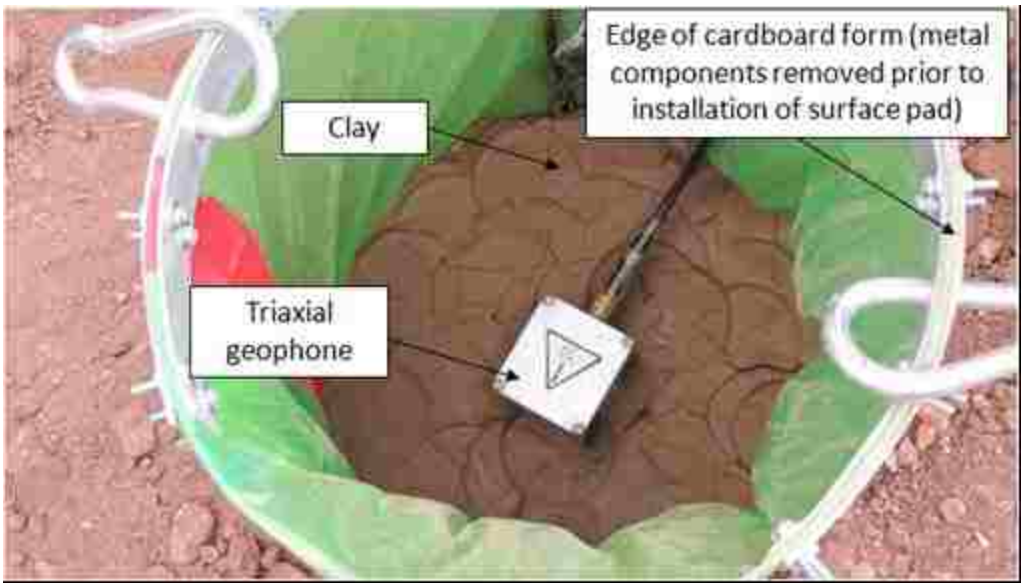

Figure 4.2. Triaxial geophone installation in clay column

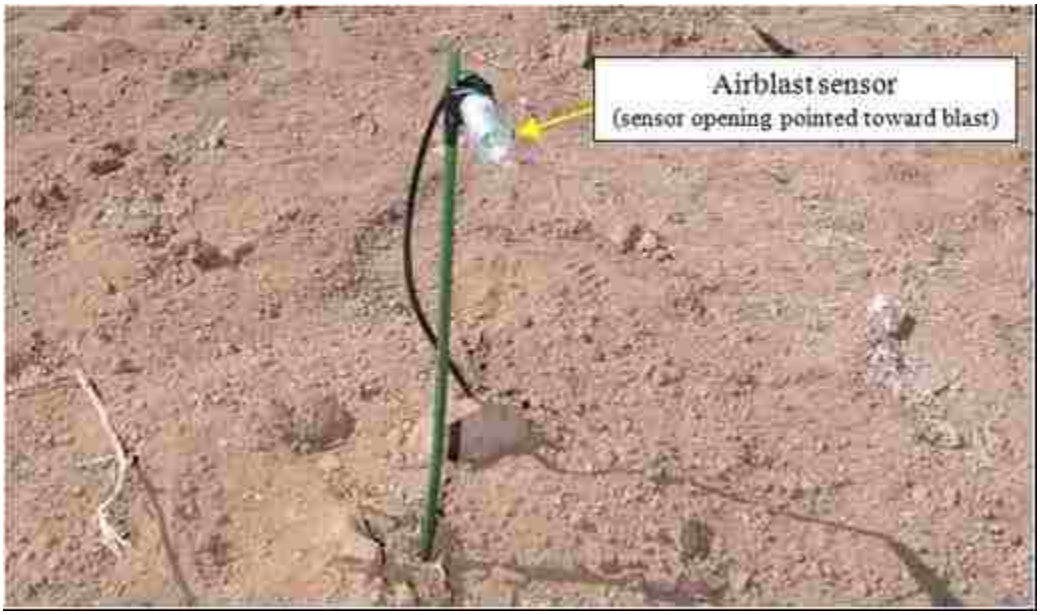

Figure 4.3. Surface airblast sensor

The annular space surrounding the clay column was backfilled with the site sandy soils placed in a loosely compacted condition (corresponding to the average density listed in Table 3.8) to minimize vibration reflections back into the clay column. A square clay pad was constructed near the ground surface to capture blast-induced crater geometries as illustrated in Figure 4.1. The pad was constructed using a 0.9 m by 0.9 m by 14 cm wooden frame placed on top of the clay column and backfill sand. The pad was built by placing undisturbed clay blocks edge to edge within the wooden frame and lightly forming the blocks to build a surface pad. The base of the clay pad was lined with plastic sheeting where it came into contact with the dry sandy soil to avoid moisture loss of the clay. A photo of the finished surface clay pad is shown in Figure 4.4.

Figure 4.4. Clay surface pad constructed to capture airblast-induced craters

The experimental explosive blasts were conducted with spherical explosive charges and axisymmetric loading conditions. The spherical charges consisted of a two-part binary explosive composed of solid ammonium nitrate oxidizer and flammable liquid nitromethane (Hallowell Manufacturing 2009). The explosive had an approximate 85% TNT equivalence. The two components were mixed together, placed into plastic bags, hand-molded into a spherical shape and detonated with an electric detonator containing 0.9 g of explosive.

The explosive charges were suspended with string above the clay surface that was strung across the surface pad and secured on either end with PVC rods as shown in Figure 4.5. The suspension of the charges was configured so that the explosive remained stationary if breezy weather conditions arose. Constant blast suspension heights (h) of 2.5 cm and 7.6 cm above the clay surface were used in the tests and the explosive mass (W) was varied.

The suspension heights were selected to be within a general range that replicated a scaled version of the energy of an equivalent TNT explosive mass, W of 2270 kg (5000 lb) and a blast height, h of 0.8 m (2.5 ft). These parameters were selected to replicate the energy seen in a hypothetical terrorist scenario of an explosive-filled box truck detonated near a structure, such as the Oklahoma City bomb terrorist attack of 1995 (Rogers and Koper 2012). This explosive mass and blast height was used to calculate a blast height that was scaled down to the explosive masses used in the experiments. A target scaled distance,

SD value of 0.06 m/kg$^{1/3}$ was therefore calculated using Equation 2.3 for the experiments in this study.

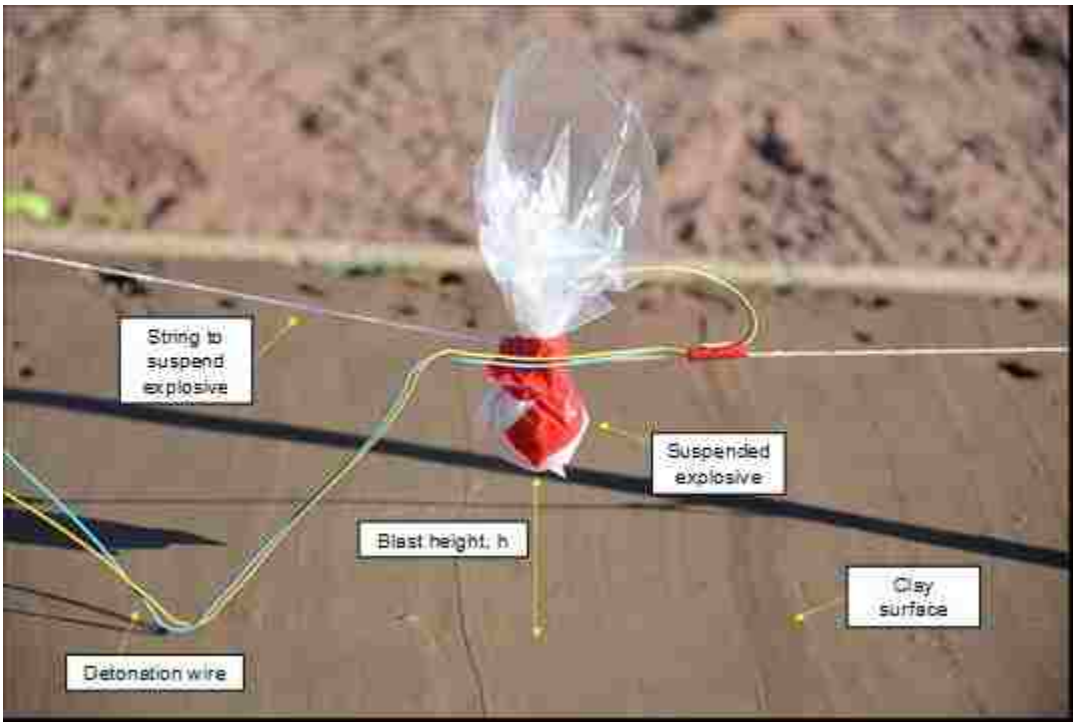

Figure 4.5. Explosive charge suspended over the clay surface (a view of approximately 20° to the surface of the clay)

Table 4.1 presents the test matrix for the blasts conducted in the study with two constant blast offset heights, h of 2.5 cm and 7.6 cm and explosive mass, W ranging from 0.9 to 100.9 g to obtain scaled distances, SD from 0.07 to 0.28 m/kg$^{1/3}$. It was not possible to conduct experiments with SD values smaller than 0.07 m/kg$^{1/3}$ since this would have required a larger explosive mass that could have damaged the shallowest geophone buried within the clay column. The experiments were conducted over the course of three separate days. The blasts were conducted in three series according to blast height and moisture conditions:

- Blast series A were performed with h = 7.6 cm, dry weather and a relatively stable clay moisture content of 28.8%.

- Blast series B were performed with h = 2.5 cm. The B blast series were performed under wet weather conditions that increased the moisture content of the upper surface of the clay pad to 36.6%.

- A new series of tests designated as the C blast series were performed during dry weather conditions so that the soil moisture conditions were the same as the A series tests. This allowed the results of the C series blasts to be directly compared to the A series to ensure that the increased moisture content in the upper few millimeters of the clay surface pad in the B series blasts did not have a large contribution to the resulting crater dimensions.

Table 4.1. Test matrix for experimental blasts (h = the blast height, W = the explosive mass, SD = the scaled distance, w = the soil moisture content)

Blast series	h (cm)	Blast number	W [(1)] (g)	SD (m/kg$^{1/3}$)	w (%)
A	7.6	A-1	5.9	0.422	28.8
		A-2	20.9	0.277	
		A-3	25.9	0.258	
		A-4	30.9	0.243	
		A-5	38.9	0.225	
		A-6	45.9	0.213	
		A-7	50.9	0.206	
		A-8	65.9	0.189	
		A-9	80.9	0.176	
		A-10	90.9	0.169	
		A-11	100.9	0.164	
B	2.5	B-1	0.9	0.265	36.6 (wet clay)
		B-2	5.9	0.141	
		B-3	10.9	0.115	
		B-4	20.9	0.092	
		B-5	30.9	0.081	
		B-6	40.9	0.074	
		B-7	50.9	0.069	
C	2.5	C-1	0.9	0.265	28.8
		C-2	10.9	0.115	
		C-3	20.9	0.092	
		C-4	30.9	0.081	
		C-5	40.9	0.074	
		C-6	50.9	0.069	

[(1)] The explosive mass includes an additional 0.9 g of explosive for the detonator.

A photographic time sequence of one of the explosive tests performed in the study is shown in Figure 4.6. The pre-blast test conditions are shown in Figure 4.6 (*a*) and show the explosive charge suspended above the surface of the clay pad. Figure 4.6 (*b*) illustrates the explosion and resulting fireball, while Figure 4.6 (*c*) provides a visual indication of the surface shock wave from the airblast as evidenced by the disturbed ground surface surrounding the blast.

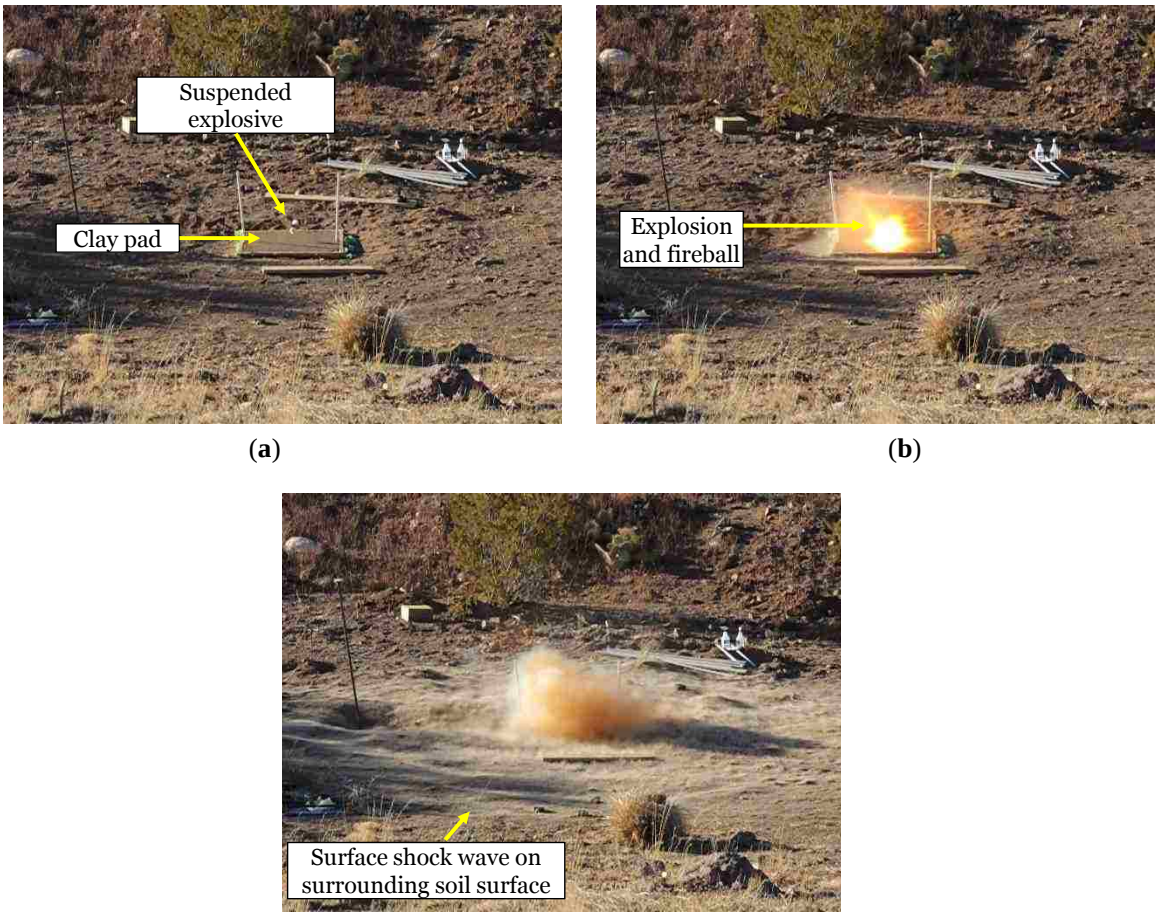

(**a**) (**b**)

(**c**)

Figure 4.6. (*a*) Pre-blast conditions with suspended charge above clay surface pad (*b*) Explosive airblast with resulting fireball (*c*) Disturbed ground from surface shock wave

The explosive blasts displaced the clay surface pad and formed craters; an example of a crater generated by a blast is shown in Figure 4.7. The dimensions of the craters generated in the clay surface pad were measured after each blast as shown in Figure 4.8 using a profiling tool placed inside the crater. Measurements included true diameter, D_T, apparent diameter, D_A and depth, d. Measurements were taken in two perpendicular directions (North to South and East to West) across the crater and traced onto cardboard to capture the profile shape. Profiles for some of the larger blasts were not fully captured because the depth of the crater exceeded the physical dimensions of the profiler. However, the diameters and depths were still measured for these craters and the profile shape was estimated from these measurements and crater photos.

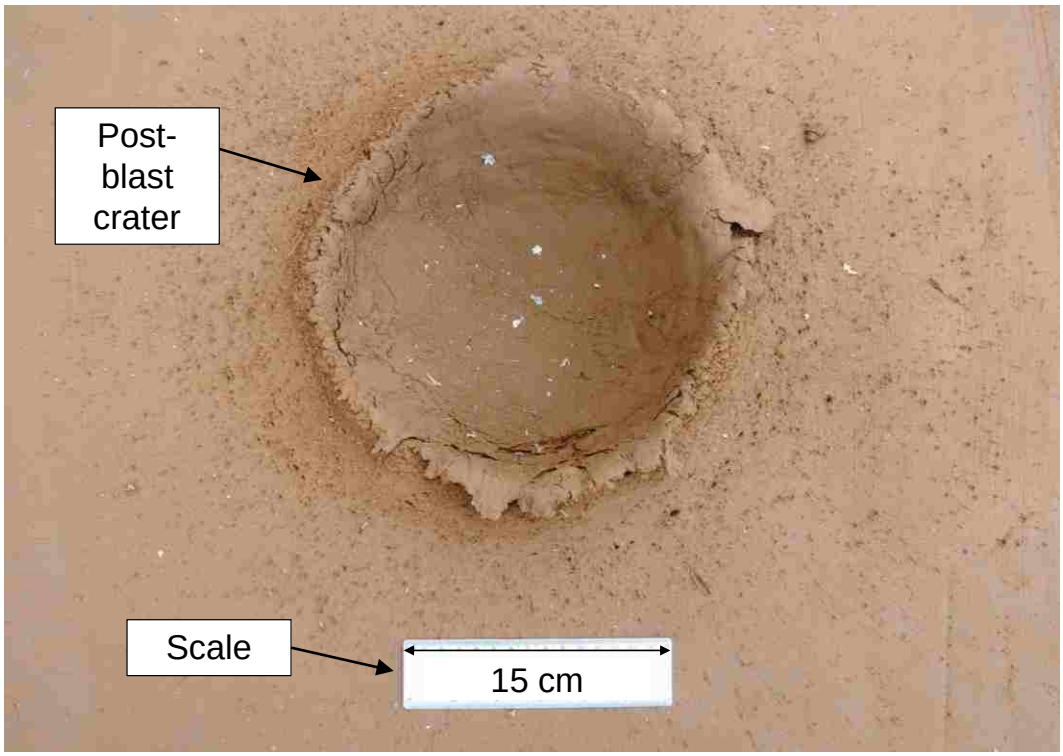

Figure 4.7. Plan view of crater formed on the clay surface after an explosive blast

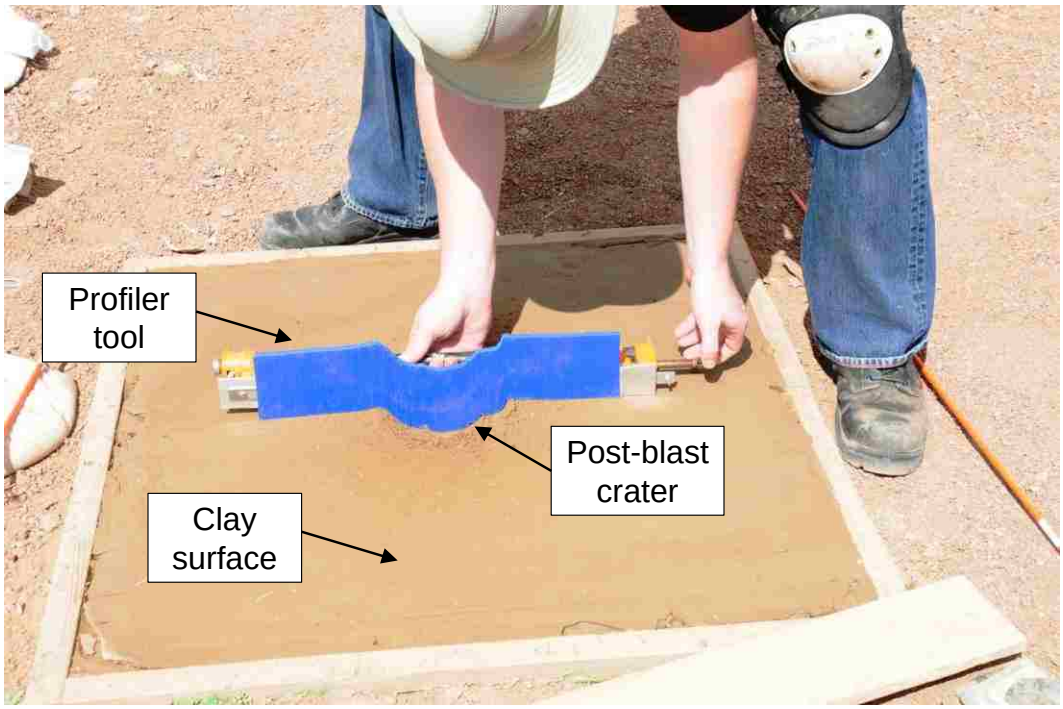

Figure 4.8. Post-blast crater profile measurement

For practical purposes a new surface pad could not be entirely reconstructed after each blast. Instead, the disturbed clay in the vicinity of the crater area was removed after each blast and fresh clay blocks were placed back into the pad, lightly formed, and smoothed to a flat surface. While each blast did result in a permanent disturbance of the clay surface pad, the disturbance was minimized during this backfill process by replacing the disturbed surface soils with clay of approximately similar density and moisture content. The surface of the clayey pad was covered with plastic sheeting until immediately prior to the start of each experiment and intermittently sprayed with a water mist to maintain the moisture content.

The two-dimensional crater profiles measured during testing were digitized into an electronic format using computer aided drafting software (Dassault Systèmes 2013) and electronically rotated to estimate the three-dimensional crater shape as shown in Figure 4.9. The crater volume was then calculated using the average true diameter and depth.

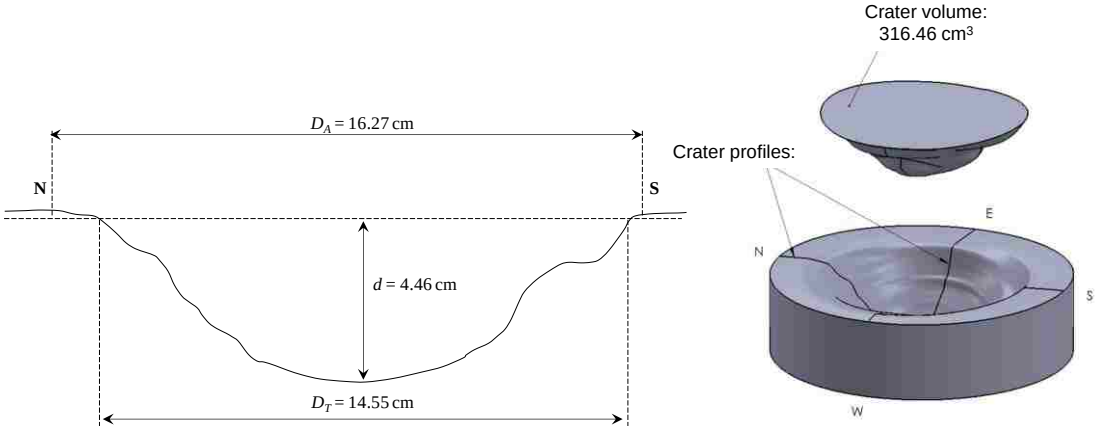

Figure 4.9. Crater profile and volume for Blast C-3

4.2 Crater Geometry Results

The two-dimensional crater profiles measured during explosive airblast testing are presented in Appendix B. The average dimensions of the craters across the perpendicular profiles are presented in Table 4.2. The table includes true diameter (D_T), apparent diameter (D_A), crater depth (d), crater volume (V), and an empirical crater volume parameter (V_C). The empirical crater volume parameter related the ratio of true diameter and depth to explosive mass, similar to the approach of Kinney and Graham (1985) and Vortman (1977). The volume parameter scaled the crater dimensions to explosive energy and is useful because diameter and depth measurements (as opposed to volume) are

easily attainted during field experiments. The volume parameter was calculated with Equation 4.1 and the results are presented in Table 4.2.

$$V_c = D_T / (d \cdot W) \qquad \text{Equation 4.1}$$

where V_c = crater volume parameter (kg^{-1}), D_T = true crater diameter (cm), d = crater depth (cm), and W = the explosive mass (kg).

The true crater diameters, D_T ranged from 3.8 to 22.9 cm, while apparent crater diameters ranged from 4.4 to 25.5 cm. Crater depth, d ranged from 0.8 to 8.4 cm and volume, V from 32.1 to 1720.6 cm^3. True crater diameter to depth ratios varied widely for the A blast series, with crater diameters approximately two to sixteen times the crater depth. Diameter to depth ratios were more consistent for the B and C blast series, with some diameters of two to six times the crater depth for the B blast series and two to three times the depth for the C blast series.

Based on the crater dimensions from the study, it was determined that the craters from the B series blasts (performed under wet conditions) did not significantly affect the crater dimension as compared to the C series blasts (which were performed under dry weather). Because the moisture was confined to the top few millimeters of clay and the clay was replaced after each blast, the excess moisture appeared to have had minimal effects on the resulting craters, and most cratering data from the B series blasts could be compared to the other series.

Table 4.2. Crater geometries from experimental blasts (D_T = the true diameter, D_A = the apparent diameter, d = the depth, V = the volume, V_c = the volume parameter)

Blast number	D_T (cm)	D_A (cm)	d (cm)	V (cm^3)	V_c (kg^{-1})
A-1	----------*No crater created*----------				
A-2	11.8	13.8	0.8	32.1	753.9
A-3	3.8	4.4	1.9	*Not calculated* [1]	*Not calculated*
A-4	14.7	15.6	1.3	90.0	361.5
A-5	15.6	19.4	1.5	137.8	267.6
A-6	18.2	19.4	1.6	169.8	241.8
A-7	20.5	22.3	1.8	186.0	222.1
A-8	18.5	19.8	3.3	346.6	84.1
A-9	22.9	24.2	2.6	468.0	110.5
A-10	22.3	25.4	5.7	921.1	42.8
A-11	22.8	25.5	4.3	930.1	52.0
B-1	6.1	7.3	2.8	54.2	2432.2
B-2	8.1	8.7	2.1	57.7	667.2
B-3	10.3	10.8	1.6	51.1	586.7
B-4	12.8	14.3	4.0	328.1	152.3
B-5	14.3	15.5	2.8	307.3	156.1
B-6	22.4	24.6	6.9	1452.6	79.8
B-7	21.6	23.2	7.5	1564.0	56.4
C-1	6.7	8.4	3.1	64.2	2425.9
C-2	9.1	11.2	2.8	83.1	297.6
C-3	14.4	15.9	4.5	316.4	154.1
C-4	16.3	17.9	6.3	801.3	83.6
C-5	20.7	25.5	7.6	1452.6	66.7
C-6	20.9	24.4	8.4	1720.6	48.9

[1] Blast A-3 crater volume was not calculated due to irregular crater shape.

The blast test A-1, with an explosive mass of 5.9 g, did not create a crater. Blast A-3 created a double crater shape with a significant spall lip and was considered to be an outlier to the experimental results. Because of the irregular shape of the A-3 crater, it was not included in the analyses and the volume could not be calculated.

Figure 4.10 depicts the relationship between true crater diameter, D_T vs scaled distance, *SD*. The data are separated by blast series with power trendlines. The R^2 value shown in the figure is the correlation coefficient and described how well the equation fits the data, with an R^2 value of 1.0 indicating an exact fit. True crater diameters ranged from 3.8 to 22.9 cm. Diameter values from the B and C blast series exhibited larger diameters than the A series since the smaller blast height from the B and C series deposited a larger amount of energy into soil. Blast A-3, which had the smallest diameter value of 3.8 cm, was considered an outlier and not included in the trendline fit.

The true crater diameters, D_T, and scaled explosive mass, *W*, were normalized by blast height, *h*, to obtain a predictive relationship as shown in Figure 4.11. A linear trendline (Equation 4.2) was fit to the data with an R^2 value of 0.97. This equation provided an empirical relationship between crater dimensions and scaled explosive mass for clay soils. This approach was similar to the empirical relationship developed by Kinney and Graham (1985) and incorporated the blast height into the function based on the approach of Ambrosini et al. (2002). The blast test A-3 was considered an outlier and was not utilized in the data fit. Crater diameters increased with increasing explosive mass, *W*, and

also increased with decreasing blast offset height, h. The largest crater diameters corresponded to the B and C test series with h = 2.5 cm.

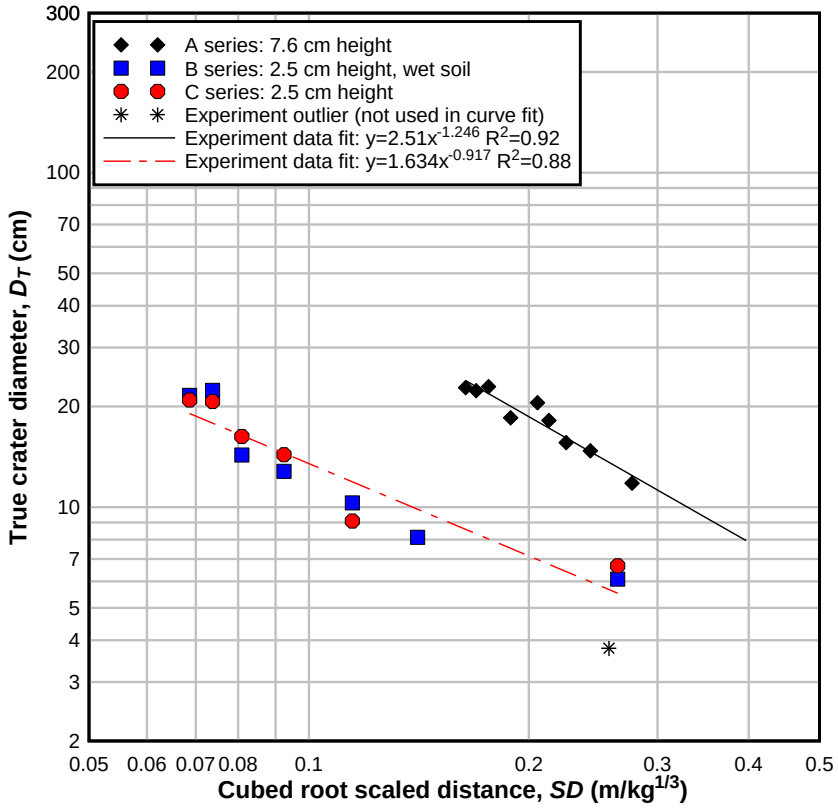

Figure 4.10. True crater diameter vs. scaled distance

$$D_T / h = -0.4528 + 0.5806 W^{1/3} / h \qquad R^2 = 0.97 \qquad \text{Equation 4.2}$$

where D_T = true crater diameter (cm), h = blast height (cm), and W = explosive mass (kg).

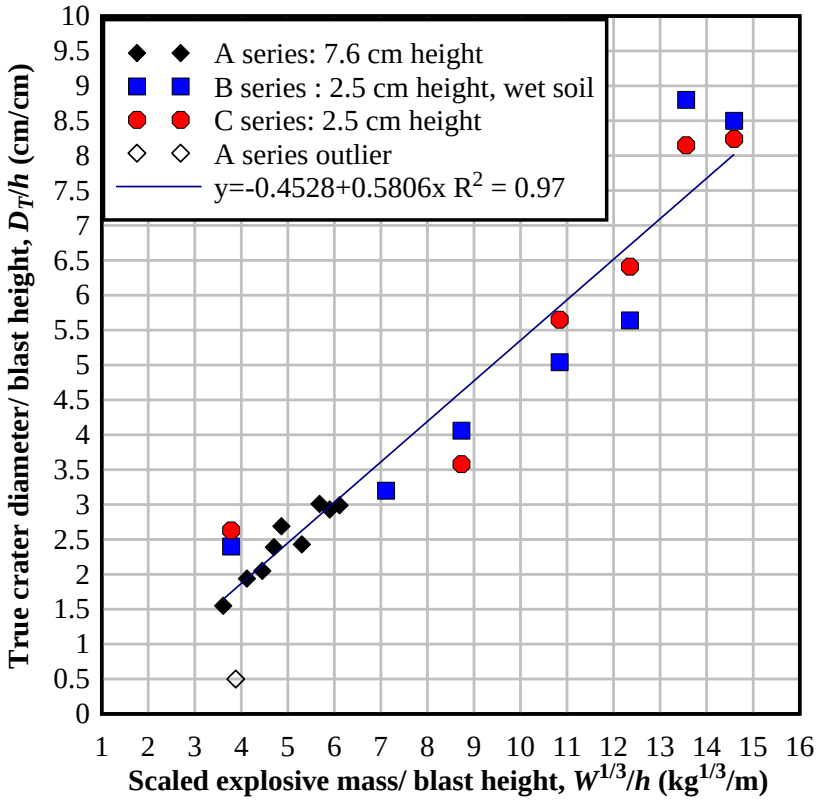

Figure 4.11. Crater diameter to blast height ratio vs. scaled explosive mass

Figure 4.12 compares the relationship between crater depth, *d* versus scaled distance, *SD*. Crater depths ranged from 0.8 to 8.4 cm, with the B and C blast series exhibiting larger crater depths than A series as expected. The depth results exhibited more data scatter than the diameter results as shown by the R^2 value of 0.79 for both trendline fits. Depths from two blasts (blasts B-1 and C-1) appeared to be outliers and were not used in the trendlines. The outlier blasts consisted of a blasting cap only with no surrounding explosive. Since the blasting cap was cylindrical in shape, the stress pulse shape from the blast was different from the spherically-shaped blasts and released more energy into the vertical direction, resulting in the creation of deeper craters.

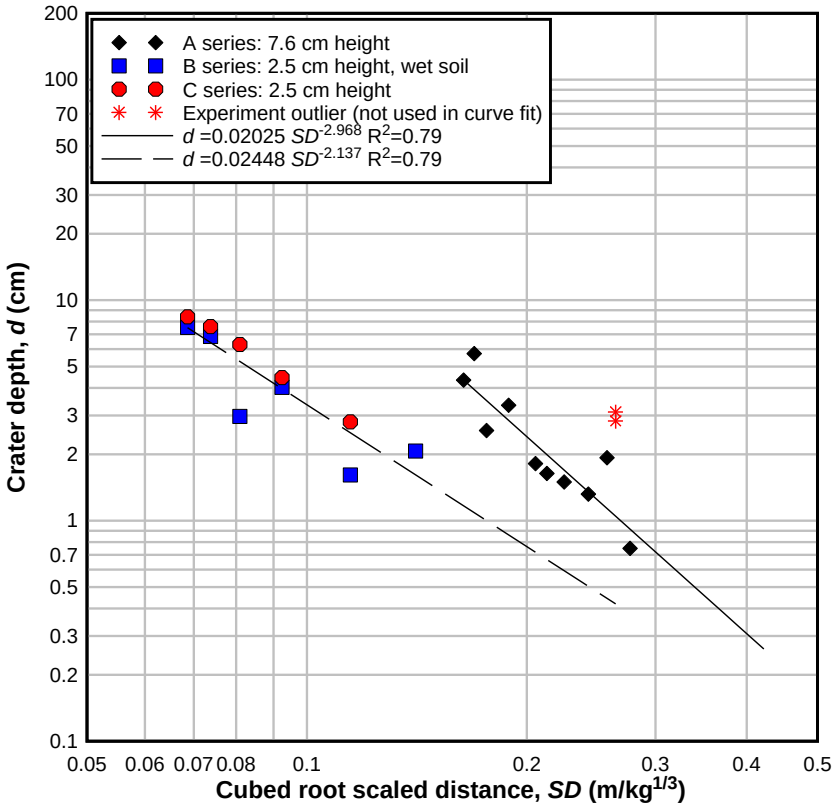

Figure 4.12. Crater depth vs. scaled distance

Crater depths, *d* were normalized by blast height, *h* as shown in Figure 4.13. The *d*/*h* ratios increased with explosive mass and decreasing blast height as more energy was imparted into the ground. A trendline was fit to the data as given by Equation 4.3. Outlier data from blasts B-1 and C-1 were not included in the trendlines. While there was some data scatter, a good fit was obtained overall.

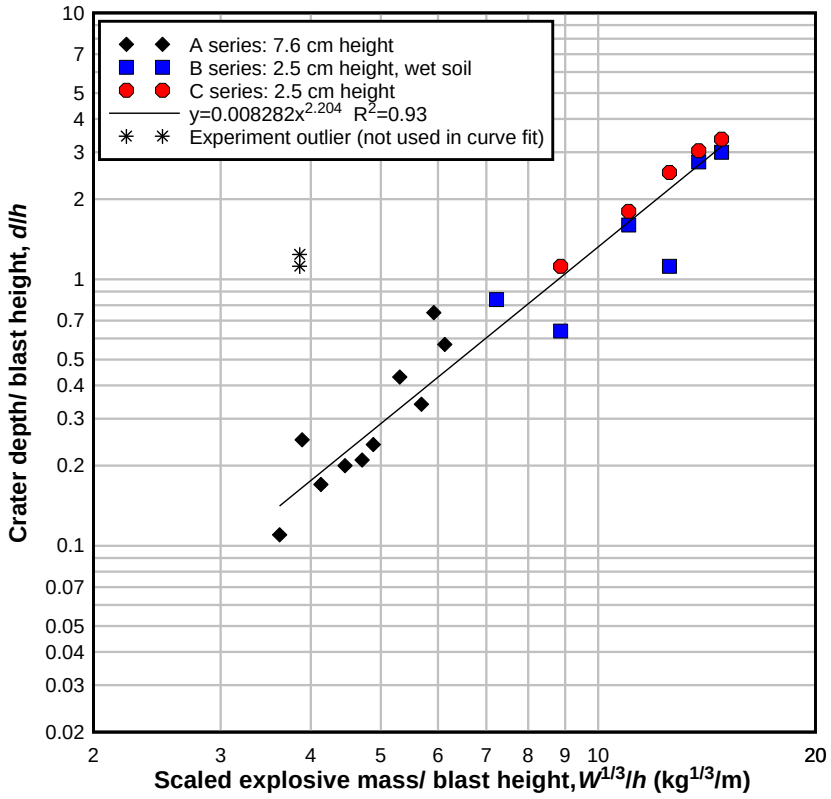

Figure 4.13. Crater depth to blast height ratio vs. scaled explosive mass

$$d/h = 0.008282\left(W^{1/3}/h\right)^{2.204} \qquad R^2 = 0.93 \qquad \text{Equation 4.3}$$

where d = crater depth (cm), h = blast height (cm), and W = explosive mass (kg).

The relationship between the crater volume, V and the scaled distance, SD was investigated as shown in Figure 4.14. Crater volumes and scaled explosive mass, W, were normalized by blast height, h as shown in Figure 4.15 to directly compare results between blast series. Crater volumes ranged from 32.1 to 1720.6 cm^3. Each blast series exhibited a trend of increasing crater volume with explosive mass. As expected, the B and C blast series with h = 2.5 cm exhibited larger crater volumes, V, than the A blast series with h =

7.6 cm, showing the larger amount of energy deposited into the ground surface with the blast charge located closer to the ground.

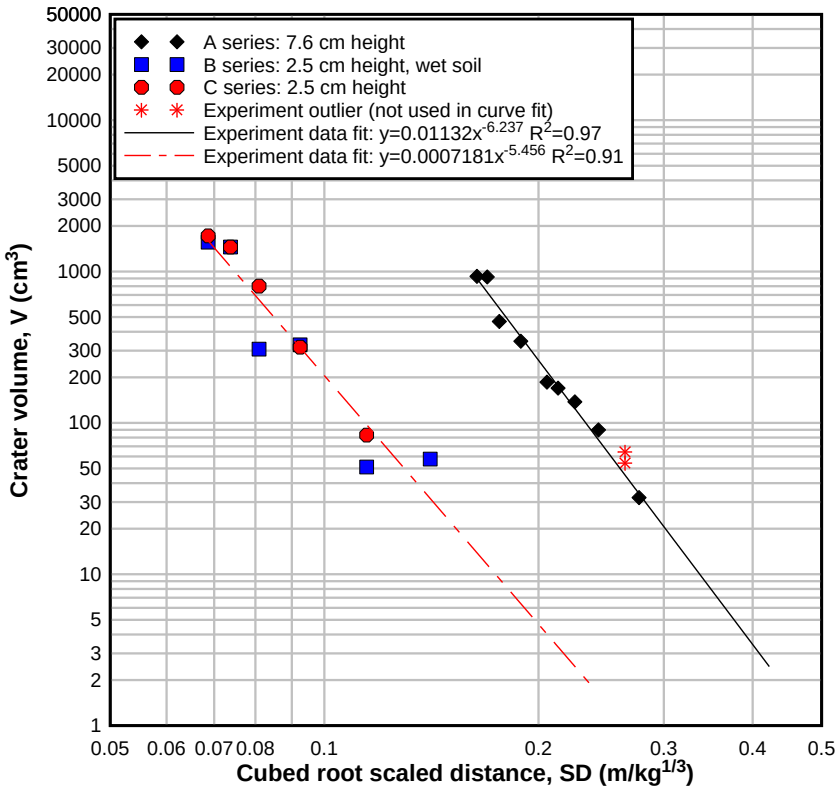

Figure 4.14. Crater volume vs. scaled distance

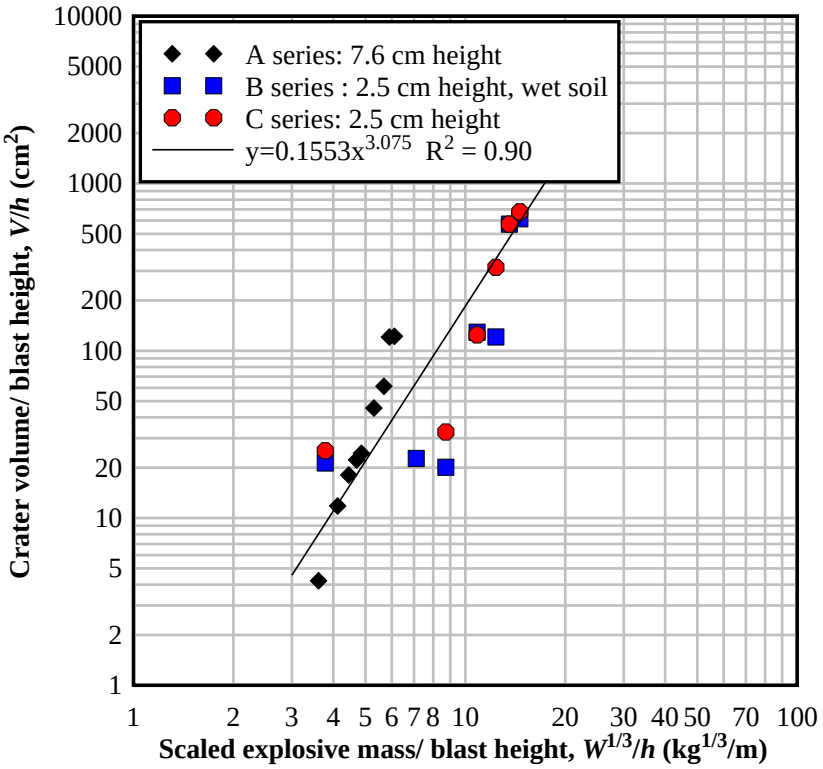

Figure 4.15. Crater volume to blast height ratio vs. scaled explosive mass

A plot of volume parameter V_C (calculated by Equation 4.1) versus *SD* is presented in Figure 4.16. The B and C blast series resulted in larger crater volume parameters than the A blast series. This was especially evident with larger values of scaled distance, where volume parameters for the B and C blast series were more than three times larger than the A blast series. The power trendlines in Figure 4.16 exhibited a slight variation between the B and C blast series, indicating that the increased moisture content on the soil surface may have minimally affected the resulting crater geometries. The wet soil present in the B blast series resulted in marginally larger crater volumes and somewhat more data scatter than the C blast series. Volume parameters for both series were very similar for $SD = 0.1$ m/kg$^{1/3}$ or less, but somewhat diverged at $SD \approx 0.12$ to 0.14 m/kg$^{1/3}$.

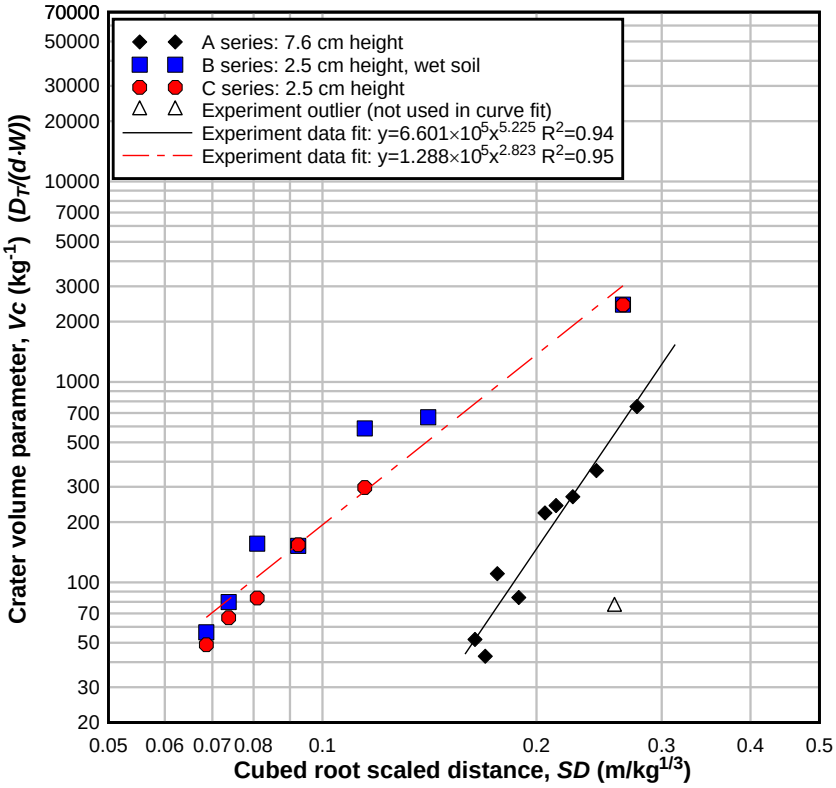

Figure 4.16. Crater volume parameter vs. scaled distance

4.3 Vibration and Airblast Results

The time history plots from subsurface geophones and surface air pressure sensors for the small-scale airblast experiments performed in this study are provided in Appendix C. Airblast time histories were constructed from peak air overpressure data obtained from the surface airblast sensors. Velocity time histories were constructed from ground motion data recorded by the subsurface geophones. An example of the *PPV* obtained from a velocity time history record from a subsurface geophone is shown in Figure 4.17 (*a*). The *PPV* value is the maximum ground motion observed during the time history. Several of the blasts with larger explosive masses generated maximum ground motion that exceeded

the capacity of the near surface geophones. *PPV* values were obtained from the ground motion histories for some of these instances by extrapolating the data curve to estimate the peak ground motion as shown in Figure 4.17 (b). This method was performed only on data curves that had a clear shape and were not overly distorted from excessive ground motions.

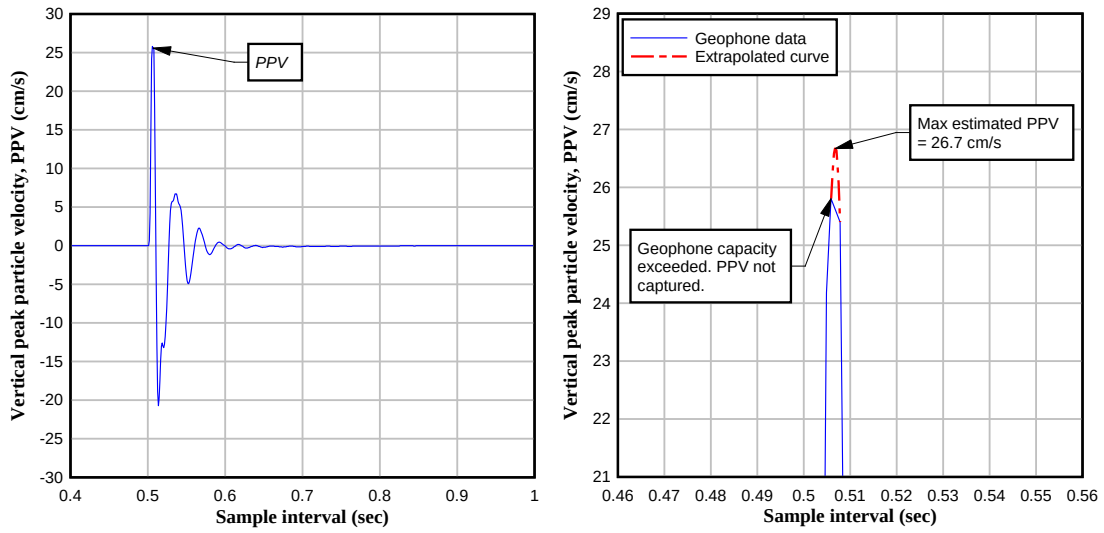

(***a***) (***b***)

Figure 4.17. (*a*) Example of peak particle velocity (*PPV*) obtained from velocity time history and (*b*) extrapolated *PPV* value obtained from exceeded capacity geophone data

Ground vibration attenuation curves were created by plotting *PPV* obtained at each geophone location against the scaled distance, *SD* (computed using Equation 2.3 and changing *h* by *D*, the distance of the geophone to the blast source) as shown in Figure 4.18. Attenuation trend lines (described by Equation 2.4) were fit to the ground vibration data to quantify vibration attenuation and to indicate the amount of energy generated by the blast.

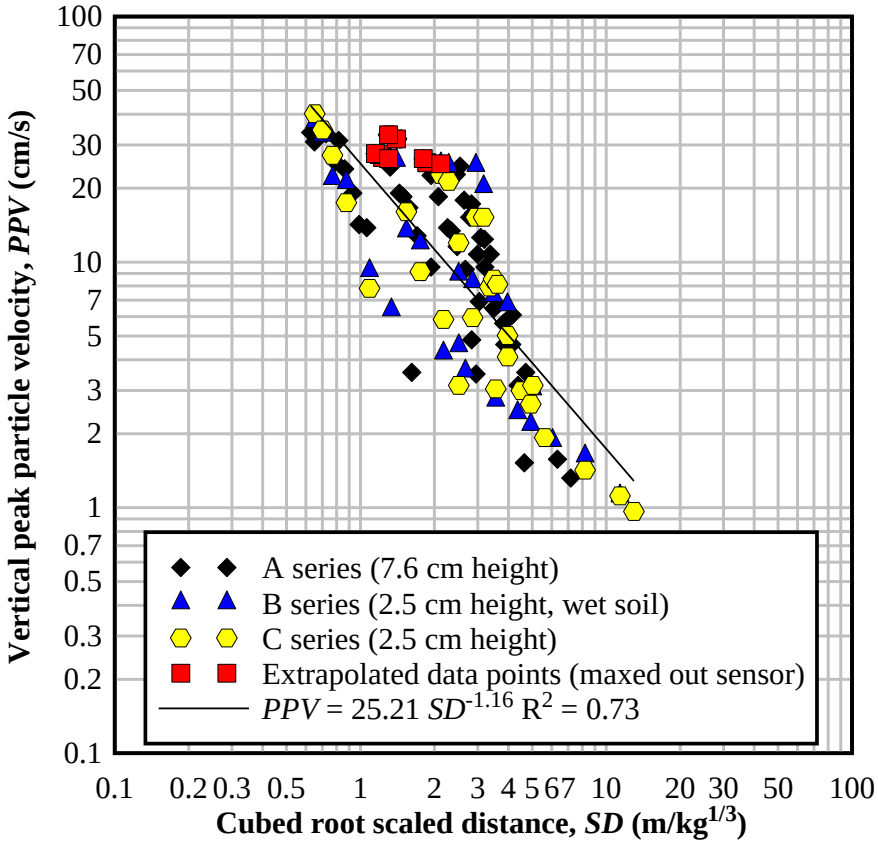

Figure 4.18. Vertical *PPV* vs. scaled distance *SD* for subsurface sensors

The *PPV* values shown in Figure 4.18 ranged from 1.0 to 40.2 cm/s and decreased with depth as indicated by the attenuation trend line. The energy generated by the blasts as described by the K-factor was 25.21. The data exhibited a moderate amount of scatter, with an R^2 value of 0.73. The data points presented in the figure did not exhibit a trend based on the different blast series, which had two different blast heights. This indicated that the scaled distance (explosive mass scaled by distance from the blast to the geophone) was a representative parameter to describe the ground vibration attenuation. *PPV* results also did not appear to be impacted by the moisture conditions of the clay on the ground surface for the B blast series, confirming that the additional moisture added to

the topsoil by the wet weather conditions did not permeate the clay column where the geophones were embedded.

Figure 4.19 shows a plot of air overpressure, *AOP* versus scaled distance, *SD* obtained from the airblast sensors for the blasts performed in this study. The air overpressures ranged from 0.6 to 18.2 kPa and decreased with distance from the blast. The data was fit by the power Equation 4.4. While there was some scatter to the airblast data as shown in the figure, a relatively good data fit was obtained with an R^2 value of 0.83.

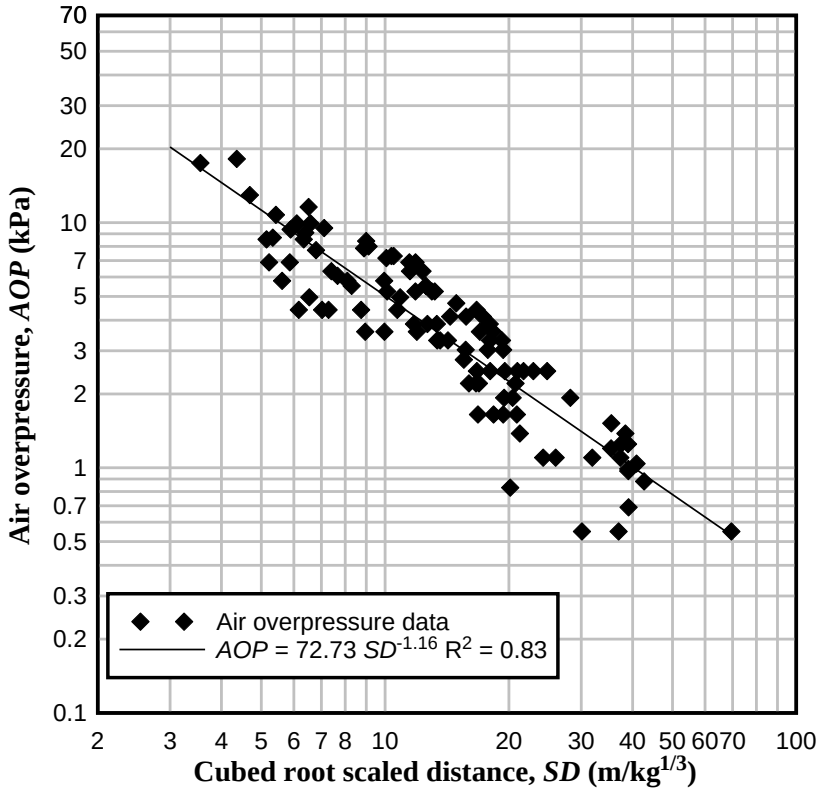

Figure 4.19. Air overpressure *AOP* vs. scaled distance *SD*

$$AOP = 72.73\,SD^{-1.16} \qquad R^2 = 0.83 \qquad \text{Equation 4.4}$$

where *AOP* = air overpressure (kPa), and *SD* = scaled distance from blast ($m/kg^{1/3}$).

5 NUMERICAL SIMULATIONS OF EXPLOSIVE AIRBLAST TESTING

Finite element simulations of the small-scale blasts were performed and compared to the results of the experimental blasts. The ability of the numerical model to simulate airblast events on cohesive soils was evaluated. This chapter discusses methodologies used in the finite element simulations and the results of the numerical study.

The finite element simulation software LS-DYNA Version 7.1.1 (LSTC 2014) was used for the simulations. Four materials (clay, sand, air and explosive) were modeled in the calculations. Appendix A presents an example of the LS-DYNA keyword input decks used in the scaled explosive blast simulations of this study.

5.1 Finite Element Hydrocode

Finite element methods discretize a domain into a finite number of elements defined by nodal points. Variables are solved at the nodal points and interpolated within each element. Shared node locations result in the governing global equations of the form given in Equation 5.1 (Nielson et al. 2013). The equations are subject to boundary conditions such as assigned displacements or velocities.

$$\mathbf{Ku} = \mathbf{f} \qquad \text{Equation 5.1}$$

where **K** = stiffness matrix, **u** = the primary variable, and **f** is the load applied from tractions on the nodal surface.

Two methods can generally be considered when performing finite element analyses: Implicit and explicit methods. Implicit methods solve for dependent variables through the

use of coupled equations; either a matrix or an iterative technique is used to solve for the dependent variables. A global stiffness matrix is constructed and inverted to obtain displacement increments at nodal points as shown by Equation 5.2 (Nielson et al. 2013). This approach is generally suited for quasi-static problems.

$$[M]\{\ddot{x}\}_{n+1}+[K]\{x\}_{n+1}=[F_{external}]_{n+1}-[F_{internal}]_{n}-[M]\{\ddot{x}\}_{n} \quad \text{Equation 5.2}$$

where [M] = mass matrix, [K] = stiffness matrix, [$F_{external}$] = external force matrix, [$F_{internal}$] = internal force matrix, and $\{\ddot{x}\}$ nodal acceleration vector.

Explicit techniques directly compute the dependent variables by summing forces at each nodal point. Nodal acceleration is computed at each node point by dividing by nodal mass as shown in Equation 5.3 (Nielson et al. 2013). The solution is obtained through numerical integration of the acceleration in time. The solution for a time step is based on the solution from the previous time step plus the results with the currently evaluated time increment (Lee 2006). Explicit methods are used to solve problems involving large deformations at high strain rates because boundary constraints are not as restrictive as implicit stiffness methods (Lee 2006).

$$[M]\{\ddot{x}\}_{n}=[F_{external}]_{n}-[F_{internal}]_{n} \quad \text{Equation 5.3}$$

where [M] = mass matrix, [$F_{external}$] = external force matrix, [$F_{internal}$] = internal force matrix, and $\{\ddot{x}\}$ nodal acceleration vector.

A finite element hydrocode is an algorithm that uses explicit methods to model fluid flow (or fluid-like behavior) in a continuous media. Solutions to the explicit methods can take the form of a Lagrangian or Eulerian formulation In the Lagrangian formulation, a computational mesh is used to define the geometry of each material for the analysis. The mesh nodes move with the material and deform, translate and rotate exactly with the material. The Lagrangian method can generate inaccurate results for analyses that involve large deformations, such as the large deformations that are commonly observed in material subjected to blast loading. In the Eulerian formulation, the computational mesh remains fixed in space during the analysis while materials move and deform within the mesh (Bouamoul and Nguyen-Dang 2008). The Eulerian method can also lead to inaccurate results for large-deformation simulations, as it can be difficult to simulate material interaction when more than one material occupies an element.

Because of the shortcomings of both Lagrangian and Eulerian methods in the simulation of a large deformation event, a combination of the two methods, the Multi-Material Arbitrary Lagrangian Eulerian (MM-ALE) method is commonly used to simulate blasting events. The MM-ALE method allows the computational mesh to move in a manner which is not equal to the movement of the material. While materials still "flow" across the mesh, the moving mesh results in fewer instances where multiple materials occupy a single element, thus reducing computational errors and improving accuracy. An MM-ALE mesh is generally directed to move with the anticipated direction of the materials which requires fewer elements in the computational mesh and reduced computation time.

However, the MM-ALE method is more computationally expensive than Lagrangian methods.

The MM-ALE method was utilized for the finite element analysis of this study. During an MM-ALE analysis, the LS-DYNA software reconstructed material interfaces for each time step based on the volumes of the materials occupying an element (Williams 2009). Each material in the analysis (soil, air, explosive) was assigned an MM-ALE multi-material group for interface reconstruction computations.

During simulations, the state of the finite element model was updated from time t to $t+\Delta t$. Explicit time integration was used in the MM-ALE analysis for this study. Explicit time integration determines the time step between each analysis cycle based on the smallest element length. This ensured that the time step was small enough to allow simulation outputs for the smallest element in the mesh. The time step was calculated by Equation 5.4 (Bouamoul and Nguyen-Dang 2008).

$$\Delta t < \frac{\Delta x}{C_s} \qquad \text{Equation 5.4}$$

where Δt = time step for explicit time integration, Δx = element width, and C_s = sound speed.

During an ALE analysis, conservation equations for the transport of mass, momentum and energy are solved for each time step using an operator splitting technique for the ALE materials (Fox and Lee 2011). An explicit Lagrangian step is first performed to

solve the conservation equations. Nodal accelerations are calculated by assigning the material masses, applied forces, and momentum balance to the node locations. Nodal velocities and displacements are then obtained and a new Lagrangian mesh is calculated by the solver. Mass, momentum, and energy are advected from the previous mesh to the newly-created mesh. The multi-phase portion of the method that allows more than one material to occupy an element uses an algorithm that calculates the strain rate for each material based on the average strain rate of the element (Fox and Lee 2011). The stress state of the element is determined through the summation of the volume fraction and the stresses on each material occupying the element.

5.2 Simulation Configuration

Finite element simulations were performed of the experimental explosive airblast tests performed in this study. The configuration of the experiment was modeled as a two-dimensional, axisymmetric calculation as shown in Figure 5.1. In the two dimensional model the x axis corresponds to the radial direction and the y axis is the axis of symmetry (Hallquist 2006). A two-dimensional model was chosen to reduce computation time and was justified based on the symmetry of the experimental configuration, which had a cylindrical clay column and a spherical explosive. The experimental craters themselves were spherical in shape, which is well described by a 2D model. While the surface clay pad was square in shape, the blast induced craters were all contained well within the pad and did not reach the edges. The two-dimensional model was therefore deemed adequate to numerically describe the experimental blasts while maximizing computational efficiency.

Non-reflecting boundary conditions were used in the finite element simulations as shown in Figure 5.1. Non-reflecting boundary conditions are commonly used on exterior boundaries in problems with a continuum domain to limit the size of the model. The conditions prevented artificial reflections from re-entering the model at the boundaries by using an impedance matching function that assumed linear material behavior (Hallquist 2014).

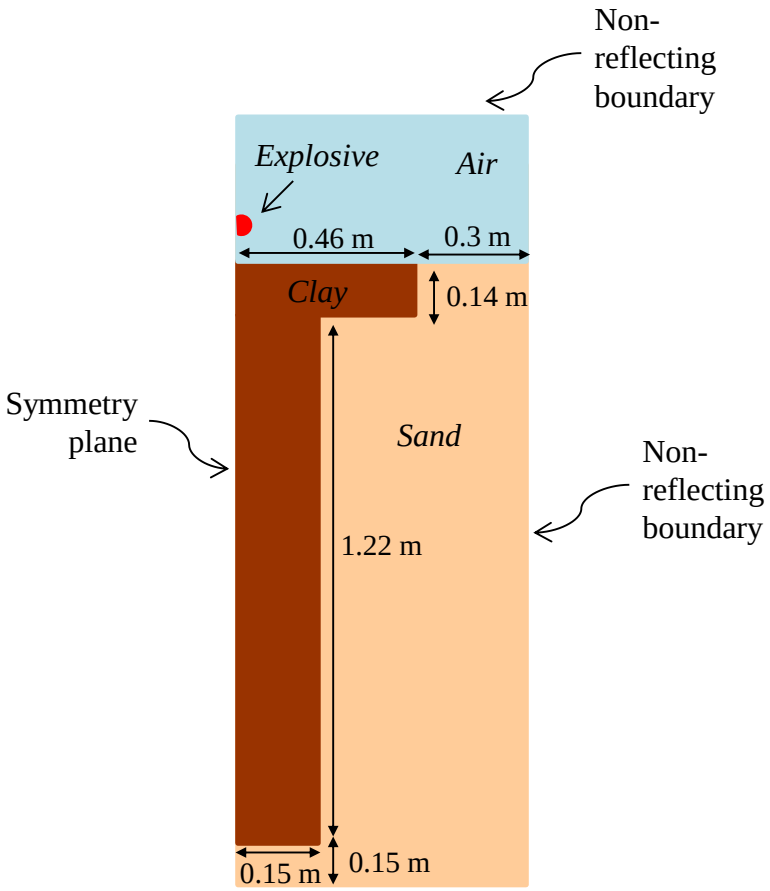

Figure 5.1. Geometry and boundary conditions for explosive blast finite element simulations (not to scale)

The finite element mesh (shown in Figure 5.2 and Figure 5.3) was constructed using two-dimensional, quadrilateral elements that were smaller in size near the explosive and transitioned to a larger size near the geometry edges. Element sizes varied based on the mesh refinement study described later in this report. Tracer nodes were placed at various locations within the mesh to obtain stress, velocity and displacement data from the simulations and are shown in Figure 5.2. The tracer nodes located in the clay material were placed directly below the explosive at the ground surface and at depths of 0.45, 0.9 and 1.4 m below ground surface. Additional tracer node locations in the clay corresponded to the geophone depths of 0.2 m, 0.5 m, 0.8 m, 1.1 m and 1.2 m below ground surface.

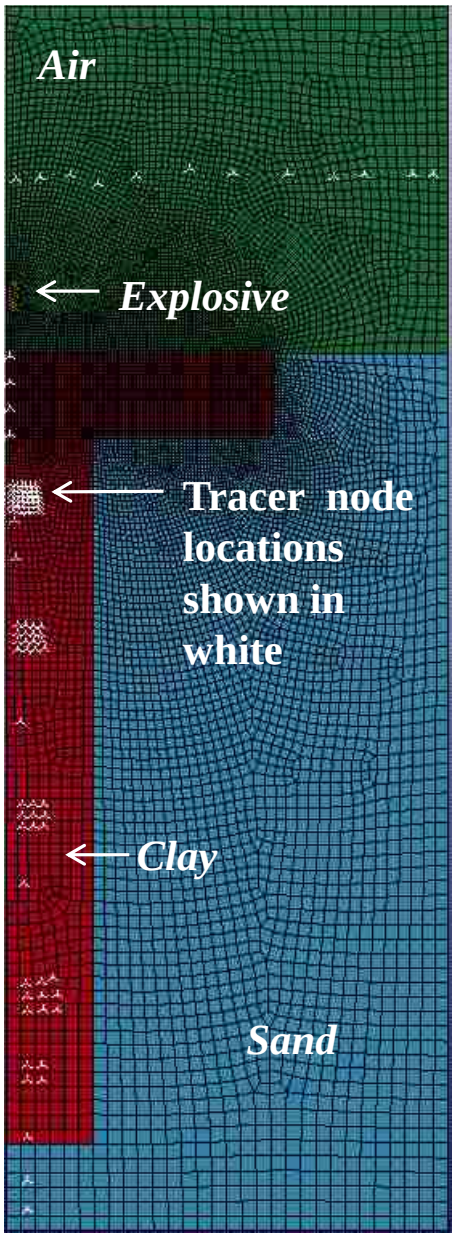

Figure 5.2. Finite element mesh and tracer node locations (tracer nodes correspond to geophone locations from field experiments)

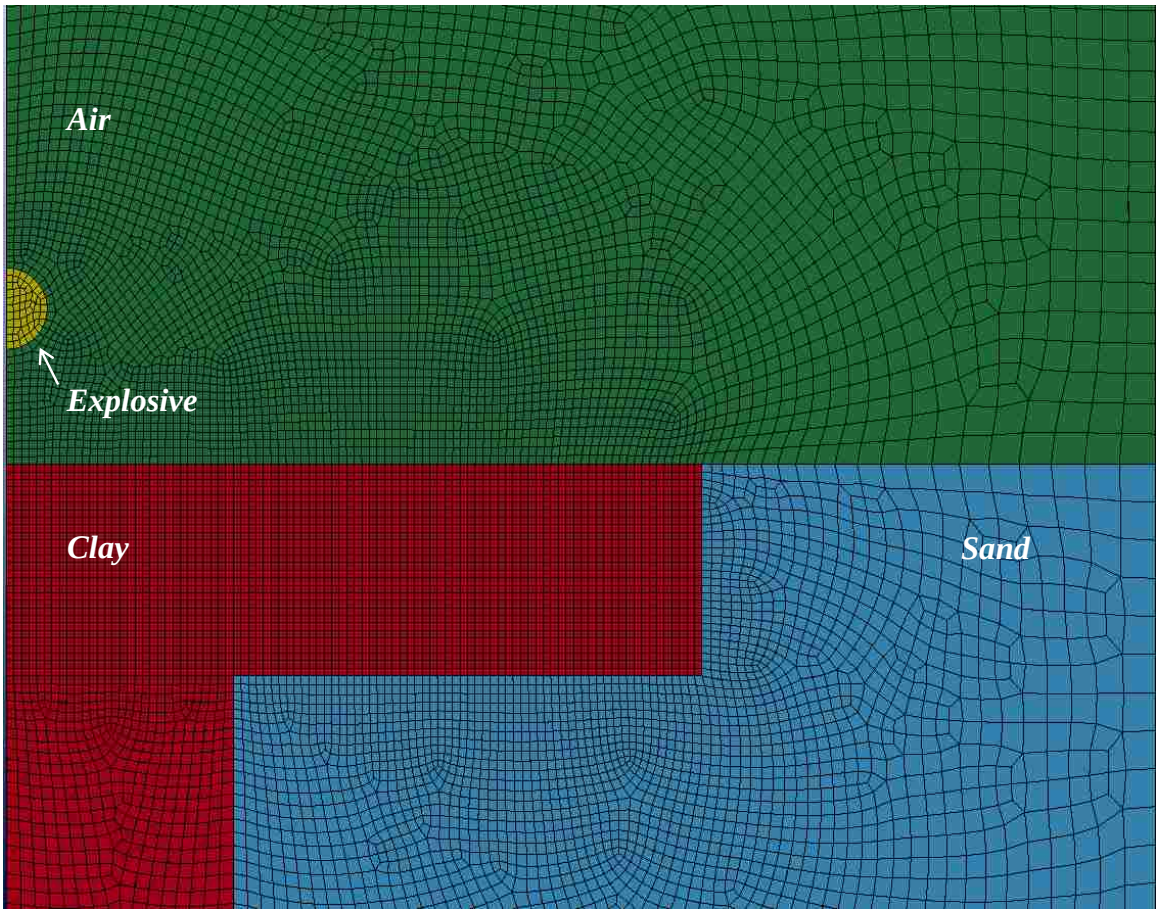

Figure 5.3. Finite element mesh (zoomed in to show detail in explosive region)

5.3 Explosive Material and Detonation Models

The explosive was modeled using the Jones Wilkins and Lee (JWL) equation of state (Equation 5.5) coupled with the LS-DYNA High Explosive Burn (HEB) material model (LS-DYNA Material Model 8). The input parameters used in the HEB model and the JWL equation of state for the binary explosive used in the experiments are provided in Table 5.1.

Table 5.1. HEB model and JWL equation of state parameters for ammonium-nitrate/ nitromethane explosive

Parameter	Value
Mass density, ρ	1.2 g/cm^3
Detonation velocity, D	6300 m/s
Chapman-Jouget pressure, P_{CJ}	12 GPa
JWL coefficient, A	600 GPa
JWL coefficient, B	15 GPa
JWL coefficient, R_1	6.0
JWL coefficient, R_2	2.0
JWL coefficient, ω	0.4
Initial internal energy, E_0	6.0 GPa

$$p = A\left(1-\frac{\omega}{R_1 V}\right)e^{-R_1 V} + B\left(1-\frac{\omega}{R_2 V}\right)e^{-R_2 V} + \frac{\omega E}{V} \qquad \text{Equation 5.5}$$

where p = blast pressure, V = current relative volume (volume of material at pressure p divided by the initial volume of un-reacted explosive), E = specific internal energy (internal energy per initial volume), and A, B, R_1, R_2, ω = JWL coefficients.

The JWL equation of state is an empirical model originally developed from cylindrical explosive tests and is widely utilized due to its simplicity and computational efficiency. The first term of the equation dominates the response at high pressures and a relative volume close to one, while the second term dominates at intermediate pressures and a

relative volume close to two (Alia and Souli 2006). The third term dominates at lower pressures where the explosive is fully expanded and relative volume increases.

While JWL coefficients for many different types of explosives have been determined and are readily available in the literature, to the author's knowledge there have been no laboratory tests performed to obtain the coefficient values for the particular explosive used in this study. Coefficient values were instead obtained from modeling studies performed for a 67% Ammonium Nitrate and 33 % Nitromethane (ANNM) explosive mixture using CHEETAH 7.0 thermochemical computer code (LSTC 2012). CHEETAH modeled the thermodynamics of explosion products using the Chapman-Jouguet theory of detonation to calculate properties of high explosives.

The HEB model described the pressure in the high explosive material by Equation 5.6 and allowed a detonation initiation time and location to be specified for the explosion (Hallquist 2014). The detonation time for each element was defined by a "lighting time", which was the time required to ignite the explosive and was calculated by Equation 5.7. The model utilized burn fractions during detonation simulation to calculate the amount of reacted explosive material and control the release of chemical energy during the detonation. The pressure from the equation of state was modified by the burn fraction functions shown in Equation 5.8 and Equation 5.9. If the burn fraction exceeded unity, it is reset to one and held constant.

$$p = Fp_{eos}(V, E) \qquad \text{Equation 5.6}$$

where p = blast pressure, F = burn fraction, p_{eos} = pressure from the equation of state, V = relative volume, and E = internal energy per unit volume.

$$t_l = \frac{L_d}{D} \qquad \text{Equation 5.7}$$

where t_l = lighting time for an explosive element, L_d = distance from center of explosive element to the nearest detonation point, and D = detonation velocity.

$$F_1 = \begin{cases} \dfrac{2(t - t_l)DA_{e\max}}{3v_e} & if \;\; t > t_l \\ 0 & if \;\; t \le t_l \end{cases} \qquad \text{Equation 5.8}$$

$$F_2 = \beta = \frac{1 - V}{1 - V_{CJ}} \qquad \text{Equation 5.9}$$

where F_1 and F_2 = burn fractions, t = current time, t_l = lighting time, D = detonation velocity, V = relative volume, V_{CJ} = Chapman-Jouguet relative volume, and v_e/A_{emax} = grid spacing.

The HEB model required a beta burn flag (*BETA*) to be defined. If *BETA* = 1, then a beta burn is defined, the high explosive is detonated through volumetric compression, and the burn fraction is defined as F_2. If *BETA* = 2 (which was the approach utilized in this study) a programmed burn was defined and the detonation was controlled by the lighting time of each element. The burn fraction was then defined by F_1. The high explosive was then

treated as an elastic perfectly-plastic solid and can be compressed without detonation. The beta burn flag can also be defined as a beta burn plus a program burn (*BETA* = 0). The burn fraction is then defined by Equation 5.10. This beta flag option treats the high explosive as an elastic perfectly-plastic solid prior to detonation. After detonation, the explosive is modeled as a gas, and the pressure-volume relationship follows the relationship defined by the equation of state.

$$F = \max(F_1, F_2) \qquad \text{Equation 5.10}$$

The LS DYNA function INITIAL_DETONATION was utilized to initiate the location of the high explosive detonations. This function required the x, y and z coordinates of the detonation point (which was assumed to be at the center of the explosive), as well as the lighting time for the detonation point to be defined. The lighting time for an explosive element was defined by the following (Hallquist 2014):

$$t_l = t_d + \frac{L_d}{D} \qquad \text{Equation 5.11}$$

where t_l = lighting time for an explosive element, t_d = lighting time for the detonator, L_d = distance from center of explosive element to the nearest detonation point, and D = detonation velocity.

5.4 Air Material Model

The air in the finite element calculations was defined using the LS-DYNA null material (LS-DYNA Material Model 9) and a linear polynomial equation of state for an ideal gas

to describe the pressure-volume relationship (Hallquist 2014). The material properties were calculated based on the conditions of the experiment, which was conducted at an elevation of 1500 m at a temperature of 10°C. The initial internal energy was assumed for standard atmosphere values (NASA 1976). The parameters for the air model are summarized in Table 5.2.

Table 5.2. Null material and linear polynomial equation of state parameters for air

Parameter	Value
Mass density, ρ	1.1 kg/m^3
Initial internal energy, E_0	101 KPa
Ideal gas constants, C_4, C_5	0.4

A linear polynomial equation of state given by and Equation 5.12 and Equation 5.13 was utilized to model the ideal gas. The equations resulted in a linear relationship between air pressure and internal energy. The equation of state was modeled for the gas with the gamma law given in Equation 5.14 through Equation 5.16 (Williams 2009). The expression for the pressure relationship of an ideal gas then took the form given by Equation 5.17, where the units of E were units of pressure (Hallquist 2014).

$$p = C_0 + C_1\mu + C_2\mu^2 + C_3\mu^3 + \left(C_4 + C_5\mu + C_6\mu^2\right)E \qquad \text{Equation 5.12}$$

$$\mu = \frac{\rho}{\rho_0} - 1 \qquad \text{Equation 5.13}$$

where p = pressure of the air, C_0 through C_6 = constants, E = internal energy per unit reference volume, ρ = current density of air, and ρ_0 = initial density of air.

$$C_0 = C_1 = C_2 = C_3 = C_6 = 0 \qquad \text{Equation 5.14}$$

$$C_4 = C_5 = \gamma - 1 \qquad \text{Equation 5.15}$$

$$\gamma = \frac{C_p}{C_v} \qquad \text{Equation 5.16}$$

where γ = ratio of specific heats, C_p = constant pressure specific heat coefficient, and C_v = constant temperature specific heat coefficient.

$$p = (\gamma - 1)\frac{\rho}{\rho_0} E \qquad \text{Equation 5.17}$$

5.5 Clay Material Model Selection

A material model comparison study was performed to select a suitable material model for simulating the explosive blast testing on clay soils. Four different material models available in LS-DYNA (LSTC 2014) were compared to evaluate their ability to simulate explosively-induced airblast loads on cohesive soils. Crater size and shape from the finite element calculations were compared to the small-scale airblast tests described in Chapter 4. Four material models were compared:

1. Soil and Foam mean stress dependent strength model (LS-DYNA Model 5)
2. Pseudo Tensor mean stress dependent strength model (LS-DYNA Model 16)

3. Federal Highway Administration (FHWA) Drucker-Prager model (LS-DYNA Model 147)

4. Two-Invariant Geologic Cap model (LS-DYNA Model 25)

Input parameters for the material models were obtained from the laboratory test results described in Chapter 3. The parameters used for each material model are presented in Table 5.3 through Table 5.5. A few soil properties were estimated based on engineering judgment by substituting typical properties based on soil type. Geotechnical, shear strength, and compressibility inputs were obtained from the recommended properties from the lab test program as discussed in Section 3.1.1. The shear strength envelope for all models was fit to the shear strength envelope obtained from laboratory testing and converted to the particular stress space used by each model. Compressibility curves for each model were treated in the same fashion and fit to laboratory data.

Some strength inputs for the FHWA model deviated slightly from the laboratory test results in order to properly fit the strength envelope by the equations used in the model. In addition, some of the more obscure input parameters for the FHWA model were obtained from an in-depth parametric study performed by Lee (2006).

Table 5.3. Input parameters for Soil and Foam Material Model (LS-DYNA Model 5) and Pseudo Tensor Material Model (LS-DYNA Model 16)

Parameter	**Input**
Model 5 Yield function constant, a_0	0.0007 MPa^2
Model 5 Yield function constant, a_1	0.0049 MPa
Model 5 Yield function constant, a_2	0.0079
Model 16 Linear Strength Envelope Equation	$(\sigma_1 - \sigma_3) = 0.154P + 0.047$
Tensile pressure cutoff, P_c	0.046 MPa
Unloading bulk modulus (true volume strain space), K_{Unload}	4504.5 MPa
Soil Compressibility	
Mean stress, P (MPa)	Bulk modulus, K (MPa)
0.0 to 0.474	15.8
> 0.474	4680.0

Table 5.4. Input parameters for FHWA Material Model (LS-DYNA Model 147)

Parameter	Input
Bulk modulus, K	4680 MPa
Skeletal bulk modulus, K_{sk}	468 MPa
Specific gravity, γ_{sp}	2.78
Cohesion, c	0.038 MPa
Friction angle, φ	5.0°
Residual friction angle, φ_{res}	5.0°
Drucker-Prager coeff., *AHYP*	0.38 MPa
Eccentricity parameter, e	0.90
Pore water effects parameter, D_1	6.6
Pore water effects parameter, D_2	0.01 MPa^{-1}
Initial damage threshold strain, ξ_0	0.10
Void formation energy, G_f	1.0 N-m
Viscosity exponent, V_n	10.0
Max iterations for plasticity algorithm	10

Table 5.5. Input parameters for Geologic Cap Material Model (LS-DYNA Model 25)

Parameter	Input
Failure envelope coefficient, α	0.035 MPa
Failure envelope coefficient, β	-0.014 MPa^{-1}
Failure envelope coefficient, θ	0.0044
Failure envelope coefficient, γ	0.02 MPa
Tensile pressure cutoff, P_c	-0.05 MPa
Cap surface axis ratio, R	1.75
Hardening coefficient, W	0.03
Hardening law exponent, D	0.3
Hardening exponent, X_0	0.0

A simulation of a single airblast test (blast A-11) from the experimental blast program was used to evaluate the material models. Blast A-11 had an explosive mass of 100.9 g and a blast height of 7.6 cm above the clay surface as summarized in Table 5.6. Simulations were performed in LS-DYNA using the two-dimensional, axisymmetric calculation set-up described in Section 5.2 . The results from the material model study on blast A-11 were used to select the final material model used to simulate the remaining experimental blasts.

Table 5.6. Blast A-11 parameters used in material model and mesh refinement study

Parameter	**Value**
Explosive mass, *W*	100.9 g
Spherical explosive diameter	54 mm
Scaled distance, *SD*	0.164 m/kg$^{1/3}$
Blast height above clay surface, *h*	7.6 cm
True crater diameter, D_T	22.8 cm
Crater depth, *d*	4.3 cm
Crater Volume, *V*	930.1 cm^3

The numerical simulations with the Soil and Foam, Pseudo Tensor, and FHWA material models ran to completion and generated craters in the clay soils for Blast A-11. The Geologic Cap material model did not run to completion but produced a “not a number” (NaN) error and terminated approximately 0.3 ms into the calculation. This error was likely generated due to errors in the plasticity algorithm caused by the large strain increments in the simulation. The time step was reduced numerous times and the

simulations were re-run to try and resolve this error with no success. Another possibility could an incompatibility of the material model with the MM-ALE solver. The material model has numerous history variables that perhaps could not be advected by volume fraction averaging over the mesh elements.

The resulting crater from the simulation using the Pseudo Tensor model is shown in Figure 5.4. The crater was approximately hemispherical in shape and had ejected material pushed up along the side of the crater to form a crater lip. The ejected clay from the blast event was clearly visible along the boundaries of the crater and displaced up above the crater. True crater dimensions were confirmed by generating density contours of the post-blast geometries as shown in Figure 5.5. As shown in the figure, the ejected material (which has a low density) does not appear due to the contour range selection. The crater shape can therefore be clearly distinguished. Simulated crater volumes were calculated in a similar manner to the experimental crater volume by rotating the two-dimensional crater profile using computer aided drafting software (Dassault Systèmes 2013) and calculating the three-dimensional volume as discussed in Chapter 4.

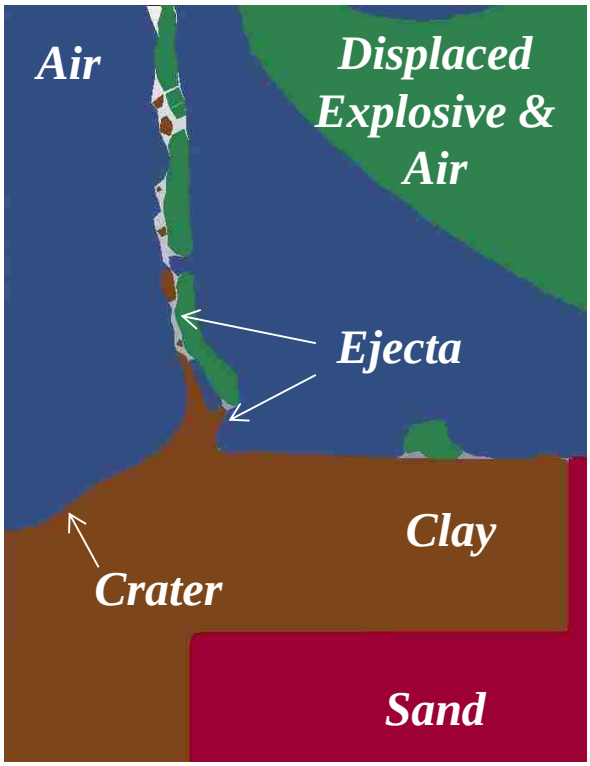

Figure 5.4. Pseudo Tensor material model crater for Blast A-11

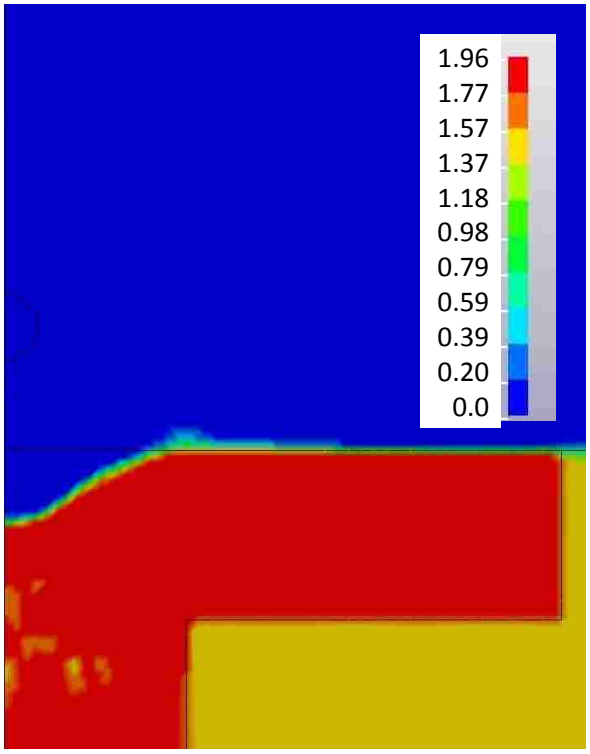

Figure 5.5. Pseudo Tensor material model density contours in (g/cm^3) for Blast A-11

Crater geometries obtained from the numerical simulations were compared to the geometry from the experimental Blast A-11. Plots of the numerically-simulated craters are shown in Figure 5.6 through Figure 5.9. The crater measured from the experimental blast was overlain on the plots to compare how well the numerically-simulated crater shape matched the experimental shape. Measurements of true diameter, D_T, depth, d and volume, V were obtained for the simulation results and compared to experimental results as summarized in Table 5.7. The percent differences between experimental and simulated dimensions are shown in Table 5.8.

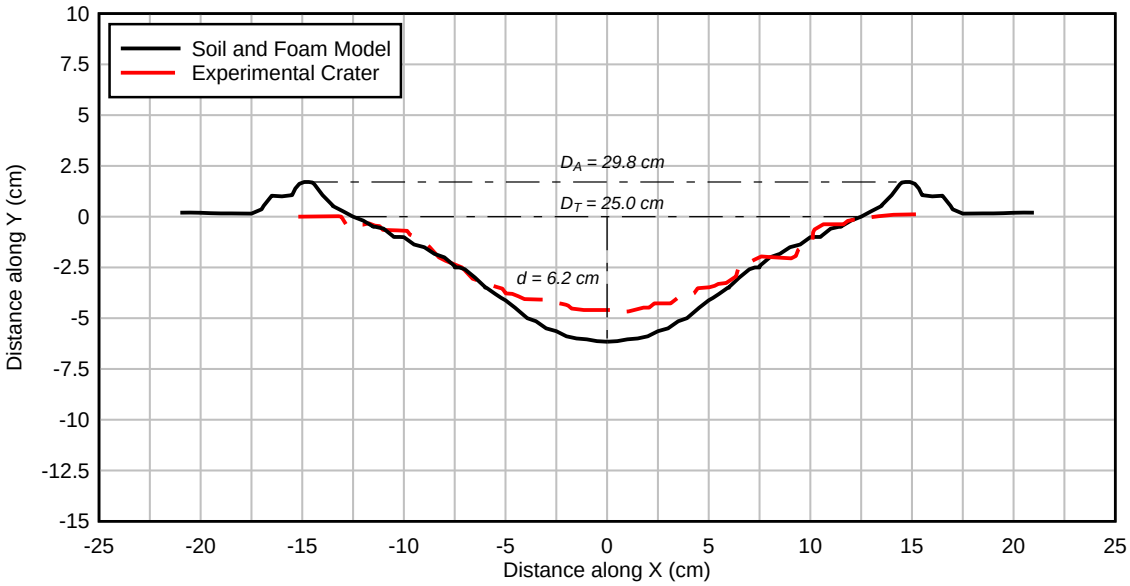

Figure 5.6. Soil and Foam model crater profile compared to experimental crater for Blast A-11

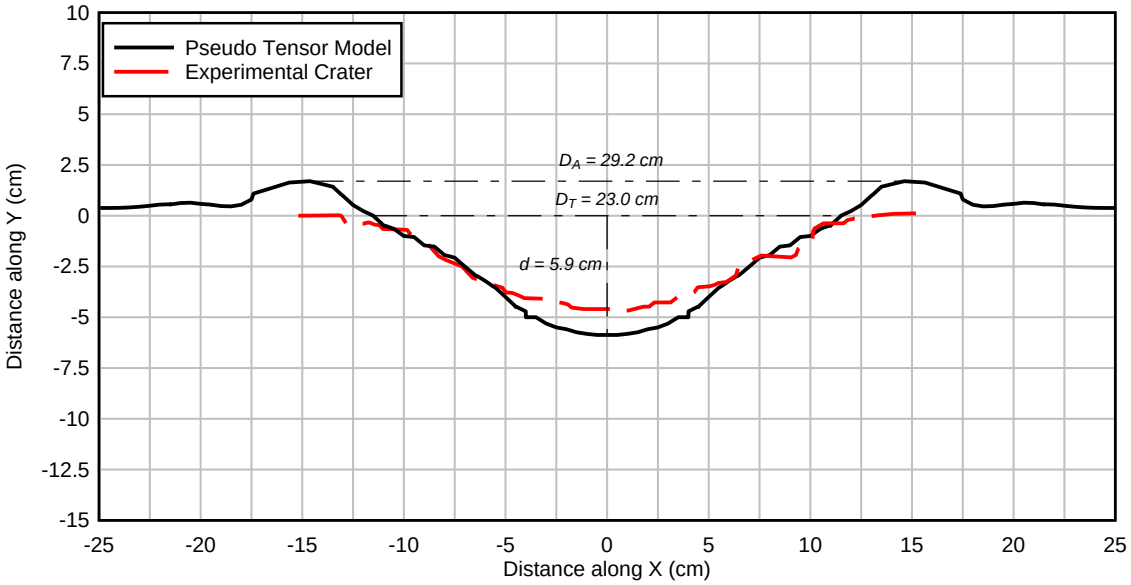

Figure 5.7. Pseudo Tensor model crater profile compared to experimental crater for Blast A-11

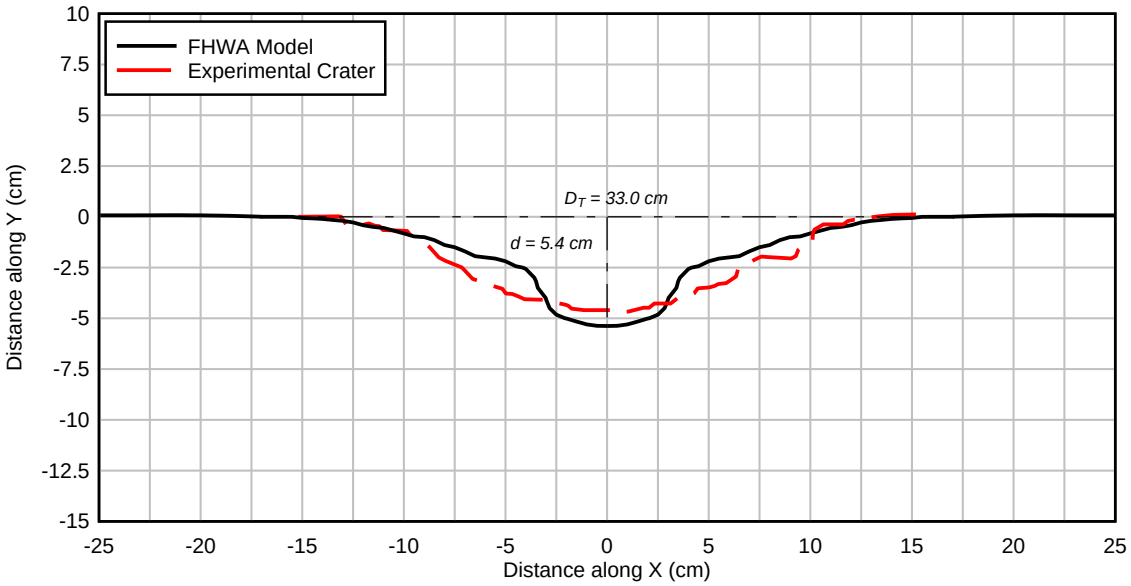

Figure 5.8. FHWA model crater profile compared to experimental crater for Blast A-11

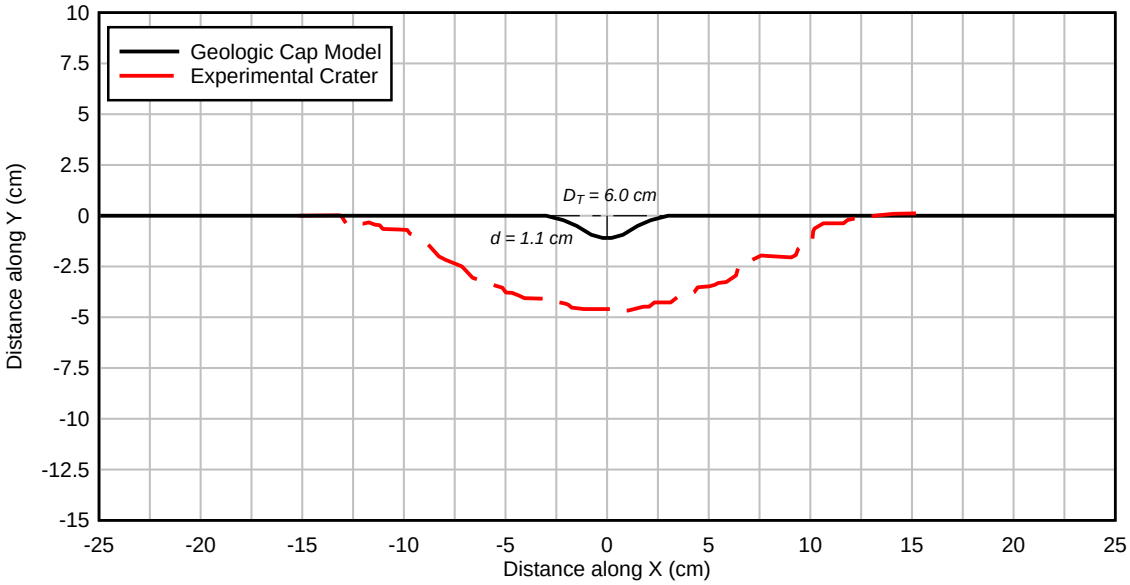

Figure 5.9. Geologic model crater profile at time = 0.3 ms compared to experimental crater for Blast A-11 (model did not successfully run to completion)

Table 5.7. Simulated crater dimensions compared to experimental crater dimensions for Blast A-11

Material Model	**True Diameter, D_T** (cm)	**Depth, *d*** (cm)	**Volume, *V*** (cm^3)
Experiment	22.8	4.3	930.1
Soil and Foam	25.0	6.2	1030.6
Pseudo Tensor	23.0	5.9	936.1
FHWA	33.0	5.4	741.2
Geologic Cap	*n/a* (calculation did not run to completion)		

Table 5.8. Difference between simulated crater and experimental crater dimensions

Material Model	Percent Difference experimental vs simulated		
	True Diameter, D_T (%)	Depth, d (%)	Volume, V (%)
Soil and Foam	9.6	44.2	10.8
Pseudo Tensor	0.9	37.2	0.6
FHWA	44.7	25.6	20.3
Geologic Cap	*n/a* (calculation did not run to completion)		

While the three working models somewhat over-predicted crater depth, the diameter and volume values from the Soil and Foam and Pseudo Tensor models compared very well to the experimental data. The crater depth from the Soil and Foam model had a 44.2% difference in depth but had only a 9.6% difference in diameter and 10.8% difference in overall crater volume as compared to experimental results. The crater depth generated by Pseudo Tensor model had a somewhat lower difference in depth than the Soil and Foam model with a percent difference of 37.2% from experimental crater depth. The model had extremely good predictions of crater diameter and depth, with a difference of only 0.9% for diameter and 0.6% in volume compared to experimental dimensions.

The crater shape from the FHWA model did not match well with experimental results and had a central depression with a steep slope transitioning to a more tapered crater slope, which resulted in an overall larger crater than experimental results. This result did not compare well to the experimental crater, which was more hemispherical in shape. Percent differences for the FHWA model compared to experimental results were 25.6% for depth, 44.7% for diameter and 20.3% for volume.

Based on these results, the simplified, mean stress dependent Pseudo Tensor strength model was chosen for modeling the explosive airblast tests for the study. While the Pseudo Tensor model overestimated crater depth, the overall crater volume and diameter compared particularly well to experimental results. Furthermore, the simplified, robust nature of the model along with the associated historical user feedback and improvement make the model well-suited for simulating soil response to blast-induced dynamic loading.

5.6 Sand Material Model

The sand backfill material was modeled with the Pseudo Tensor mean stress dependent strength model (LS-DYNA Material Model 16) for all simulations. The compressibility response of the was modeled based on numerical studies of sand behavior under high-stress environments with high deformation rates (Resnyansky and Wildegger-Gaissmaier 2001, Grujicic et al. 2008). The studies accounted for the soil constituent materials including solid mineral particles and pore water and proposed compaction curves with a soft stiffness response at low pressures that transitioned to a high stiffness at high pressures.

The compressibility curves proposed by the authors could be "shifted" by porosity difference for sands with varying porosities. Based on this approach the compaction equation of state was modeled for the sands used in this study based on the porosity obtained from lab test data (as calculated by Equation 3.5). A summary of the input parameters for the material model is given in Table 5.9.

Table 5.9. Sand material input parameters for Pseudo Tensor Material Model (LS-DYNA Model 16)

Parameter	Input
Tensile pressure cutoff, P_c	0.0 MPa
Unloading bulk modulus, K_{Unload}	48,000 MPa
Strength Envelope Inputs:	
Mean stress, P (MPa)	Yield stress, (σ_1- σ_3) (MPa)
0.0	0.0
112.27	128.3
143.5	155.05
176.1	178.04
204.4	192.2
244.04	204.7
279.4	212.2
313.3	217.4
437.6	221.8
6000.0	225.0
Compressibility Curve Inputs	
Mean stress, P (MPa)	True volume strain, ε_{log}
0.0	0.0
38.89	-0.1807
77.79	-0.3323
180.83	-0.4904
256.85	-0.5323
304.96	-0.5504
654.90	-0.5822
1508.33	-0.6011
7496.41	-0.6908

5.7 Mesh Refinement

A mesh refinement study was performed for the clay soils using the Pseudo Tensor material model (LS-DYNA material model 16) to evaluate the optimum mesh size that reduced computation time while still matching experimental results. Simulation crater geometries (volume, V true diameter, D_T and depth, d) were compared to experimental crater geometries to evaluate the mesh refinement results. Fine to coarse element sizes varying from 2 mm to 6 mm in width were used to determine which size produced accurate results while minimizing computation time. Elements larger than 6 mm resulted in an unstable fluid surface in the MM-ALE algorithm that made it difficult to determine crater shape. The optimum element size was selected that retained a controlled fluid surface for crater delineation.

The crater geometry results from the mesh refinement study compared to experiment results are shown in Figure 5.10. Element sizes 5 mm and smaller were closest to experiment results for crater diameter and volume as shown in Figure 5.10 (*a*) and (*c*), respectively. Results began to deviate after 6 mm in size, and the fluid surface was not distinct for elements larger than 6 mm. While depth results were fairly stable as shown in Figure 5.10 (*b*), all element sizes (6 mm or less) somewhat over predicted crater depth. However all element sizes were close to experimental results and still provided adequate results.

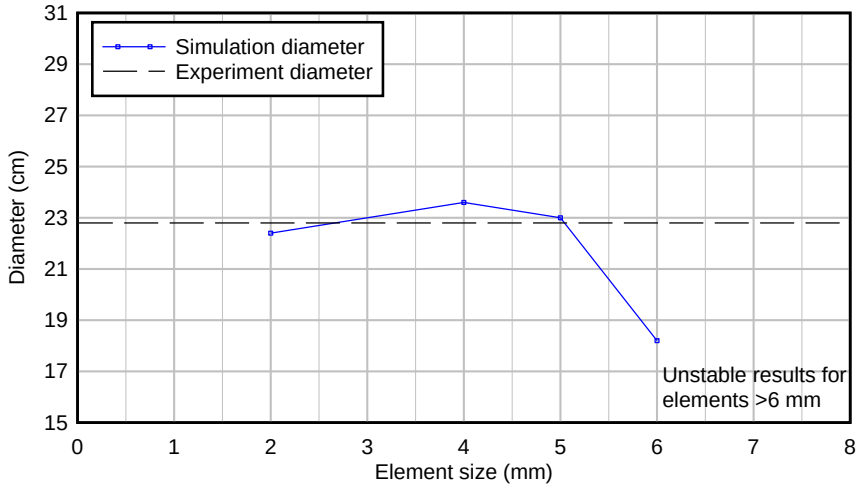

(**a**)

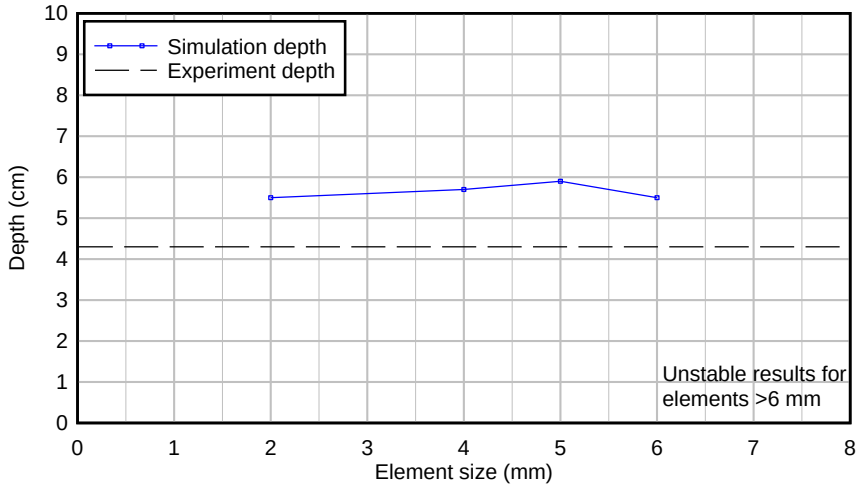

(**b**)

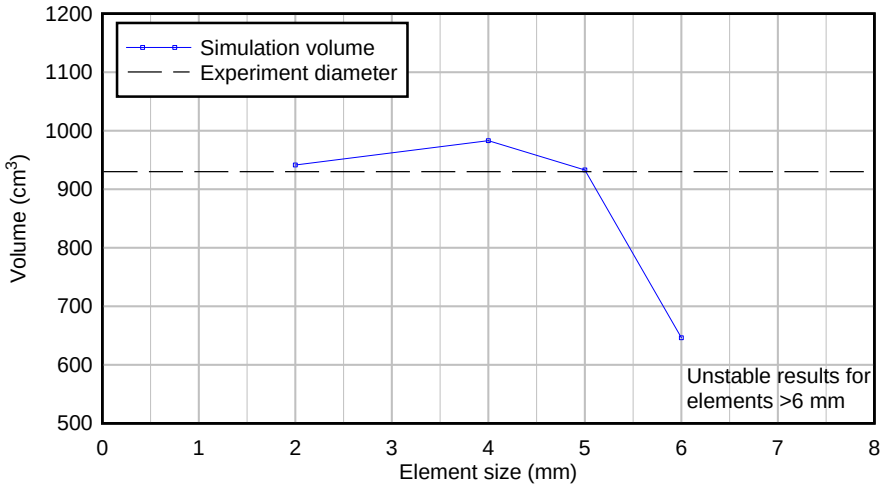

(**c**)

Figure 5.10. Crater results from mesh refinement study for (*a*) true diameter, D_T (*b*) depth, *d* and (*c*) Volume, *V*

Based on the results of the mesh refinement study, it was determined that the 5 mm element size provided adequate results while still having an efficient computation time. The mesh size corresponded to approximately ten percent of the spherical explosive diameter. The 5 mm mesh (0.005 m) size also corresponds to 3% of the scaled distance, *SD* value (given in $m/kg^{1/3}$). These results were used to calculate the maximum allowable mesh size for each of the simulated blast events, which had varying explosive diameters and *SD* values. However, an element size of 5 mm was not exceeded in the clay soils for any simulation.

5.8 Simulation Results

Finite element simulations of the experimental explosive blasts were performed in LS-DYNA using the Pseudo Tensor material model. Results from the numerical simulations included crater geometries and ground vibration response. Stress and velocity response from individual tracer nodes was also obtained to examine the convergence of the model and the adequacy of the model to capture the stress response of the soil. The following sections discuss the results of the simulated explosive blasts.

5.8.1 Crater Geometry

Crater dimensions from the simulated blasts were compared to experimental blasts using the same graphical relationships presented in Section 4.2. A plot of true crater diameter, D_T versus scaled distance, *SD* for experimental and simulated blasts is shown in Figure 5.11. Crater diameters from the finite element calculations ranged from 6.3 to 23.4 cm and compared very well to the experimental results. While the simulated crater diameters

were slightly larger than experimental diameters the same trends were observed of increasing diameter with decreasing scaled distance (which corresponded to higher energy). Trendlines were fit through the combined simulation and experimental data for each blast series to describe this relationship.

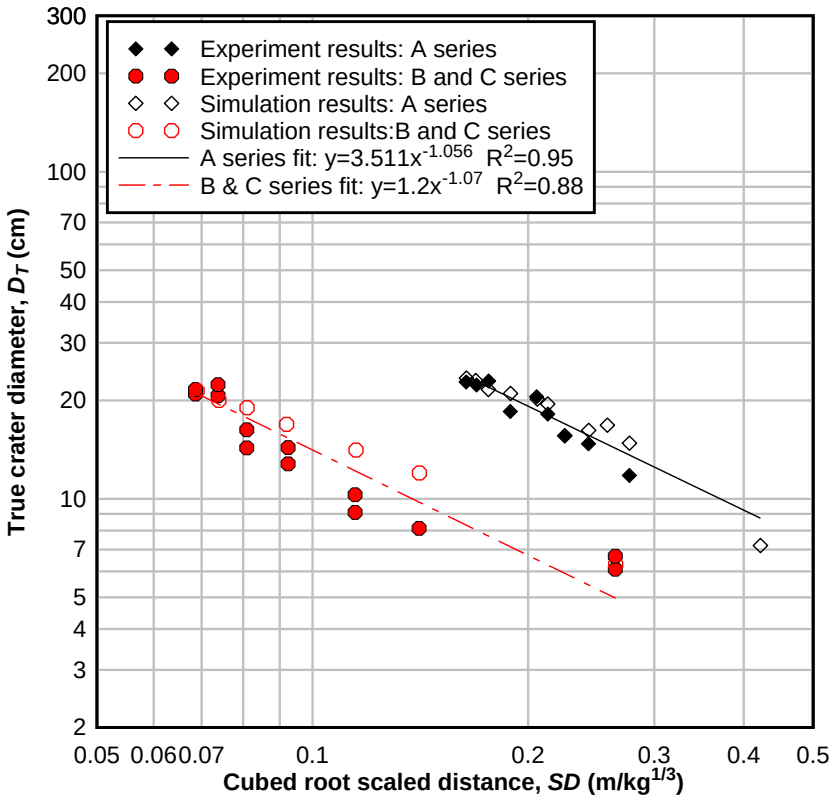

Figure 5.11. True crater diameter vs. scaled distance for experimental and simulated blasts

True crater diameters, D_T, and scaled explosive mass, W, were normalized by blast height, h for the simulated blasts as shown in Figure 5.12. Simulated results compared very well to experimental results when normalized by blast height. This was particularly true for the A series blasts, where simulated results plotted nearly on top of experimental

results. A single trendline was therefore fit through simulated and experimental data to illustrate the trend.

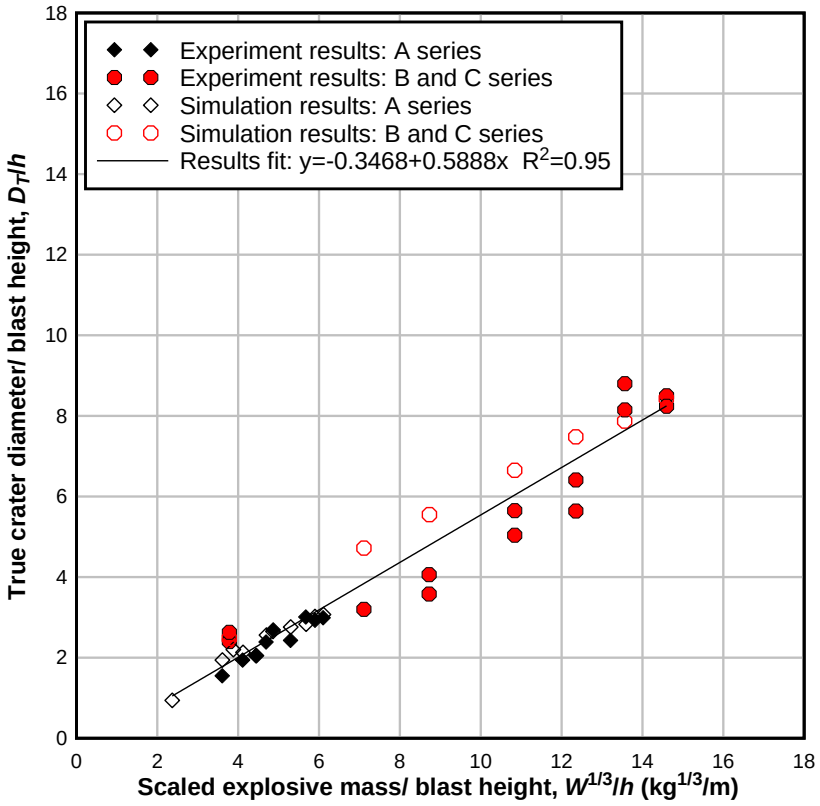

Figure 5.12. Crater diameter to blast height ratio vs. scaled explosive mass for experimental and simulated blasts

A plot of crater depth, *d* versus scaled distance, *SD* for simulated and experimental results is shown in Figure 5.13. Simulated crater depths, *d* normalized by blast height, *h* are shown in Figure 5.14. Simulated crater depths ranged from 1.2 to 9.0 cm, with the B and C blast series exhibiting larger crater depths than the A series. Simulated depths were larger than the experimental results as seen in the figures. This was especially apparent for larger *SD* values, which correspond to smaller explosive masses that imparted lower energy into the ground. Simulated depth results converged closer to experiment results at

smaller SD values, which corresponded to blasts with higher energy. The material model therefore appeared to capture the soil response (as described by crater depth) of higher-energy blasts better than blasts with lower energy. Depth results were more comparable to experimental results when normalized by blast height as shown in Figure 5.14. However, simulation results were not included in the trendline fits because of their divergence from experimental results.

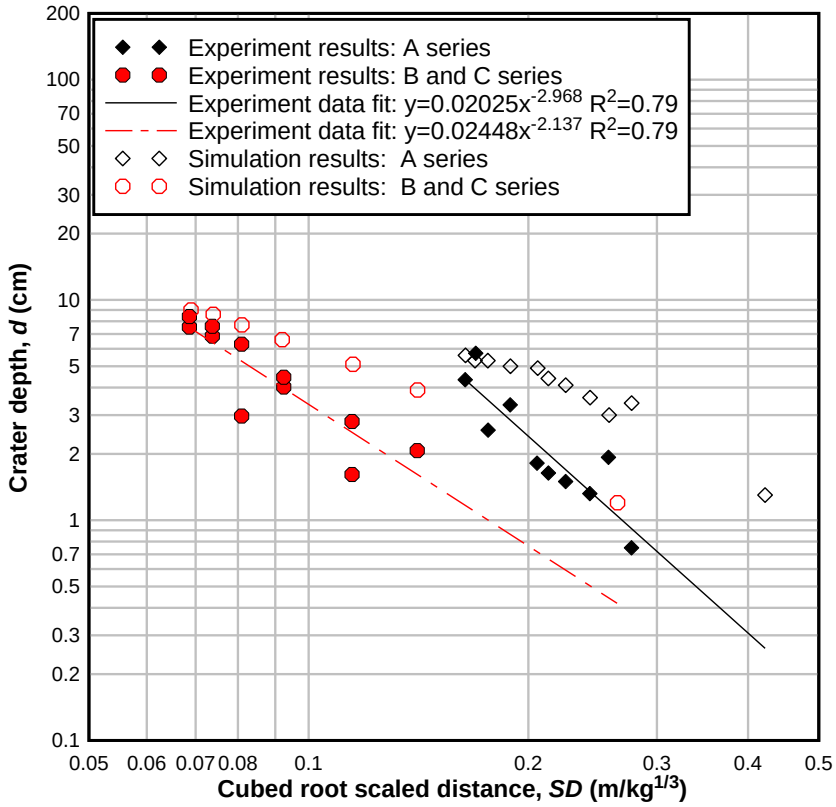

Figure 5.13. Crater depth vs. scaled distance for experimental and simulated blasts

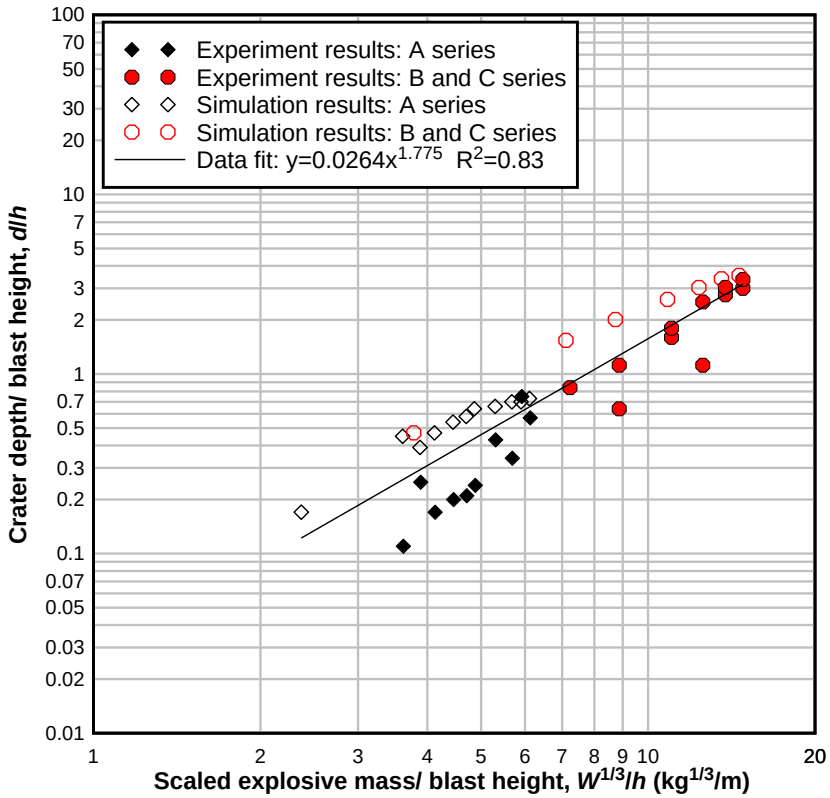

Figure 5.14. Crater depth to blast height ratio vs. scaled explosive mass for experimental and simulated blasts

A plot of simulated and experimental crater volume, *V* versus scaled distance, *SD* is shown in Figure 5.15. Crater volume and explosive mass normalized by blast height are shown in Figure 4.15 to directly compare results between blast series. Simulated crater volumes ranged from 8.2 to 1800.5 cm^3 and were somewhat larger than experimental results due to the over-predicted depth from the material model. However, simulated volumes still had a reasonably close fit to experimental results and captured the trend of increasing crater volume with decreasing scaled distance. A plot of the crater volume parameter, V_c as calculated by Equation 4.1 for simulated results is presented in Figure 5.17. The simulated volume parameter results were somewhat smaller than experimental

results due to increased depth but similar trends were still maintained. Trendlines were fit to combined simulated and experimental results in Figure 5.15 and Figure 5.17.

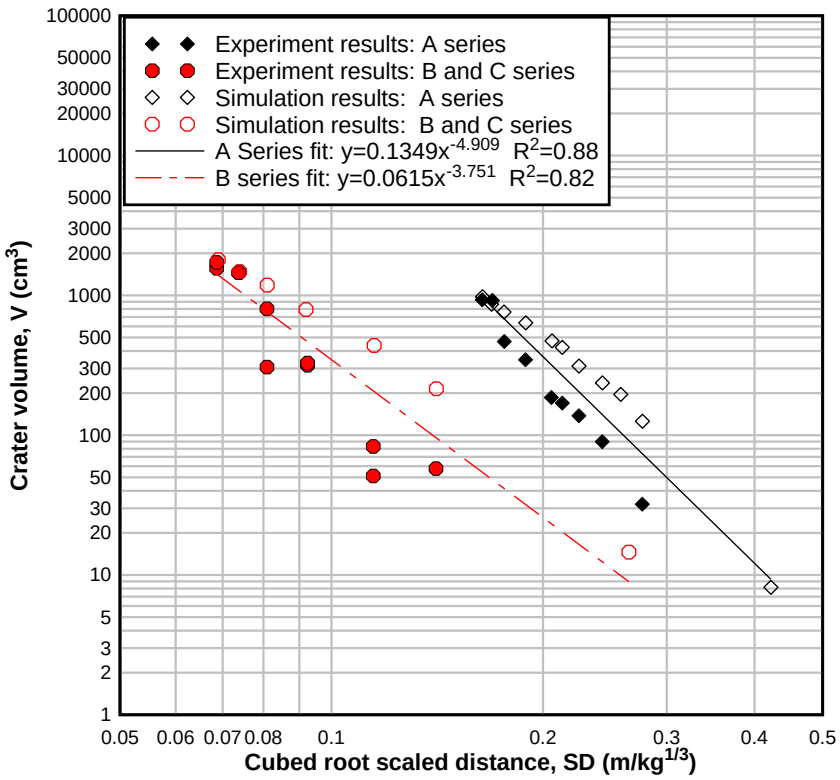

Figure 5.15. Crater volume vs. scaled distance for experimental and simulated blasts

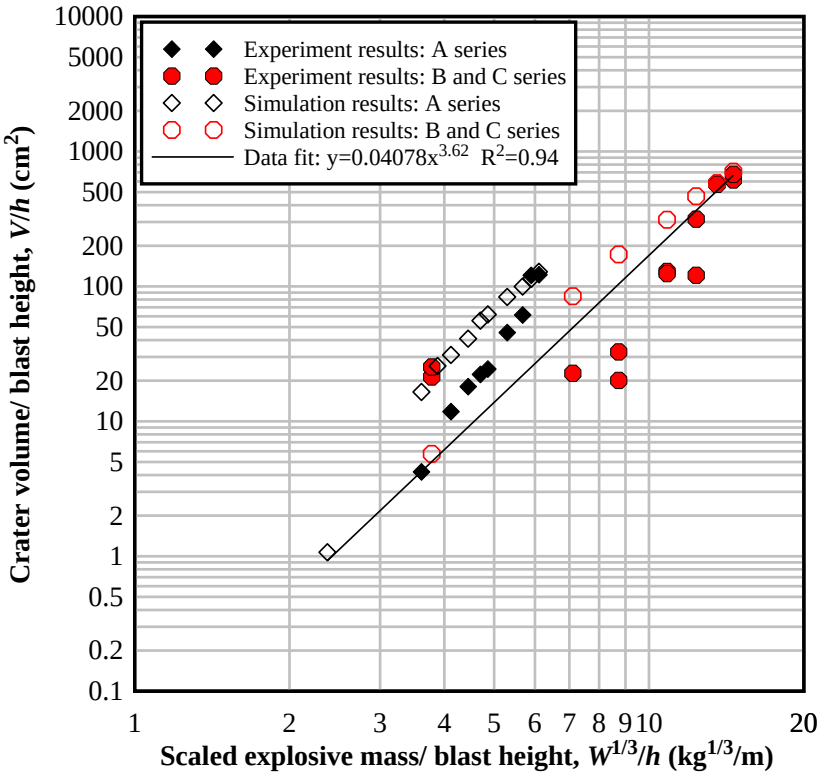

Figure 5.16. Crater volume to blast height ratio vs. scaled explosive mass for experimental and simulated blasts

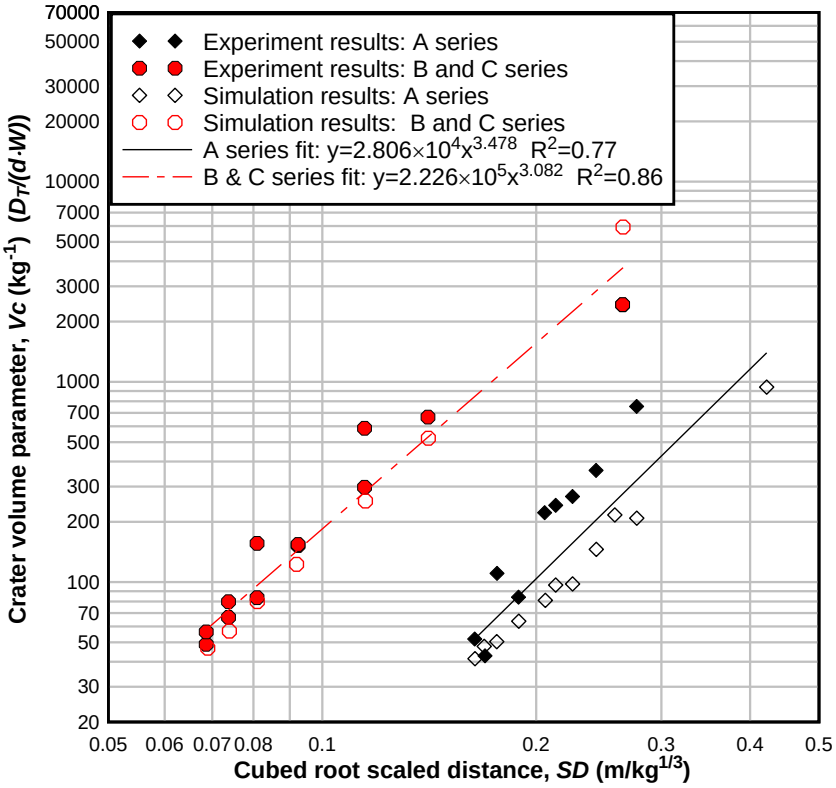

Figure 5.17. Crater volume parameter vs. scaled distance for experimental and simulated blasts

5.8.2 Ground Vibration and Airblast

Ground motion results from the finite element simulations were obtained from tracer node outputs and compared to experimental ground motion data recorded by the subsurface geophones. The peak particle velocity, *PPV* value was defined as the maximum ground motion observed during the tracer node time history record. A plot of *PPV* versus scaled distance for the experimental data and simulation results is shown in Figure 5.18. *PPV* results for the finite element simulations were averaged over a 25 cm^2 area at each geophone location, which was equivalent to the area of the 5 cm by 5 cm

housing dimensions of the geophones utilized in the field experiments. This approach allowed the simulation and experimental results to be directly compared.

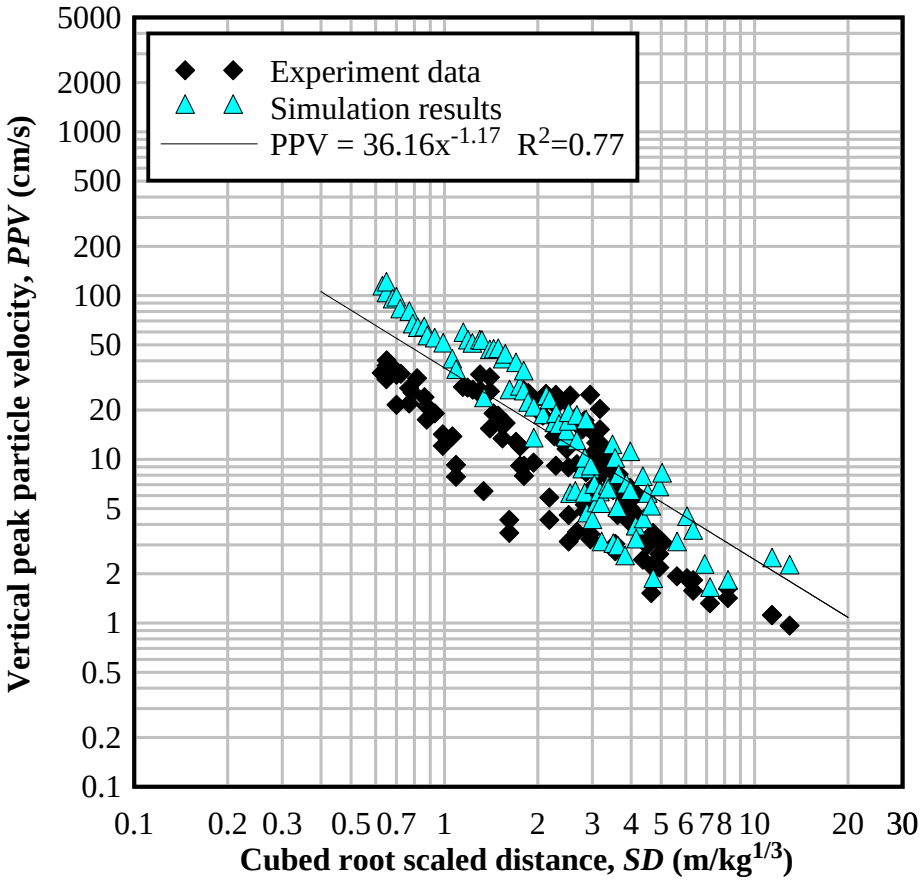

Figure 5.18. Vertical *PPV* vs. scaled distance, *SD* for experimental and simulated blasts

The ground vibration magnitude and attenuation was captured fairly well by the simulations as shown in Figure 5.18. Simulated *PPV* values ranged from 1.6 to 116.6 cm/s. The *PPV* for small *SD* values corresponding to greater blast energy was overestimated by the material model, indicating that the attenuation and material damping was not quite captured for high-energy blasts. This was likely attributed to material

variation for the experimental blasts. The stiffness and air porosity likely varied for the experiential blasts and caused the material attenuation to vary from the attenuation calculated by the compressibility curve utilized in the numerical simulations. However, *PPV* results were overall fairly representative of the experimental results.

The simulated air overpressure, AOP results are plotted with the experimental results in Figure 5.19. The placement of the air overpressure sensors during the experiment resulted in larger SD values and provided data of anticipated air overpressure at distances farther from the blast source. Experimental air overpressures decreased with distance from the blast source and ranged from 0.6 to 18.2 kPa. The simulation provided anticipated values for overpressure at distances close to the blast source (and low SD values) and therefore had much higher values that ranged from 31.9 to 2,618 kPa.

The slope of the simulation fit was steeper than the experimental slope, with attenuation exponent values of -1.87 and -1.16, respectively. This may indicate that the simulated blast pressures may have been larger than the blast pressures seen during the experiments. The steeper slope seen in the simulation results may also be due to the effects of surface reflection, which may have produced higher pressures closer to the blast source and resulted in a discontinuous slope for distances farther from the source. In addition, simulated air overpressures likely approximated experimental values due to the good correlations obtained between experimental and simulated crater dimensions.

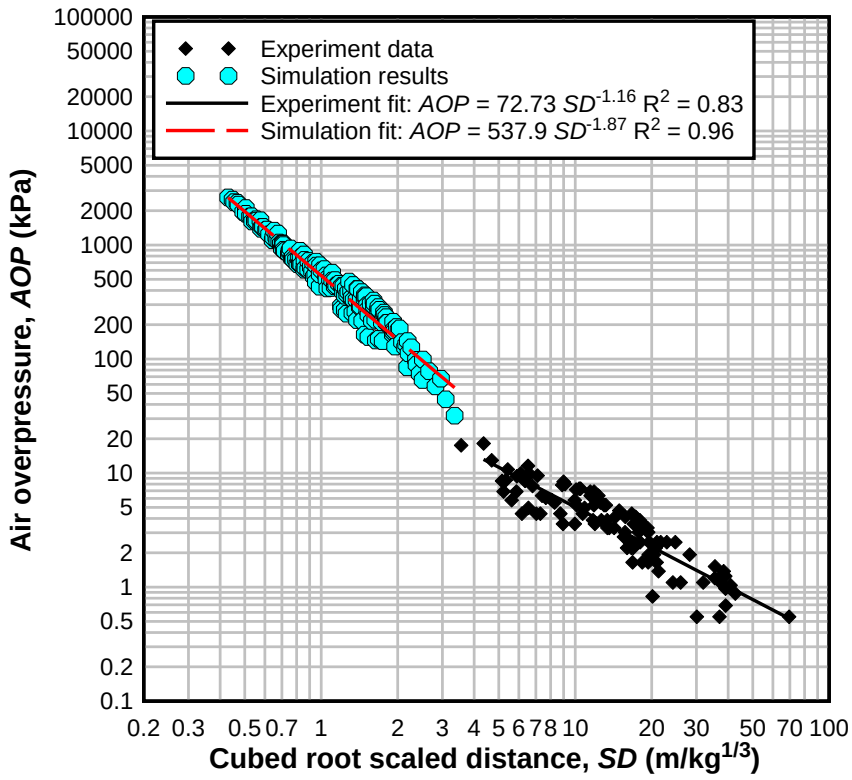

Figure 5.19. Air Overpressure (*AOP*) vs. scaled distance, *SD* for experimental and simulated blasts

5.8.3 Stress Response

Stress and velocity time histories from individual tracer nodes were examined to determine how the material modeled the stress response of the soil under blast loading. Mean stress (pressure) vs. time was plotted for blast A-11 as shown in Figure 5.20 from a tracer node located 5 cm below ground surface near the crater region. Mean stress is positive in compression in the figure. The material model successfully captured the initial shock front as shown by the abrupt increase in pressure. Pressure decreased with time and eventually returned to zero as the shock wave passed through the material.

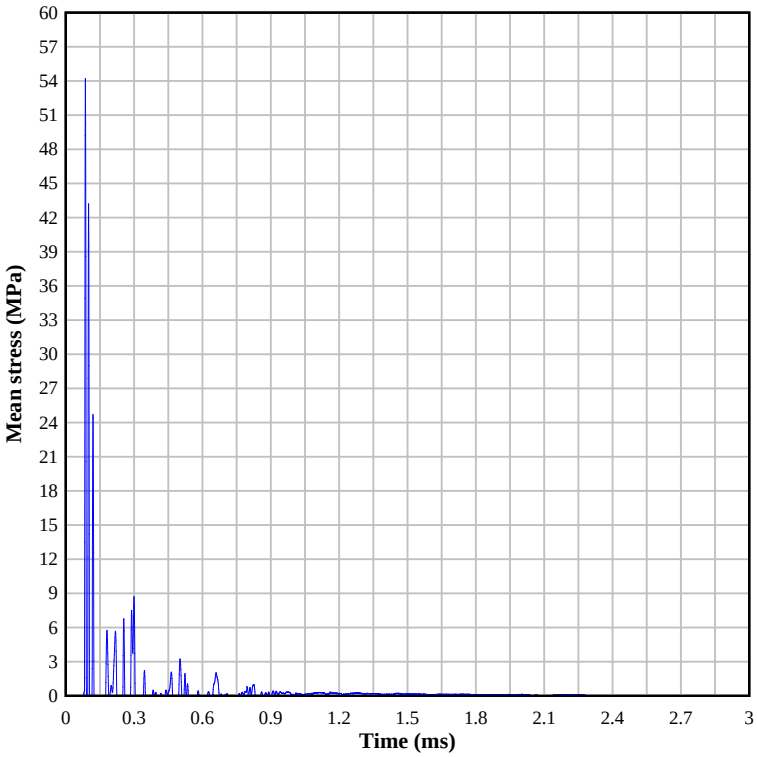

Figure 5.20. Mean stress vs. time for Blast A-11 near crater region

A plot of mean stress and vertical particle velocity vs. time for Blast A-11 from a tracer node located 22 cm below ground surface (corresponding to the location of the shallowest subsurface geophone) is shown in Figure 5.21. Mean stress is positive in compression and vertical particle velocity is negative in the downward direction in the figure. The soil model captured the compressive pressure increase from the blast which resulted in a sharp increase in particle velocity. The soil particle velocity decreased as pressure decreased. While vertical particle velocity hovered close to zero at late history, there was still a residual, positive velocity observed for the entire run time. This indicates that the soil model continues to deform a small amount, which could lead to erroneous results for late time histories.

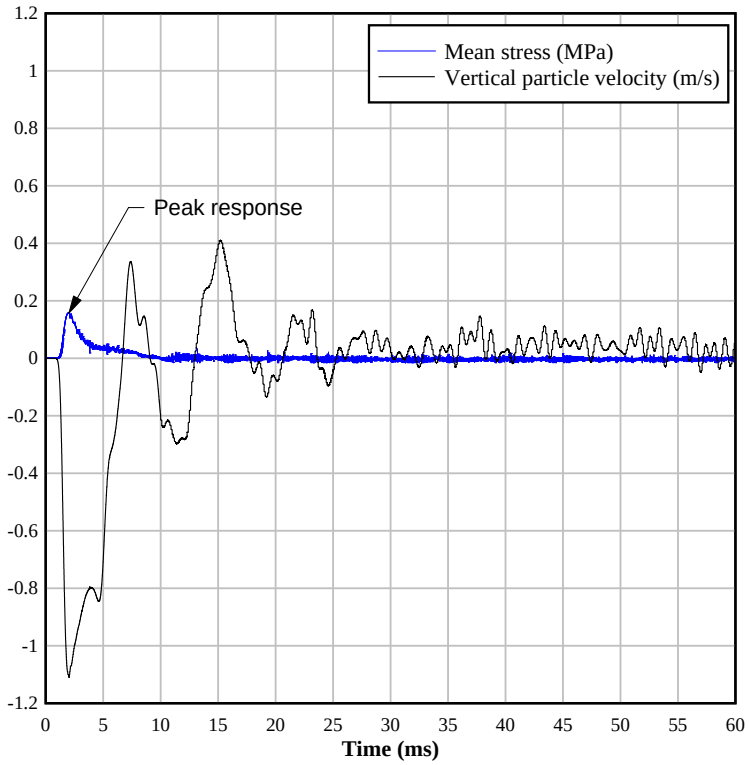

Figure 5.21. Mean stress and vertical particle velocity vs. time for Blast A-11 at 22 cm below ground surface

The compressibility curve for the material model was changed to include only the undrained portion of the compressibility curve with a bulk modulus, *K* value of 4680 MPa as given in Table 3.6. This input was selected to investigate the response of the model to a single, stiff modulus scenario that would occur if all air voids were crushed out of the material. A plot of mean stress and vertical particle velocity vs. time for blast A-11 from a tracer node located 22 cm below ground surface for this scenario is shown in Figure 5.22. The initial shock front was captured as shown by the increase in pressure. As pressure decreased the tensile cutoff value was reached. After this point, the pressure results flatlined with a small "jump" at approximately 0.29 ms. While the tensile cutoff value should have restricted the pressure from becoming more tensile than the cutoff value, the pressure should have returned to the compressive regime and numerous

compressive pulses should be expected from the blast event. The material model instead appeared to erroneously "zero-out" the pressure response after the tensile cutoff value was reached.

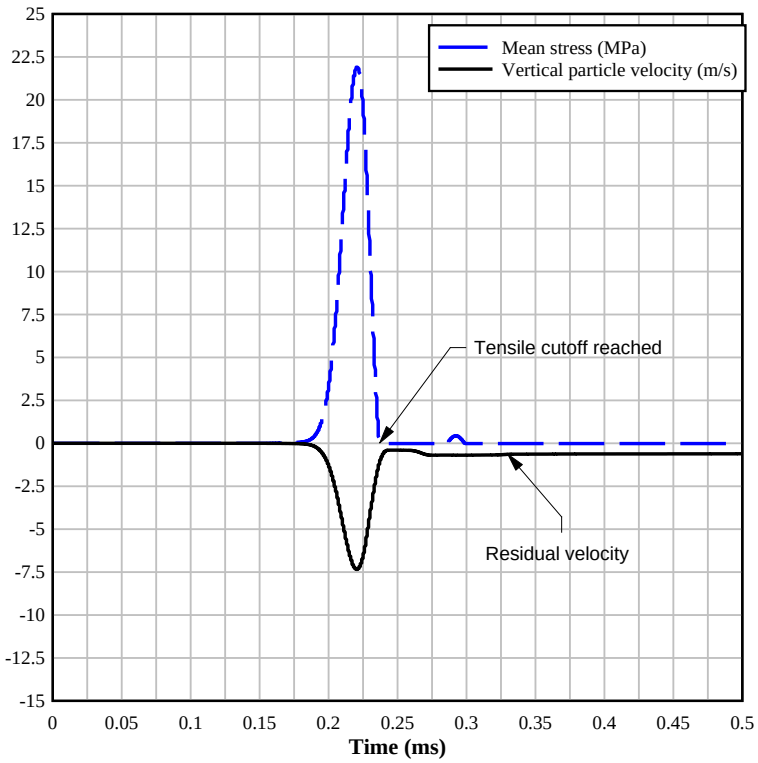

Figure 5.22. Mean stress and vertical particle velocity vs. time for Blast A-11 at 22 cm below ground surface (single modulus model corresponding to no air-filled voids)

The ground vibration results as shown by the vertical particle velocity in Figure 5.22 also exhibited instabilities. The particle velocity did not alternate phases as would be expected for a ground shock event. In addition, once the tensile cutoff value was reached the velocity did not return to zero but instead exhibited a small, residual velocity for the remainder of the time history. While the majority of the velocity response (and therefore soil deformation/ crater formation) occurred during the initial pressure pulse from the

blast, the post peak response was not captured. Large errors could result for very late time histories due to these instabilities.

Based on the stress history results shown in Figure 5.21 and Figure 5.22 the Pseudo Tensor material model appeared to capture the first-order response of the soil in terms of crater formation and the initial stress pulse from the blast. The crater deformation response was captured as indicated by the reasonable correlations between the experiment and simulated crater geometry. However, the model did not capture the post-peak response as exhibited by instabilities in the mean stress and particle velocity responses. Late time history results from the single bulk modulus version of the model appeared to be particularly unstable based on the stress and particle velocity response. The model instabilities could possibly be attributed to instabilities in the MM-ALE solver in LS-DYNA, which may not have adequately captured the post peak material response. It is therefore recommended that while the material model can be used to estimate general deformations anticipated in a soil subjected to an airblast load, it cannot be relied on to capture post-peak or stress path response, particularly for late time history.

6 DEFORMATION-INDUCED STABILITY OF EARTHEN EMBANKMENT DAMS SUBJECTED TO EXPLOSIVE AIRBLAST LOADING

Finite element simulations were performed of explosive airblast events located on the downstream toe of a hypothetical earthen embankment dam composed of the same cohesive soils used in the small-scale experimental blasts. The seepage and stability of the embankment dam was evaluated. Traditional limit equilibrium methods were used to evaluate dam stability. The effects of varying reservoir levels and engineered drainage were investigated. A discussion of the analyses methods and results for the finite element simulations, seepage modeling, and slope stability modeling are presented in this chapter.

6.1 Numerical Simulations

Finite element calculations of explosive airblast loads on an earthen embankment dam were performed and post-blast geometries were obtained. A description of simulation methodologies and results is provided in the following sections.

6.1.1 Simulation Methodology

Finite element simulations of explosive airblast loads on an earthen embankment dam were performed using the software LS-DYNA Version 7.1.1 (LSTC 2014). Appendix A presents an example of the LS-DYNA keyword input decks used in the embankment dam simulations of this study. Explicit time integration with a Multi-Material Arbitrary Lagrangian Eulerian (MM-ALE) formulation was used to simulate the explosive blasts. The dam was assumed to consist of the homogeneous, soft, clay soils used in the experimental blasts of this study.

The embankment dam was assumed to be a small dam consisting of homogenous soil founded on a rigid, impermeable foundation. A sketch of the dam geometry is provided in Figure 6.1. Dimension guidelines were obtained from design manuals for small earth dams (Stephens 2010, USBR 2004). The dam was assumed to be 30 m high with a crest width of 9 m. An upstream slope of 3 m horizontal to 1 m vertical (3H:1V) and a downstream slope of (2H:1V) was assumed. Two drainage conditions were investigated in this study: 1) no engineered drainage and 2) a 20 m horizontal toe drain located at the downstream toe. The effects of reservoir levels varying from 10 m to 25 m were also investigated in the study.

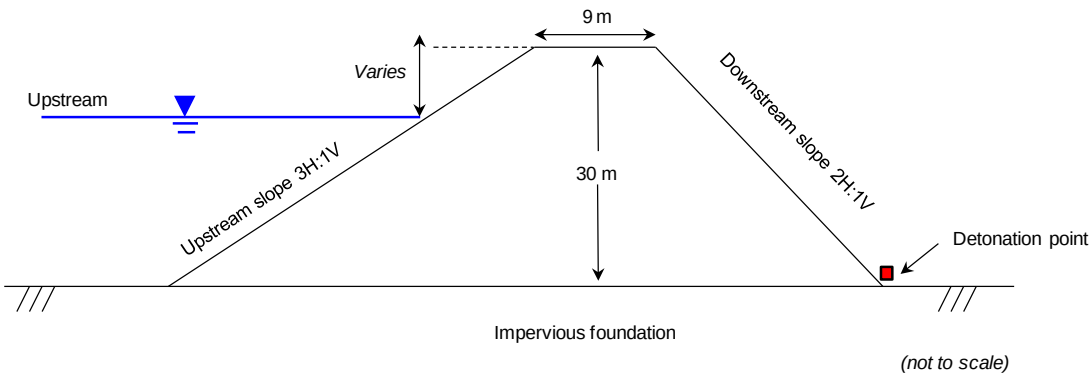

Figure 6.1. Geometry of earthen embankment dam (not to scale)

Explosive airblast loads were imposed by a cubically-shaped explosive located at the downstream toe as illustrated in Figure 6.1. The explosive was located 0.8 m above the dam surface to correspond to the height of a box truck vehicle positioned near the dam. The explosive was positioned at the dam toe assuming that this location is more readily accessible to a commercial vehicle due to current security restrictions that limit access to

the dam crest for many dams. In addition, a blast at the toe is located close to the phreatic surface and may induce greater instabilities upon detonation. Explosive masses varied from 1.0 metric tons up to 44.4 metric tons.

The explosive was assumed to consist of the same two-part binary explosive used in the explosive blasts performed in this study (as described in Chapter 4). The explosive properties were modeled using the Jones Wilkins and Lee (JWL) equation of state (Equation 5.5) coupled with the LS-DYNA High Explosive Burn (HEB) material model (Equation 5.6). Explosive model inputs are provided in Table 5.1 of Section 5.3.

Simulations were performed using a three-dimensional numerical calculation with half plane symmetry and non-reflecting boundaries as shown in Figure 6.2. A three-dimensional calculation was required to properly model the cubical explosive, which could not be modeled with a two-dimensional, plane-strain calculation. Only the toe area of the dam was simulated as this was the main area of interest near the explosive. This approach also reduced the number of elements (and therefore computation time) for the calculation. A hexahedral mesh was constructed of elements sized 0.2 m by 0.1 m by 0.2 m as shown in Figure 6.3. Element sizes were chosen based on a balance between the mesh refinement study described in Section 5.7 and to maintain a total number of elements that resulted in reasonable computation times. The dam slope surface was stepped to ensure hexahedral elements and increased computational efficiency.

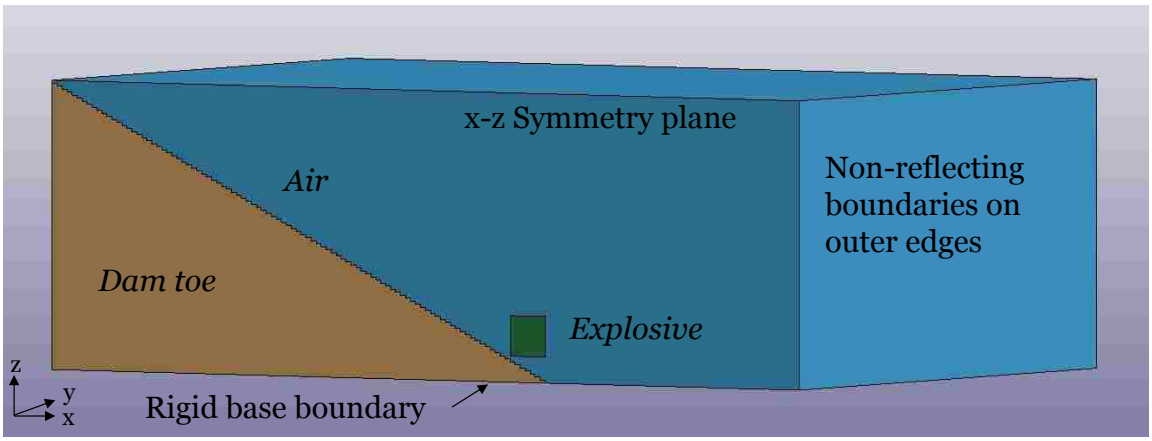

Figure 6.2. Geometry and boundary conditions for embankment dam finite element simulations

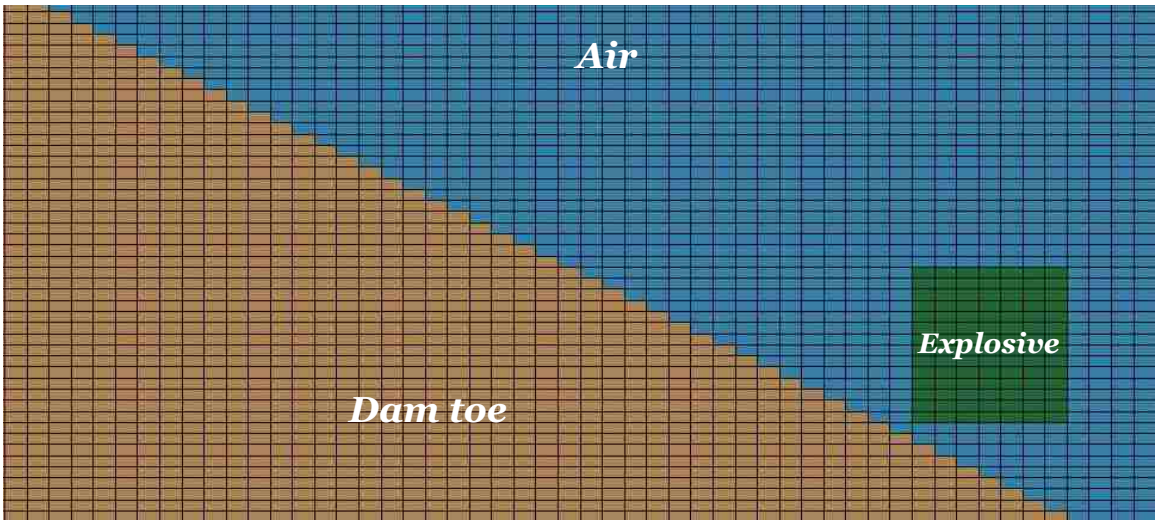

Figure 6.3. Finite element mesh for embankment dam simulations (zoomed in view near explosive region)

The dam was assumed to consist of the clay soils used in the experimental blasts of this study and characterized by lab testing as described in Sections 3.1 and 3.1.1. The geotechnical and strength properties of the soils determined from laboratory testing are provided in Table 3.5. Undrained compressibility properties used in the model are provided in Table 3.6. Only the undrained response was used in the simulations since it

was assumed that the embankment dam consisted of soils that had no air voids due to long-term consolidation of the soils.

The Pseudo Tensor soil material model (LS-DYNA material model 16) was used to simulate undrained soil response to blast loading in the finite element simulations based on the results of the material model study described in Section 5.5. Material model inputs are given in Table 6.1. Mohr-Coulomb strength data was converted to tabulated values of stress difference (σ_1 - σ_3) versus mean stress (p) as required by the material model. The model was coupled with a compaction equation-of-state (formulated in terms of tabulated mean stress vs logarithmic true volume strain) to describe soil compressibility. The soil compressibility was described by linear compressibility with a single, high stiffness modulus to simulate the conditions that would be present in an earthen dam that has been in place long enough for consolidation to occur.

Table 6.1. Input parameters for Pseudo Tensor Material Model used in embankment dam simulations (LS-DYNA Model 16)

Parameter	**Input**
Linear Strength Envelope	$(\sigma_1 - \sigma_3)$ (MPa) = 0.154P + 0.047
Tensile pressure cutoff, P_c	0.046 MPa
Bulk modulus, K (MPa)	4680.0 MPa
Unloading bulk modulus (true volume strain space), K_{Unload}	4609.0 MPa

A summary of the simulation scenarios performed for varying reservoir levels, drainage conditions, and explosive masses is presented in Table 6.2. For each explosive mass, simulations were performed for each reservoir level with undrained and toe drain configurations.

Table 6.2. Embankment dam simulation matrix

Drainage Conditions	Reservoir level (m)	Explosive mass (metric tons)
No engineered drainage and	10	1.0
Horizontal toe drain	15	2.8
	20	4.9
	25	9.6
		19.5
		44.4

6.1.1 Simulation Results

The embankment dam explosive airblast simulations ran successfully to completion. The finite element simulations resulted in the creation of craters on the downstream slope surface and erosion of the dam toe. An example of the resulting crater is shown in Figure 6.4. The craters were irregular in shape due to the cubic geometry of the explosive and the position of the explosive with respect to the dam toe. The material at the toe of the dam was scoured away by the blast which resulted in a reduction of the overall horizontal dimension.

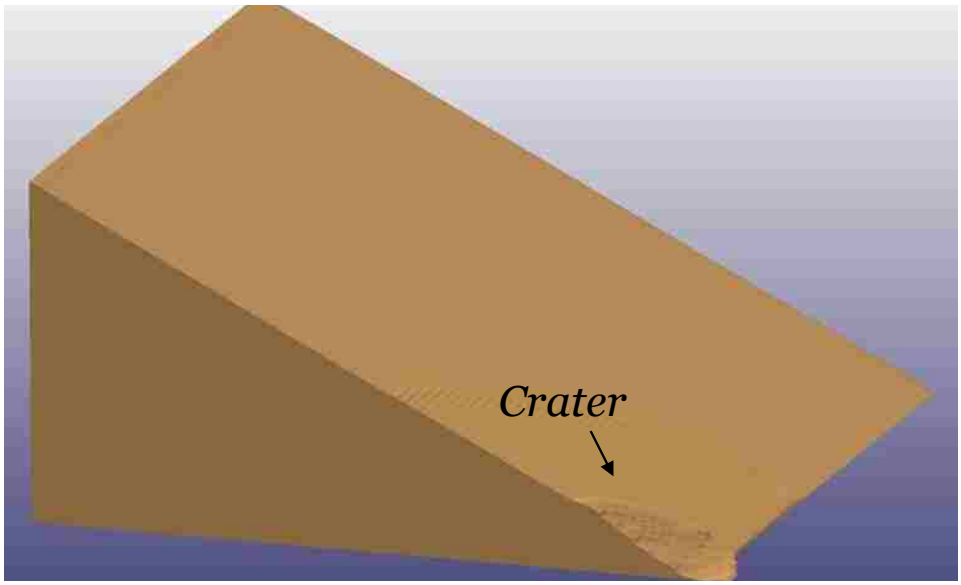

Figure 6.4. Post-blast crater formed on downstream slope of embankment dam

A two-dimensional section was created along the symmetry plane to inspect the crater dimensions for each of the blasts as shown in Figure 6.5. Larger explosive masses resulted in more material removed from the embankment dam toe. The energy imparted into the soil from the airblast event did not result in significant crater dimensions due to reduced energy being transferred into the soil from energy loss into the air. The craters created on the downstream slope reduced the horizontal dimension of the dam toe by approximately 4.5 m to 10.0 m from the original configuration for explosive masses of 1.0 tons and 44.4 tons, respectively. Each subsequent explosive mass reduced the horizontal dam toe dimension by approximately 2 m.

Pressure (mean stress) contour plots were created as shown in Figure 6.6 to illustrate stress propagation within the dam from the simulated airblast events. The initial blast is seen at time equal to 0.5 ms with a pressure pulse located on the dam toe and beginning

to propagate across the slope. The pressure wave can be seen interacting with the rigid boundary at 2.0 ms as the pressure contour changes shape and becomes irregular. The pressure pulse continues to propagate through the embankment dam from 3.0 ms and beyond.

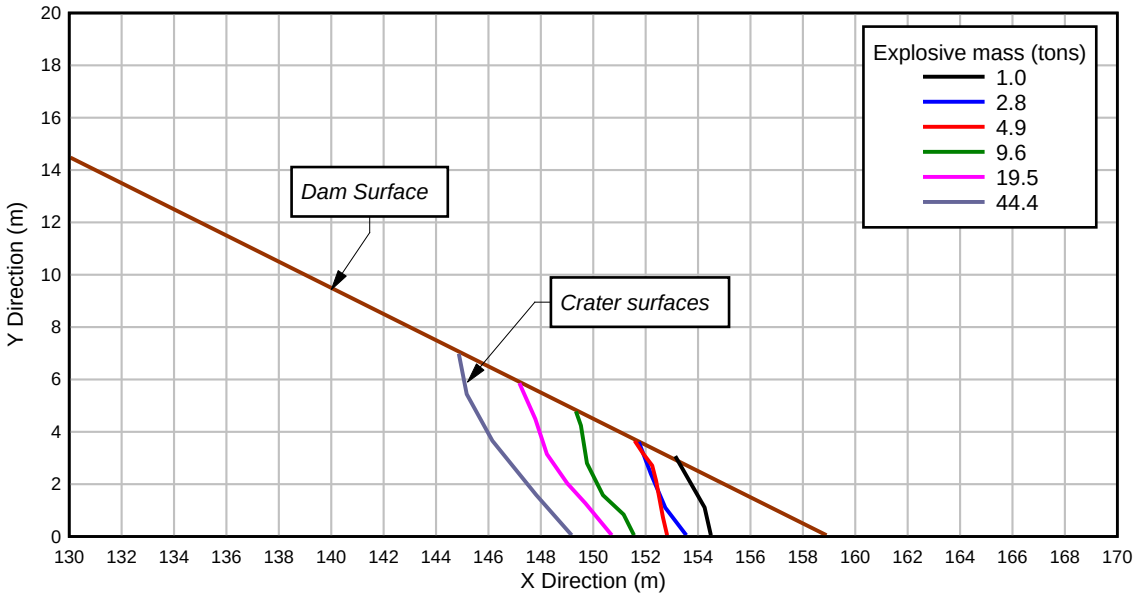

Figure 6.5. Post-blast craters formed by each explosive mass on downstream slope of embankment dam

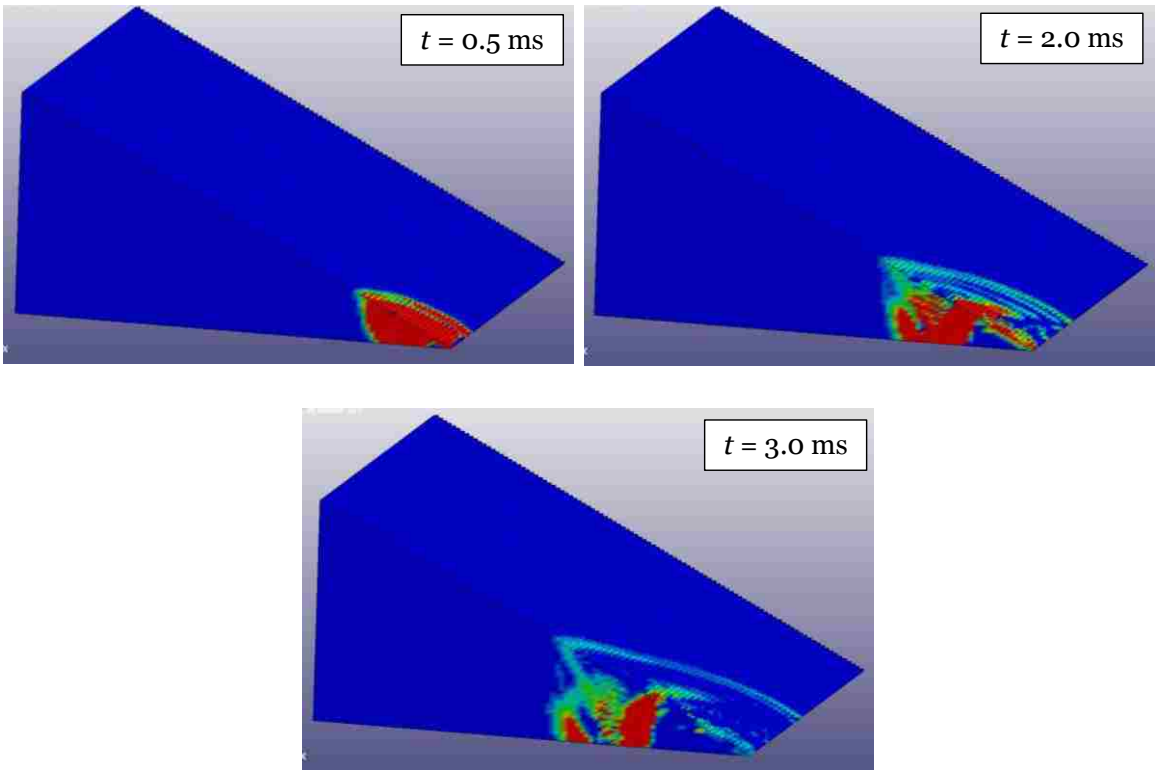

Figure 6.6. Pressure contours from the explosive airblast simulation

6.2 Seepage and Slope Stability Analyses

Seepage and slope stability analyses were performed for both initial and post-blast conditions to assess the stability of the embankment dam after explosive airblast loading. The analysis methodologies and results are discussed in the following sections.

6.2.1 Analysis Methodology

The phreatic surface for both initial and post-blast conditions was determined using the numerical seepage modeling software SEEP/W (GEO-SLOPE International Ltd. 2015a). The software mathematically simulates water flowing through a porous medium using Darcy's law. A two-dimensional section of the embankment dam geometry was defined and assigned to a single region consisting of a single, cohesive soil material. The software

soil material model was selected to accommodate both unsaturated and saturated conditions for locations above and below the phreatic surface, respectively.

Boundary conditions were drawn on region edges as shown in Figure 6.7 and included the reservoir level, potential seepage face, and zero pressure conditions at drainage locations. The potential seepage face was defined along the entire downstream slope of the dam, while zero pressure conditions were defined at a point at the toe of the dam for no engineered drainage conditions and along a 20 m line along the downstream edge for horizontal toe drain conditions.

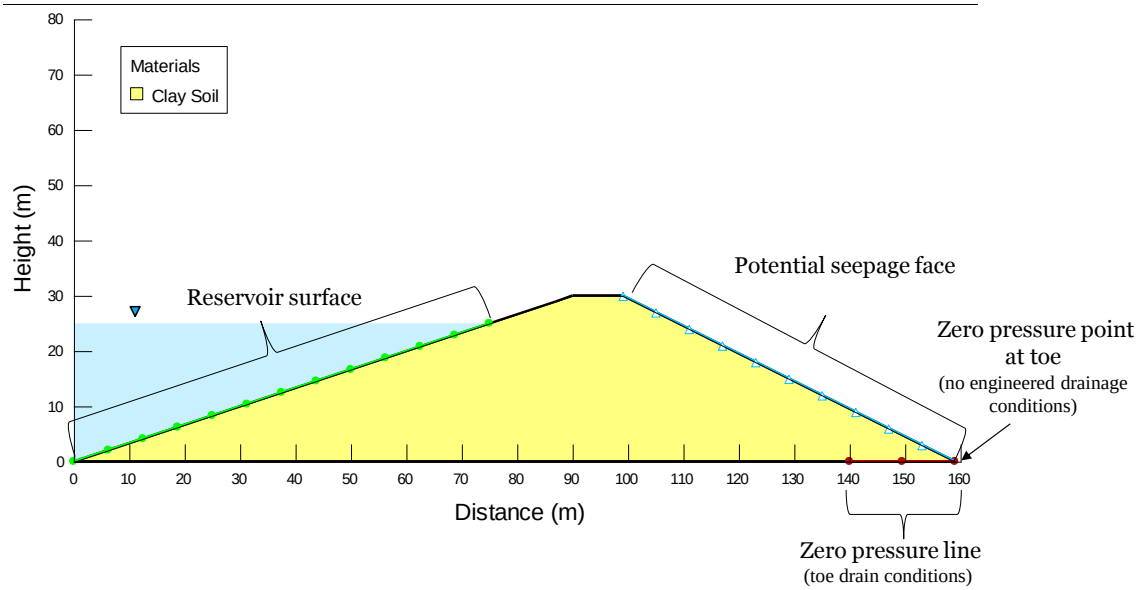

Figure 6.7. Boundary conditions for seepage analysis

A volumetric water content function was used to calculate soil water storage capacity under matric pressure changes from soil drainage. The function described the soil saturation based on porosity for saturated soils and both the porosity and matric suction

for unsaturated soils. The volumetric water content function was automatically estimated by the software using inputs for volumetric saturated and residual water content. These values were applied to a sample function for clay based on typical water content functions for general soil types as shown in Figure 6.8.

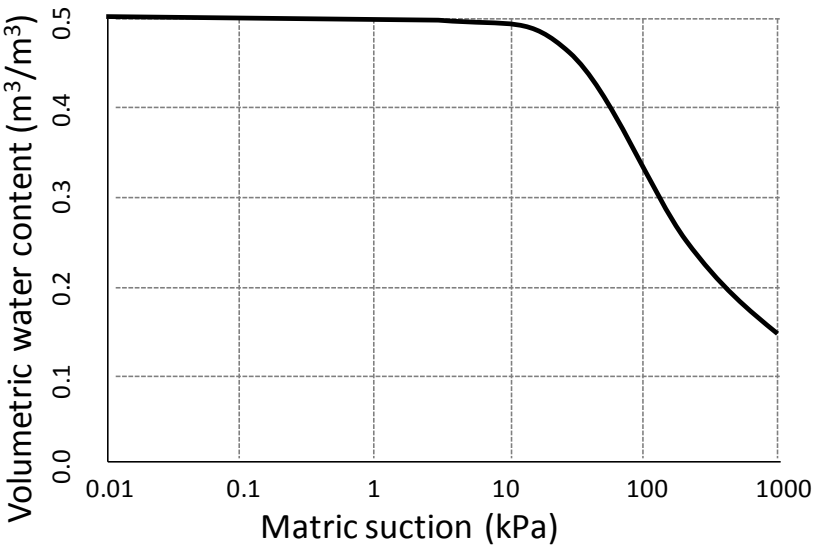

Figure 6.8. Volumetric water content function for clay (GEO-SLOPE International Ltd. 2015a)

A hydraulic conductivity function was used to describe the variation of conductivity with changes in suction. The function was estimated using the volumetric water content function and curve fitting parameters with the Van Genuchten (1980) method, which describes conductivity as a function of matric suction as given by Equation 6.1. The curve fitting parameters were automatically estimated by the software using the volumetric water content function at a point located halfway between the residual and saturated water content. Inputs for the hydraulic material properties used in the seepage analysis are summarized in Table 6.3.

$$k_w = k_s \frac{\left[1-\left(a\psi^{(n-1)}\right)\left(1+\left(a\psi^{n}\right)^{-m}\right)\right]^2}{\left[(1+a\psi)^{n}\right]^{m/2}}$$ Equation 6.1

where k_w = hydraulic conductivity, k_s = saturated hydraulic conductivity; a, n, m = curve fitting parameters; n = 1/(1-m); and Ψ = required suction range.

Table 6.3. Hydraulic soil properties used in seepage analysis

Property	Value
Volumetric saturated water content,	0.57
Volumetric residual water content	0.20
Saturated hydraulic conductivity, k_s	$1.0(10^{-6})$ m/s

The dam region was discretized with an automatically generated numerical mesh of quadrilateral elements that was 2.5 m in width to remain within the number of elements allowed by the software. A flow net was delineated by the software to determine flow quantity through the embankment dam using a steady state seepage analysis and the phreatic surface was calculated.

Slope Stability Modeling of the embankment dam structure was performed for both initial and post-blast conditions using the numerical stability modeling software SLOPE/W (GEO-SLOPE International Ltd. 2015a). The software numerically analyzed the stability of a slope using limit equilibrium methods with circular slip surfaces and discretization of the mass into slices. The Morgenstern-Price formulation was utilized to calculate the

minimum factor of safety (FOS) by calculating interslice forces and satisfying moment and force equilibrium for each slice.

Soil shear strength was modeled using an effective stress Mohr-Coulomb model. The Mohr-Coulomb plasticity model was discussed in 2.6.1 and the shear strength envelope is shown in Equation 2.5. The dam was assumed to consist of the soft clays used in the experiment blasts described in this paper since soil properties were already obtained through laboratory testing. Total (undrained) shear strength properties from triaxial testing of the experiment clays were converted to effective strength values based on empirical correlations between Atterberg limits/ undrained cohesion and effective shear strength (Das 2009, Wright 2005, and McEniry 1978). An effective friction angle, φ' of 32°and effective cohesion, c' of 3 kPa were used in the analysis. The high undrained cohesion (and associated low undrained friction angle) translated to a high effective friction angle and low effective cohesion when converted to drained shear strength values.

6.2.2 Seepage and Stability Results

Seepage analyses were performed for each reservoir level and phreatic surfaces were calculated for initial and post blast conditions. Appendix D provides comprehensive results of the seepage analyses. The phreatic surface was calculated at a higher elevation in the dam as reservoir levels increased. An example of the seepage analysis results for pre-blast conditions and a 15 m reservoir level is shown in Figure 6.9. The figure depicts total head contours and the calculated phreatic surface for (*a*) no engineered drainage and (*b*) horizontal toe drain conditions. The phreatic surface for no engineered drainage was

higher in elevation, while the toe drain lowered the phreatic surface to the drain location at the base of the dam. Soil shear strength was therefore expected to increase for dams with engineered drainage due to the lower elevation of the phreatic surface.

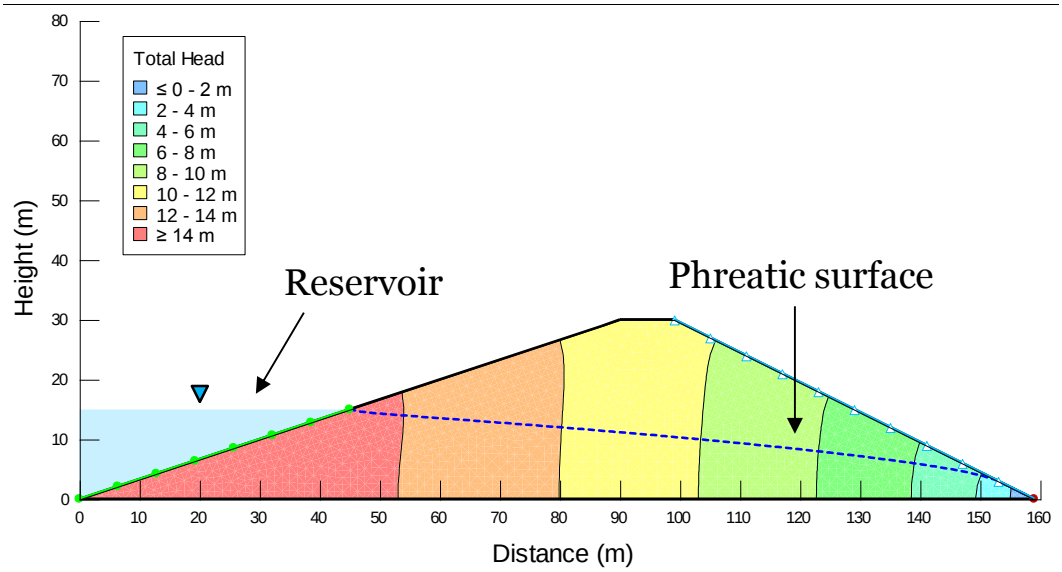

(***a***)

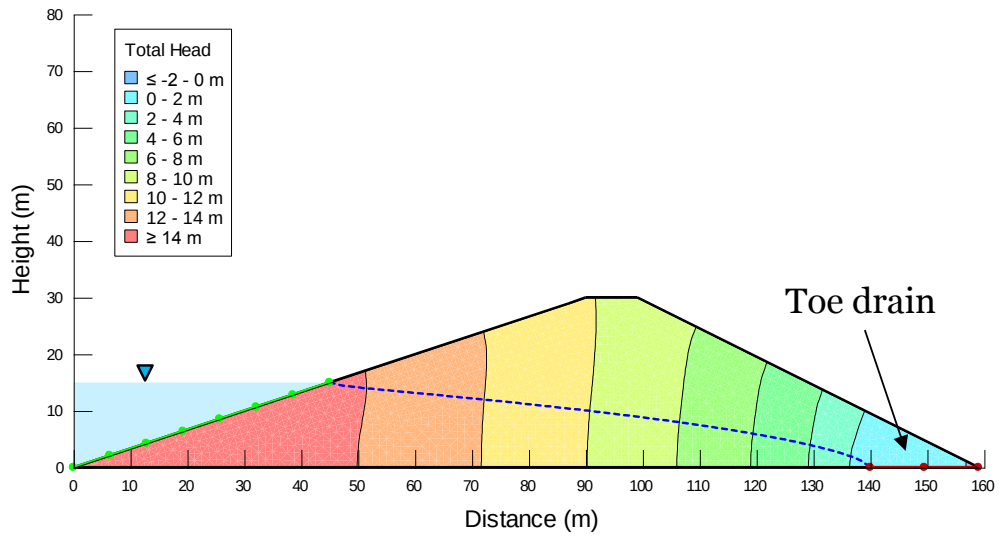

(***b***)

Figure 6.9. Seepage analysis results for 15 m reservoir level with (*a*) no engineered drainage and (*b*) horizontal toe drain

Slope stability analyses were performed for both initial and post-blast conditions. Appendix D provides comprehensive results of the slope stability analyses. Slip surfaces and minimum FOS values were calculated for each configuration. FOS values for initial (pre-blast) conditions are shown in Table 6.4. FOS values ranged from 1.08 to 1.52 for dams with no engineered drainage and 1.40 to 1.59 for dams with a horizontal toe drain. The initial FOS values were quite low due to the dam being constructed of a single layer of soft clay; this embankment dam configuration could therefore be considered as a suggested "worst-case" scenario of a small earthen embankment dam from a stability standpoint in terms of shear strength. However, all FOS values were above the slope stability failure limit (as denoted by an FOS value of less than one).

Table 6.4. Initial (pre-blast) FOS values from slope stability analyses

Reservoir level (m)	**FOS No engineered drainage**	**FOS Toe drain**
10	1.52	1.59
15	1.42	1.59
20	1.28	1.55
25	1.08	1.40

An example of the slope stability results for a 25 m reservoir level and a 19.5 ton blast with no engineered drainage are shown in Figure 6.10. Figure 6.10 (*a*) depicts the slip surface and minimum FOS of approximately 1.08 for initial conditions. Figure 6.10 (*b*) shows the reduction of the dam toe dimensions from the explosive blast and the corresponding lower FOS value of approximately 1.00. The creation of craters on the

dam toe lowered the location of the phreatic surface and caused it to daylight at the crater surface. This resulted in structural instability and reduced the FOS.

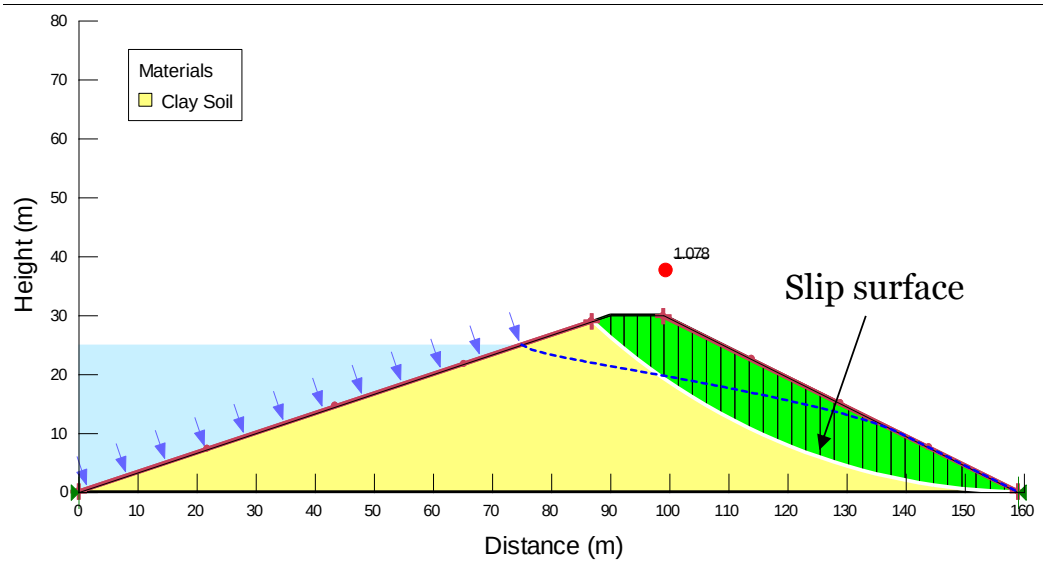

(*a*)

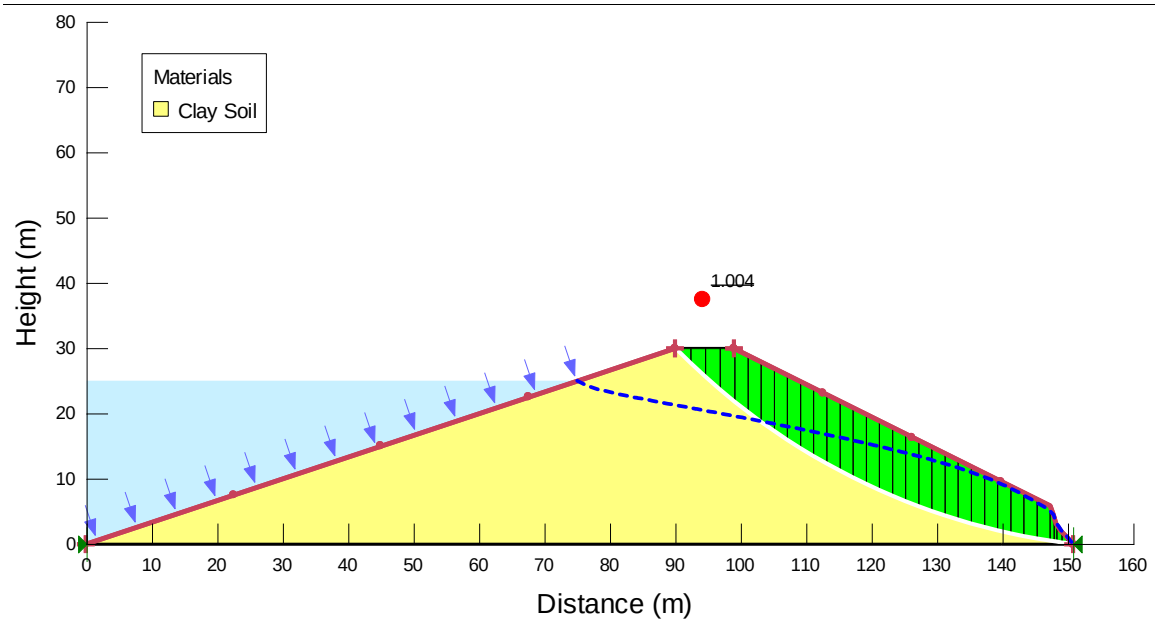

(*b*)

Figure 6.10. Slope stability analysis results for 25 m reservoir level for (*a*) initial conditions and (*b*) post-blast conditions from 19.5 ton explosive mass with no engineered drainage

The reservoir level had a large impact on calculated minimum FOS in the analyses. Figure 6.11 (*a*) and (*b*) depicts the slip surfaces and resulting FOS values for a 4.9 ton blast event with reservoir levels of 25 m and 10 m, respectively. Higher reservoir levels resulted in more deep-seated failure due to the higher elevation of the phreatic surface and the corresponding reduced shear strength of the soil. This resulted in lower overall FOS values as the phreatic surface intersected the crater. Lower reservoir levels resulted in lower elevation of the phreatic surface and increased shear strength in the downstream dam slope. The increased strength led to higher FOS values and shallow slip surfaces on the downstream slope.

The presence of a horizontal toe drain also had a large impact on FOS results for the stability analyses as shown in Figure 6.12. FOS values for dams with a horizontal toe train were higher than for dams with no engineered drainage. The toe drain lowered the location of the phreatic surface, which no longer intersected the blast crater at the dam toe and resulted in greater structural stability. While reservoir levels of 25 m still resulted in deep seated slip surfaces through the phreatic surface, reservoir levels 20 m and lower resulted in shallow slip surfaces and higher FOS values than conditions with no engineered drainage.

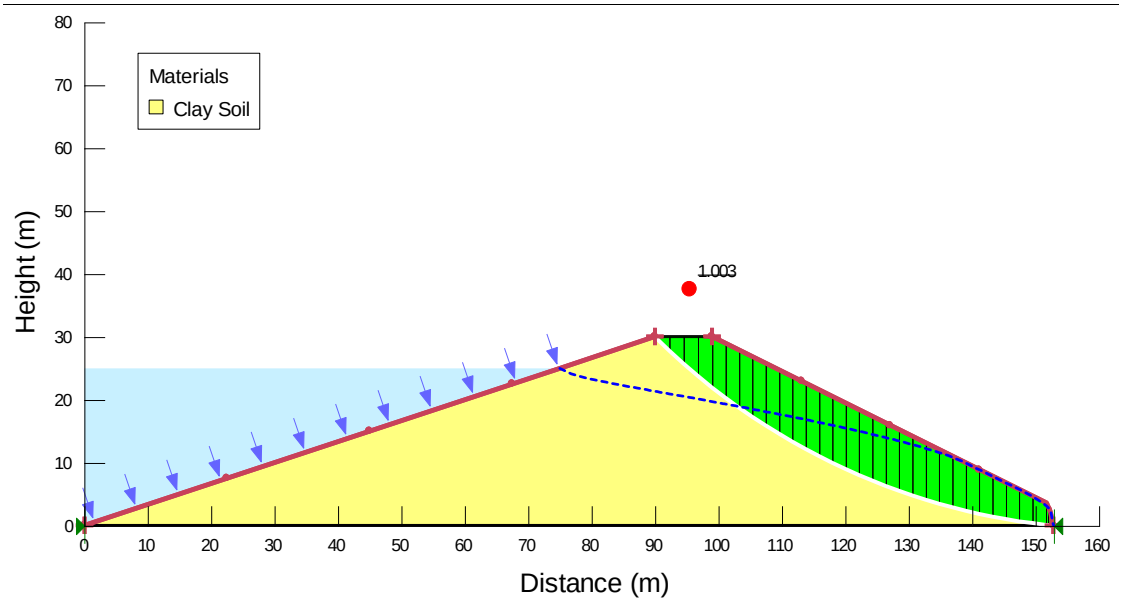

(*a*)

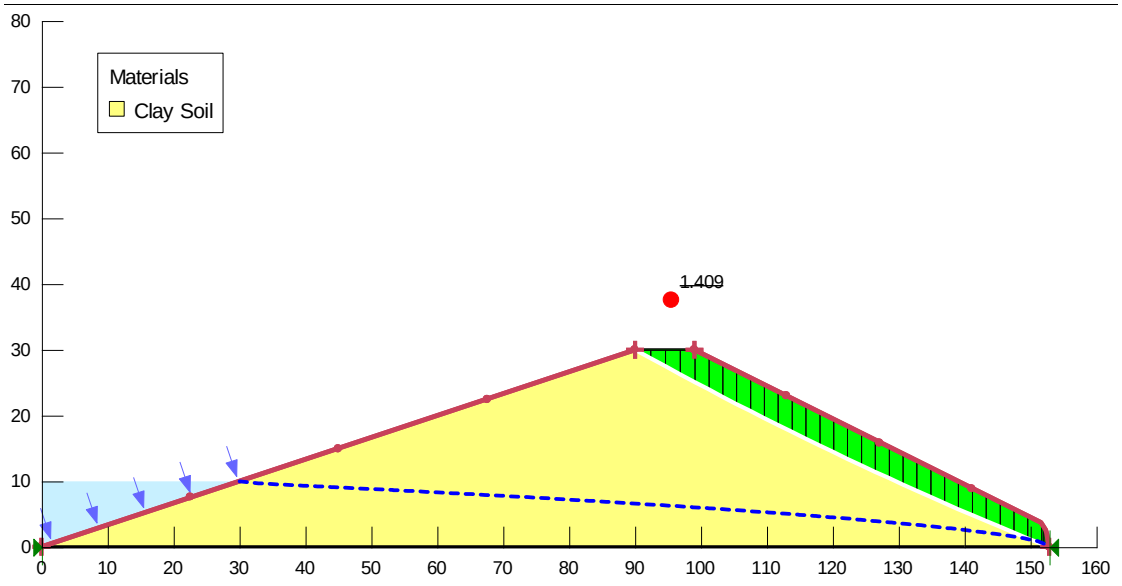

(*b*)

Figure 6.11. Effects of reservoir level on minimum FOS for a 4.9 ton blast with no engineered drainage and (*a*) 25 m reservoir level and (*b*) 10 m reservoir level

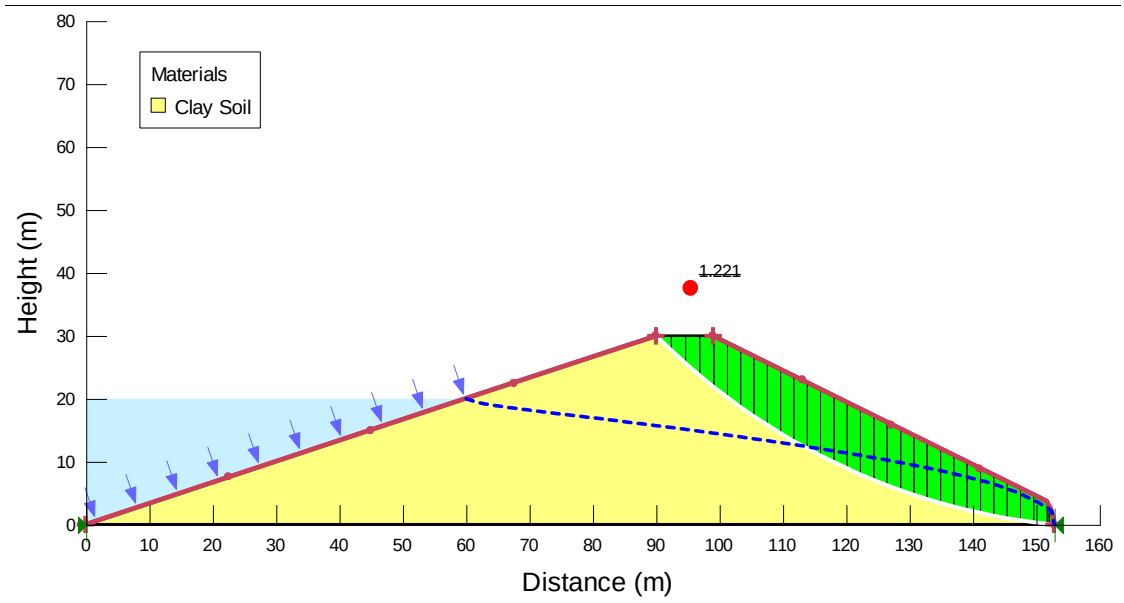

(***a***)

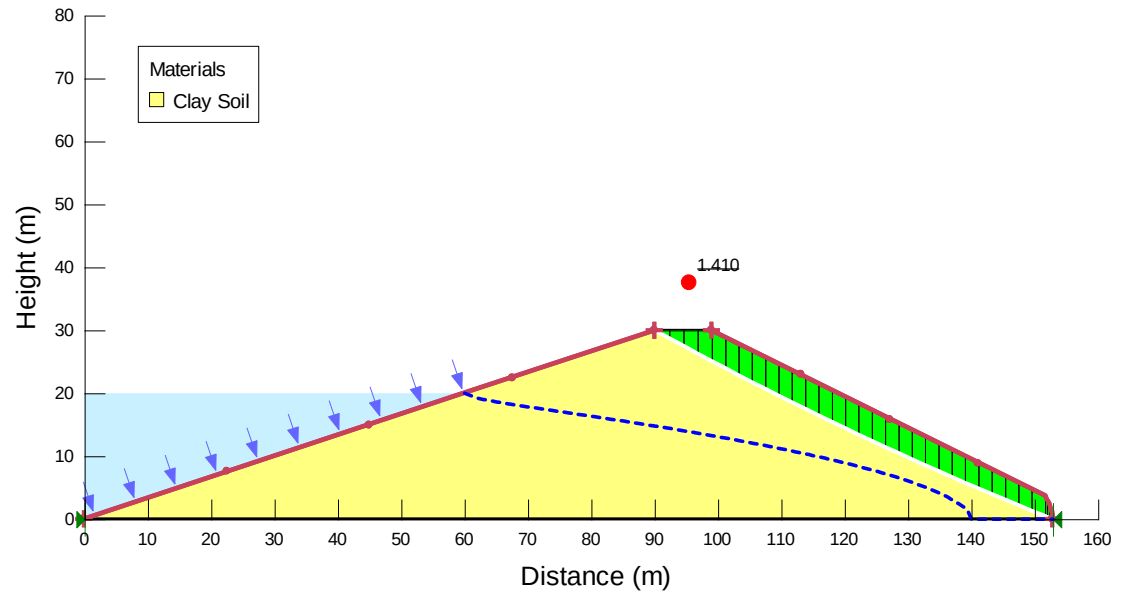

(***b***)

Figure 6.12. Effects of drainage conditions on minimum FOS for a 4.9 ton blast with 20 m reservoir level and (*a*) no engineered drainage and (*b*) horizontal toe drain

A summary of the post-blast FOS results for the varying explosive masses and reservoir levels performed in this study is presented in Figure 6.13 and Figure 6.14. Figure 6.13 presents results for dams with no engineered drainage. In the figure, pre-blast FOS values had the greatest reduction for explosive masses up to approximately 5 tons due to the creation of craters in the downstream slope. Pre-blast FOS values were reduced by a maximum value of 0.21. After 5 tons FOS results decreased only minimally due to insufficient pressures from energy loss in air. This effect was observed even for very large explosive masses, which did not have a significant impact on reduction of dam stability.

The dam with the 25 m reservoir level, which corresponded to 80 percent dam capacity, exhibited the lowest FOS values. Failure (as defined by FOS less than unity) was induced only for this reservoir level due to reduction in soil shear strength. The reduced strength caused the circular failure surface to intersect the crater and cause structural instability. Based on these results the explosive airblasts posed a possibility of crater-induced dam failure only for a dam with no engineered drainage close to full reservoir capacity.

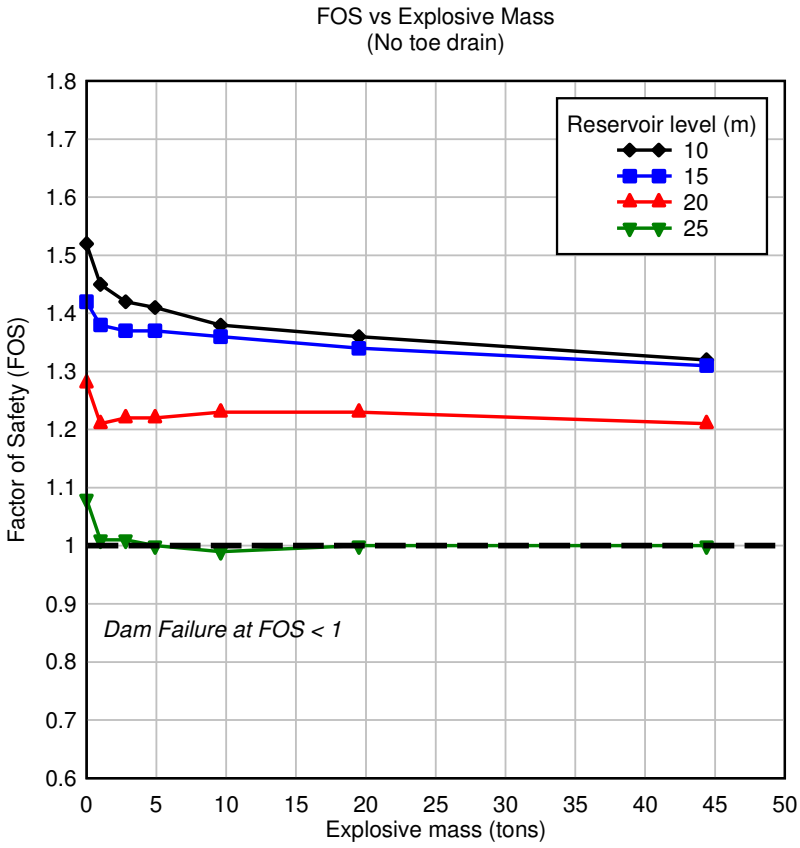

Figure 6.13. FOS results for varying explosive mass and reservoir level with no engineered drainage

Figure 6.14 presents a summary of FOS results for dams with a horizontal toe drain. Safety factor values were higher than those for dams with no engineered drainage for all reservoir levels. A similar trend to Figure 6.13 was observed for the largest decrease in FOS values for explosive masses up to 5 tons. The FOS was decreased by a maximum value of 0.27 from pre-blast conditions. Safety factors decreased only minimally explosive masses greater than 5 tons.

Safety factors were reduced most significantly for the 25 m reservoir height, which caused the phreatic surface to intersect the post-blast crater due to decreased the shear strength. The FOS results for reservoir levels less than 25 m were almost identical as shown in Figure 6.14. At reservoir levels less than 25 m the phreatic surface was lowered away from the downstream slope and did not intersect post-blast craters. Slip surfaces for lower reservoir levels were indicative of shallow slope failures that did not involve the blast crater, which explains the matching results for all reservoir levels less than 25 m.

Failure of the embankment dam (as indicated by FOS less than unity) could not be induced for any reservoir level. The use of engineered drainage diverted the phreatic surface far enough away from the blast craters to effectively eliminate failure for all reservoir levels.

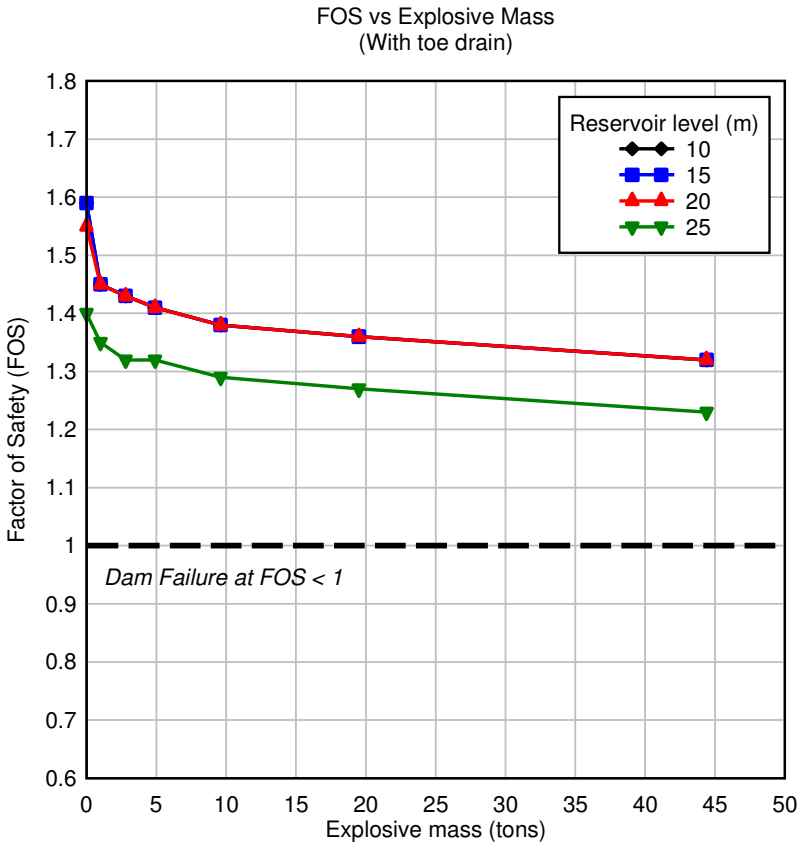

Figure 6.14. FOS results for varying explosive mass and reservoir level with horizontal toe drain

7 CONCLUSIONS AND RECOMMENDATIONS

The following sections discuss the conclusions obtained from this study and recommendations for future work. Conclusions from the small scale explosive airblast experiments on clay soils as well as numerical simulations of the experiments are discussed. In addition, the outcome of the deformation-induced stability evaluation of an earthen embankment dam subjected to explosive airblast loading is reviewed.

7.1 Explosive Airblast Testing

The explosive airblast testing study examined the effects of small scale airblast experiments on clay soils to obtain relationships for ground vibration attenuation and crater geometry with explosive mass and offset height. Thirty-three small scale blasts were conducted to record airblast measurements. Of these, twenty-four tests were performed to measure ground motions and record crater dimensions with offset heights of 2.5 and 7.6 cm above the ground surface and explosive masses ranging from 0.9 g to 100.9 g. The experiment results provided a data set with which to compare the results of numerical simulations of small airblast loads on clay soils.

Vibration attenuation trend lines were fit to vertical peak particle velocity, *PPV* versus scaled distance from the blast source. *PPV* decreased with depth and ranged from 1.0 to 40.2 cm/s. The energy generated by the blasts as described by the K-factor was 25.21. True crater diameters ranged from 3.8 to 22.9 cm, while apparent crater diameters ranged from 4.4 to 25.5 cm. Crater depth ranged from 0.8 to 8.4 cm and volume from 32.1 to 1720.6 cm3.

Plots of crater volume, V and volume parameter, V_c versus scaled distance, SD were constructed with power trendlines fit through the data. Crater volume increased with explosive mass and was larger for blasts located closer to the ground surface when more energy was coupled into the ground. Increased moisture content in the clay soils resulted in slightly larger V_c values and more data scatter. Crater diameter, depth, and scaled explosive mass were normalized by blast height to obtain a predictive relationship for crater geometry with known blast height and explosive mass. Crater diameter and depth increased with decreasing blast offset height, h when more energy was coupled into the soil.

7.2 Numerical Modeling of Explosive Airblast Testing

The results from the small scale airblast experiments on clay soils were compared to numerical solutions obtained through two-dimensional Multi-Material Arbitrary Lagrangian Eulerian (MM-ALE) finite element simulations. Geotechnical characterization and shear strength laboratory tests were conducted to characterize the experiment soils and obtain input parameters for the numerical material model. Finite element calculations of the blasts were performed in LS-DYNA. The simulated results were compared to experimental results to determine how well the numerical model compared to the field experiments.

A material model study was performed for the clay soils that compared four material models available in LS-DYNA. Simulated crater dimensions were compared to experimental results to evaluate the accuracy of each material model with predicting

craters from the small scale, experimental explosive airblasts. The Pseudo Tensor Material Model (LS-DYNA Material Model 16) had the most accurate predictions for crater geometries and was selected for use in the remaining simulations of the study.

Crater dimensions from the simulation results generally compared well to the experimental blasts. The simulated craters captured the shape of the experimental craters well. Simulated crater diameter compared particularly well to experimental data. Simulated depths were larger than the experimental results, especially for larger *SD* values that corresponded to smaller explosive masses that imparted lower energy into the ground. Simulated depth results converged closer to experiment results at smaller *SD* values that corresponded to blasts with higher energy. The material model therefore captured the crater depth of higher energy blasts more accurately than lower energy blasts. Depth results were more comparable to experimental results when normalized by blast height. Trendlines relating crater diameter and depth to explosive mass normalized by blast height were presented.

Simulated volumes had a reasonably close fit to experimental results and captured the trend of increasing crater volume with decreasing scaled distance. Simulated crater volumes were somewhat larger than experimental results due to the over-predicted depth from the material model. This also resulted in smaller simulated volume parameter, V_c results than experimental results. However, simulated trends were still similar to experiment results.

Vibration attenuation trend lines were fit to vertical peak particle velocity, *PPV* versus scaled distance, *SD* from the blast source. Simulated *PPV* decreased with depth and followed the overall trend of experimental data. The *PPV* for small *SD* values corresponding to greater blast energy was somewhat overestimated, indicating that the attenuation and material damping was overestimated for high-energy blasts. This could have been due to more material variation in the experimental blasts that could not be captured by an idealized model. However, overall *PPV* results were representative of the experimental results and provided a good correlation for blast-induced energy coupled into the soil.

Stress and velocity time histories from the finite element model were examined to determine how the material modeled the stress response of the soil under blast loading. The soil deformation (in terms of vertical particle velocity) was compared to the applied pressure (mean stress) from the blast for the two-part compressibility material model. The soil model appeared to adequately capture the rapid stress increase associated with the blast load, which caused the majority of the deformation observed in the model. However, pressure instabilities were observed after the peak pressure, with pressure values that showed an erroneous resonance, possibly due to numerical instabilities. The linear compressibility version of the material model corresponding to the undrained soil response exhibited an erroneous flatline in pressure and particle velocity after the tensile cutoff was reached. In addition, once the tensile cutoff value was reached the velocity did not return to zero but exhibited a small, residual velocity for the remainder of the time history. While the majority of the velocity response (and therefore soil deformation and

crater formation) occurred during the initial pressure pulse from the blast, the post peak response was not captured.

The Pseudo Tensor material model appeared to capture the first-order response of the soil in terms of crater formation and the initial stress pulse from the blast. However, the model did not capture the post-peak response as exhibited by instabilities in the stress and particle velocity responses. While an MM-ALE analysis performed with the Pseudo Tensor material model can be used to estimate general deformations anticipated in a soil subjected to an airblast load, it cannot be relied on to capture post-peak or stress path response, particularly for late time histories.

7.3 Stability of Embankment Dams Subjected to Explosive Airblast Loading

This study investigated the effects of deformation (crater) induced stability failure on a homogeneous earthen embankment dam composed of cohesive soils. The results of small-scale, experimental airblast tests from a previous study were used to compare numerical results and evaluate the ability of the numerical model to simulate explosive airblast events on cohesive soils. Multi-Material Arbitrary Lagrangian Eulerian (MM-ALE) finite element simulations were then performed of explosive airblast events located on the downstream toe of a hypothetical earthen embankment dam composed of the same cohesive soils used in the small-scale experimental blasts. Explosive masses ranged from 1.0 to 44.4 metric tons. The craters generated from the blasts were delineated and traditional limit equilibrium methods were used to evaluate dam stability. The effects of reservoir levels ranging from 10 m to 25 m and the use of a horizontal toe drain were investigated.

The airblast simulations resulted in the creation of craters on the downstream slope surface and reduction of the dam toe. While larger explosive masses resulted in the removal of more material from the embankment dam, the energy imparted into the soil from the airblast events did not result in significant crater dimensions due to energy loss in free air.

Slip surfaces and minimum factor of safety (FOS) values were calculated for each reservoir level and drainage configuration. Pre-blast FOS values had the greatest reduction for explosive masses up to 5 tons due to the creation of craters in the downstream slope. After 5 tons FOS results decreased only minimally due to insufficient pressures from energy loss in air. This effect was observed even for very large explosive masses, which did not have a significant impact on reduction of dam stability.

Reservoir levels had a significant impact on calculated minimum FOS. Higher reservoir levels resulted in more deep-seated slip surfaces due to the higher elevation of the phreatic surface and corresponding reduction in shear strength. Circular slip surfaces intersected the crater and reduced stability for high reservoir levels.

Drainage conditions had the largest effect on stability results. Failure (as defined by FOS less than unity) was induced only for a dam with no engineered drainage at 80 percent reservoir capacity or greater. The drainage conditions caused the circular slip surface to intersect the crater, which resulted in structural instability. Dams with engineered

drainage increased soil shear strength on the downstream slope by forcing the phreatic surface to drain at the base of the dam. The increased strength led to shallow slip surfaces and higher FOS values. The use of engineered drainage diverted the phreatic surface far enough away from the blast craters to effectively eliminate failure for all reservoir levels.

It was concluded that the explosive airblast events simulated in this study posed a possibility of dam failure only for dams with no engineered drainage close to full reservoir capacity.

7.4 Limitations

The relationships obtained in this study are applicable only for the clay soil (with its associated material properties) used in this study. The effects of varying soil properties are known to have a significant effect on crater geometry from explosive blasts. The clay material in the study was soft and close to fully saturated. The material had very low shear strength but a very stiff undrained compressibility due to the almost completely saturated conditions.

Laboratory tests used to characterize the soil were performed at low stresses compared to those seen during large blast events. Due to the impossibility of performing lab testing under pressures equivalent to the magnitude seen during a blast event, it was assumed that the material properties obtained from lab testing were still applicable for use in the extremely high stress regime seen during a large-scale blast event.

The soil models utilized in this study did not account for the effects of strain rate, which can cause a marked increase in undrained shear strength. Low to medium strain rates of 10-7/s to 10-4/s have been shown to increase shear strength by approximately five to twenty percent (Martindale et al. 2013). The extremely high strain rate applied to a soil during an airblast load could increase the shear strength by a much higher percentage. Strain rate enhanced strength during a blast event is generally modeled using functions of strength increase versus applied strain rate obtained from triaxial compression testing. The functions are assumed to predicatively apply to the high strain rates expected during blast loading. Shear strength increase due to applied strain rate was not investigated in this study and laboratory tests were not performed at varying strain rates. The soil therefore had a higher strength response than what was modeled, and this may have caused some of the discrepancies seen between experimental and simulated results.

The experimental airblasts performed in this study were small in scale as it was not feasible to conduct a large-scale blasting program. While scaled distance, *SD* values for the small-scale blasts were selected to represent a scaled version of the energy observed from a larger-scale blast event, it cannot be completely determined that the small-scale results correlated to large scale events. The constitutive material models used in the finite element analysis were validated against small scale experimental results only and it was assumed that the model could be used to describe the response of large scale blasts on an earthen embankment dam.

The small-scale explosive airblast experiments performed under this study were performed under confined conditions as it was not feasible to construct an embankment dam structure out of homogeneous, cohesive soils and reconstruct after each of the tests conducted in the study. While the crater deformation took place near the ground surface where confining stress was low, there was still some confinement to the soils that would not be observed on the slope of an embankment dam. It was assumed that the material models validated through the numerical simulations of the experimental blasts still applied to an embankment dam geometry even though confinement conditions varied between the two scenarios.

Empirical relationships determined from the small-scale blasting program are also a function of the particular explosive utilized in this study (ANNM binary explosive) and may not apply to other explosive types, particularly those with geometries that are not spherical in shape or have a higher energy. For example, craters generated from a cylindrically-shaped explosive detonated above a soil surface would likely be less hemispherical in shape and have a larger depth than craters generated by a spherical charge of the same explosive.

The numerical simulations of an earthen embankment dam performed in this study are applicable to the particular soil type (almost fully saturated soils with low shear strength) coupled with the explosive type used in the study. Explosive blasts on earthen dams composed of a different soil type or with a significantly different explosive than the ones modeled in this study would result in different crater geometries that have different

effects on the dam seepage and stability. This study focused only on investigating deformation (crater) induced stability failure on an earthen embankment dam. Stability effects due to pore water pressure, seepage, or piping were not investigated.

Relationships obtained from the experimental and simulated blasts are valid for blast loading only. The results may not be used to predict relationships for other dynamic loading conditions such as earthquakes. Frequencies from an earthquake event differ greatly from blast frequencies and the duration of loading is much longer than a blast event (Kramer 1996). Pore water pressures can also dissipate during earthquake loading, which results in a markedly different strength and compressibility soil response than that seen with the undrained response of soils during a blast event.

The simulations of this study were performed exclusively with LS-DYNA and other software products were not compared. Software products such as Abaqus FEA (Dassault Systèmes 2016) have recently developed and implemented explicit solvers that utilize coupled Eulerian-Lagrangian (CEL) methods. This software has been successfully used to model blast loading in soils (Jablonski et al. 2012).

7.5 Recommendations

Recommended future work includes the investigation of the effects of both surface and buried explosions on the stability of a homogeneous earthen embankment dam. Surface and optimally buried charges impart more energy into a structure and would likely cause more damage than an airblast event. In addition, further parametric studies could include parametric studies for varying dam geometries such as height, upstream slope angle, and

downstream slope angle on the resulting factor of safety (FOS) values after an explosive event.

The effects of varying soil properties, such as moisture content, shear strength, dry porosity, and compressibility were not investigated in this study. These material properties are known to have a significant effect on the resulting craters from a near-surface explosive blast as well as dam stability. While a parametric material property study was outside the scope of this study, future work could include variations of soil properties and correlations for resulting dam stability.

Further recommended work includes the application of more recent material models, such as the Disturbed State Concept, to attempt to adequately capture stress path and post peak response of clay soils under airblast loads. The incorporation of a user-specific material model coupled with equations of state to describe the response of each of the soil phases (solid, air and water) could also be investigated.

The simulations of this study were performed in LS-DYNA with the associated material models available within the software. While LS-DYNA has historically been seen as the most robust software for use in shock and impact analysis, it may be of interest to examine other software products such as Abaqus FEA (Dassault Systèmes 2016) to simulate explosive airblasts in soils. Results generated from different software packages can be compared to the experimental work of this study to determine which produces the most satisfactory outcome.

8 REFERENCES

Abaqus FEA, (2016), (computer software), Dassault Systèmes SolidWorks Corporation, Vélizy-Villacoublay, France.

Abbo, A. J., and Sloan, S. W. (1995). "A smooth hyperbolic approximation to the Mohr-Coulomb yield criterion," *Computers and Structures*, 54(3), 427 – 441.

Afriyie, G. A. (2014). "Effects of explosions on embankment dams," thesis, presented to Carleton University at Ottawa, Ontario in partial fulfillment of the requirements for the degree of Master of Applied Science.

Alia, A. and Souli, M. (2006). "High explosive simulation using multi-material formulations." *Applied Thermal Engineering*, 26, 1032-1042.

Ambrosini, R. D., Luccioni, B. M., Danesi, R. F., Riera, J. D., Rocha, M. M. (2002). "Size of craters produced by explosive charges on or above the ground surface." *Shock Waves*, 12, 69–78.

Ambrosini, R. D. and Luccioni, B. M. (2006). "Craters produced by explosions on the soil surface," *Transactions of the ASME*, 73, 890-900.

An, J., Tuan, C. Y., Cheeseman, B. A., Gazonas, G.A. (2011). "Simulation of soil behavior under blast loading." *Int. J. Geomech.*, 11(4), 323–334.

American Society for Testing and Materials (ASTM). (2006), "Standard test methods for amount of material in soils finer than no. 200 (75-μm) sieve." *D1140*, West Conshohocken, PA.

American Society for Testing and Materials (ASTM). (2007), "Standard test method for unconsolidated-undrained triaxial compression test on cohesive soils." *D2850*, West Conshohocken, PA.

American Society for Testing and Materials (ASTM). (2009), "Standard test methods for laboratory determination of density (unit weight) of soil specimens." *D7263*, West Conshohocken, PA.

American Society for Testing and Materials (ASTM). (2009), "Standard test methods for particle-size distribution (gradation) of soils using sieve analysis." *D6913*, West Conshohocken, PA.

American Society for Testing and Materials (ASTM). (2010), "Standard test methods for laboratory determination of water (moisture) content of soil and rock by mass." *D2216*, West Conshohocken, PA.

American Society for Testing and Materials (ASTM). (2010), "Standard test methods for liquid limit, plastic limit, and plasticity index of soils." *D4318*, West Conshohocken, PA.

American Society for Testing and Materials (ASTM). (2011), "Standard practice for classification of soils for engineering purposes (unified soil classification system)." *D2487*, West Conshohocken, PA.

American Society for Testing and Materials (ASTM). (2011), "Standard test method for direct shear test of soils under consolidated drained conditions." *D3080*, West Conshohocken, PA.

Baker, W. (1973). *Explosions in air*. University of Texas Press, Austin, TX.

Billington, D. P. and Jackson, D. C. (2006). *Big dams of the new deal era: a confluence of engineering and politics*, University of Oklahoma Press, Norman, OK.

Blouin, S. E. and Kwang, J. K. (1984). *Undrained compressibility of saturated soil*, DNA-TR-87-42, Technical report prepared for the Defense Nuclear Agency, Washington, DC.

Bouamoul, A., and Nguyen-Dang, T. V. (2008). *High explosive simulation using arbitrary Lagrangian-Eulerian formulation*, TM 2008-254, Defense Research and Development Canada, DRDC Valcartier, QC Quebec, Canada.

Charlie, W. A., Lewis, W. A., Doehring, D. O. (2001). "Explosive induced pore pressure in a sandfill dam," *Geotechnical Testing Journal*, 24(4), 391–400.

CHEETAH version 7.0, (2012), (computer software), Livermore Software Technology Corporation (LSTC), Livermore, CA.

Chen, W. F. and Baladi, G. Y. (1985). *Soil plasticity theory and implementation, developments in geotechnical engineering*, Elsevier Science Publishing Company Inc., New York, NY.

Cooper, P. W. (1996). *Explosives engineering*, Wiley-VCH Publications, New York, NY.

Das, B. M. (2009). *Principles of geotechnical engineering, 7th edition*, Cengage Learning Inc., Stamford, CT.

Das, B. M. and Ramana, G. V. (2011). *Principles of soil dynamics, second edition*, Cengage Learning, Stamford, CT.

SolidWorks student edition, (2013), (computer software), Dassault Systèmes SolidWorks Corporation, Vélizy-Villacoublay, France.

De, A., Butler, S. and Zimmie, T. F. (2013). "Effects of surface explosions on top of earthen embankment dams," *Geotechnical Special Publication: Geo-Congress 2013*, 231, 444–447.

Defense Nuclear Agency (1979). *Nuclear geoplosics sourcebook, volume IV, part II, empirical analysis of nuclear and high explosive cratering and ejecta*, DNA 6501H-4-2, Washington, DC.

Desai, C. S. and Siriwardane, H. J. (1984). *Constitutive laws for engineering materials with emphasis on geologic materials*, Prentice Hall, Inc., Englewood Cliffs, NJ.

Desai, C. S. (2001). *Mechanics of materials and interfaces: the disturbed state concept*, CRC press LLC, Boca Raton, FL.

Dowding, C. H. (2000). *Construction vibrations, second edition*, CH Dowding.

Drucker, D. C., Gibson, R.E., Henkel, D.J. (1957). "Soil mechanics and work hardening theories of plasticity," *Transactions of the American Society of Civil Engineers*, 122(1), 338–346.

GeoStudio student edition version 8.15.5.11777, (2015a), (computer software), GEO-SLOPE International Ltd., Calgary, Alberta, Canada.

GEO-SLOPE International Ltd. (2015b). *Stability modeling with SLOPE/W: an engineering methodology, June 2015 ed.*, GEO-SLOPE International Ltd., Calgary, Alberta, Canada..

Grujicic, M., Pandurangan, B., Cheeseman, B. A., Roy, W. N., Skaggs, R. R. (2008). "Application of the modified compaction material model to the analysis of landmine detonation in soil with various degrees of water saturation," *Shock and Vibration*, 15(1), 79–99.

Ha, I. S. (2013). "Estimation of shear wave velocity of earth dam materials using artificial blasting test," *Soil Dynamics and Earthquake Engineering*, 55, 120–129.

Hall, J. B. (2000). *Principles of naval weapons systems*, Kendall Hunt Publishing Company, Dubuque, IA.

Hallowell Manufacturing (2009). *Kinepak^{TM} technical data sheet*, Hallowell Manufacturing, LLC, Columbus, KS.

Hallquist, J. O. (2006). *LS-DYNA theoretical manual*, Livermore Software Technology Corporation, Livermore, CA.

Hallquist, J. O. (2014). *LS-DYNA keyword user's manual*, Livermore Software Technology Corporation, Livermore, CA.

Hatzor, Y. H., Gvirtzman, H., Wainshtein, I., Orian, I. (2009). "Induced liquefaction experiment in relatively dense, clay-rich sand deposits," *Journal of Geophysical Research*, 114(B02311).

Helwany, S. M. B. and A. Chowdhury (2004). "Laboratory impulse tests for soil-underground structure interactions," *Journal of Testing and Evaluation*, 32 (4), 262–273.

Hunt, R. E. (2005). *Geotechnical engineering investigation handbook, second edition*, Taylor and Francis Group, LLC, Boca Raton, FL.

Isenberg, J., Vaughan, D.K., Sandler, I.S. (1978). *Nonlinear soil-structure interaction*, Electric Power Research Institute, EPRI NP-945, Weidlinger Associates.

Jablonski, J., Carlucci, P., Thyagarajan, R., Nandi, B., Arata, J. (2005). "Simulating underbelly blast events using Abaqus/explicit - CEL," *Proceedings of the 2012 SIMULIA Customer Conference*, Providence RI.

Katti, D. R. and Desai, C. S. (1995). "Modeling and testing of cohesive soil using disturbed-state concept," *J. Eng. Mech.*, 121, 648–658.

Kinney, G. F. and Graham, K. J. (1985). *Explosive shocks in air*, 2nd ed., Springer Verlag, Berlin, Germany.

Klisinski, M. (1985). *Degradation and plastic deformation of concrete*, Institute of Fundamental Technology Research (IFTR), Report 38, Polish Academy of Sciences, Warsaw, Poland.

Kramer, S. L. (1996). *Geotechnical earthquake engineering*, Prentice Hall, Upper Saddle River, NJ.

Kumar, R., Choudhury, D., Bhargava, K. (2014). "Prediction of blast-induced vibration parameters for soil sites," *Int. J. Geomech.*, 14(3), 04014007.

Larcher, M. (2007). *Simulation of the effects of an air blast wave*, European Commission Joint Research Centre, Institute for the Protection and Security of the Citizen, JRC41337, Luxembourg.

Lee, W. Y. (2006). "Numerical modeling of blast-induced liquefaction," thesis, presented to Brigham Young University, Provo, UT in partial fulfillment of the requirements for the degree of Doctor of Philosophy.

Lewis, B. A. (2004). *Manual for LS-DYNA soil material model 147*, FHWA-HRT-04-095, Federal Highway Administration, Research and Development, McLean, VA.

Li, Y., Contestabile, E., Braimah, A., Wilson, D. (2007). *Preliminary vulnerability of an embankment dam due to explosions*, CERL Report 2007-01 (CF).

LS-DYNA version SMP D R7.1.1, (2014), (computer software), Livermore Software Technology Corporation (LSTC), Livermore, CA.

Martindale, H., Chakraborty, T., Basu, D. (2013). "A strain-rate dependent clay constitutive model with parametric sensitivity and uncertainty quantification," *Geotech. Geol. Eng.*, 31, 229–248.

McEniry, G. P. (1978). "The estimation of the effective shear strength parameters of Leda clay," thesis, presented to University of Ottawa, Ottawa, Canada in partial fulfillment of the requirements for the degree of Master of Applied Science.

Mellegard, K. D., DeVries, K. L., Callahan, G. D. (2005). "Lode angle effects on the deformational properties of natural rock salt," *Proceedings of the 40th U.S. Symposium on Rock Mechanics (USRMS): Rock Mechanics for Energy, Mineral and Infrastructure Development in the Northern Regions*, Anchorage, AK.

Morgenstern, N. R. and Price, V. E. (1965). "The analysis of the stability of general slip surfaces," *Geotecnique*, 15, 79–93.

National Aeronautics and Space Administration (NASA) (1976). *U.S. standard atmosphere*, National Oceanic and Atmospheric Administration, National Aeronautics and Space Administration, United States Air Force, NASA-TM-X-74335, Washington, D.C.

Nicholls, H. R., C. F. Johnson, Duvall, W. I. (1971). *Blasting vibrations and their effects on structures*, United States Department of the Interior Office of Surface Mining Reclamation and Enforcement, Bureau of Mines Bulletin 656, Washington, DC.

Nielson, C. V., Zhang, W., Alves, L. M., Bay, N., Martins, P. (2013). *Modeling of thermo-electro-mechanical manufacturing processes*, Springer, London.

Ozcan, D. M., Bayraktar, A., Altunisik A. C. (2012). "Comparison of damage criteria for structures to near-field blast-induced ground motions," J*ournal of Testing and Evaluation*, 40(1), 148–157.

Reid, J. D., Coon, B. A., Lewis, B. A., Murray, Y. D. (2004). *Evaluation of LS-DYNA soil material model 147*, Federal Highway Administration, Research and Development, FHWA-HRT-04-094, McLean, VA.

Resnyansky, A. D. and Wildegger-Gaissmaier, A. E. (2001). "Hydrocode modeling of high-velocity jet penetration into sand." *Nineteenth International Symposium of Ballistics*, Interlaken, Switzerland, 1561–1567.

Rogers, J. D. and Koper, K. D. (2012) "Some practical applications of forensic seismology," *Missouri University of Science and Technology,* <http://library.canterbury.ac.nz/services/ref/asce.shtml> (April 27, 2012).

Sandler, I.S. and Rubin, D. (1979). "An algorithm and a modular subroutine for the cap model," *Int. J. Numer. Analy. Meth. Geomech.*, 3, 173-186.

Schwer, L. E. and Murray, Y. D. (1994). "A three-invariant smooth cap model with mixed hardening," *Int. J. Numer. Analy. Meth. Geomech.*, 18, 657–688.

Sharp, M. K., Seda-Sanabria, Y., Matheu E. E. (2011). "Recent efforts on blast damage mitigation for dams," *Applied Mechanics and Materials*, 82, 428–433.

Simo, J. C., Ju, J. W., Pister, K. S., Taylor, R. L. (1988). "An assessment of the cap model: consistent return algorithms and rate-dependent extension," *J. Eng.Mech. Eng.*, 114(2), 191-218.

Simo, J. C., Ju, J. W., Pister, K. S., Taylor, R. L. (1990). "Softening response, completeness condition, and numerical algorithms for the cap model," *Int. J. Numer. Analy. Meth. Eng*.

Stephens, T. (2010). *Manual on small earth dams: a guide to siting, design and construction*, FAO Irrigation and Drainage Paper Issue 64, Food and Agriculture Organization of the United Nations, Rome, Italy.

Stark, T. D. and Eid, H. T. (1994). "Drained residual strength of cohesive soils," *J. Geotech. Engrg.*, 120(5), 856 – 871.

Stark, T. D. and Hussain, M. (2013). "Empirical correlations: drained shear strength for slope stability analyses," *Journal of Geotechnical and Environmental Engineering*, 139, 853 – 862.

Thomas, M. A., Chitty, D. E., Gildea, M. L., T'Kindt, C. M. (2008). *Constitutive soil properties for Cuddeback Lake, California and Carson Sink, Nevada,* CR-2008-215345, National Aeronautics and Space Administration, Langley Research Center, Hampton, VA.

Tong, X. and Tuan, C. Y. (2007). "Viscoplastic cap model for soils under high strain rate loading," *J. Geotech. Geoenviron. Eng.*, 133(2), 206–214.

United States Army (1990). *Structures to resist the effects of accidental explosions,* Joint Departments of the U.S. Army, Navy and Air Force, TM5-1300/ NAVFAC P-397/ AFR 88-22, Washington, DC.

U.S. Bureau of Reclamation (USBR) (2004). *Design of small dams*, United States Department of The Interior, Washington, DC.

United States Naval Academy (2010). "Fundamentals of naval weapons systems." <http://www.fas.org/man/dod-101/navy/docs/fun/index.html> (Aug. 31, 2010).

Van Genuchten, M. T. (1980). "A closed-form equation for predicting the hydraulic conductivity of unsaturated soils," *Soil Science Society of America Journal*, 44(5), 892-898.

Vortman, L. J. (1977). "Craters from surface explosions and energy dependence – a retrospective view." *Impact and Explosion Cratering*, Pergamon Press, New York, NY, 1215 – 1229.

Wang, Z., Wang, H. and Cates, M. E. (2001). "Effective elastic properties of solid clays." *Geophysics*, 66(2), 428-440.

Wang, Z., Lu, Y. and Hao, H. (2004). "Numerical investigation of effects of water saturation on blast wave propagation in soil mass." *Journal of Engineering Mechanics*, 130(5), 551-561.

Williams, G. D. (2009). "Analysis and response mechanisms of blast-loaded reinforced concrete columns," thesis, presented to University of Texas at Austin, in partial fulfillment of the requirements for the degree of Doctor of Philosophy.

Wright, S. G. (2005). *Evaluation of soil shear strengths for slope and retaining wall stability analyses with emphasis on high plasticity clays*, Report No. 5-1874-01-1, Texas Department of Transportation, Austin, TX.

Zimmie, T. F., Abdoun, T., Tessari, A. (2010). "Physical modeling of explosive effects on tunnels." *Fourth International Symposium on Tunnel Safety and Security*, Frankfurt, Germany, 159–168.

List of Appendices

APPENDIX A LS-DYNA KEYWORD INPUTS

Appendix A presents examples of the LS-DYNA keyword inputs used in the simulations of this study. The appendix includes inputs for the scaled explosive blast A-11 and the embankment dam simulation with explosive mass of 4.9 metric tons using the Pseudo Tensor Material Model (LS-DYNA Material Model 16) for the clay soils.

```
$# LS-DYNA keyword Input deck for explosive blast A-11
$#
$#
*KEYWORD
$# Model units: g, mm, ms, N, MPa
$#
*CONTROL_ALE
$#     dct      nadv      meth      afac      bfac      cfac      dfac      efac
        -1         1        -2      -1.0       0.0       0.0       0.0       0.0
$#   start       end     aafac     vfact      prit      ebc      pref   nsidebc
       0.0   1.0E+20       1.0    1.0E-6         0         0       0.0       0.0
$#    ncpl      nbkt    imascl    checkr
         1        50         0       0.0
*CONTROL_ENERGY
$#    hgen      rwen    slnten     rylen
         2         2         2         2
*CONTROL_TERMINATION
$#  endtim    endcyc     dtmin    endeng    endmas
      15.0         0       0.0       0.0       0.0
*CONTROL_TIMESTEP
$#  dtinit    tssfac      isdo    tslimt     dt2ms      lctm     erode     ms1st
         0       0.1         0       0.0       0.0         0         0         0
$#  dt2msf   dt2mslc     imscl    unused    unused     rmscl
       0.0         0         0         0         0       0.0
$#
*DATABASE_BINARY_D3PLOT
$#      dt      lcdt      beam     npltc    psetid
      0.10         0         0         0         0
$#   ioopt
         1
*DATABASE_TRHIST
$#      dt    binary      lcur     ioopt
    0.0010         1         0         1
*BOUNDARY_NON_REFLECTING_2D
         1
*SECTION_ALE2D_TITLE
ale_section
$#   secid   aleform       aet    elform
         1        11         0        14
*PART
clay
$#     pid     secid       mid     eosid
         1         1         1         3
*PART
sand
         2         1         2         4
*PART
air
         3         1         3         1
*PART
he
         4         1         4         2
*MAT_NULL_TITLE
air
$#     mid        ro
         3 1.038E-06
*EOS_LINEAR_POLYNOMIAL_TITLE
air
$#   eosid        c0        c1        c2        c3        c4        c5        c6
$#      e0        v0
         1       0.0       0.0       0.0       0.0       0.4       0.4       0.0
    0.1013       1.0
*MAT_HIGH_EXPLOSIVE_BURN_TITLE
he
$#     mid        ro         d       pcj      beta
```

```
         4  1.20E-03    6300.0   12540.0       2.0
*EOS_JWL
$#   eosid         a          b         r1         r2      omeg         e0         v0
         2  616342.0   15311.9       5.95        2.0    0.4268     5510.5        1.0
$#
$#
*INITIAL_DETONATION
$#     pid         x          y          z         lt
         4       0.0      103.0        0.0       0.00
$#
$#
$# Clay material model
$$#(2-part compressibility)
$
*MAT_PSEUDO_TENSOR
$#     mid        ro          g         pr
         1  0.001964       2.70
$#    sigf        a0         a1         a2        a0f        a1f         b1        per
    0.0460       0.0        0.0        0.0        0.0        0.0        0.0        0.0
$#      er       prr       sigy       etan        lcp        lcr
       0.0       0.0        0.0        0.0          0          0
$#      x1        x2         x3         x4         x5         x6         x7         x8
       0.0       1.0        2.0        4.0        6.0       10.0      100.0      200.0
$#      x9       x10        x11        x12        x13        x14        x15        x16
     300.0     400.0      500.0      600.0      700.0      800.0      900.0     2000.0
$#     ys1       ys2        ys3        ys4        ys5        ys6        ys7        ys8
      0.05      0.20       0.36       0.66       0.97       1.59      15.47      30.90
$#     ys9      ys10       ys11       ys12       ys13       ys14       ys15       ys16
     46.32     61.75      77.17      92.60     108.02     123.44     138.87     308.54
*EOS_TABULATED_COMPACTION
$#   eosid      gama         e0         vo
         3       0.0        0.0        1.0
$#           ev1             ev2             ev3             ev4             ev5
             0.0         -0.0305         -0.0356         -0.0408         -0.0460
$#           ev6             ev7             ev8             ev9            ev10
         -0.0513         -0.1054         -0.2231         -0.3567         -0.5108
$#            c1              c2              c3              c4              c5
             0.0           0.474            23.4            46.8            70.2
$#            c6              c7              c8              c9             c10
            93.6           327.6           795.6          1263.6          1731.6
$#            t1              t2              t3              t4              t5

$#            t6              t7              t8              t9             t10

$#            k1              k2              k3              k4              k5
          4504.5          4504.5          4504.5          4504.5          4504.5
$#            k6              k7              k8              k9             k10
          4504.5          4504.5          4504.5          4504.5          4504.5
$#
$# Sand material model
*MAT_PSEUDO_TENSOR
$#     mid        ro          g         pr
         2   0.00141  28.00E+3
$#    sigf        a0         a1         a2        a0f        a1f         b1        per
       0.0       0.0        0.0        0.0        0.0        0.0        0.0        0.0
$#      er       prr       sigy       etan        lcp        lcr
       0.0       0.0        0.0        0.0          0          0
$#      x1        x2         x3         x4         x5         x6         x7         x8
       0.0    112.27      143.5      176.1      204.4     244.04      279.4      313.3
$#      x9       x10        x11        x12        x13        x14        x15        x16
     437.6    6000.0
$#     ys1       ys2        ys3        ys4        ys5        ys6        ys7        ys8
       0.0     128.3     155.05     178.04      192.2      204.7      212.2      217.4
$#     ys9      ys10       ys11       ys12       ys13       ys14       ys15       ys16
     221.8     225.0
```

```
*EOS_TABULATED_COMPACTION
$#   eosid      gama         e0         vo
         4       0.0        0.0        1.0
$#            ev1              ev2              ev3              ev4              ev5
              0.0          -0.1807          -0.3323          -0.4904          -0.5323
$#            ev6              ev7              ev8              ev9             ev10
          -0.5504          -0.5822          -0.6011          -0.6908
$#            c1               c2               c3               c4               c5
              0.0            38.89            77.79           180.83           256.85
$#            c6               c7               c8               c9              c10
           304.96           654.90          1508.33          7496.41
$#            t1               t2               t3               t4               t5

$#            t6               t7               t8               t9              t10

$#            k1               k2               k3               k4               k5
         48.0E+03         48.0E+03         48.0E+03         48.0E+03         48.0E+03
$#            k6               k7               k8               k9              k10
         48.0E+03         48.0E+03         48.0E+03         48.0E+03         48.0E+03
$#
*ALE_MULTI-MATERIAL_GROUP
$Clay
$#     sid    idtype    gpname
         1         1
$Sand
         2         1
$Air
         3         1
$He
         4         1
$#
*INCLUDE
mesh_ALL_A11.k
*INCLUDE
NodeSetsTracers_5mmEls_A11.k
*END
```

```
$# LS-DYNA keyword Input deck for 4.9 metric ton dam blast
$#
$#
*KEYWORD
$# Model units: g, mm, ms, N, MPa
$#
*CONTROL_ALE
$#     dct      nadv      meth      afac      bfac      cfac      dfac      efac
        -1         1        -2      -1.0       0.0       0.0       0.0       0.0
$#   start       end     aafac     vfact      prit       ebc      pref   nsidebc
       0.0   1.0E+20       1.0    1.0E-6         0         0       0.0       0.0
$#    ncpl      nbkt    imascl    checkr
         1        50         0       0.0
*CONTROL_ENERGY
$#    hgen      rwen    slnten     rylen
         2         2         2         2
*CONTROL_TERMINATION
$#  endtim    endcyc     dtmin    endeng    endmas
      30.0         0       0.0       0.0       0.0
*CONTROL_TIMESTEP
$#  dtinit    tssfac      isdo    tslimt     dt2ms      lctm     erode     ms1st
         0       0.3         0       0.0       0.0         0         0         0
$#  dt2msf   dt2mslc     imscl    unused    unused     rmscl
       0.0         0         0         0         0       0.0
$#
*DATABASE_BINARY_D3PLOT
$#      dt      lcdt      beam     npltc    psetid
       0.5         0         0         0         0
$#   ioopt
         1
*DATABASE_TRHIST
$#      dt    binary      lcur     ioopt
     0.001         1         0         1
*BOUNDARY_NON_REFLECTING
         1
*BOUNDARY_SPC_SET
         1         0         1         1         1         1         1         1
         2         0         0         1         0         1         0         1
         3         0         0         1         0         1         0         1
         4         0         0         1         0         1         0         1
*SECTION_SOLID_TITLE
ElForm11_1Point_MMALE_Element
$#   secid    elform
         1        11
*SECTION_SOLID
$#   secid    elform
         2        11
*SECTION_SOLID
$#   secid    elform
         3        11
*PART
dam
$#     pid     secid       mid     eosid
         1         1         1         1
*PART
air
         2         2         2         2
*PART
he
         3         3         3         3
*MAT_NULL_TITLE
air
$#     mid        ro
         2 1.038E-06
*EOS_LINEAR_POLYNOMIAL_TITLE
```

```
air
$#   eosid        c0        c1        c2        c3        c4        c5        c6
$#      e0        v0
         2       0.0       0.0       0.0       0.0       0.4       0.4       0.0
    0.1013       1.0
*MAT_HIGH_EXPLOSIVE_BURN_TITLE
he
$#     mid        ro         d       pcj      beta
         3  1.20E-03    6300.0   12540.0       2.0
*EOS_JWL
$#   eosid         a         b        r1        r2      omeg        e0        v0
         3  616342.0   15311.9      5.95       2.0    0.4268    5510.5       1.0
$#
$#
*INITIAL_DETONATION
$#     pid         x         y         z        lt
         3  158000.0       0.0    1800.0       0.0
$#
$#
*MAT_PSEUDO_TENSOR_TITLE
Clay (single modulus)
$#     mid        ro         g        pr
         1  0.001964      2.70
$#    sigf        a0        a1        a2       a0f       a1f        b1       per
    0.0460       0.0       0.0       0.0       0.0       0.0       0.0       0.0
$#      er       prr      sigy      etan       lcp       lcr
       0.0       0.0       0.0       0.0         0         0
$#      x1        x2        x3        x4        x5        x6        x7        x8
       0.0       1.0       2.0       4.0       6.0      10.0     100.0     200.0
$#      x9       x10       x11       x12       x13       x14       x15       x16
     300.0     400.0     500.0     600.0     700.0     800.0     900.0    5000.0
$#     ys1       ys2       ys3       ys4       ys5       ys6       ys7       ys8
      0.05      0.20      0.36      0.66      0.97      1.59     15.47     30.90
$#     ys9      ys10      ys11      ys12      ys13      ys14      ys15      ys16
     46.32     61.75     77.17     92.60    108.02    123.44    138.87    771.28
*EOS_TABULATED_COMPACTION
$#   eosid      gama        e0        vo
         1       0.0       0.0       1.0
$#            ev1               ev2               ev3               ev4               ev5
              0.0           -0.0305           -0.0356           -0.0408           -0.0460
$#            ev6               ev7               ev8               ev9              ev10
          -0.0513           -0.1054           -0.2231           -0.3567           -2.9957
$#             c1                c2                c3                c4                c5
              0.0             140.4             163.8             187.2             210.6
$#             c6                c7                c8                c9               c10
            234.0             468.0             936.0            1404.0            4446.0
$#             t1                t2                t3                t4                t5

$#             t6                t7                t8                t9               t10

$#             k1                k2                k3                k4                k5
           4609.4            4609.4            4609.4            4609.4            4609.4
$#             k6                k7                k8                k9               k10
           4609.4            4609.4            4609.4            4609.4            4609.4
$#
*ALE_MULTI-MATERIAL_GROUP
$Dam
$#     sid    idtype    gpname
         1         1
$Air
         2         1
$He
         3         1
$#
*DEFINE_TRANSFORMATION
```

```
         1
     SCALE    1000.0    1000.0    1000.0
*INCLUDE_TRANSFORM
DamMesh_Toe_4915kg.k



         1
*INCLUDE
Database_Tracers.k
*END
```

APPENDIX B CRATER PROFILES AND VOLUMES

The two-dimensional crater profiles measured during explosive airblast testing are presented in Appendix B. *Crater dimensions in Appendix B are presented in inches.* Profiles were measured using a profiling tool, digitized into an electronic format, and electronically rotated to calculate the crater volume. Profiles for some of the larger blasts were not fully captured because the depth of the crater exceeded the physical dimensions of the profiling tool. However, the diameters and depths were still measured during the experiments and the profile shape was estimated from the measurements and crater photos. Blast test A-1 did not generate a crater and was therefore not presented in this appendix.

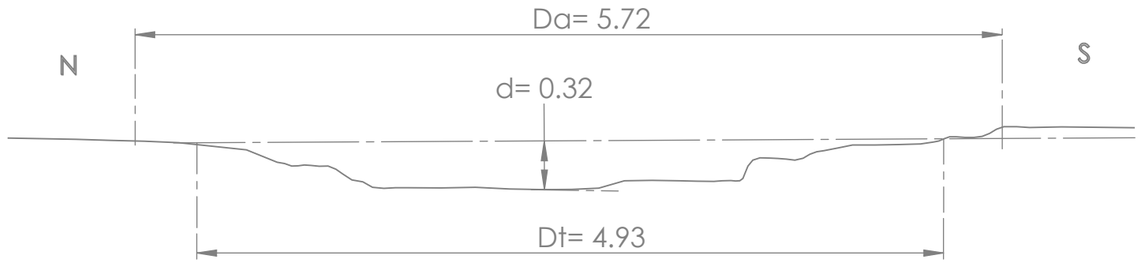

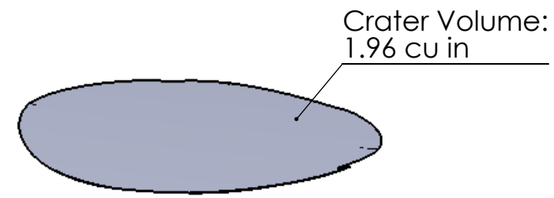

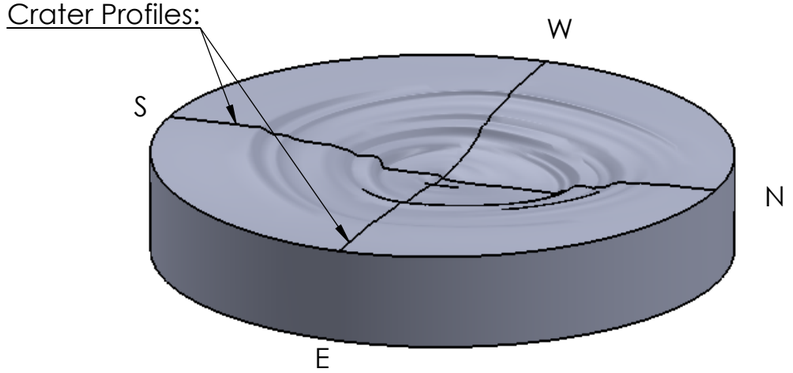

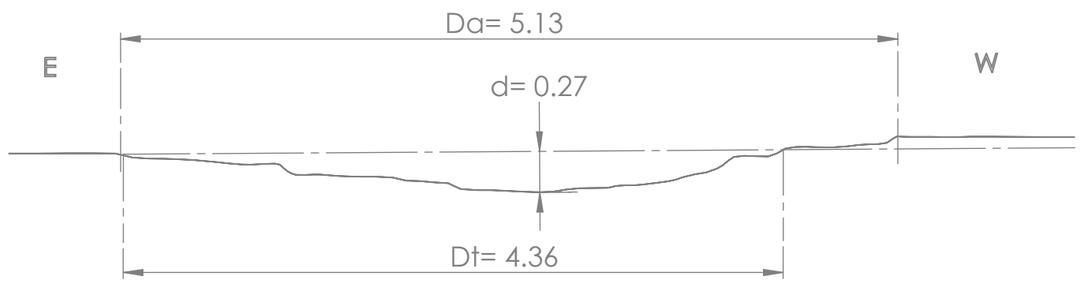

SIZE	FIG. NO.	
B	BLAST A-02	
CHARGE MASS: 20.9g	BLAST HEIGHT:3 in	
SCALE: 1"=1"		

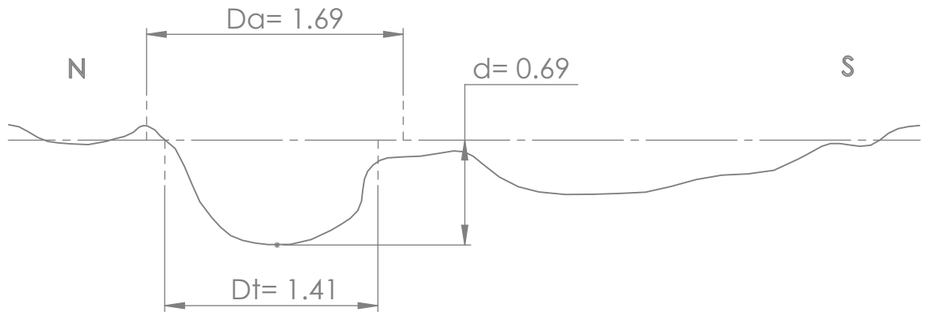

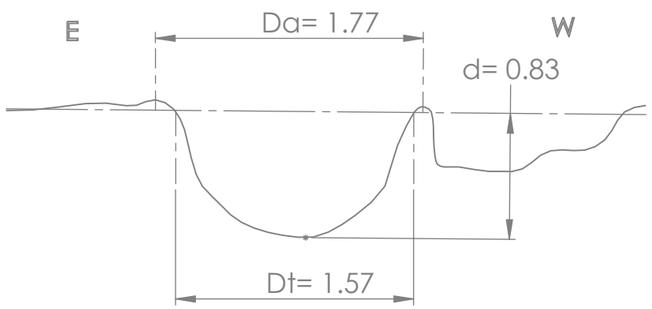

Crater Profiles:

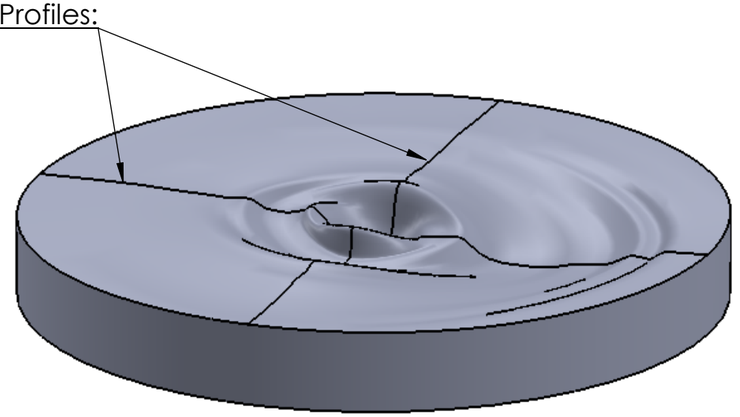

Crater geometry was considered as an outlier.
Crater volume was not calculated.

SIZE	FIG. NO.
B	BLAST A-03
CHARGE MASS: 25.9 g	BLAST HEIGHT: 3 in
SCALE: 1"=1"	

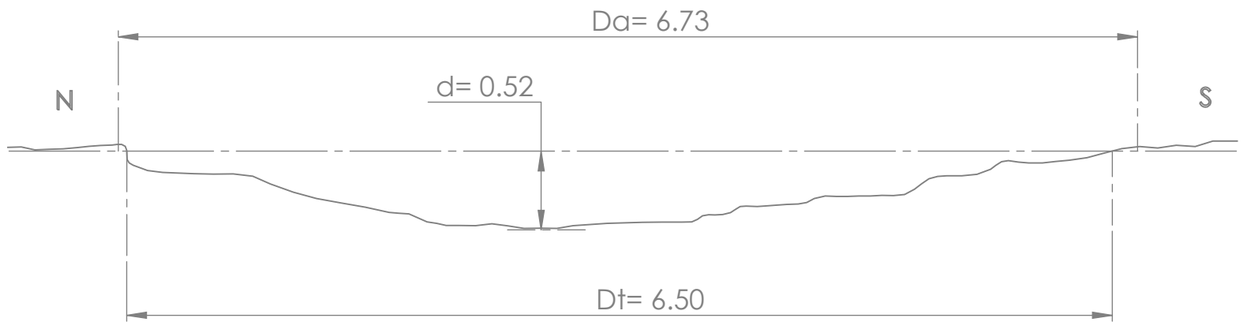

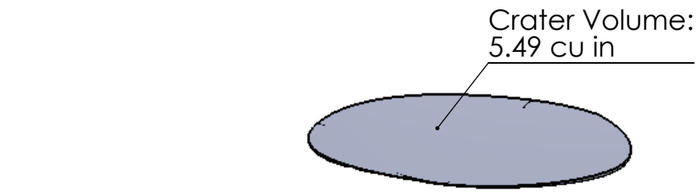

Crater Profiles:

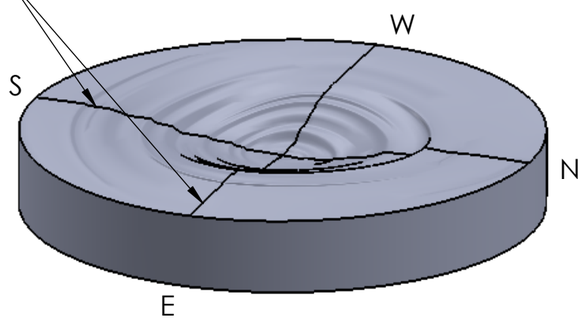

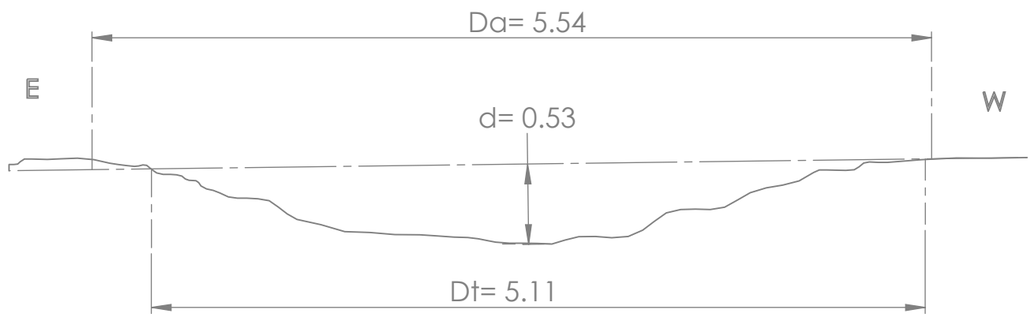

SIZE	FIG. NO.	
B	BLAST A-04	
CHARGE MASS: 30.9 g		BLAST HEIGHT: 3 in
SCALE: 1"=1"		

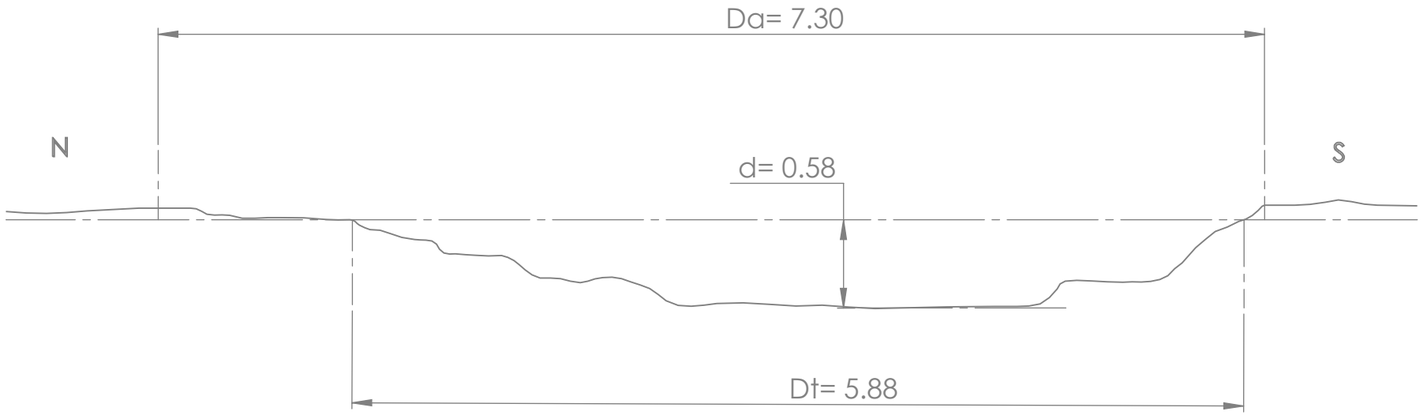

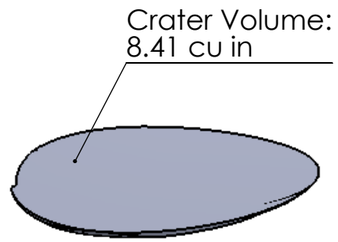

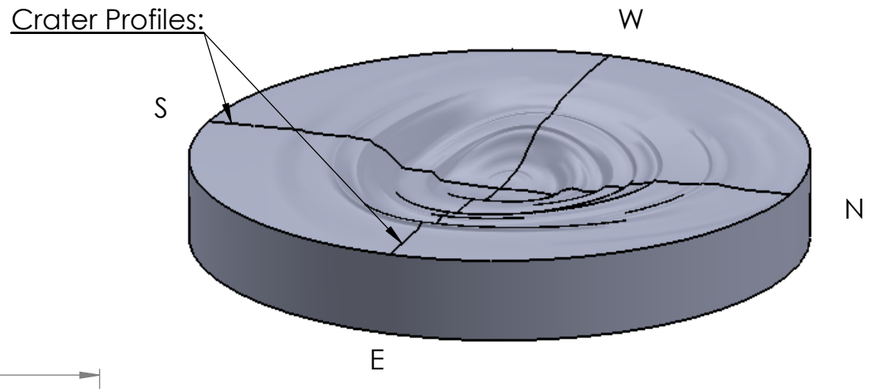

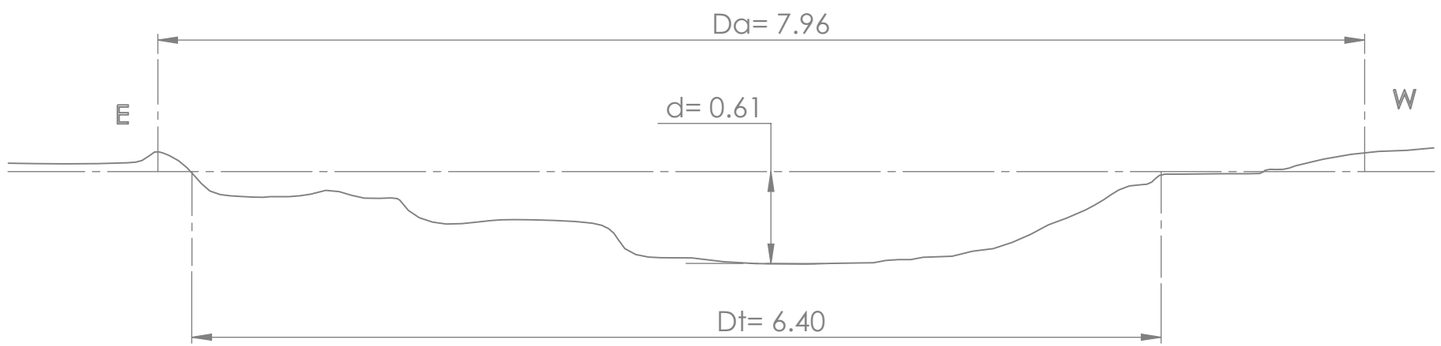

SIZE	FIG. NO.
B	BLAST A-05
CHARGE MASS: 38.9 g	BLAST HEIGHT: 3 in
SCALE: 1"=1"	

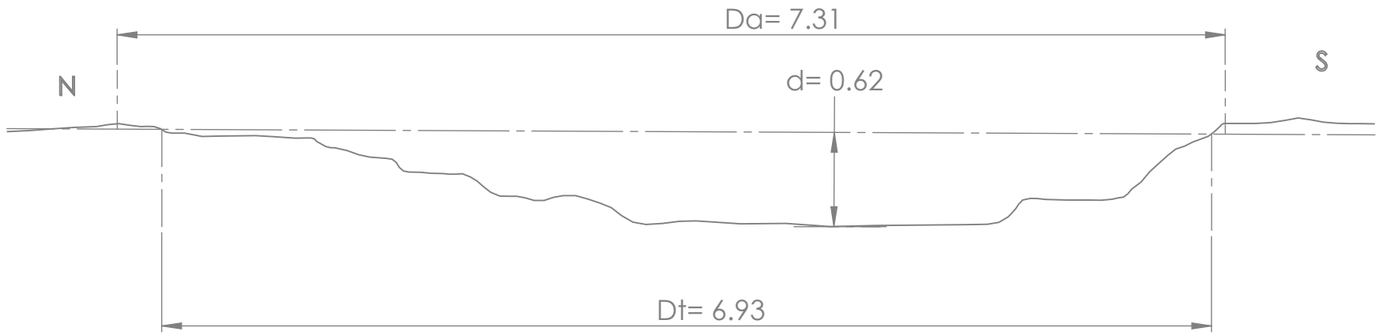

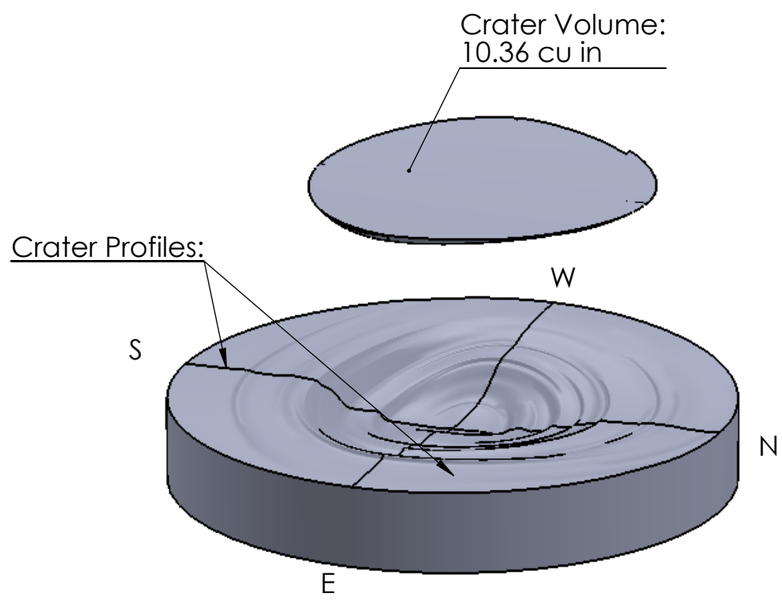

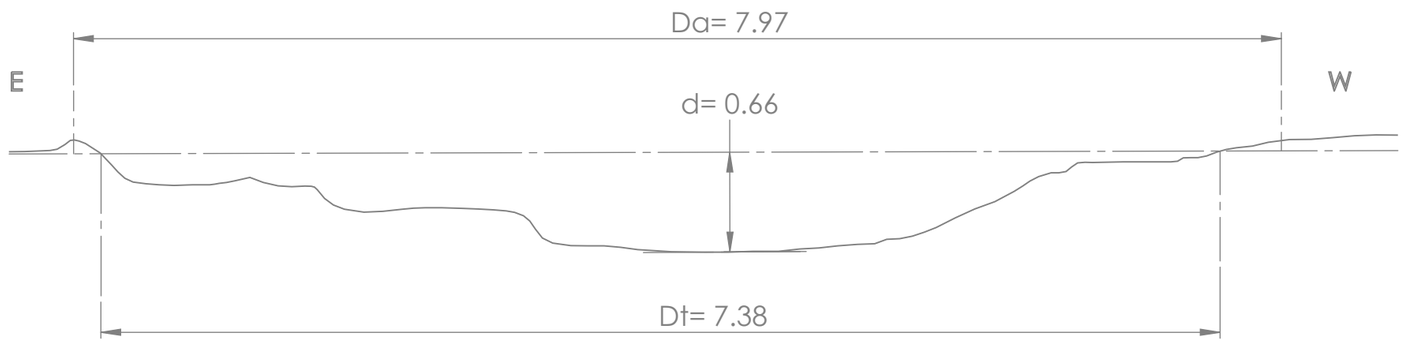

SIZE	FIG. NO.
B	BLAST A-06
CHARGE MASS: 45.9 g	BLAST HEIGHT: 3 in
SCALE: 1"=1"	

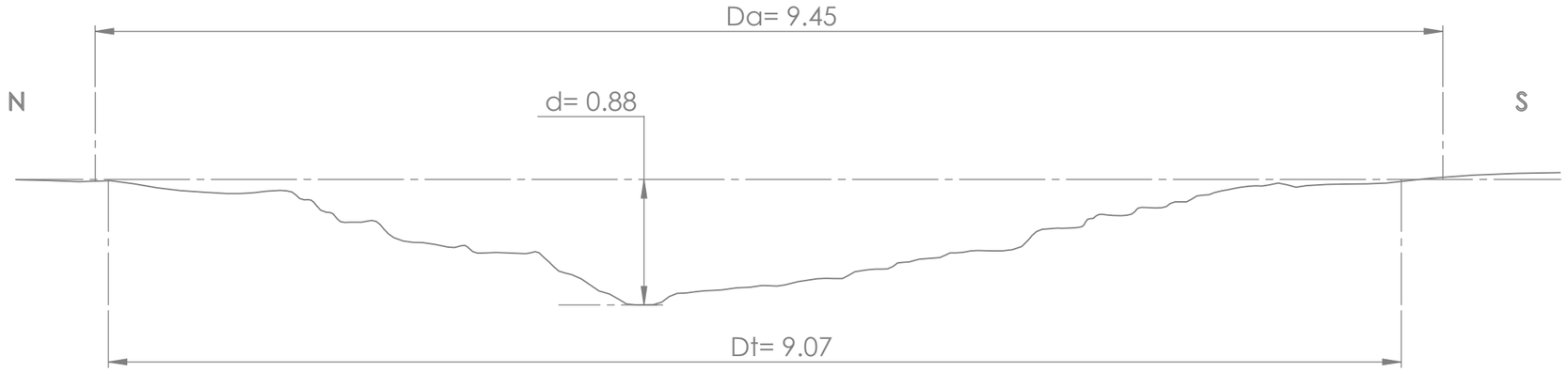

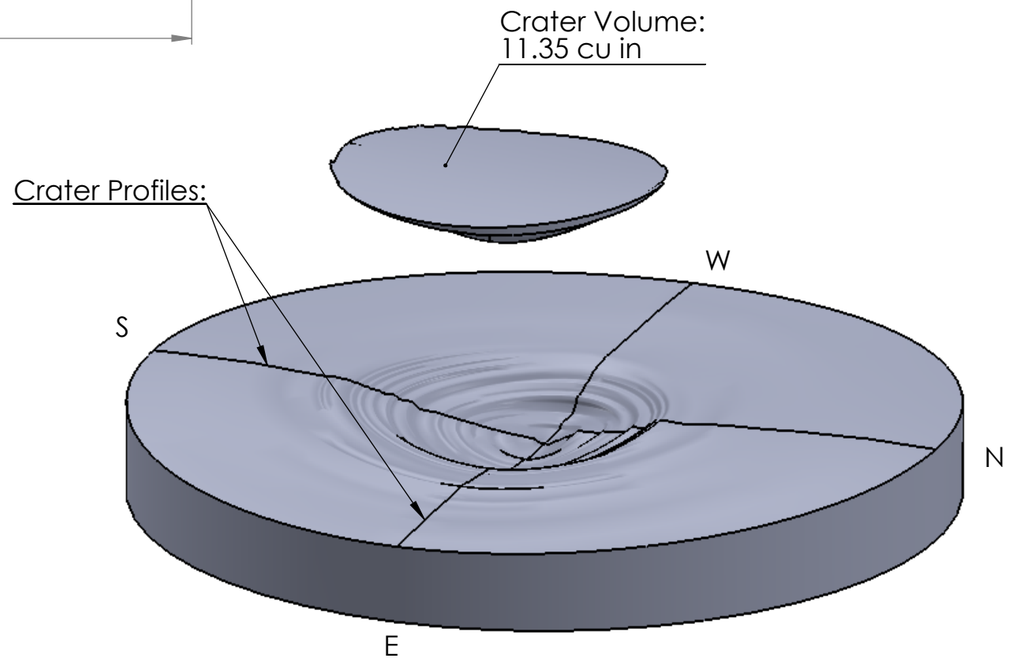

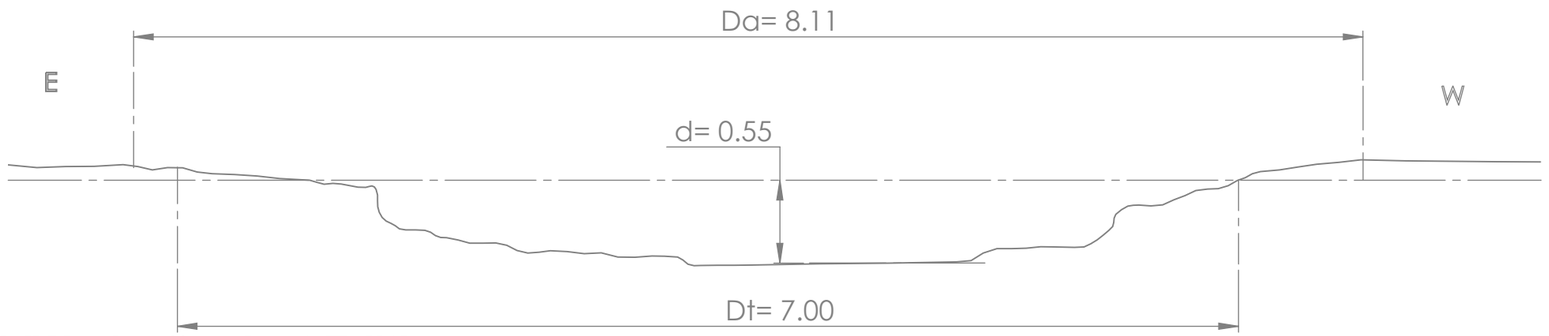

SIZE	FIG. NO.
B	BLAST A-07
CHARGE MASS: 50.9g	BLAST HEIGHT: 3in
SCALE: 1"=1"	

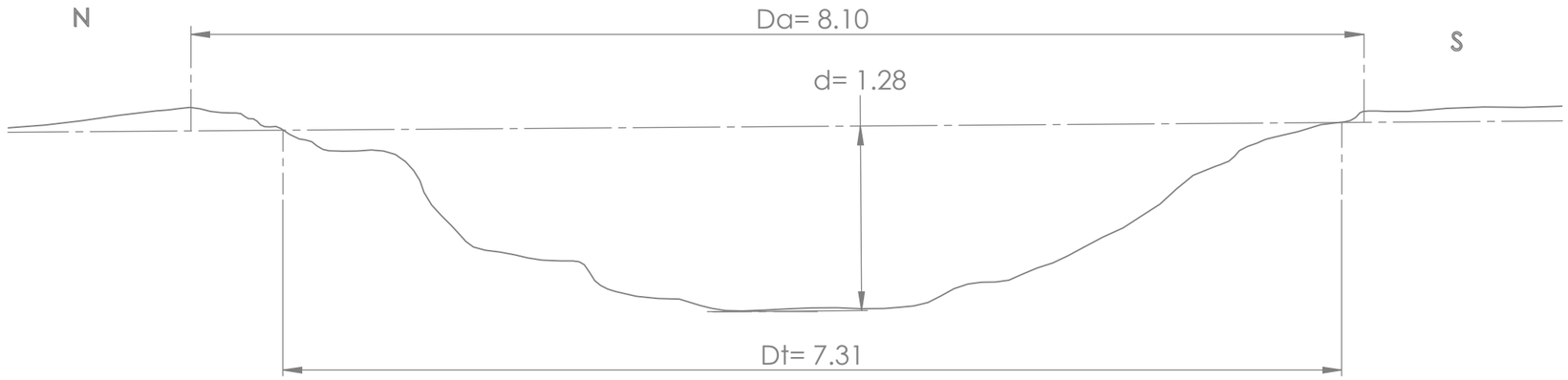

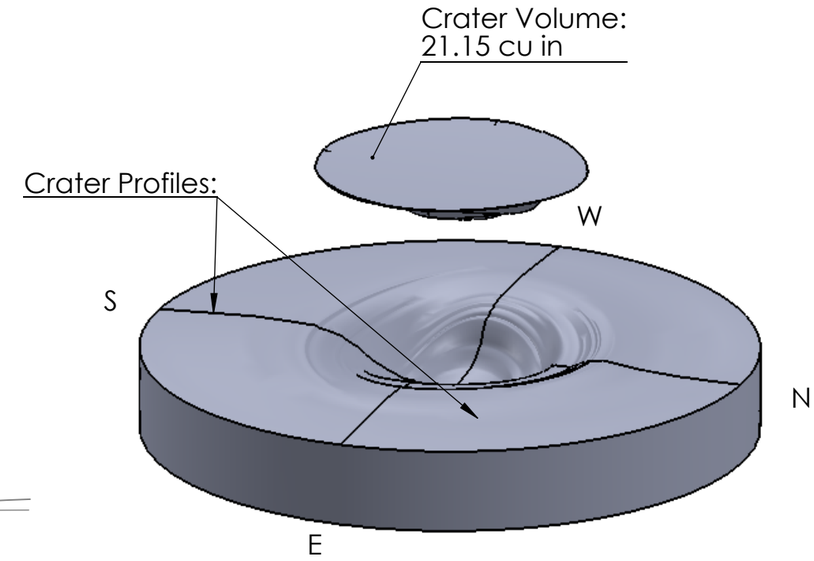

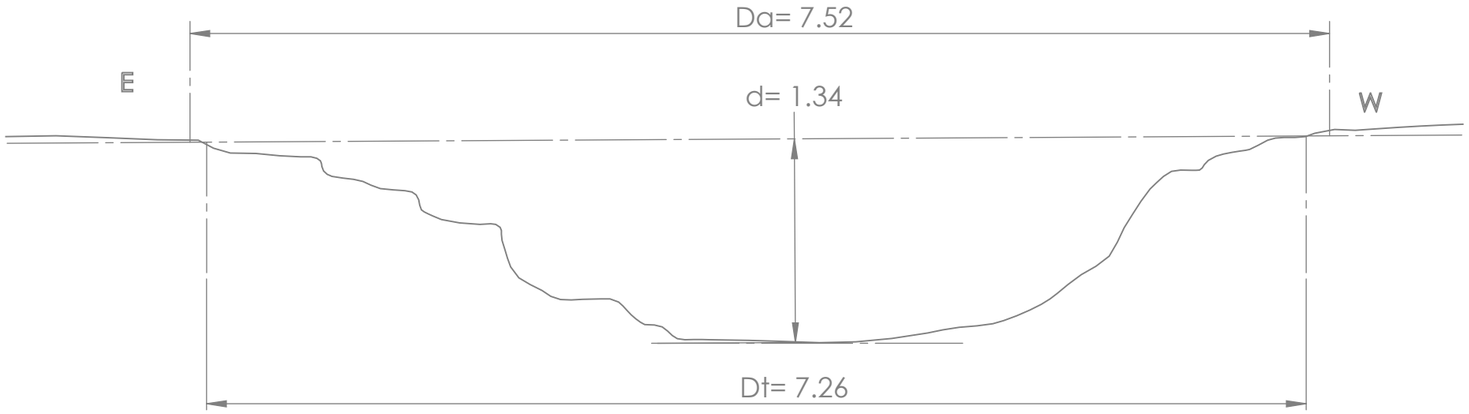

SIZE	FIG. NO.	
B	BLAST A-08	
CHARGE MASS: 65.9 g	BLAST HEIGHT: 3 in	
SCALE: 1"=1"		

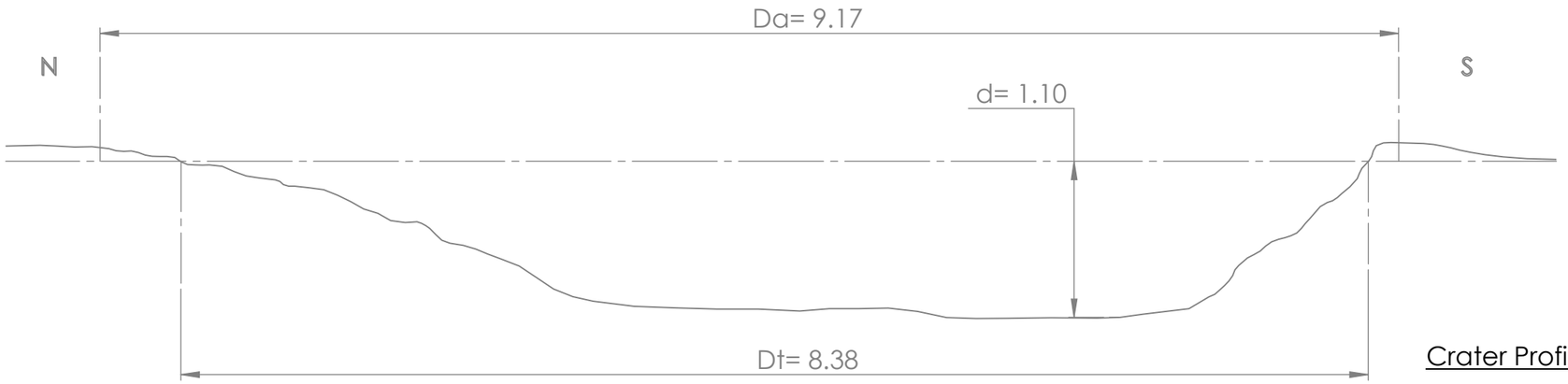

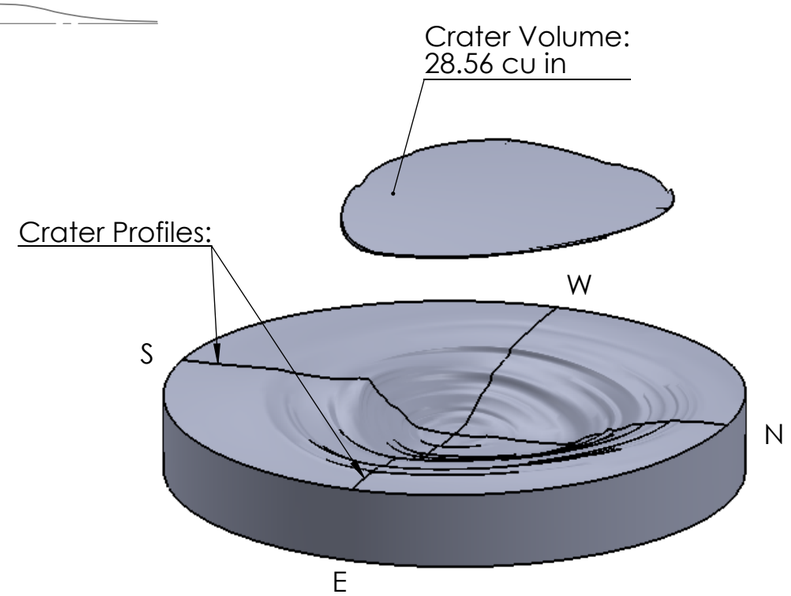

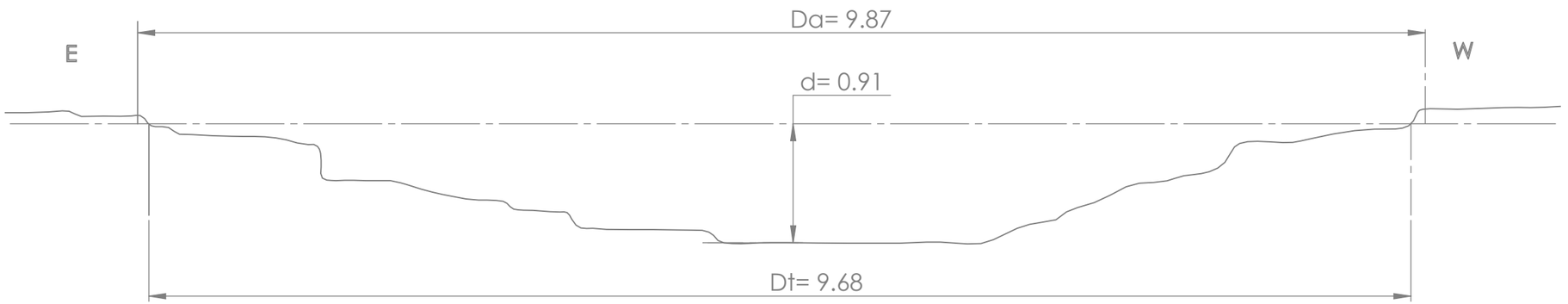

SIZE	FIG. NO.
B	BLAST A-09
CHARGE MASS: 80.9g	BLAST HEIGHT: 3in
SCALE: 1"=1"	

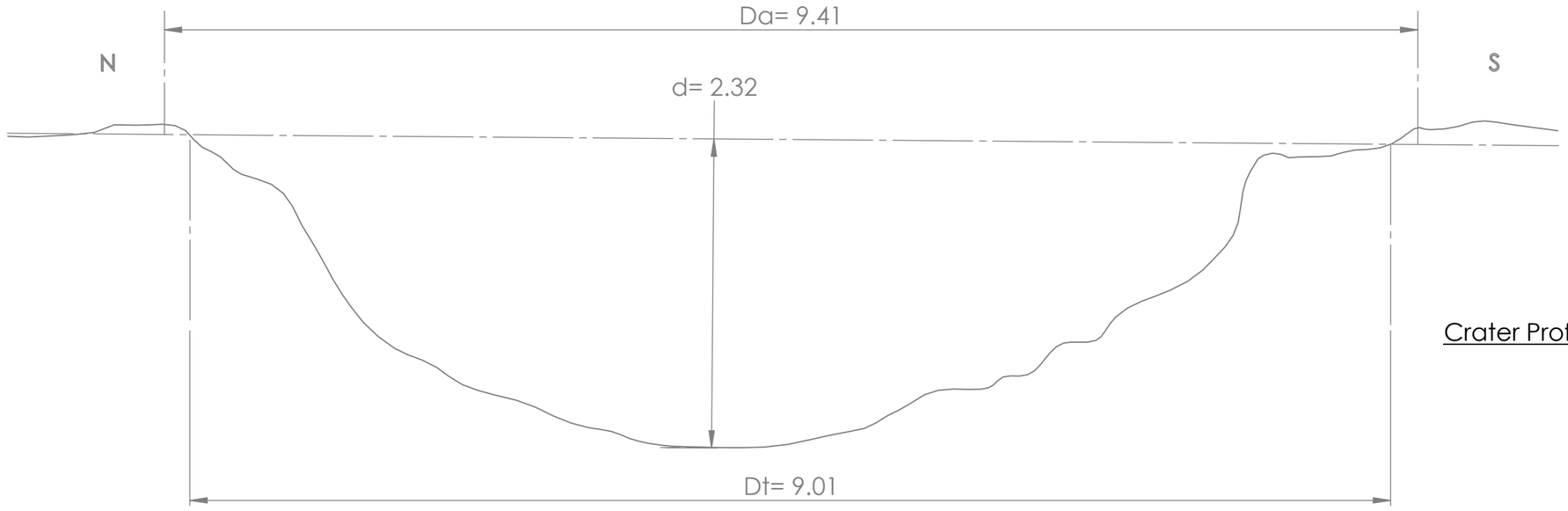

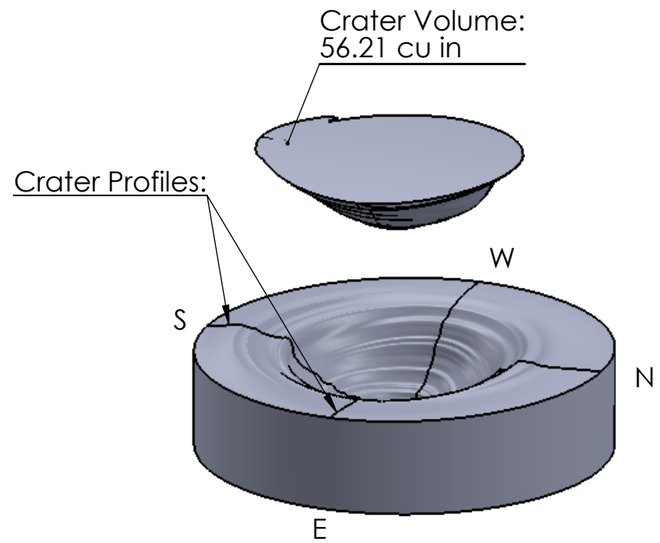

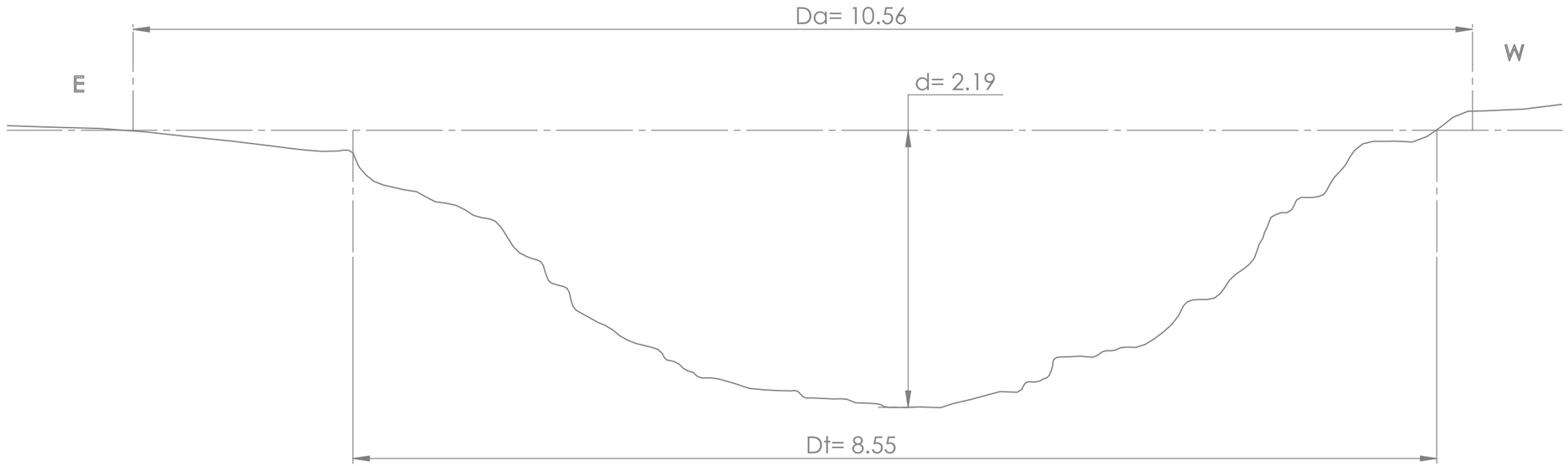

SIZE	FIG. NO.
B	BLAST A-10
CHARGE MASS: 90.9 g	BLAST HEIGHT: 3 in
SCALE: 1"=1"	

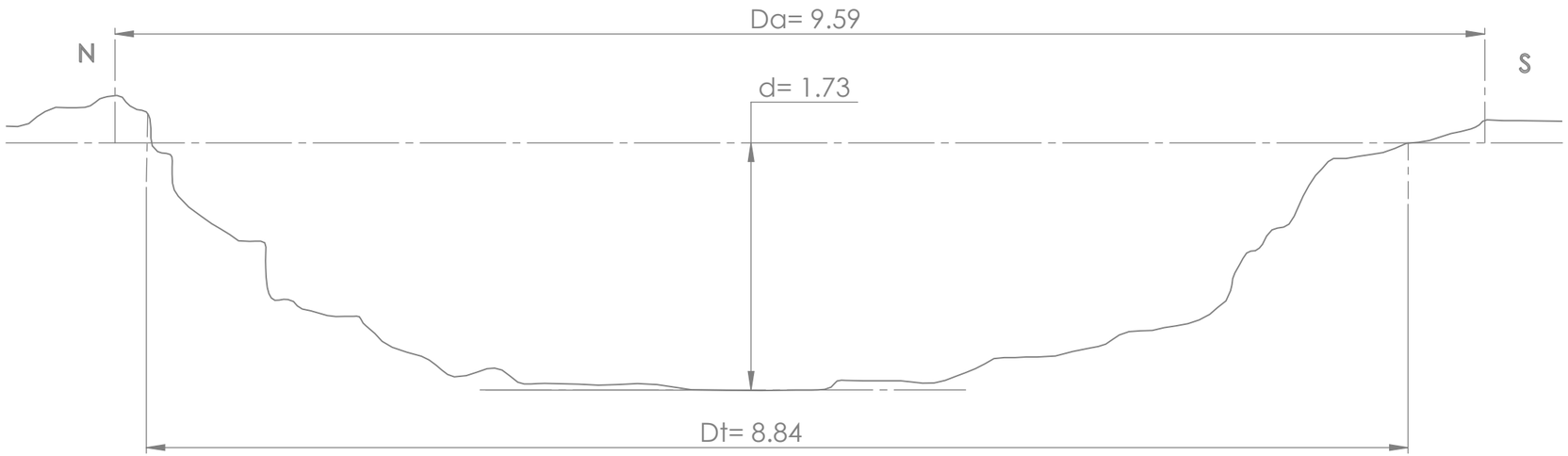

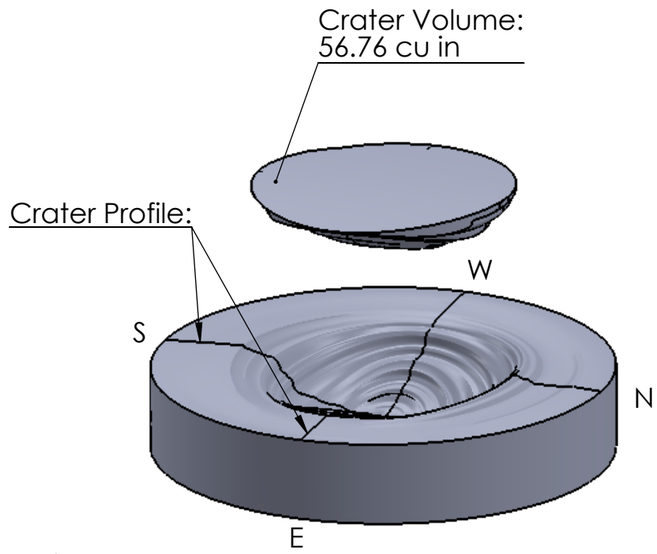

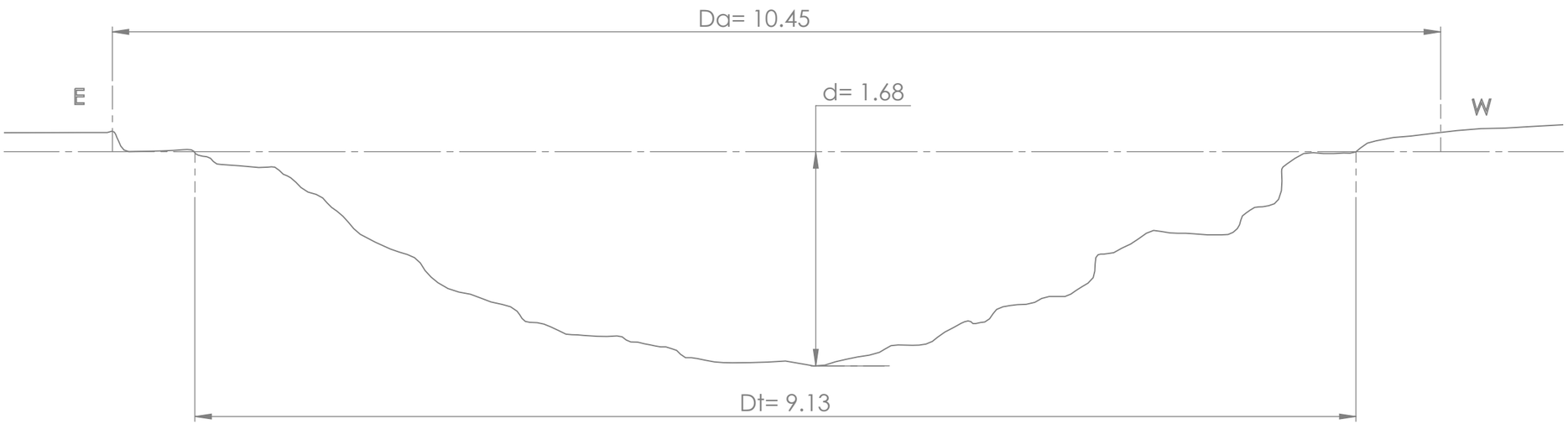

SIZE	FIG. NO.
B	BLAST A-11
CHARGE MASS: 100.9 g	BLAST HEIGHT: 3 in
SCALE: 1"=1"	

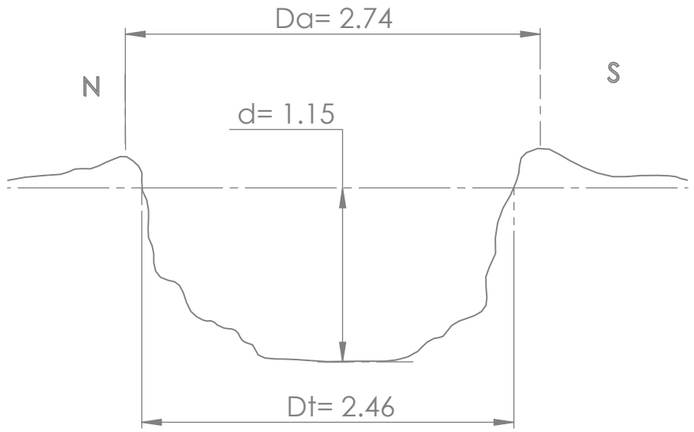

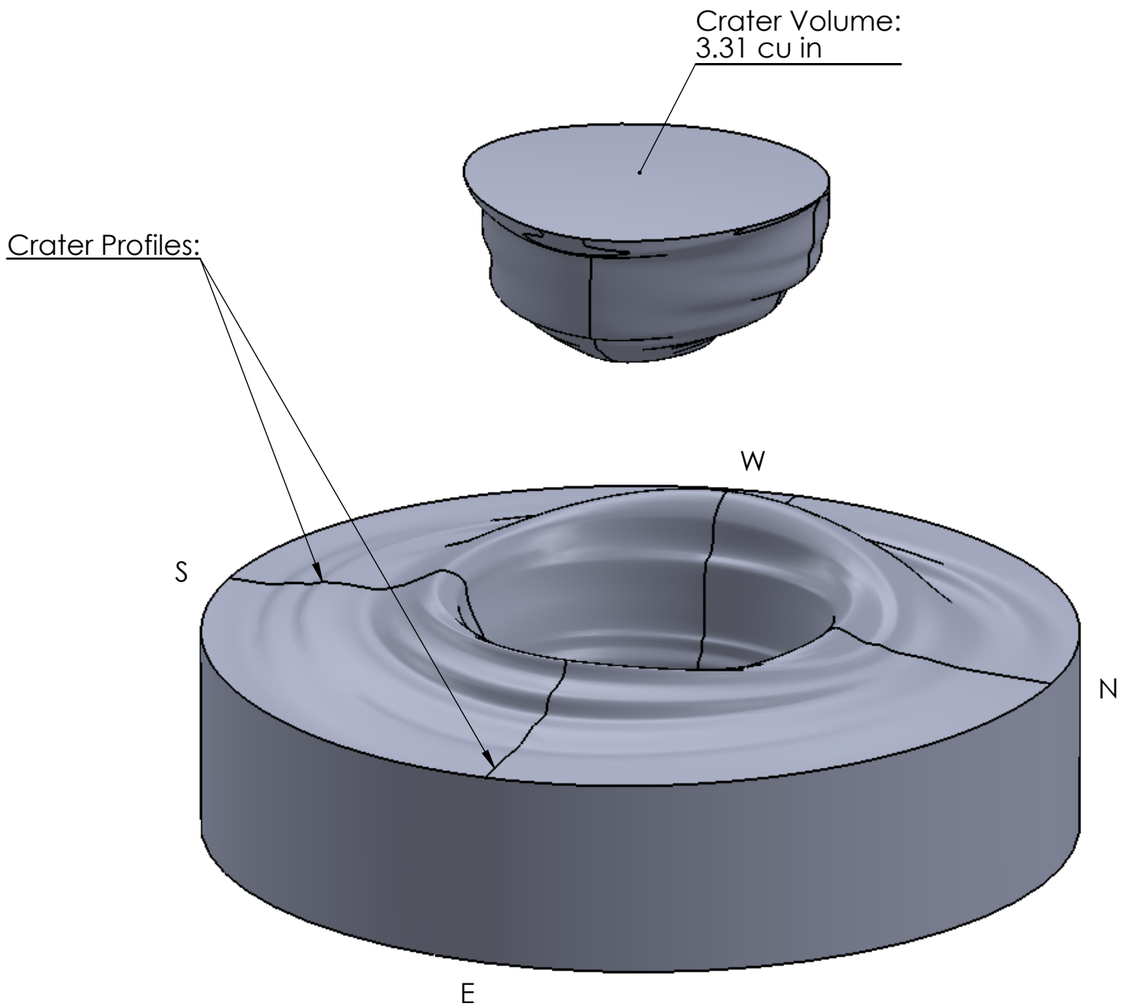

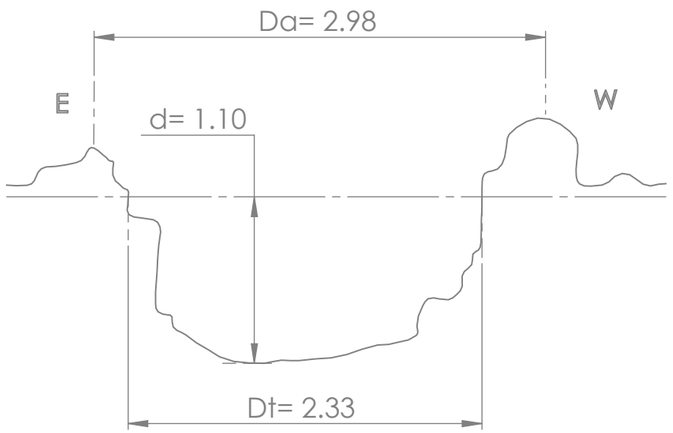

SIZE	FIG. NO.
B	BLAST B-01
CHARGE MASS: 0.9 g	BLAST HEIGHT: 1 in
SCALE: 1"=1"	

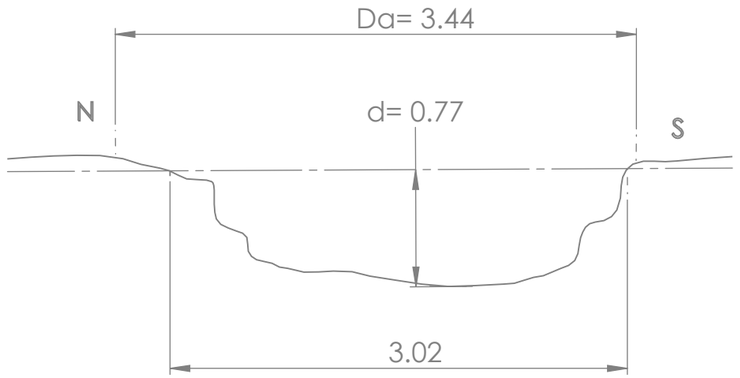

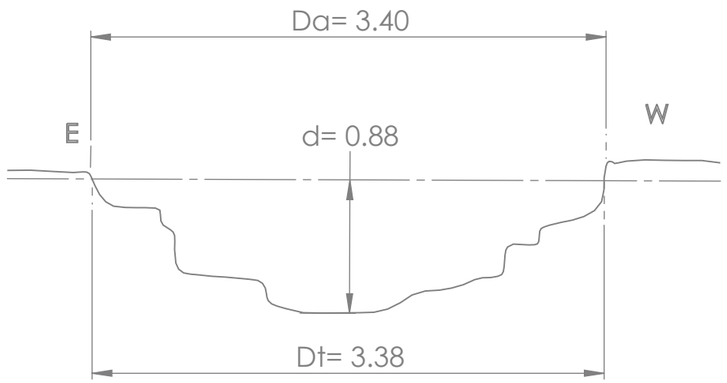

Crater Volume:
3.52 cu in

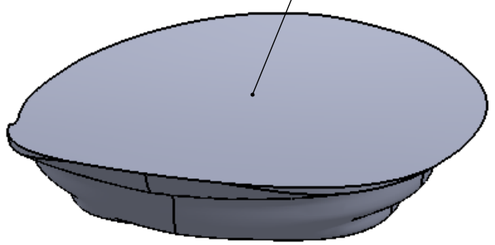

Crater Profiles:

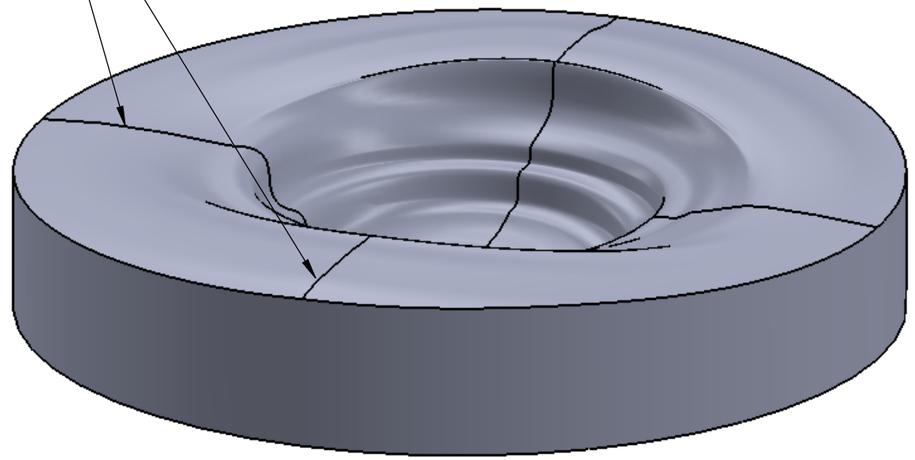

SIZE	FIG. NO.	
B	BLAST B-02	
CHARGE MASS: 5.9 g		BLAST HEIGHT: 1 in
SCALE: 1"=1"		

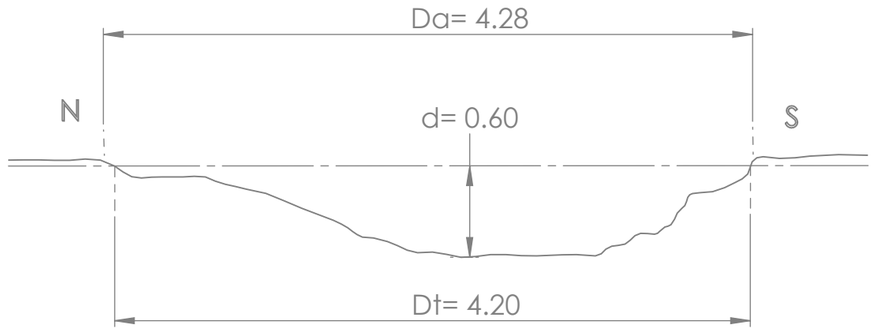

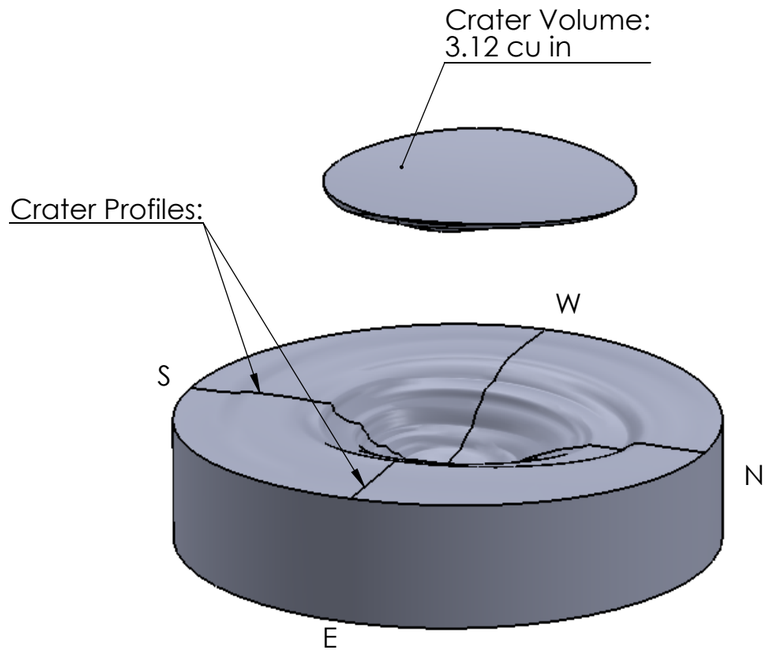

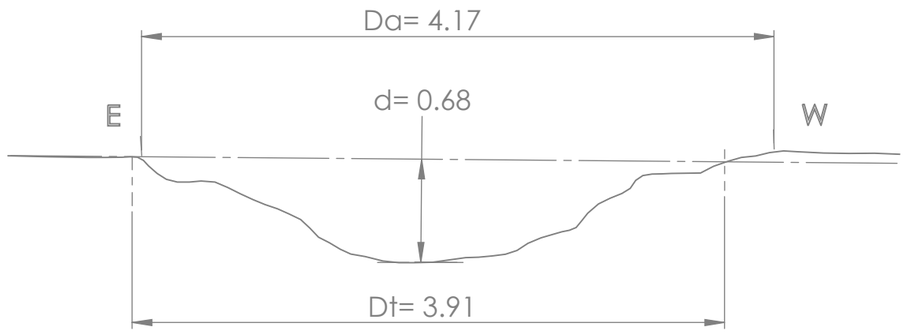

SIZE	FIG. NO.
B	BLAST B-03
CHARGE MASS: 10.9 g	BLAST HEIGHT: 1 in
SCALE: 1"=1"	

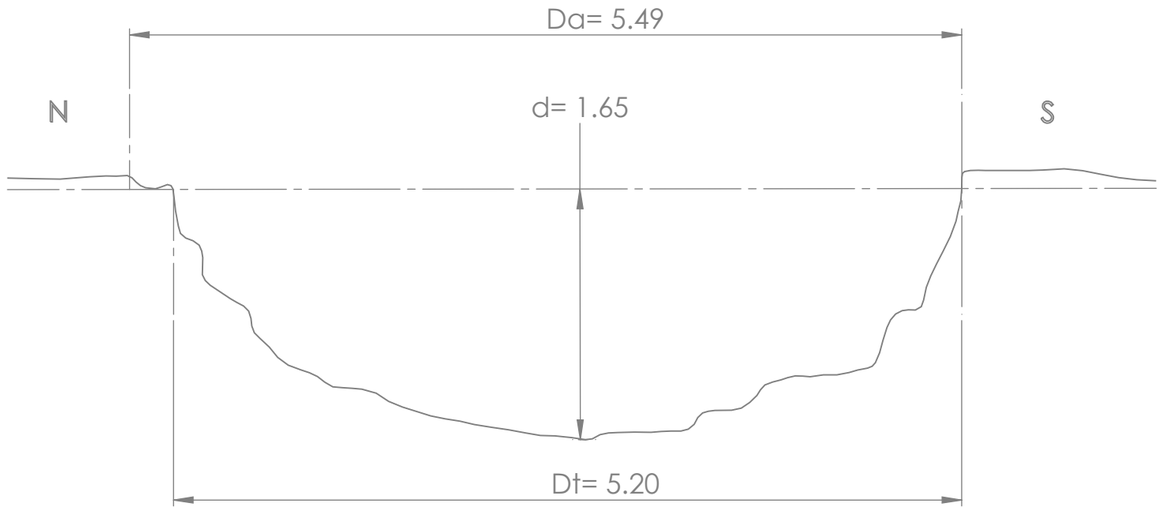

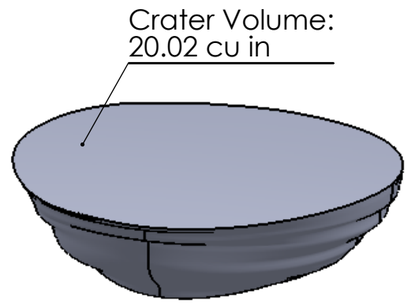

Crater Profiles:

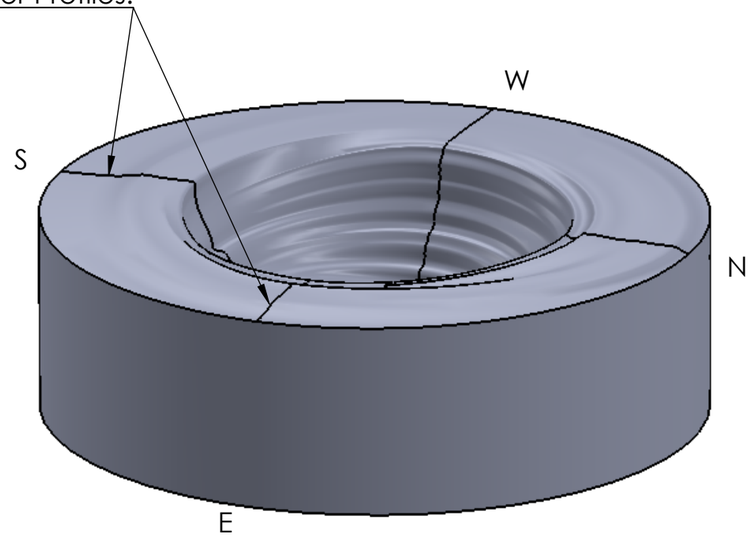

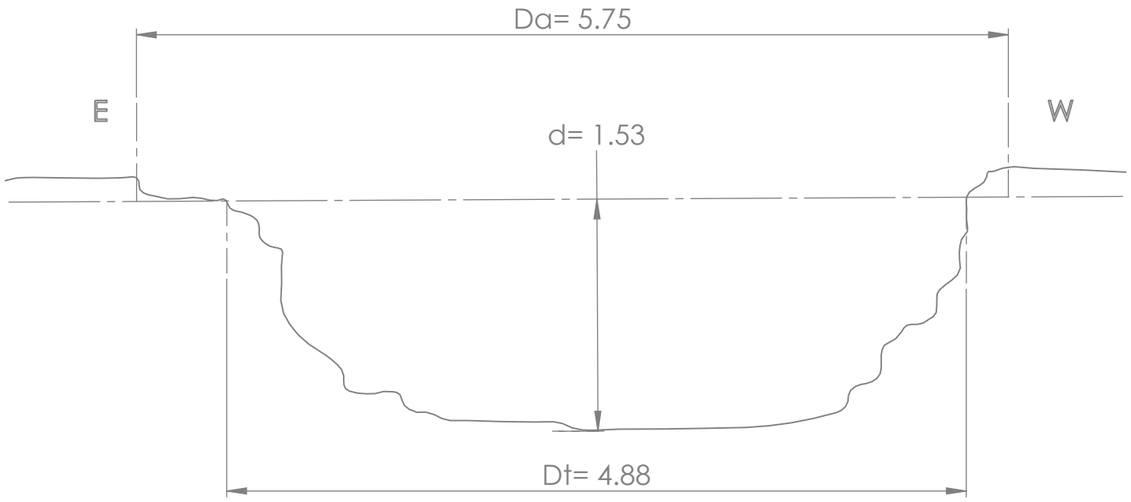

SIZE	FIG. NO.
B	BLAST B-04
CHARGE MASS: 20.9 g	BLAST HEIGHT: 1 in
SCALE: 1"=1"	

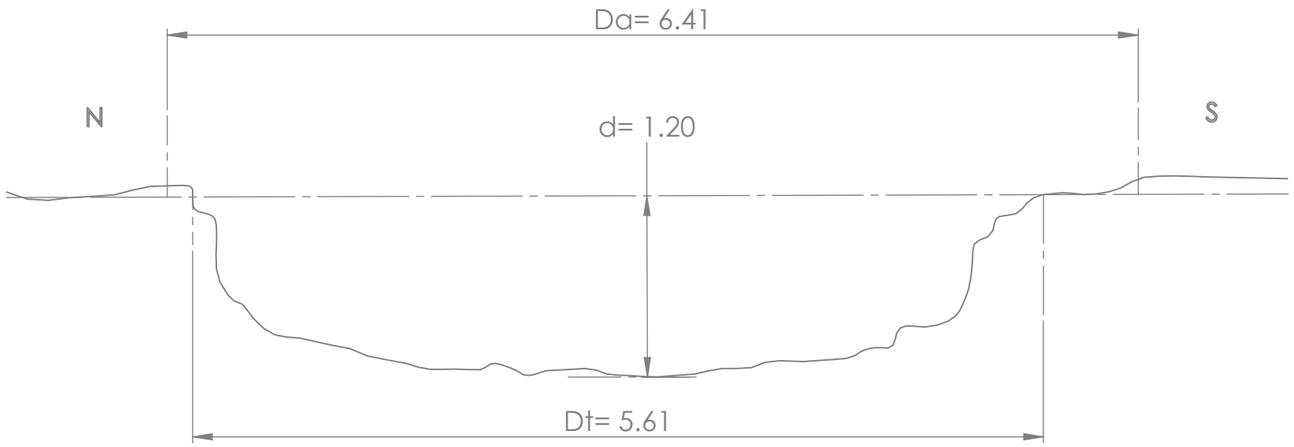

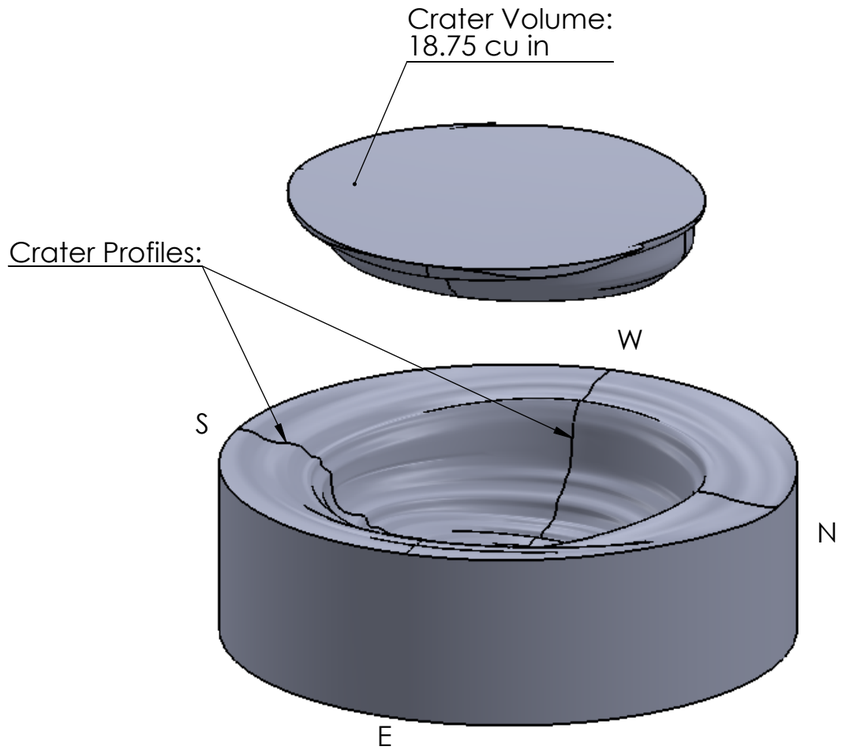

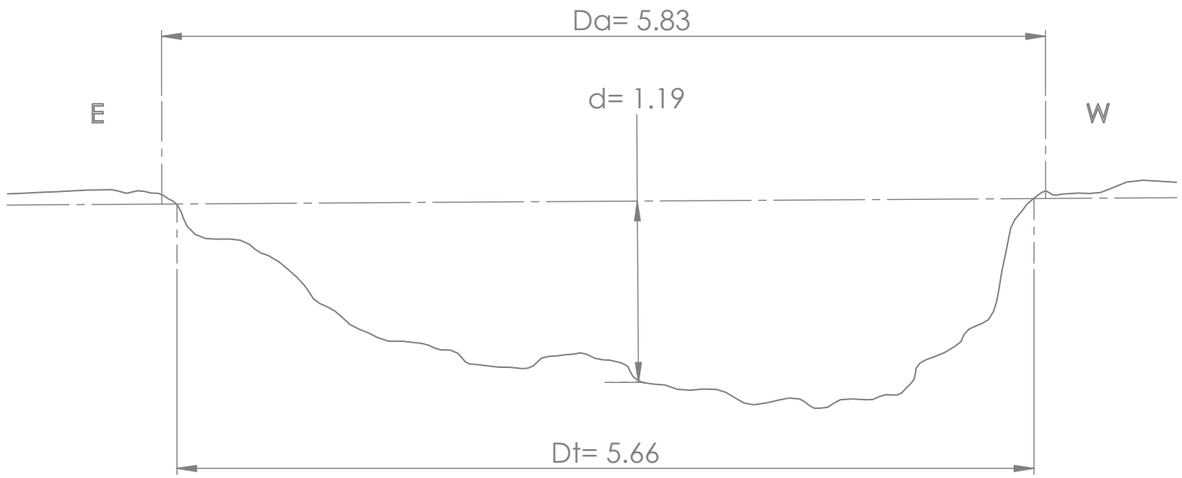

SIZE	FIG. NO.
B	BLAST B-05
CHARGE MASS: 30.9 g	BLAST HEIGHT: 1 in
SCALE: 1"=1"	

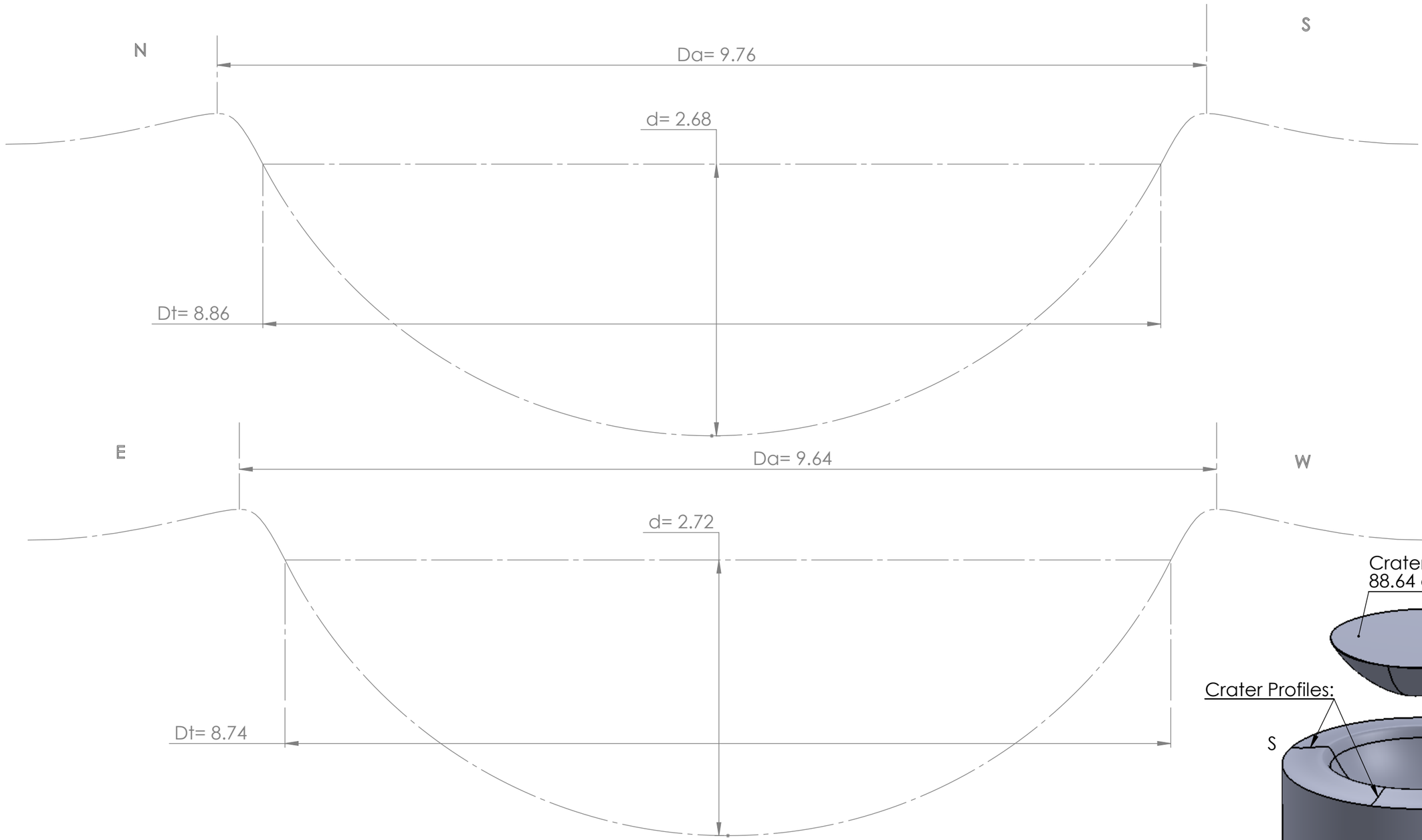

Estimated crater geometry constructed from diameter and depth measurements.

SIZE	FIG. NO.	
B	BLAST B-06	
CHARGE MASS: 40.9 g		BLAST HEIGHT: 1 in
SCALE: 1"=1"		

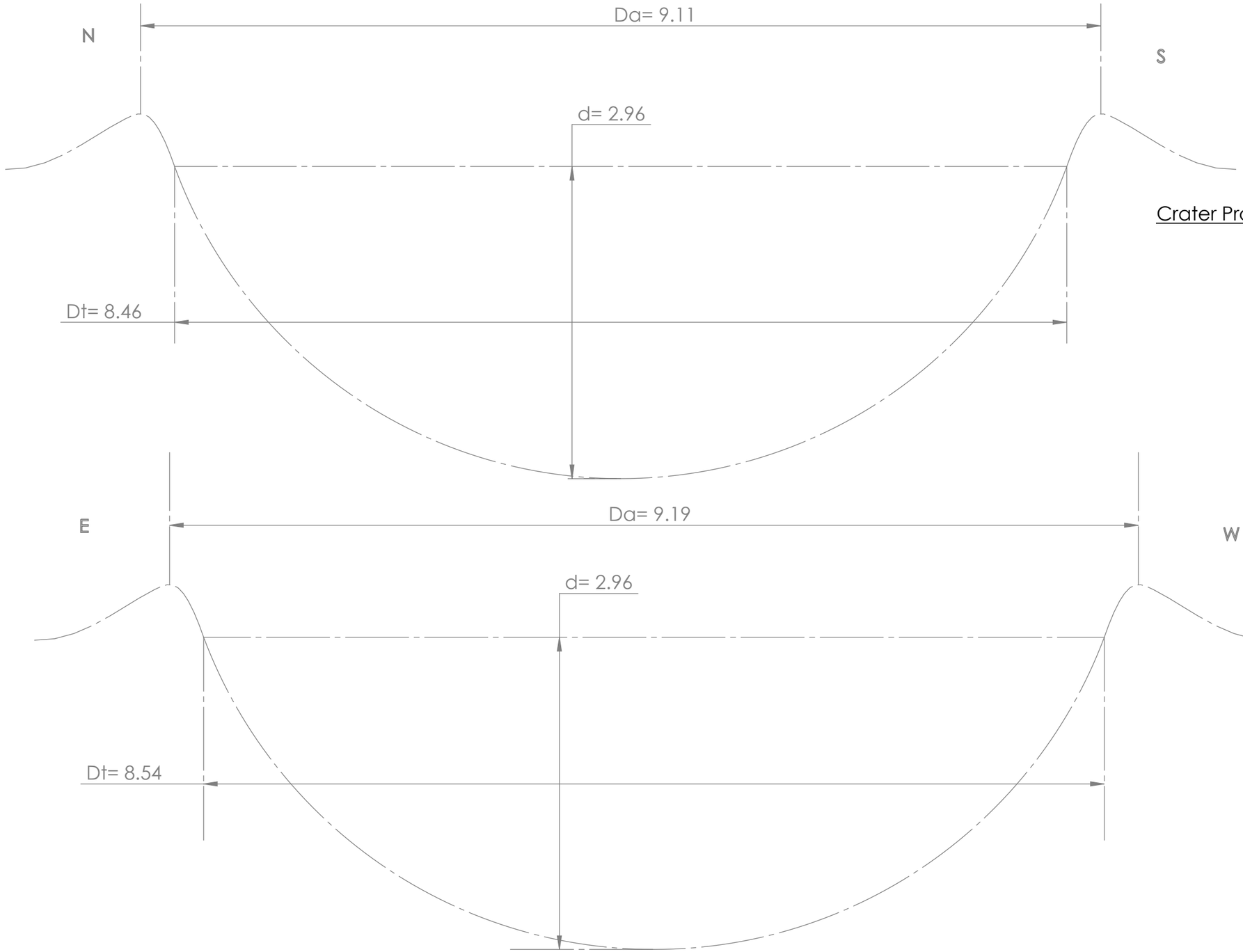

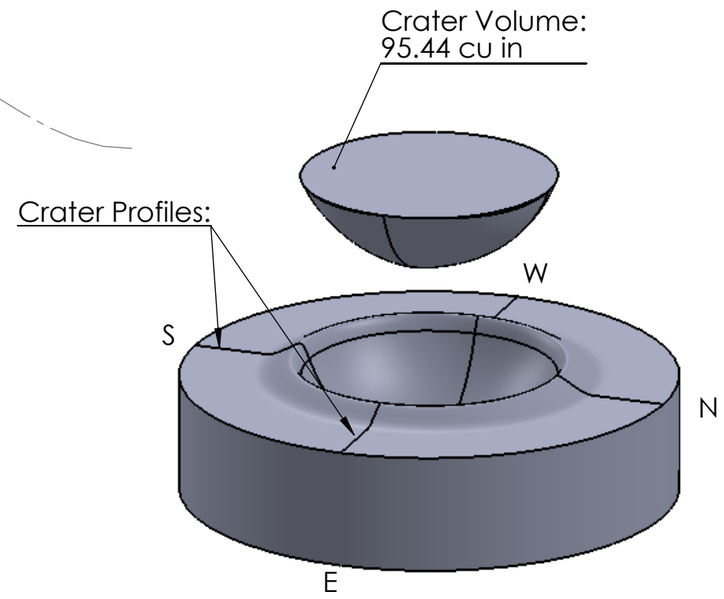

Estimated crater geometry constructed from diameter and depth measurements.

SIZE	FIG. NO.	
B	BLAST B-07	
CHARGE MASS: 50.9 g	BLAST HEIGHT: 1 in	
SCALE: 1"=1"		

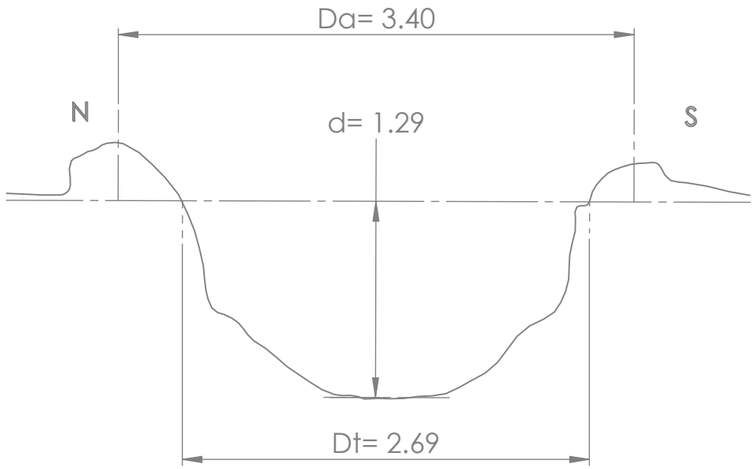

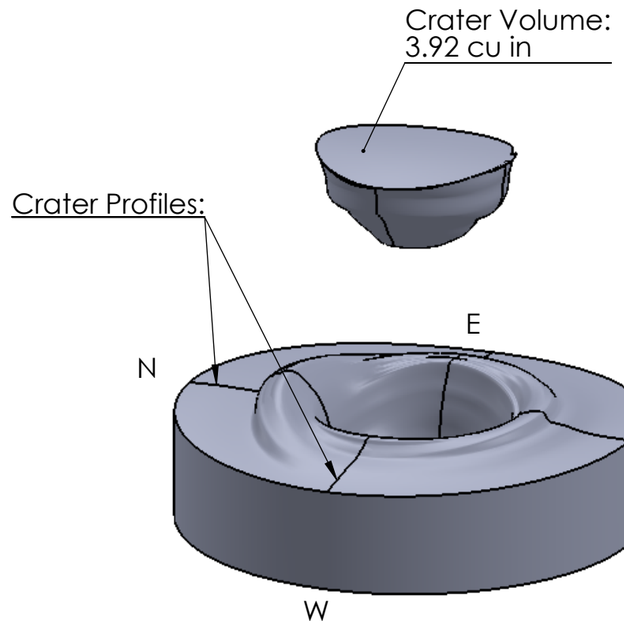

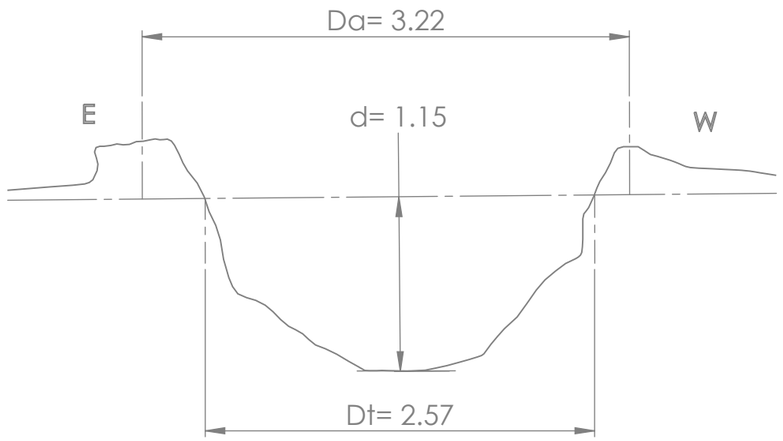

SIZE	FIG. NO.	
B	BLAST C-01	
CHARGE MASS: 0.9 g		BLAST HEIGHT: 1 in
SCALE: 1"=1"		

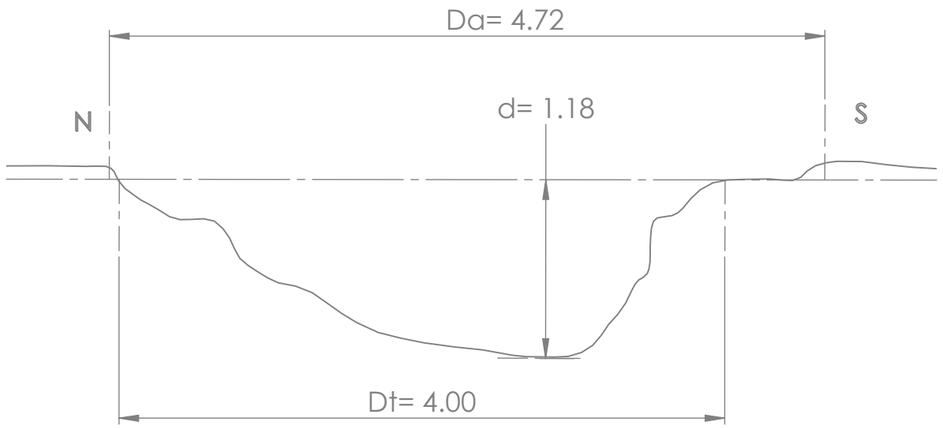

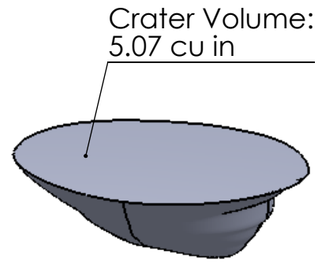

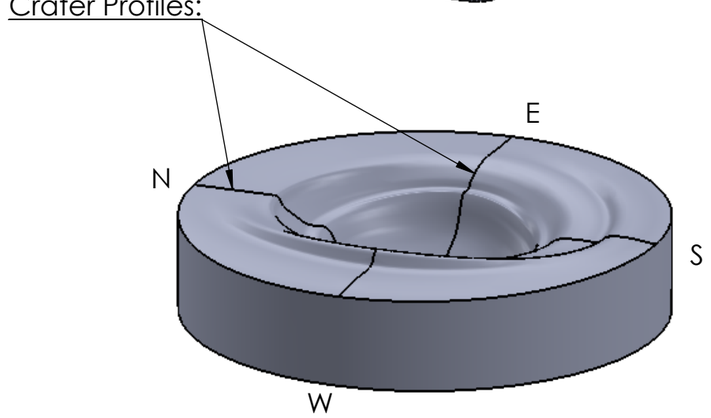

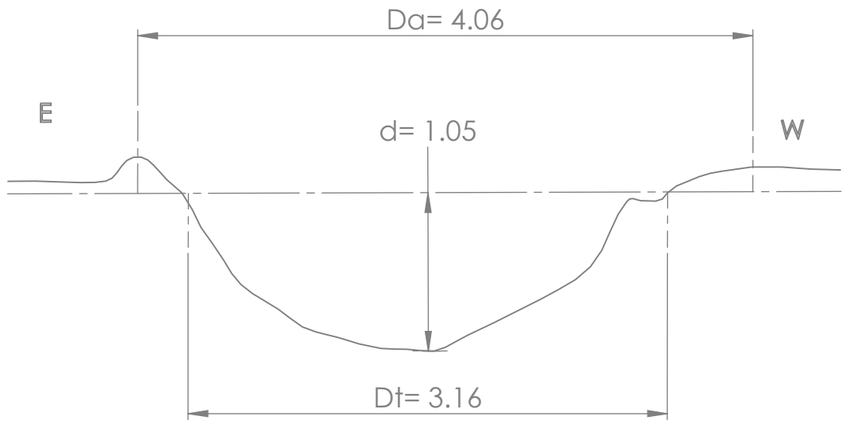

SIZE	FIG. NO.
B	BLAST C-02
CHARGE MASS: 10.9 g	BLAST HEIGHT: 1 in
SCALE: 1"=1"	

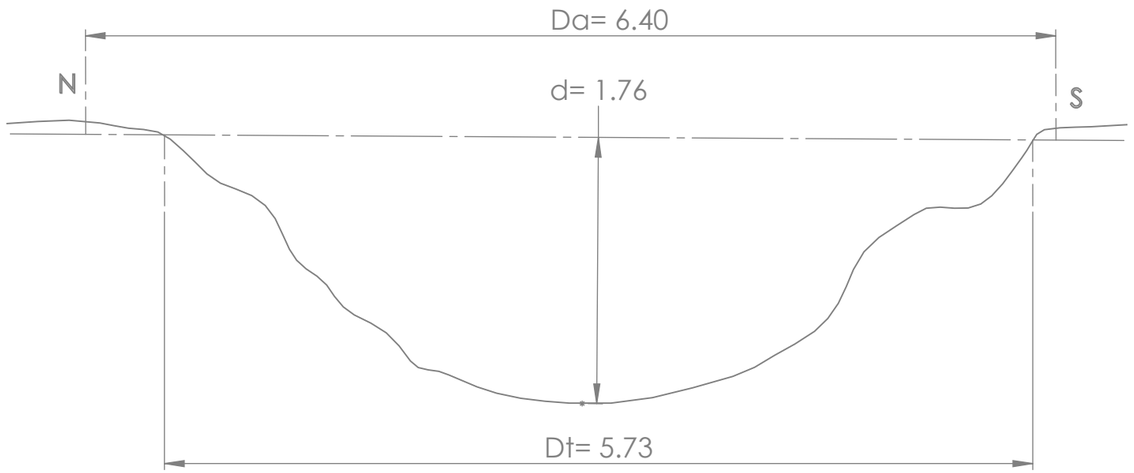

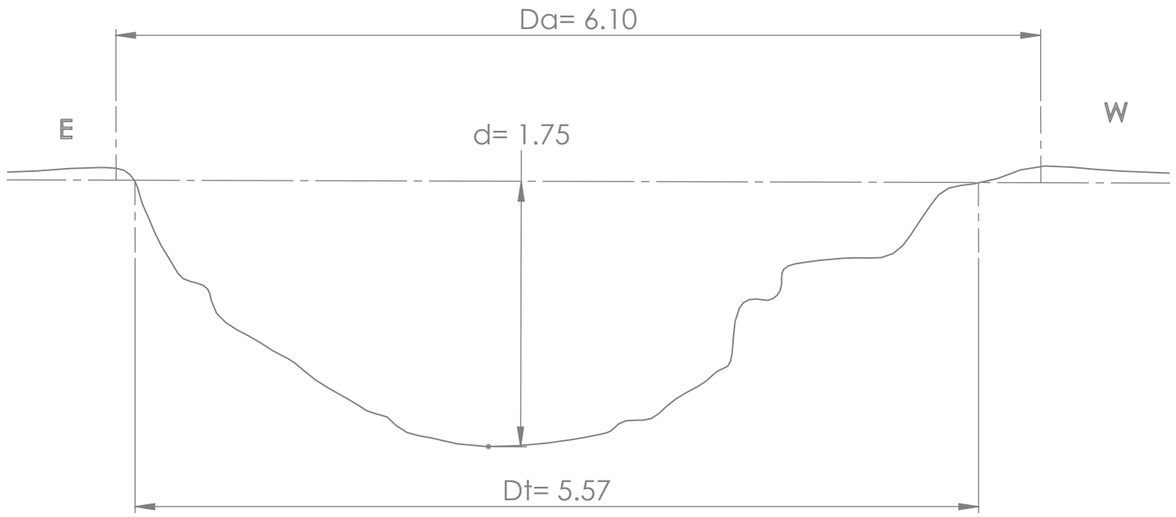

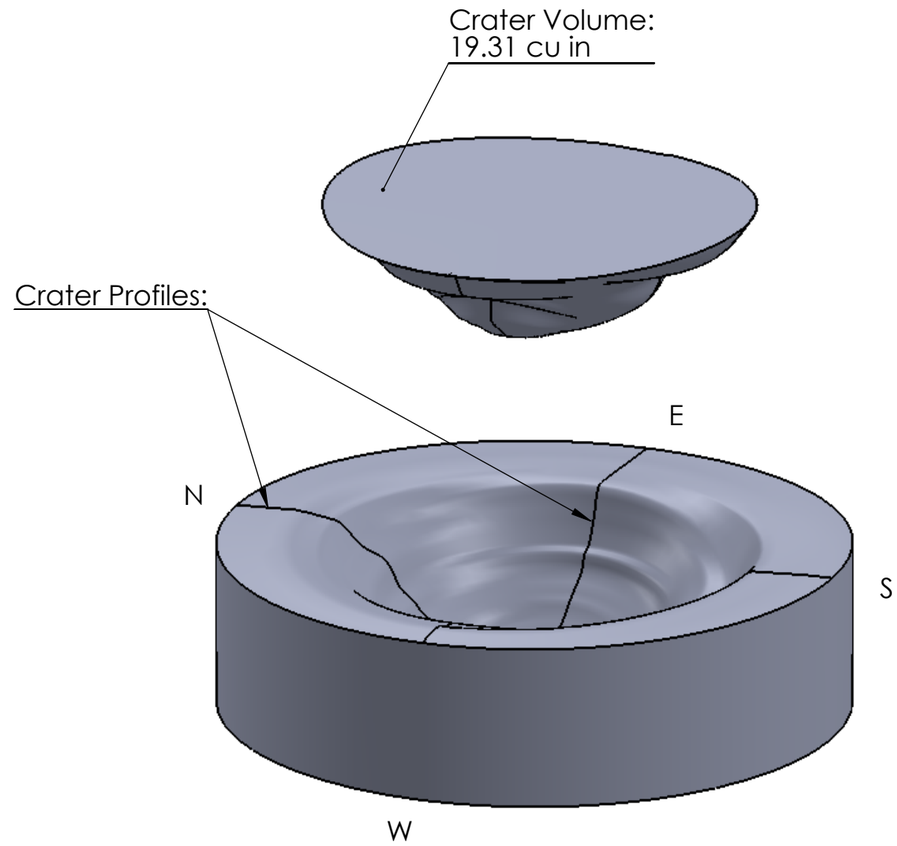

SIZE	FIG. NO.
B	BLAST C-03
CHARGE MASS: 20.9 g	BLAST HEIGHT: 1 in
SCALE: 1"=1"	

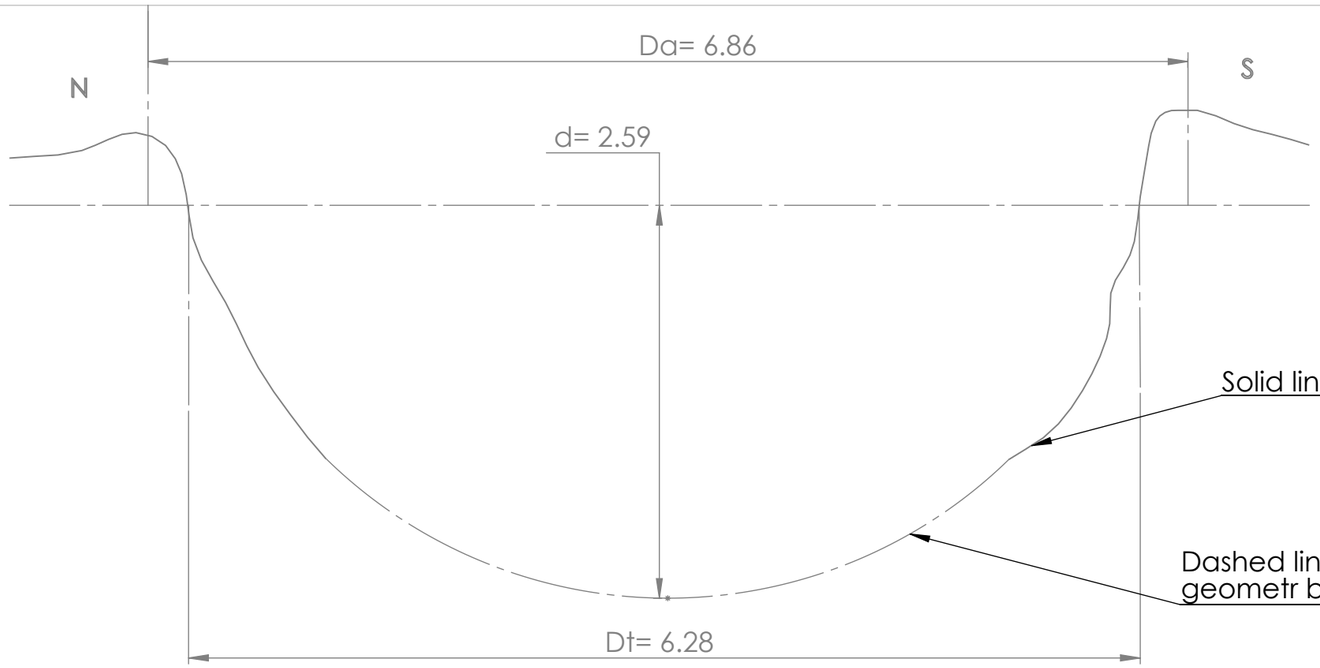

Solid line represents measured crater geometry.

Dashed line represents estimated crater geometr based on depth measurement.

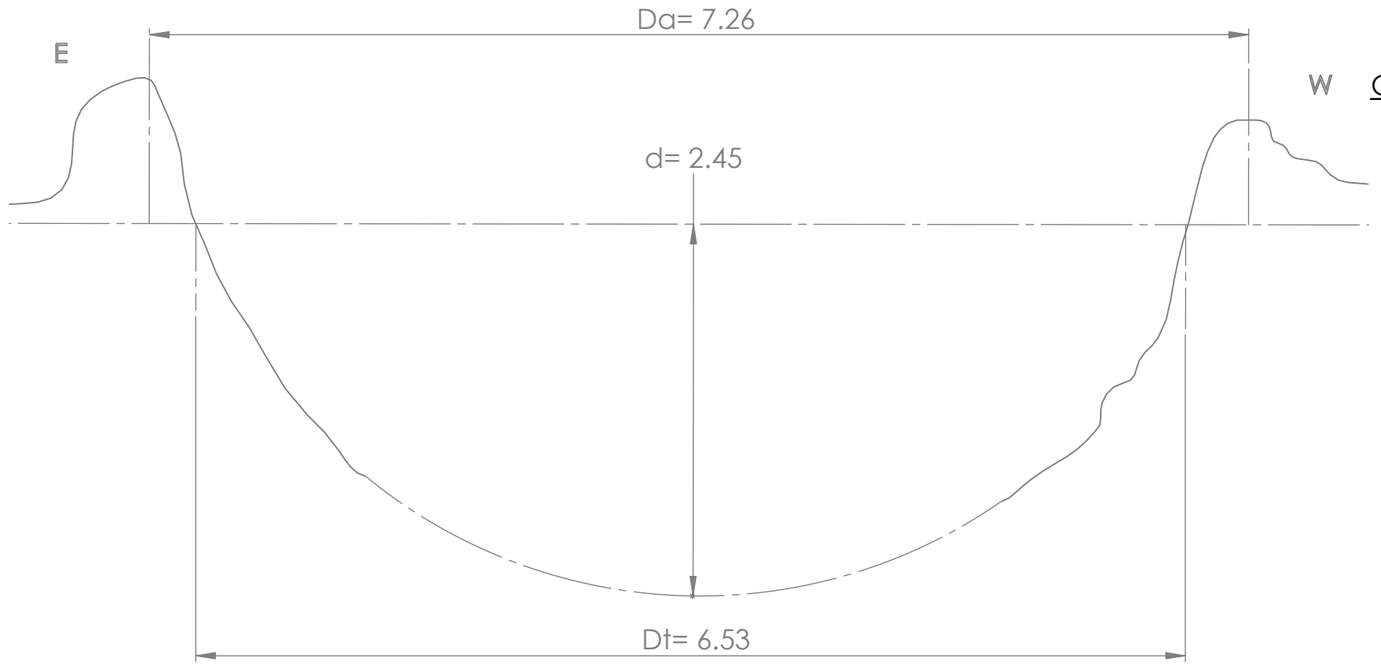

Crater Volume:
48.9 cu in

Crater Profiles:

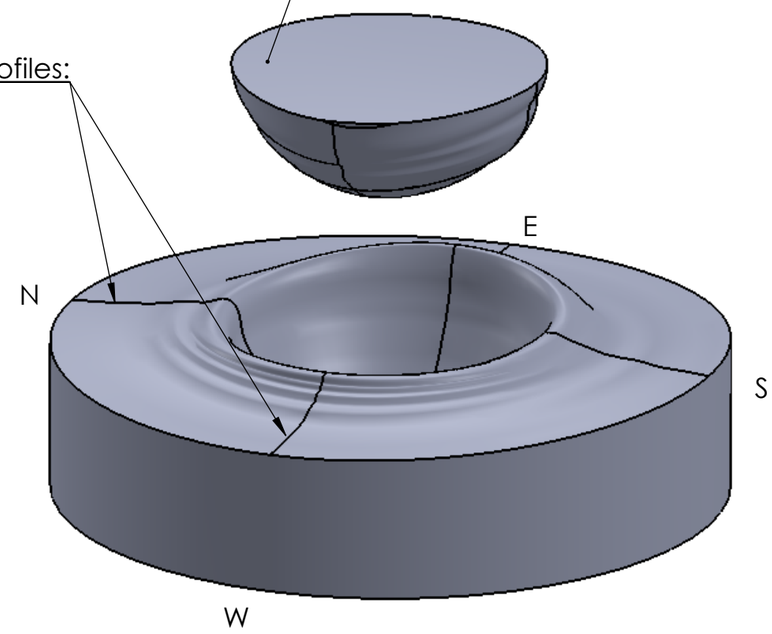

SIZE	FIG. NO.
B	BLAST C-04
CHARGE MASS: 30.9 g	BLAST HEIGHT: 1 in
SCALE: 1"=1"	

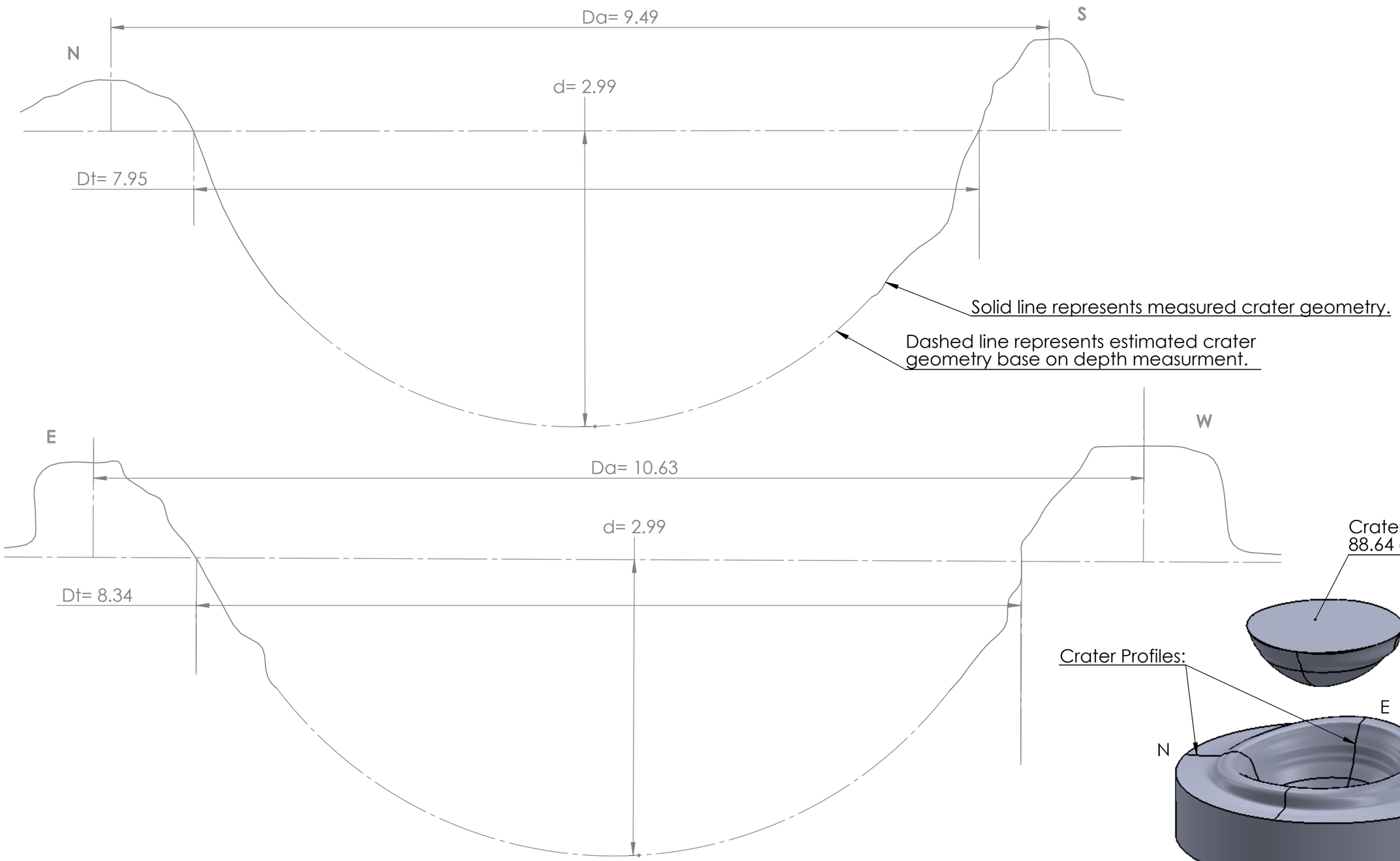

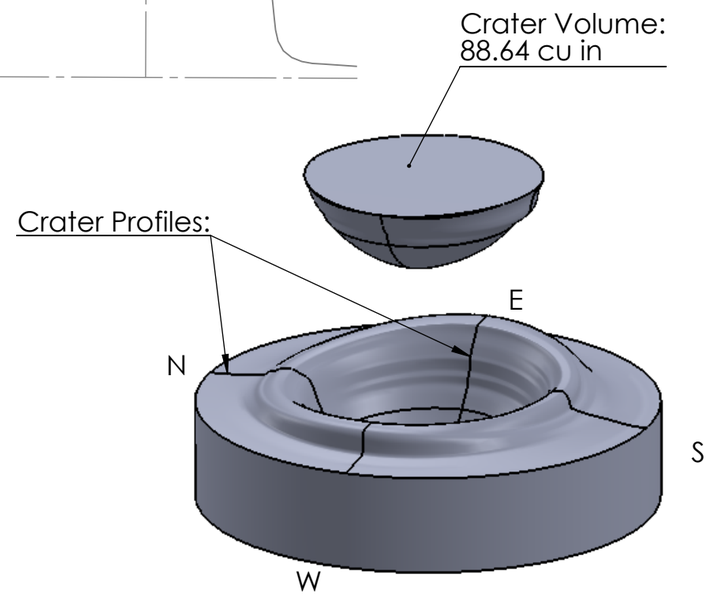

SIZE	FIG. NO.	
B	BLAST C-05	
CHARGE MASS: 40.9 g		BLAST HEIGHT: 1 in
SCALE: 1"=1"		

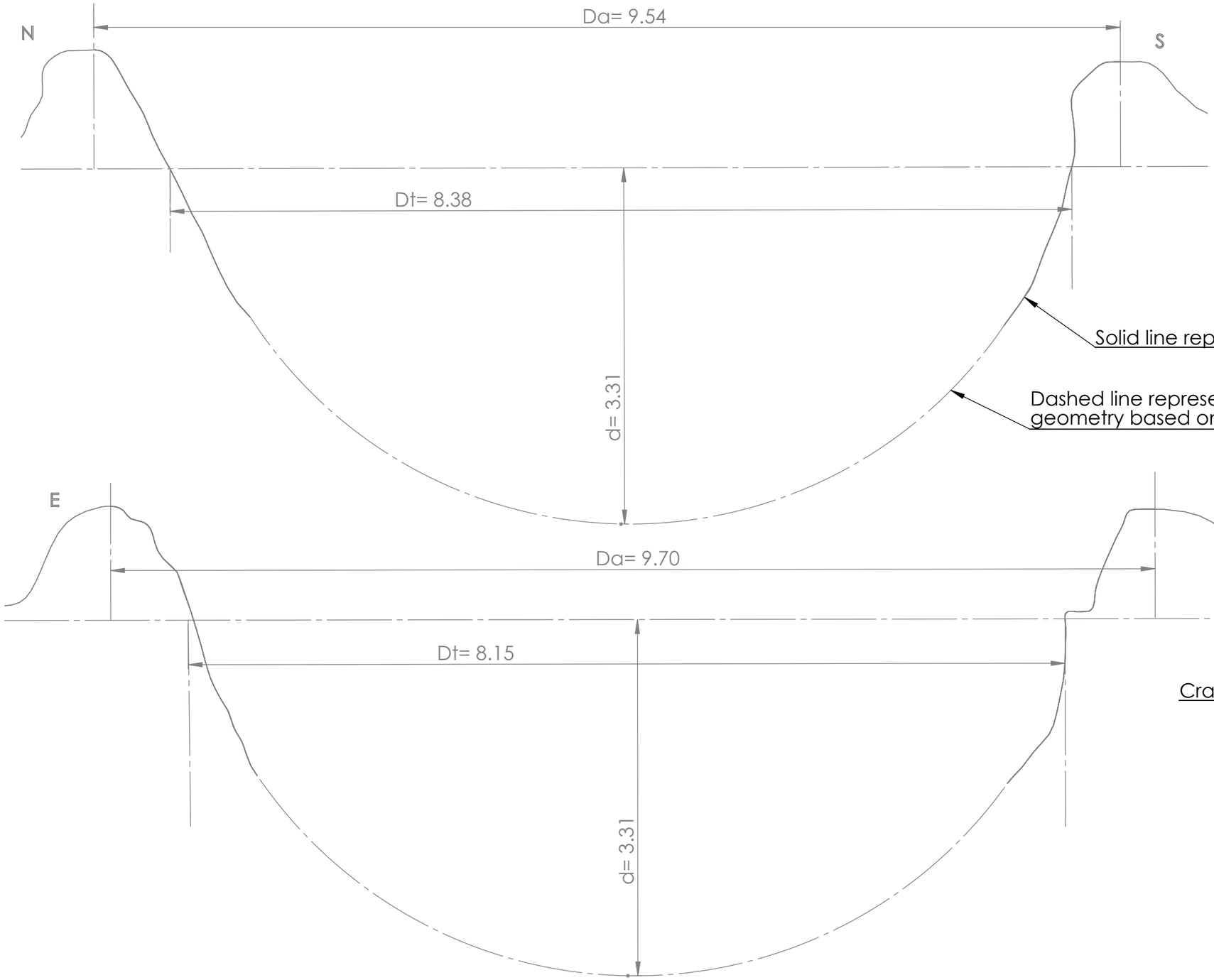

Solid line represents measured crater geometry.

Dashed line represents estimated crater geometry based on depth measurement.

Crater Volume:
105.00 cu in

Crater Profiles

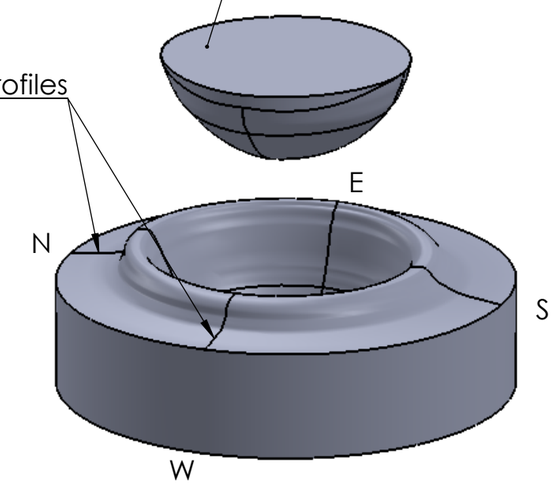

SIZE	FIG. NO.	
B	BLAST C-06	
CHARGE MASS: 60.9 g		BLAST HEIGHT: 1 in
SCALE: 1"=1"		

APPENDIX C GEOPHONE AND AIR SENSOR RECORDS

The time history plots from subsurface geophones and surface air pressure sensors for the small-scale airblast experiments performed in this study are provided in Appendix C. Waveforms that were overly distorted from excessive ground motions were not included in the appendix. The following tables summarize the sensor location and sensor identification number (denoted as *SN* on the time history plots) for each blast.

Table C.1 Identification number and locations of geophone sensors

	Geophone Sensor ID at Depth Below Ground Surface				
Blast ID	0.2 m	0.5 m	0.8 m	1.1 m	1.2 m
All Blasts	*2408*	*1793*	*3048*	*3046*	*4040*

Table C.2 Identification number and locations of airblast sensors

Blast ID	Test Time	Test Date	Air Sensor ID (Distance from Blast)		
A-1	10:56	17 March	*2408* (1.9 m)	*3046* (3.8 m)	*4040* (5.8 m)
A-2	17:05	23 Feb	*5069* (2.7 m)	*5039* (5.3 m)	*785* (7.8 m)
A-3	11:27	17 March	*3048* (1.9 m)	*3046* (3.8 m)	*4040* (5.8 m)
A-4	17:46	23 Feb	*5069* (2.7 m)	*5039* (5.3 m)	*785* (7.8 m)
A-5	16:00				
A-6	17:16				
A-7	16:20				
A-8	17:59				
A-9	16:33				
A-10	17:27				
A-11	16:47				
B-1	10:40	24 Feb	*5069* (1.6 m)	*785* (3.7 m)	*5039* (6.7 m)
B-2	11:05				
B-3	11:25				
B-4	11:51				
B-5	12:10				
B-6	13:19				
B-7	12:30				
C-1	09:01	17 March	*3048* (1.9 m)	*3046* (3.8 m)	*4040* (5.8 m)
C-2	10:36	17 March	*2408* (1.9 m)	*3046* (3.8 m)	*4040* (5.8 m)
C-3	11:09	17 March	*3048* (1.9 m)	*3046* (3.8 m)	*4040* (5.8 m)
C-4	11:48				
C-5	13:07				
C-6	12:34				

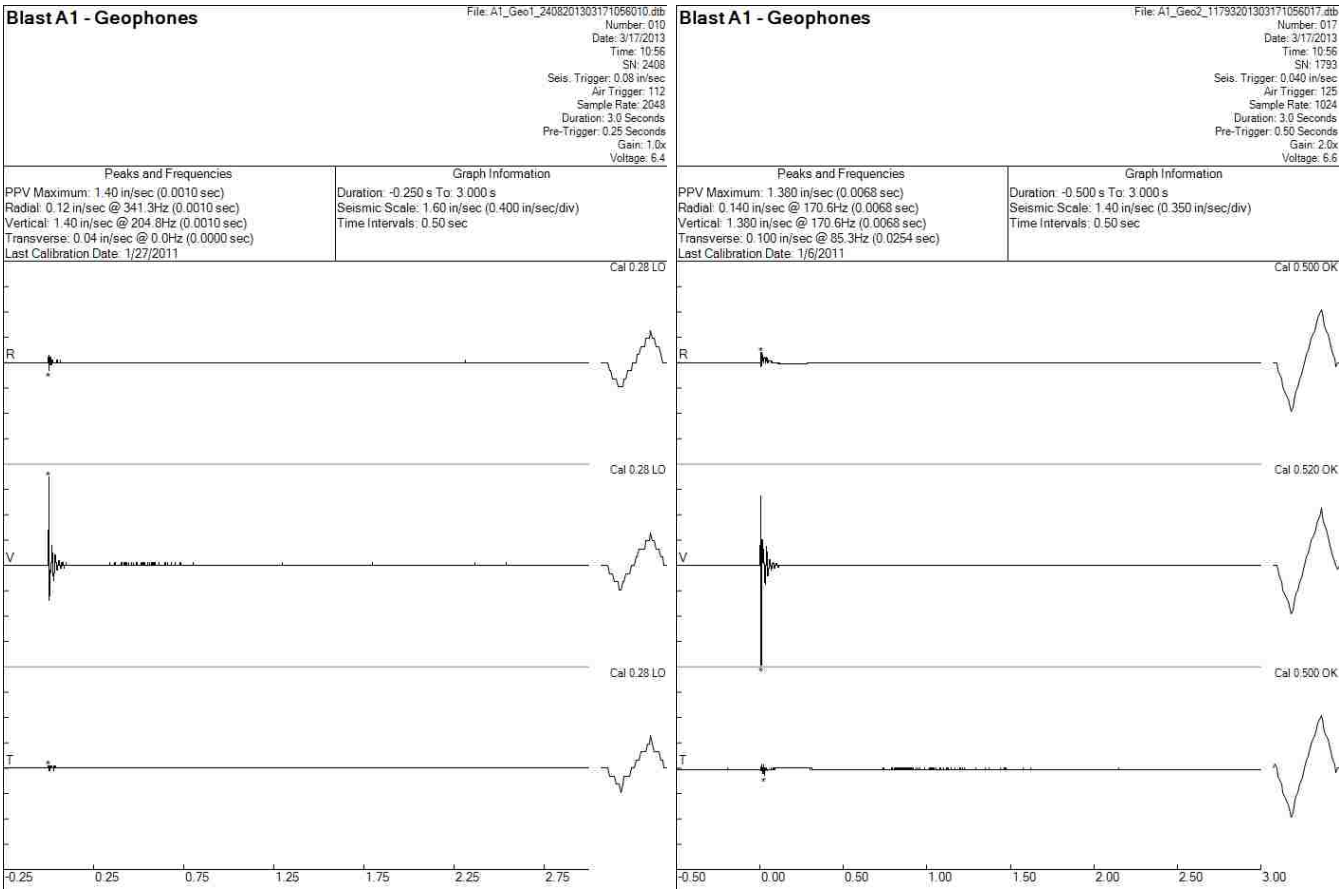

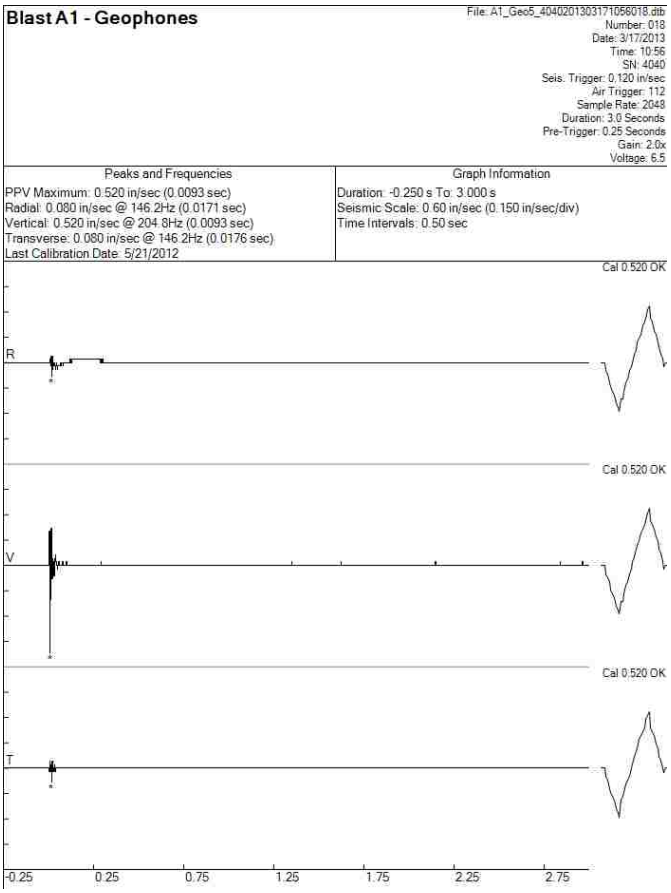

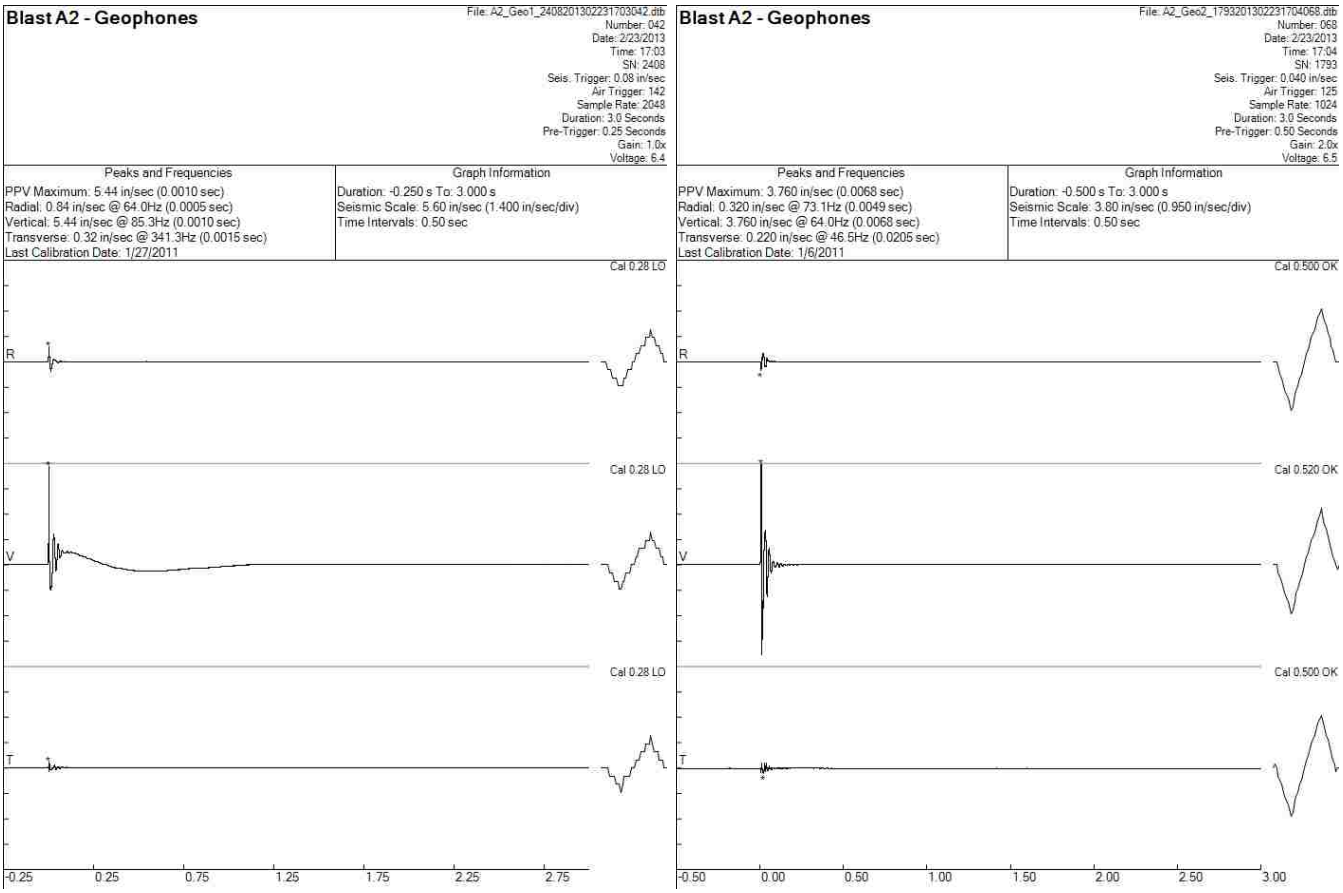

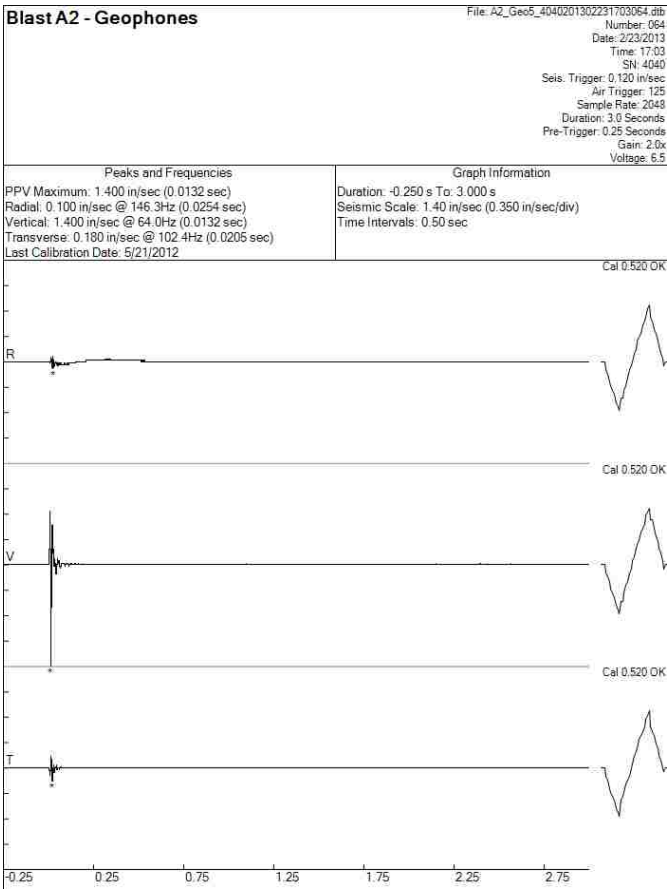

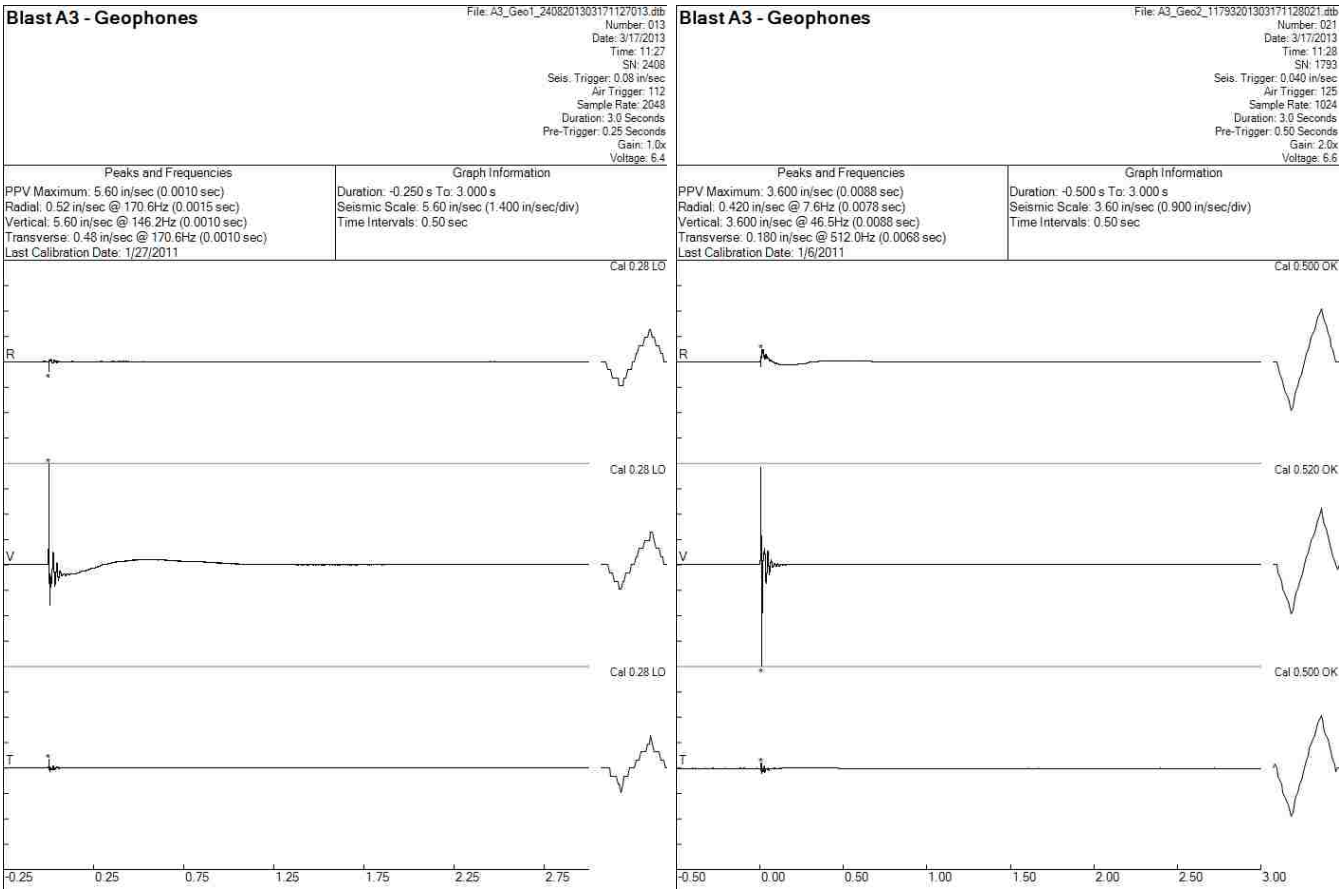

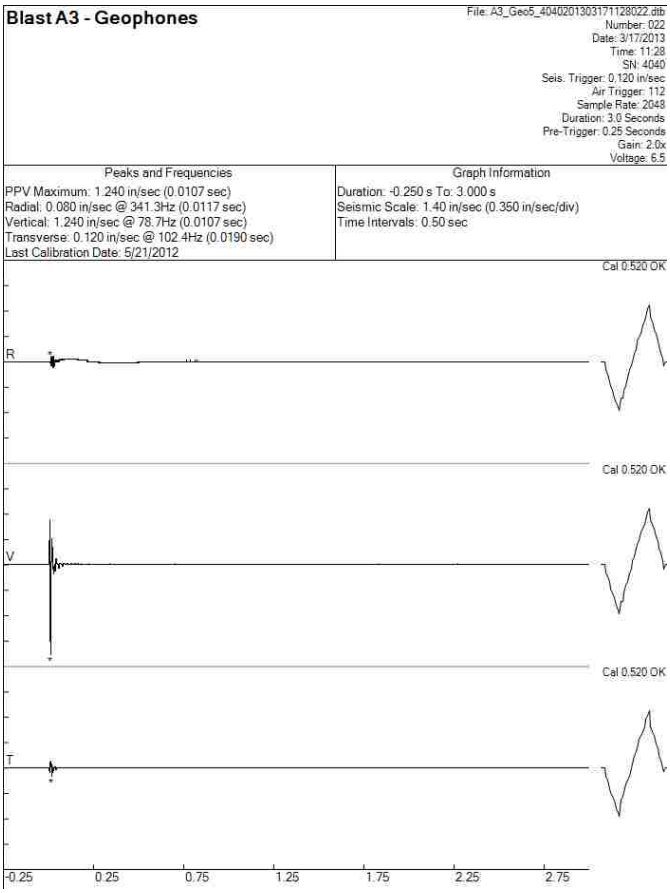

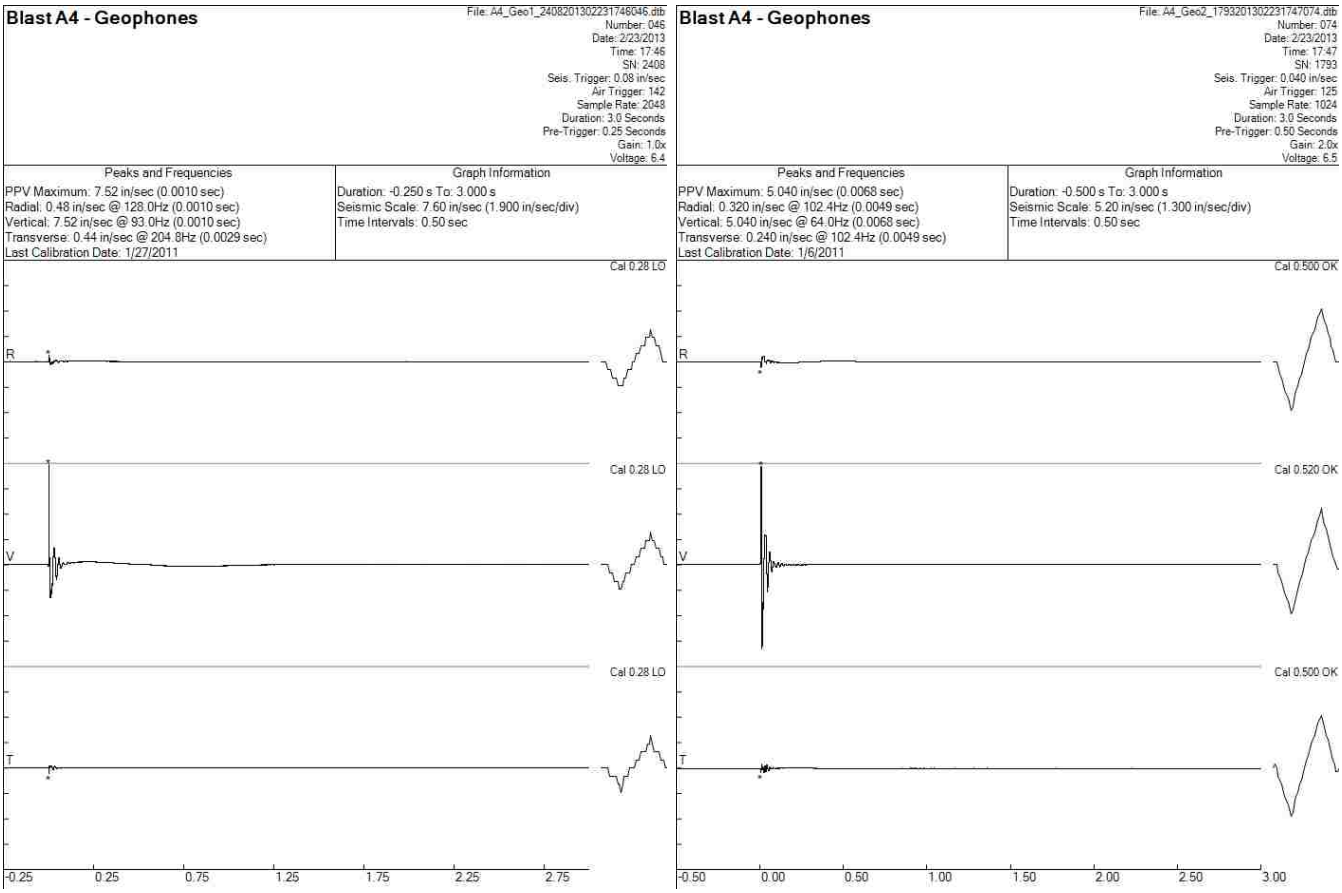

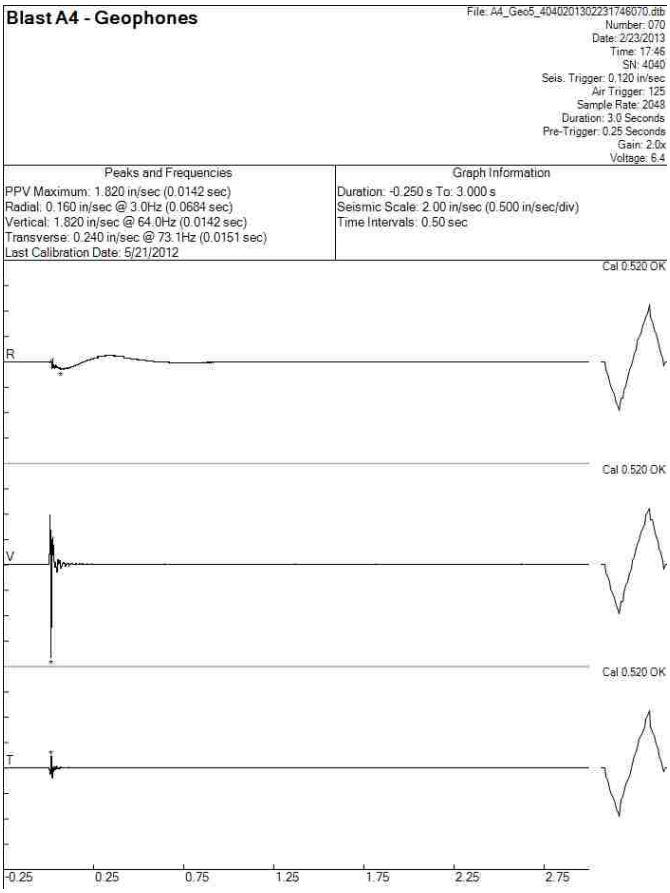

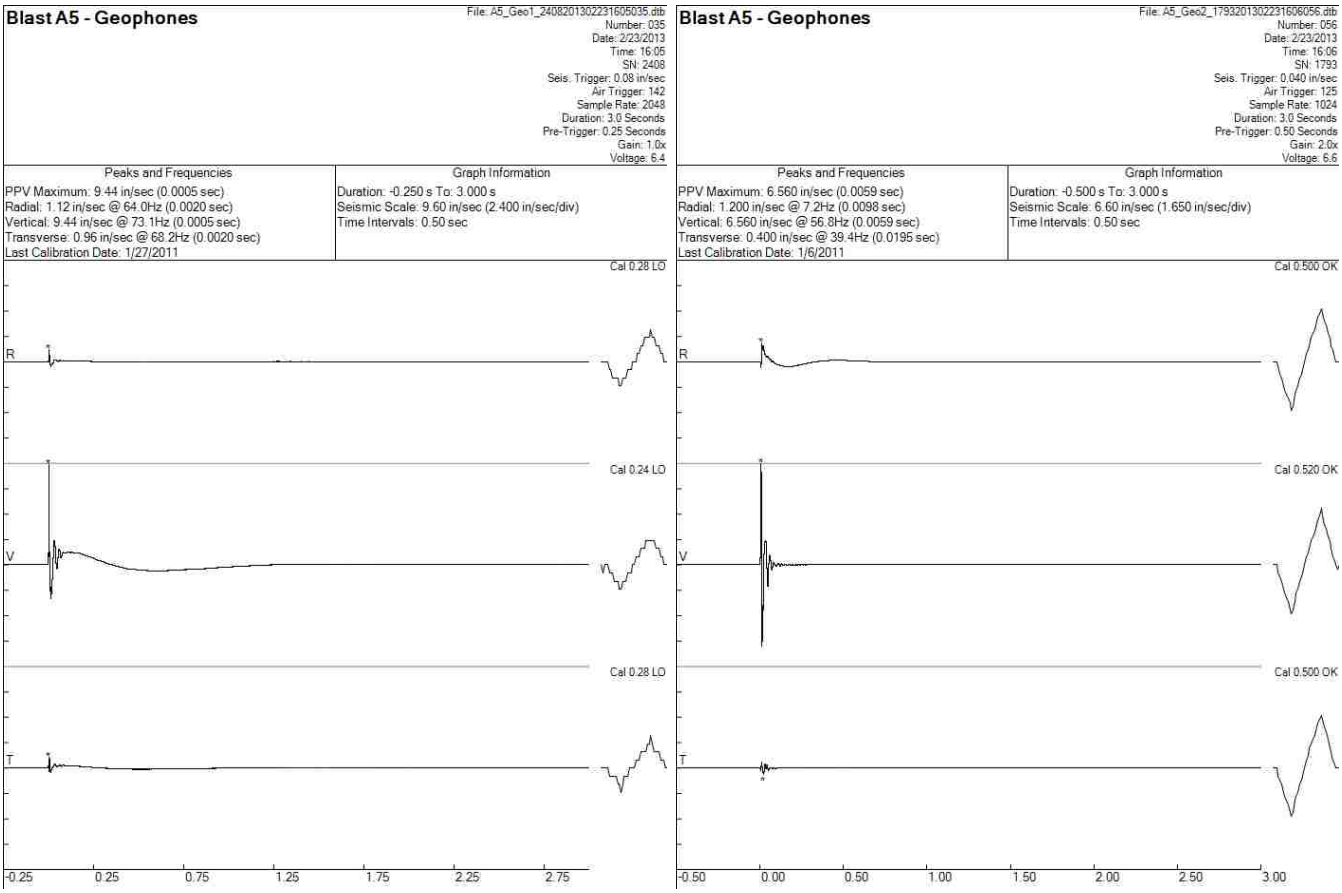

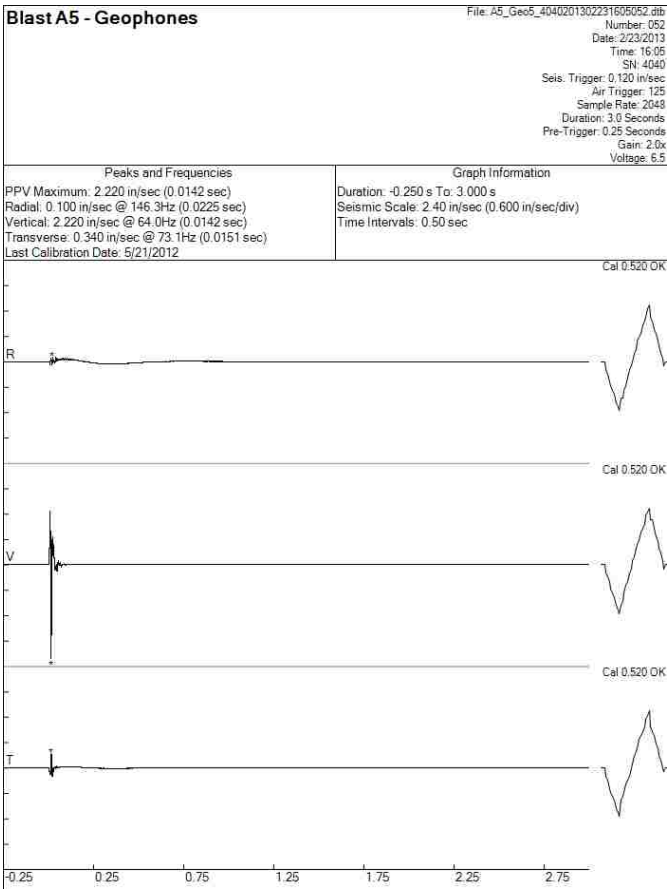

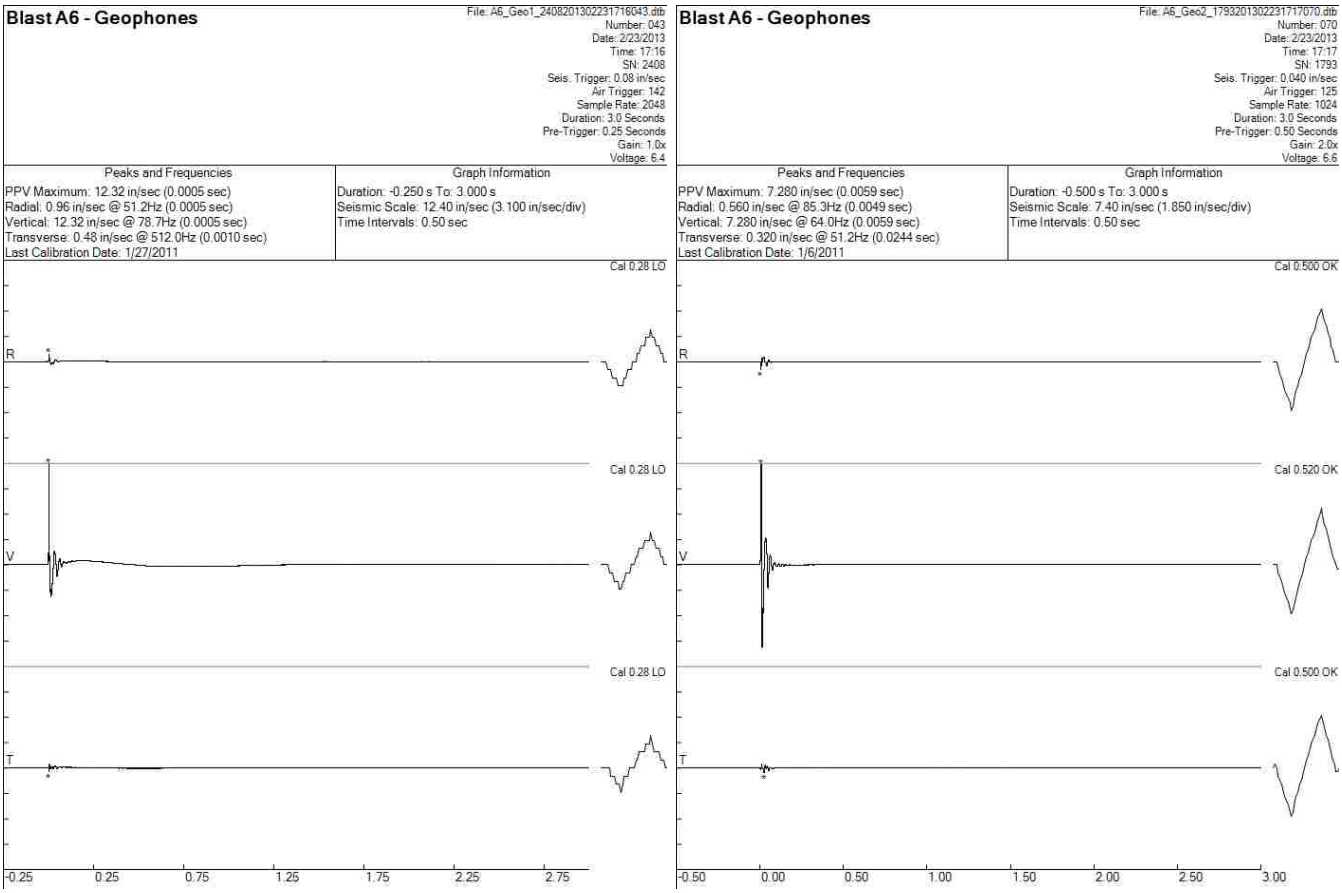

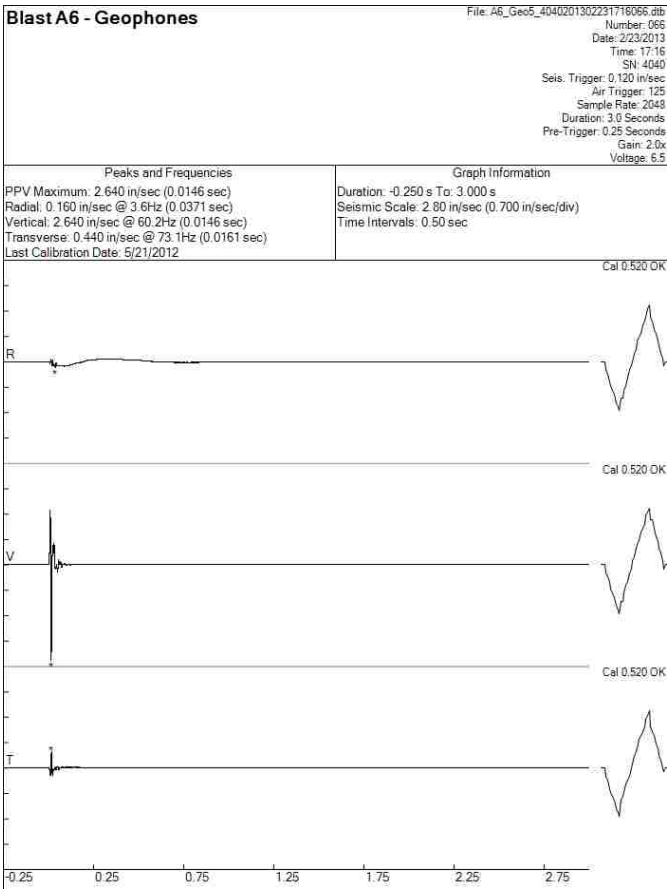

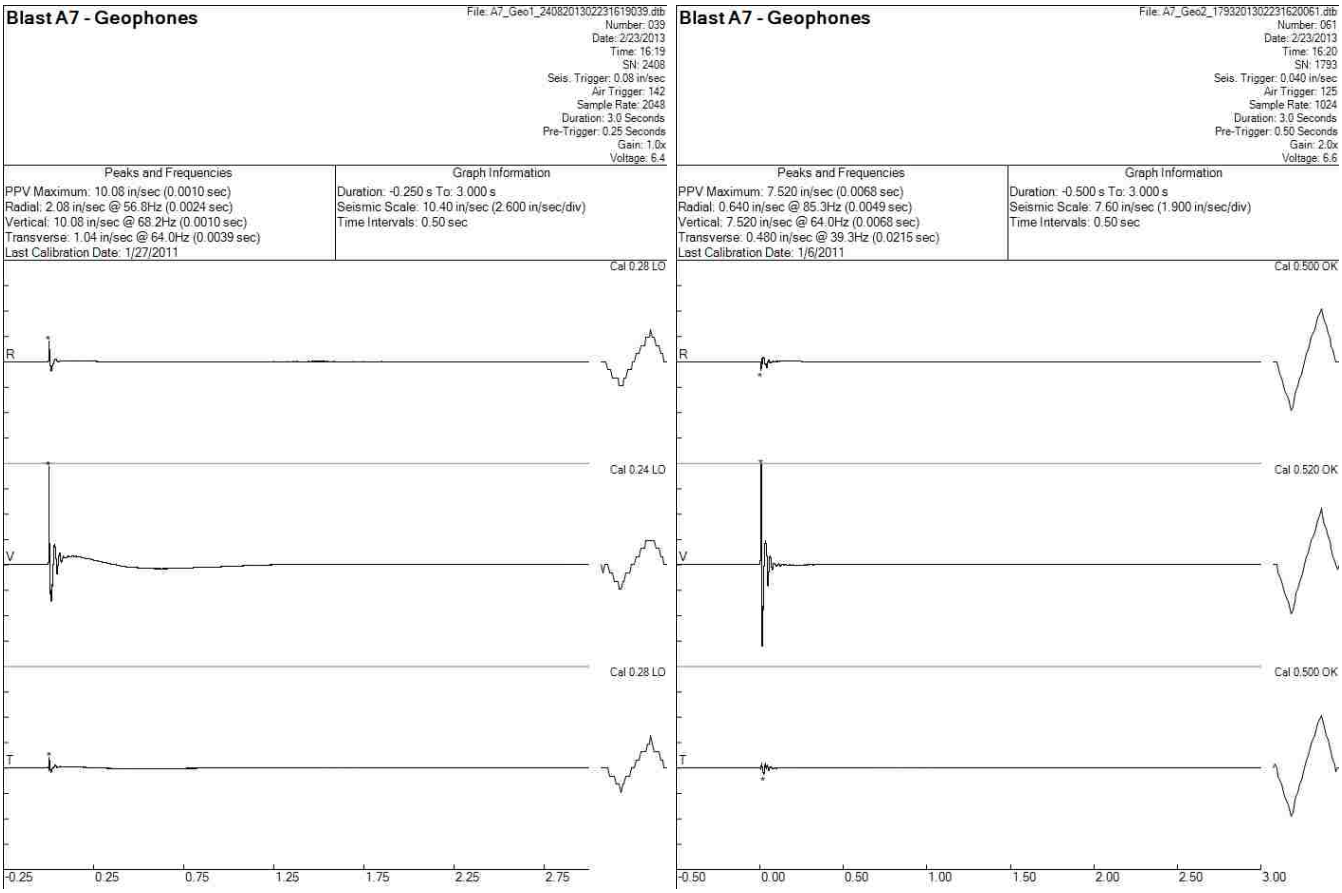

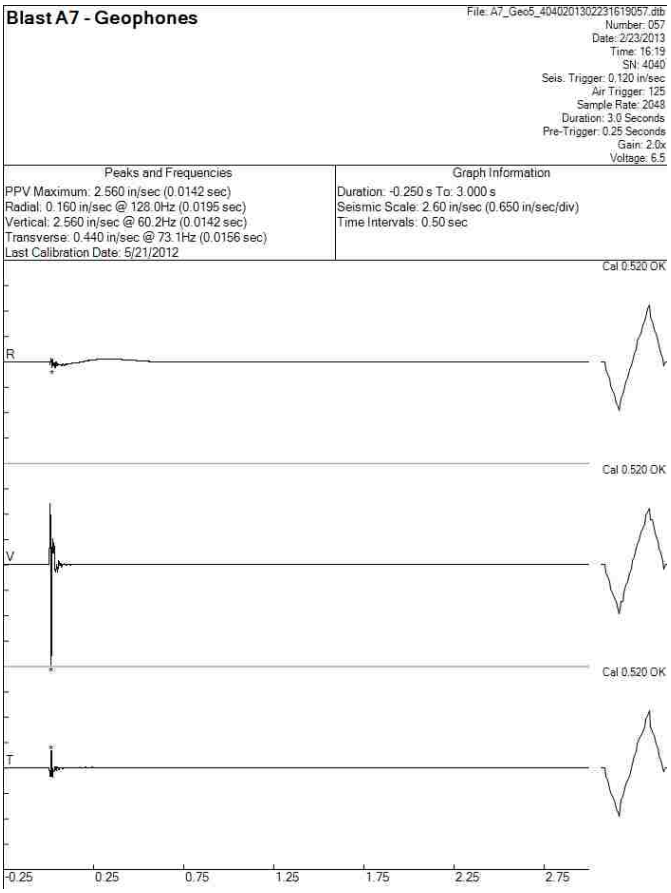

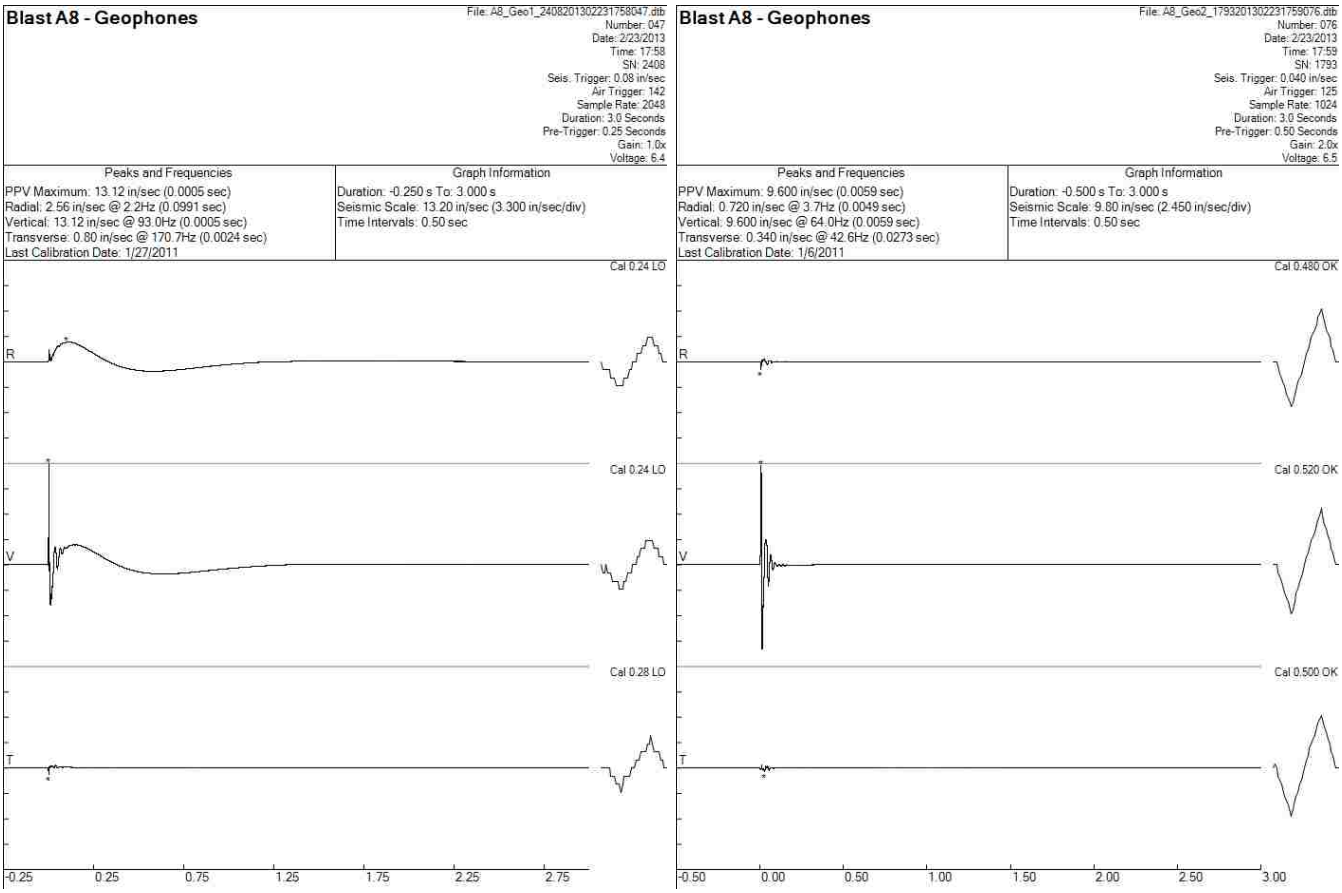

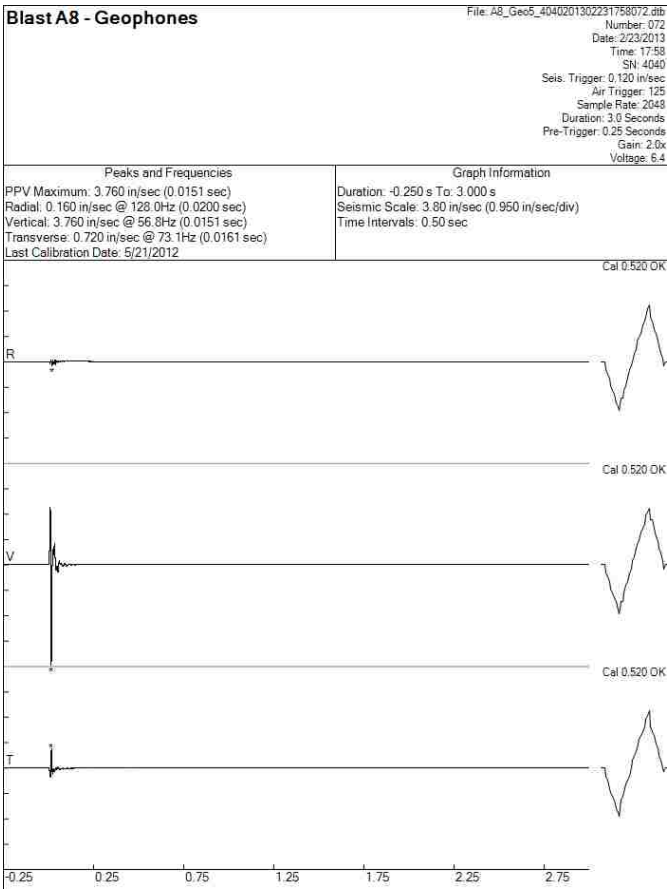

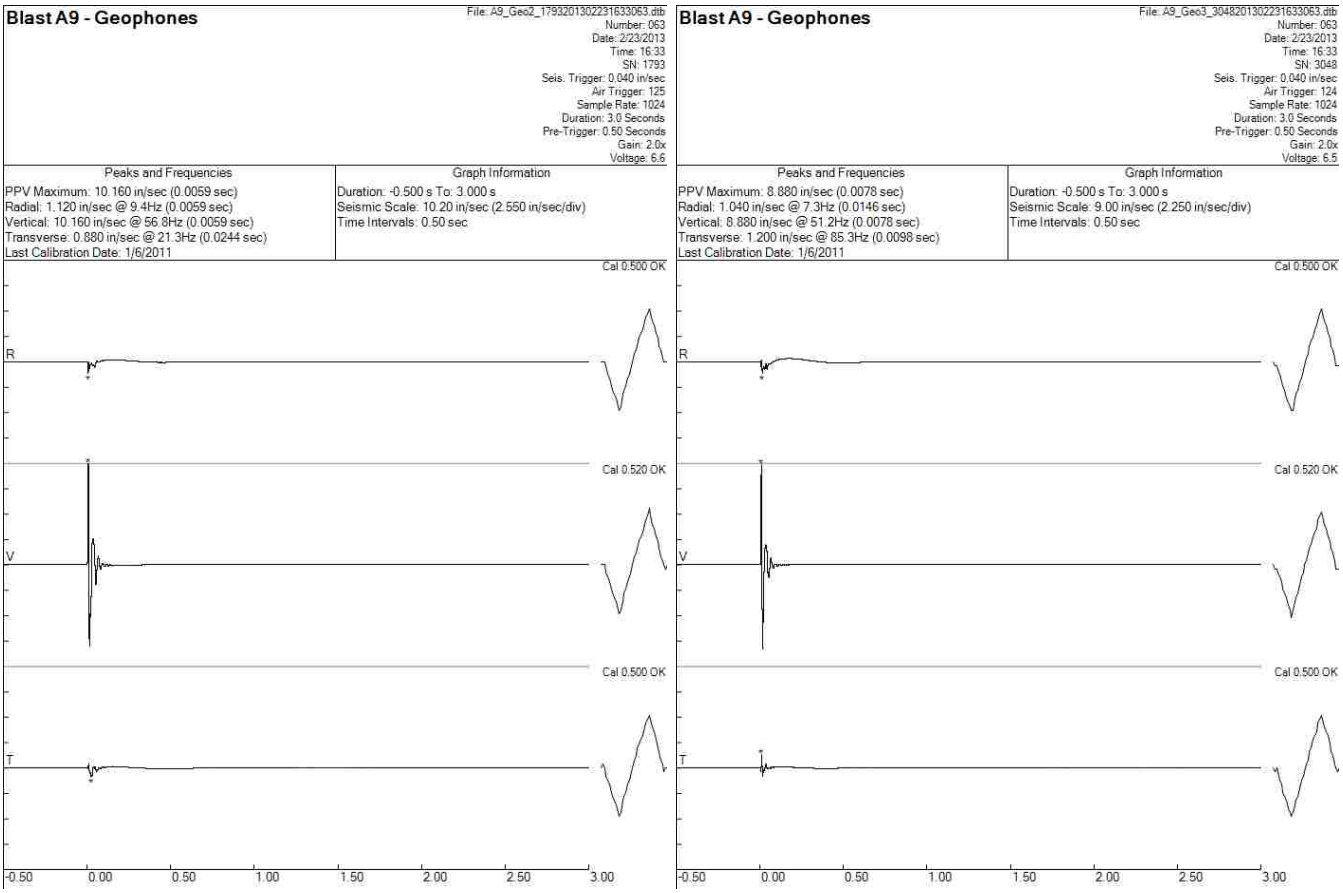

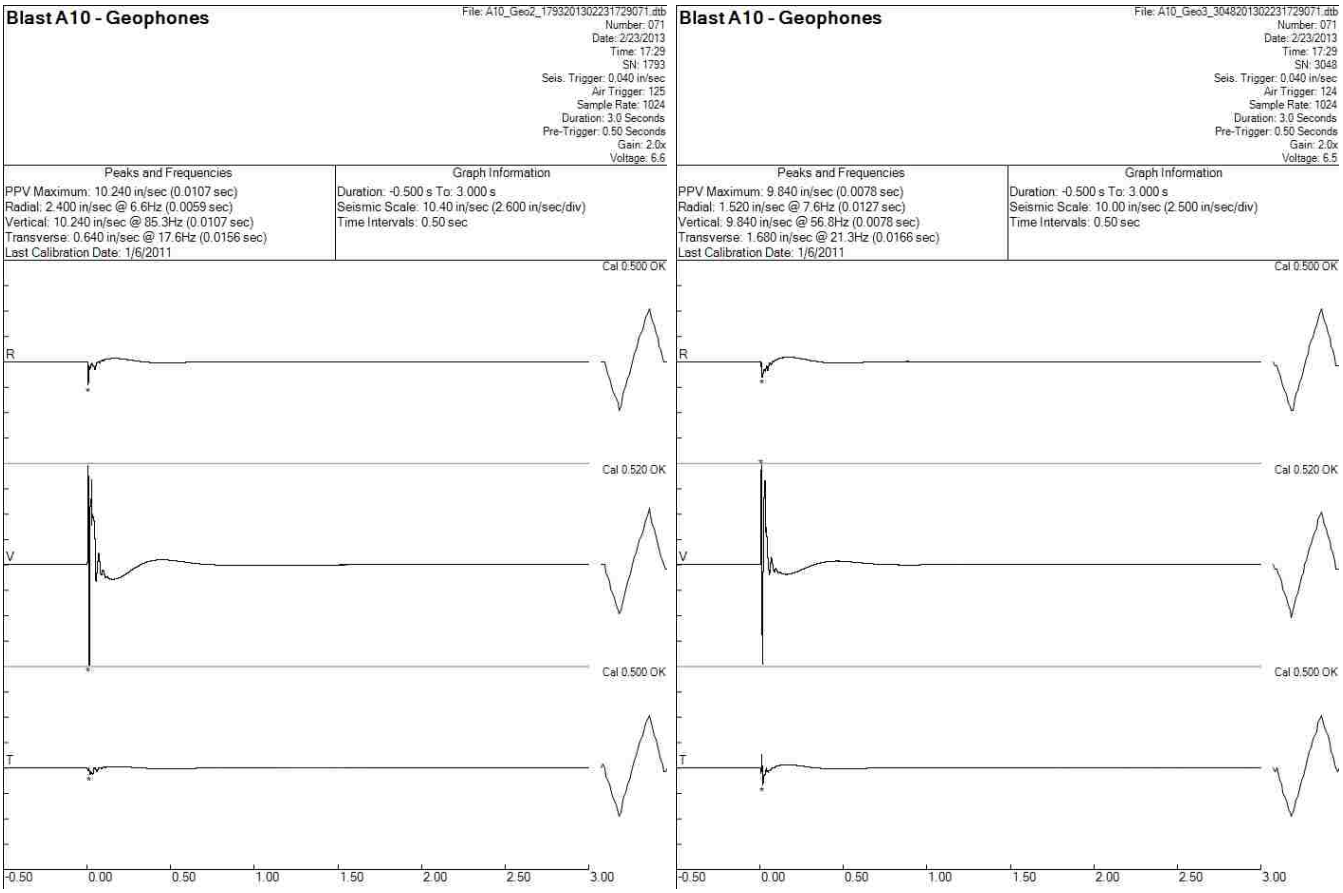

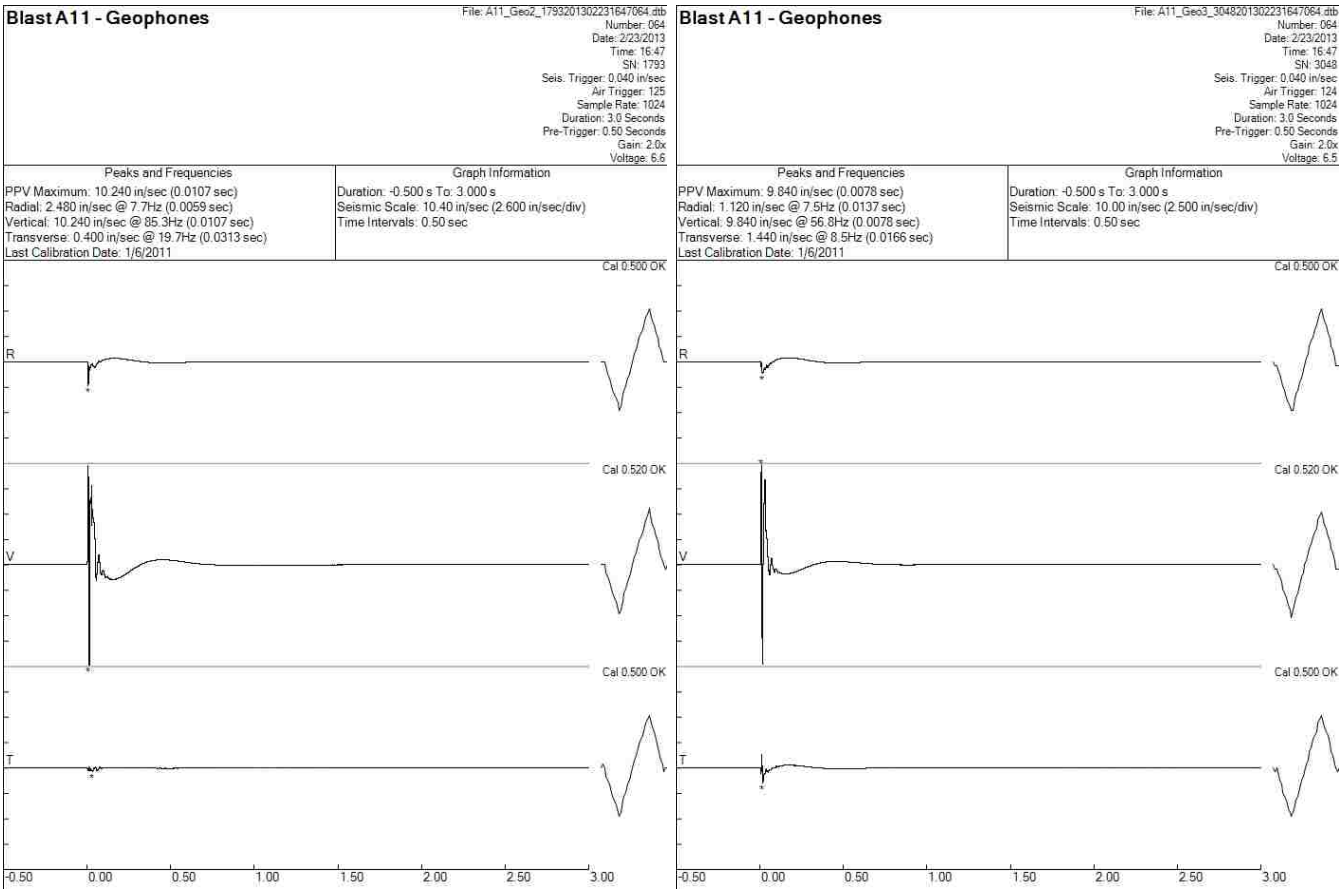

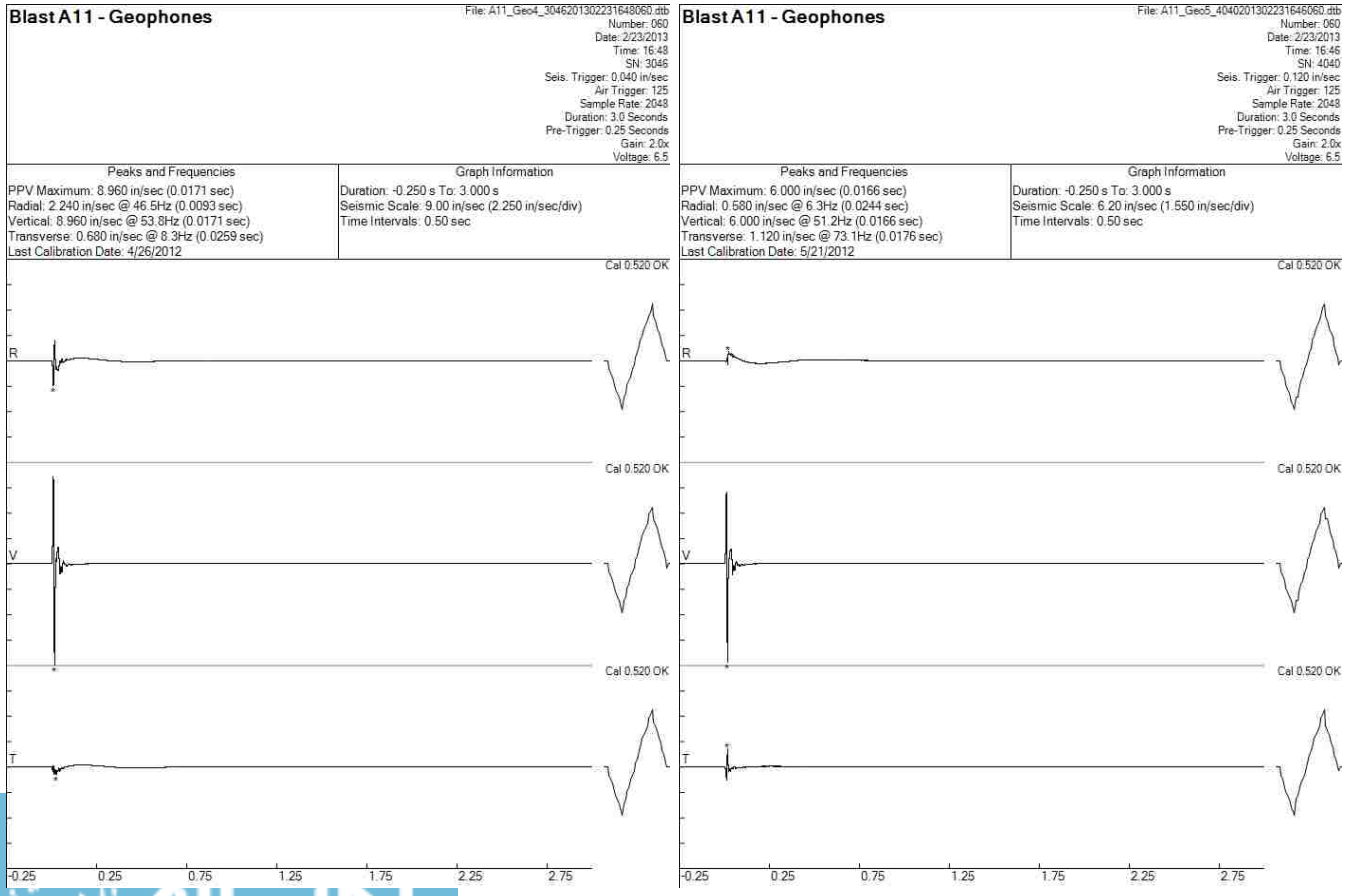

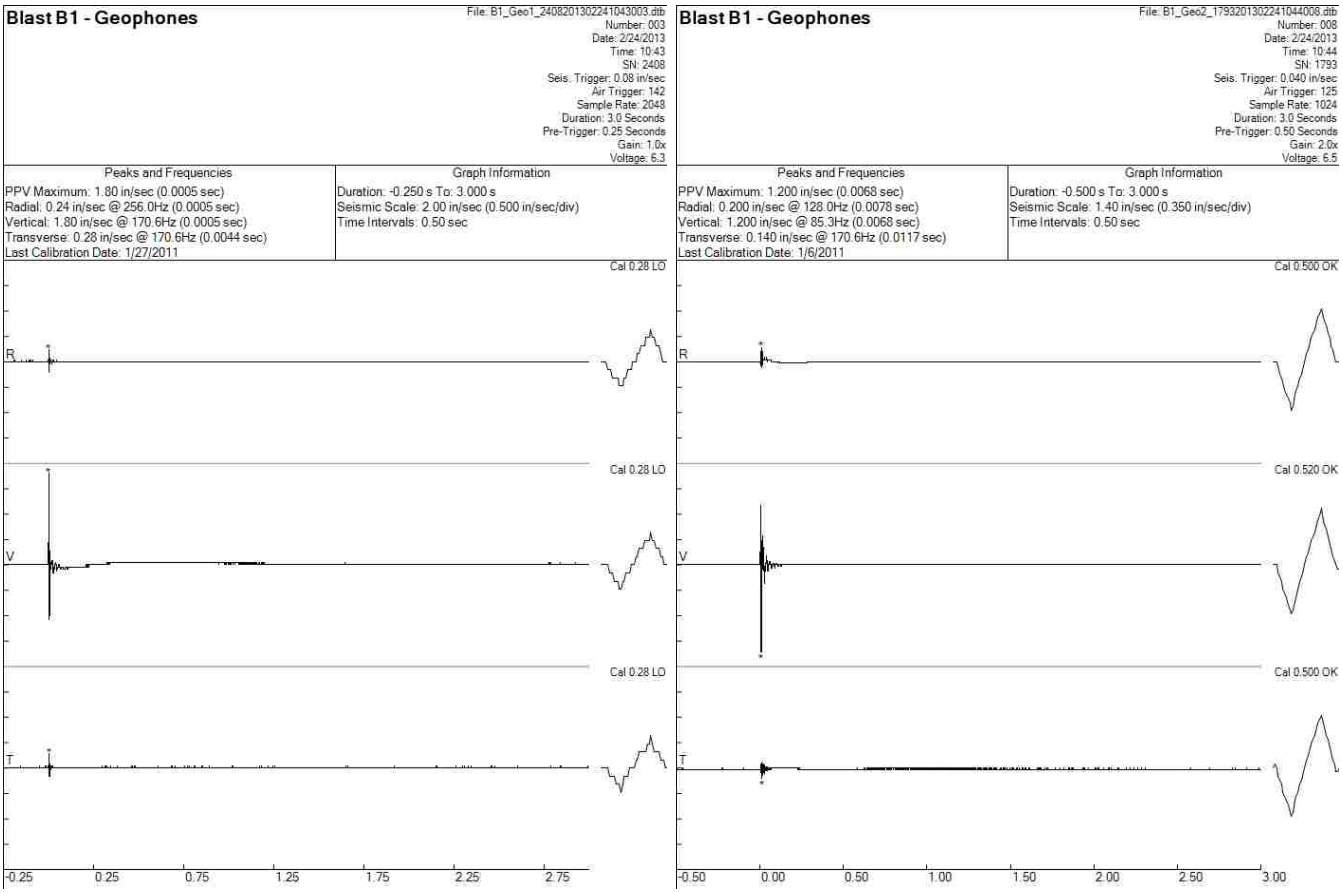

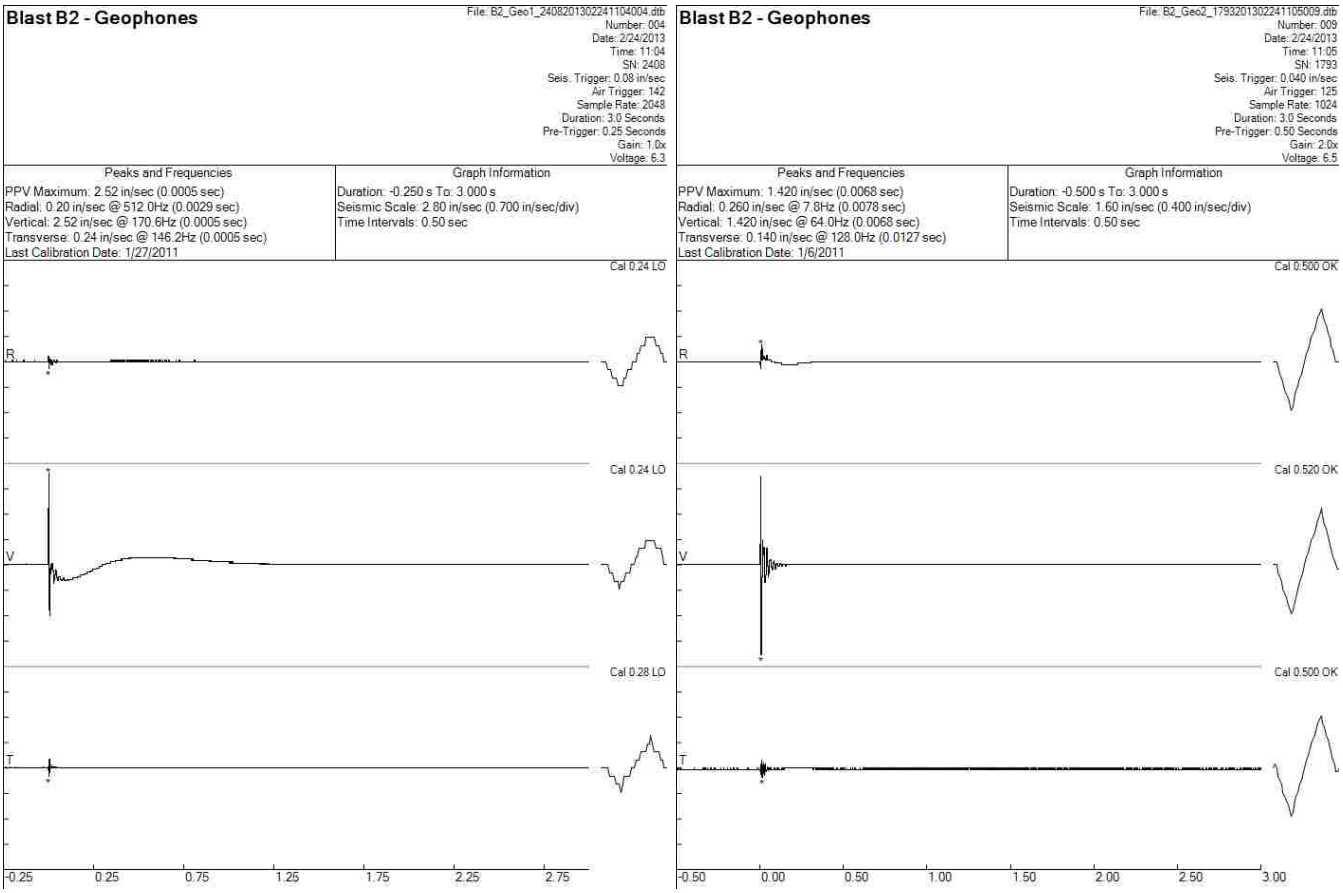

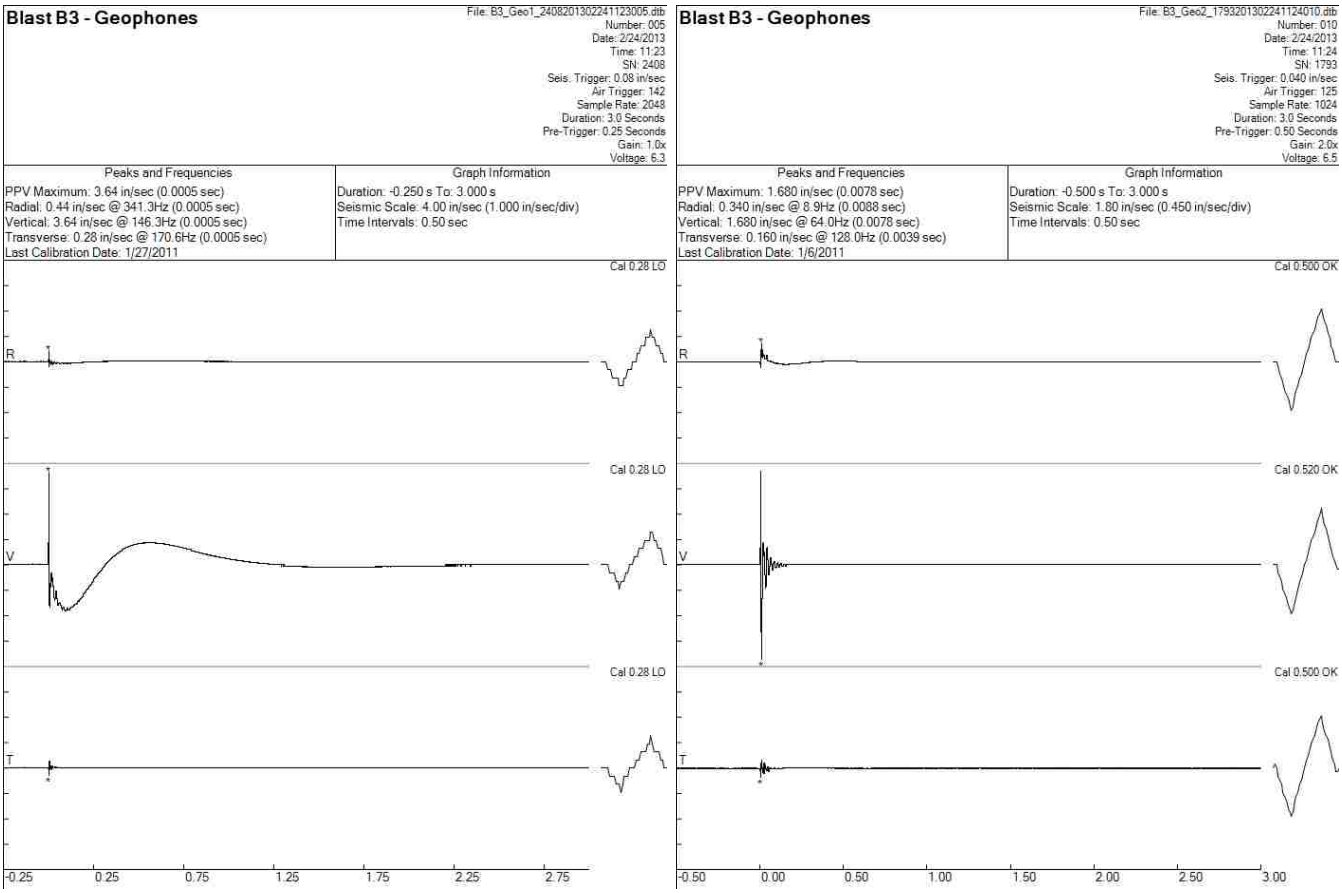

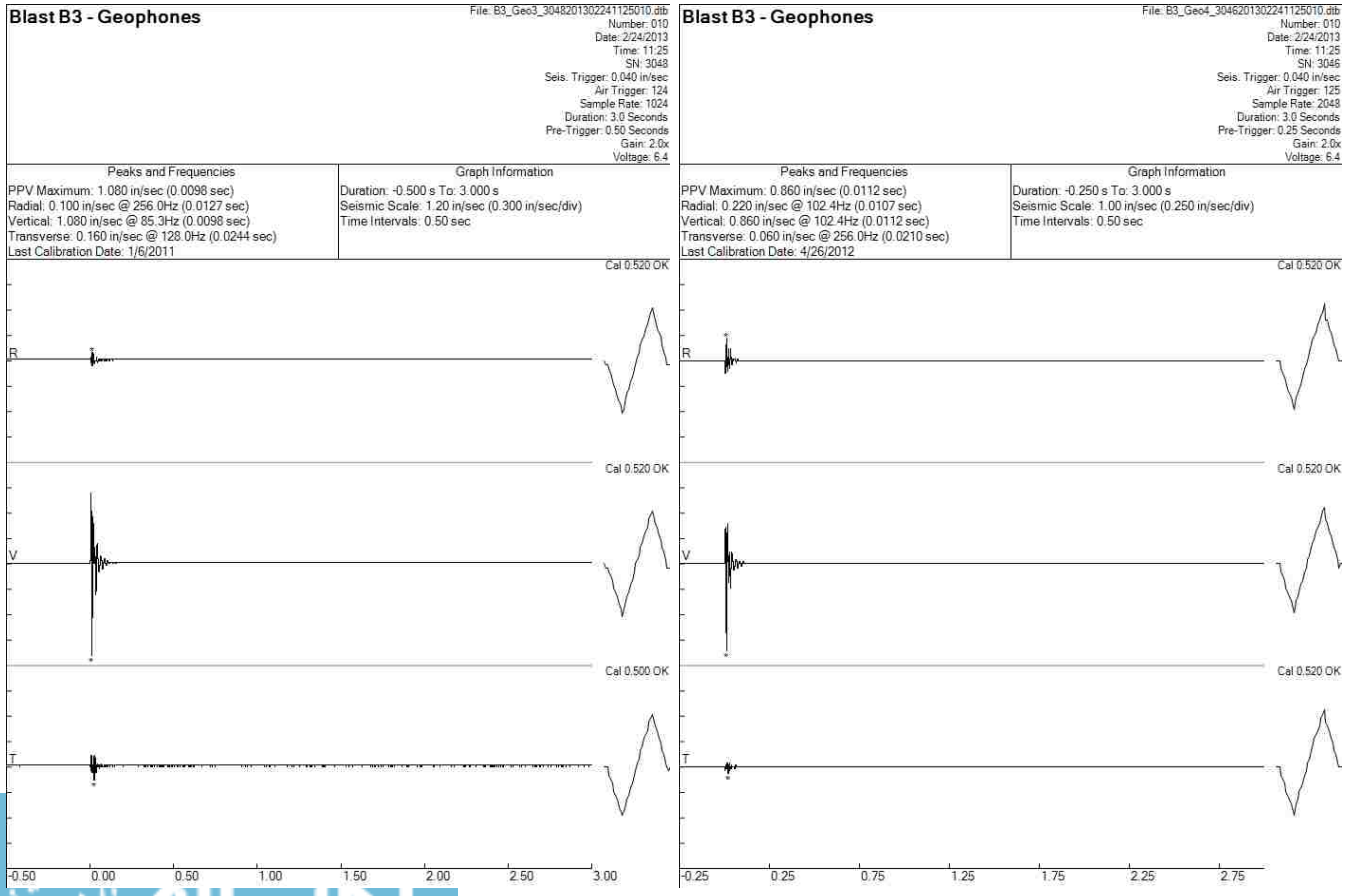

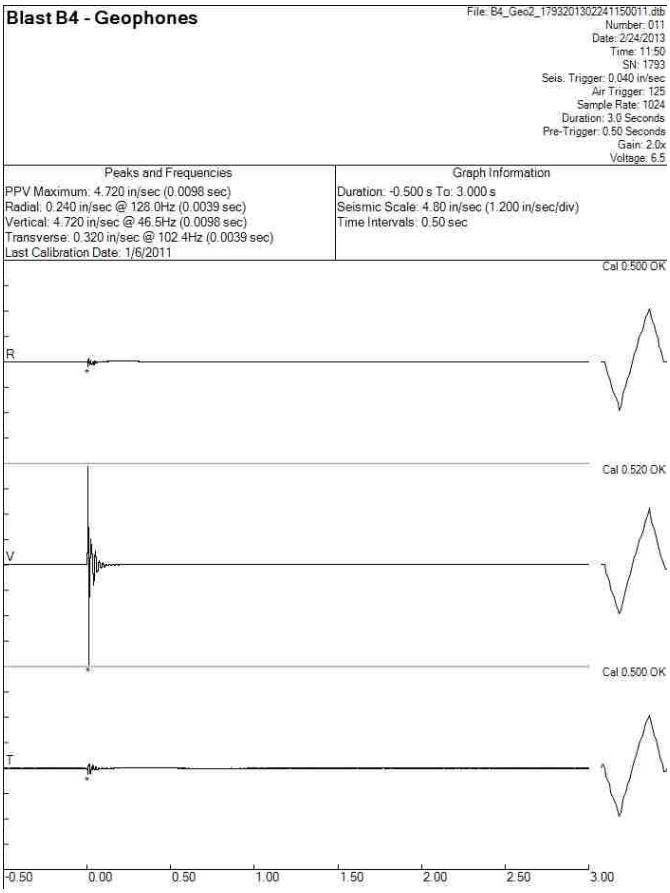

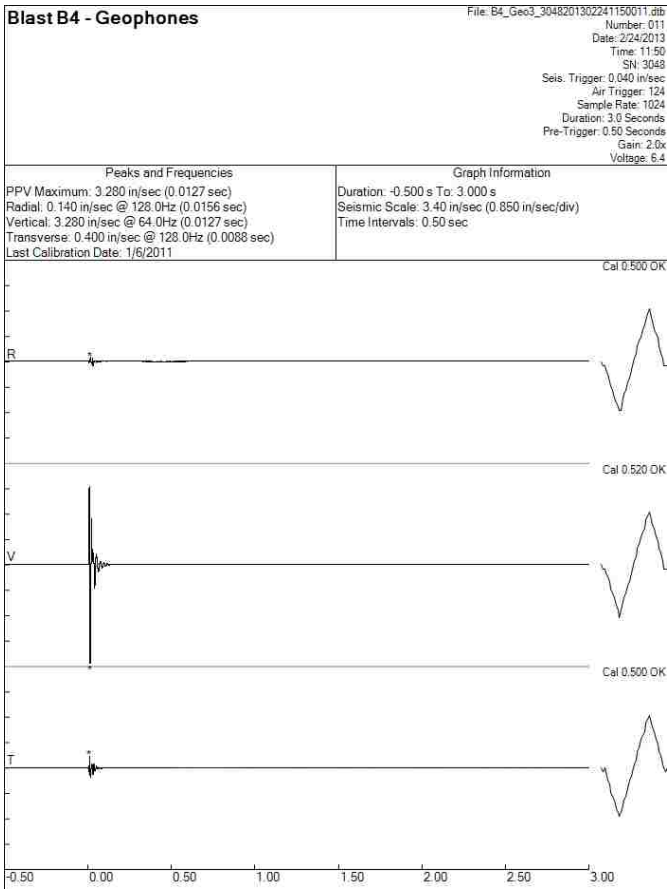

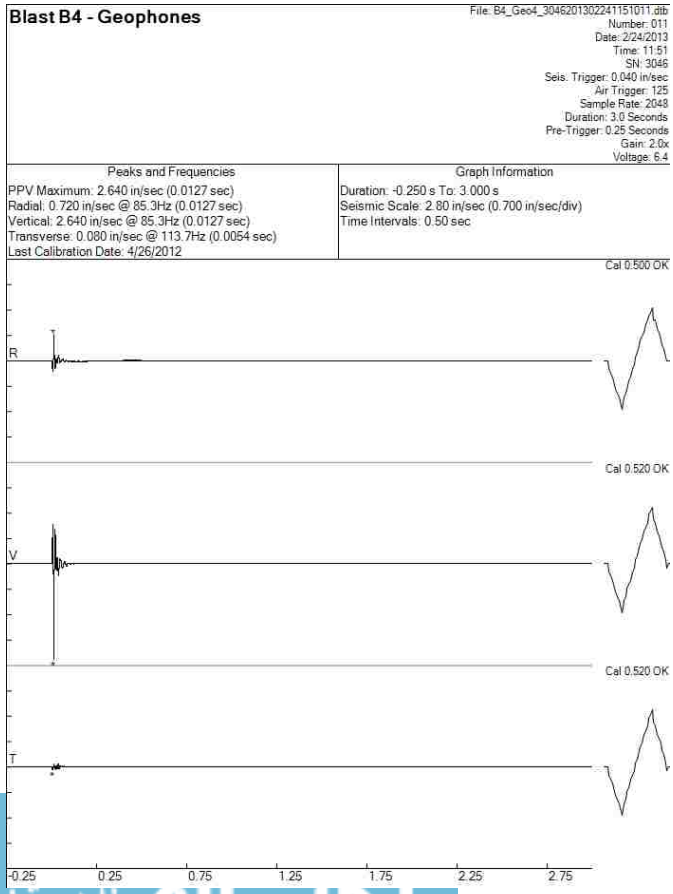

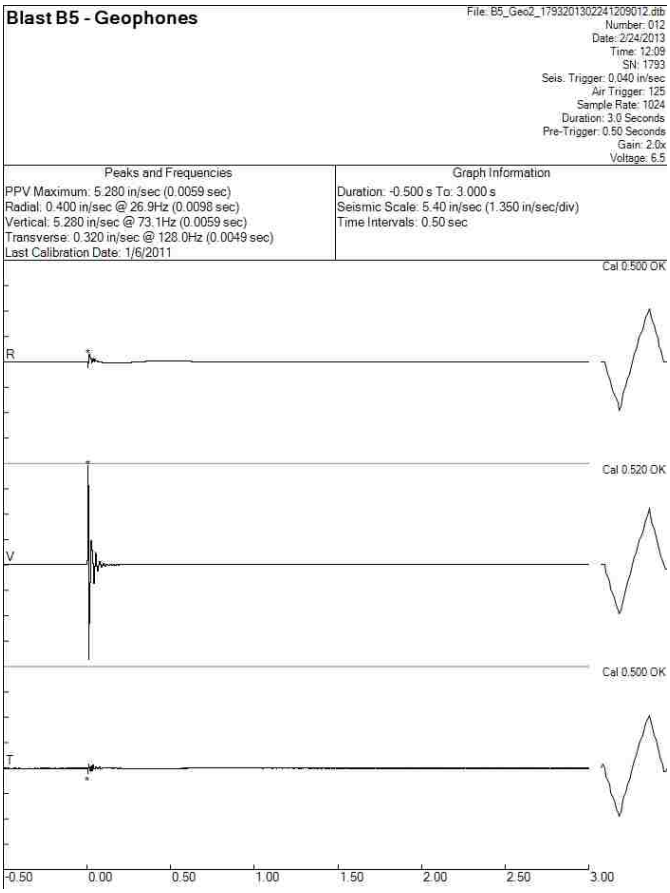

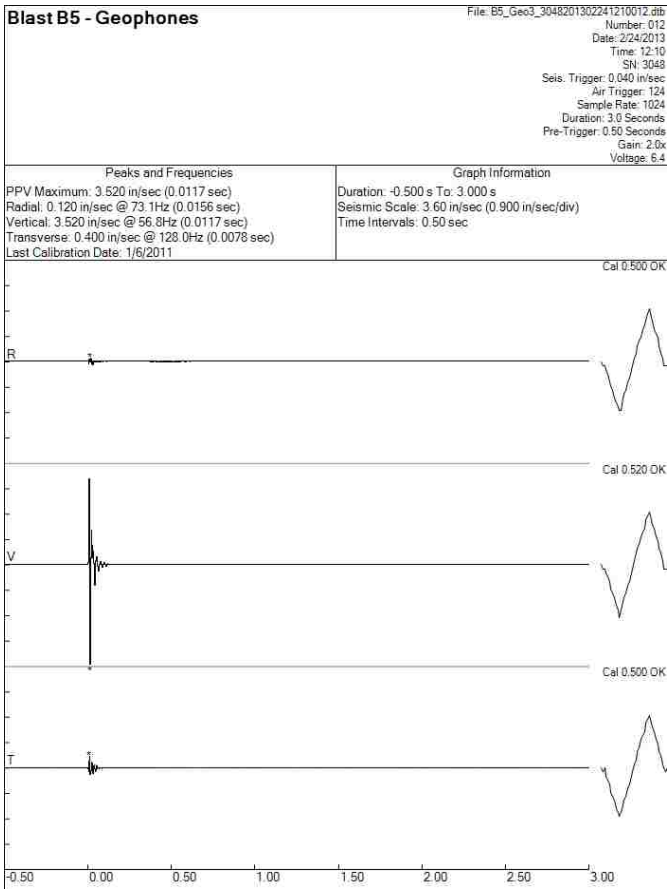

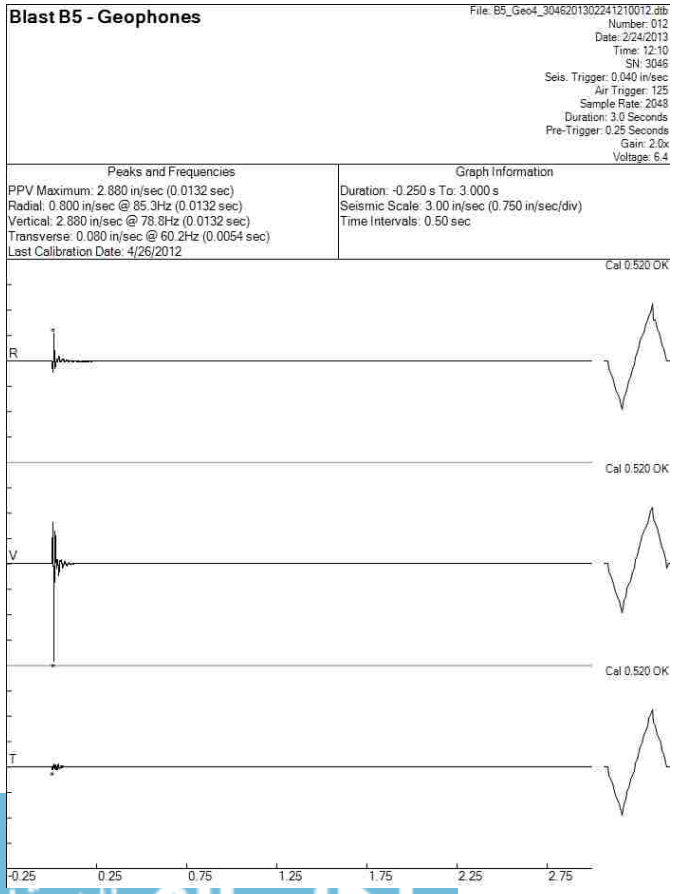

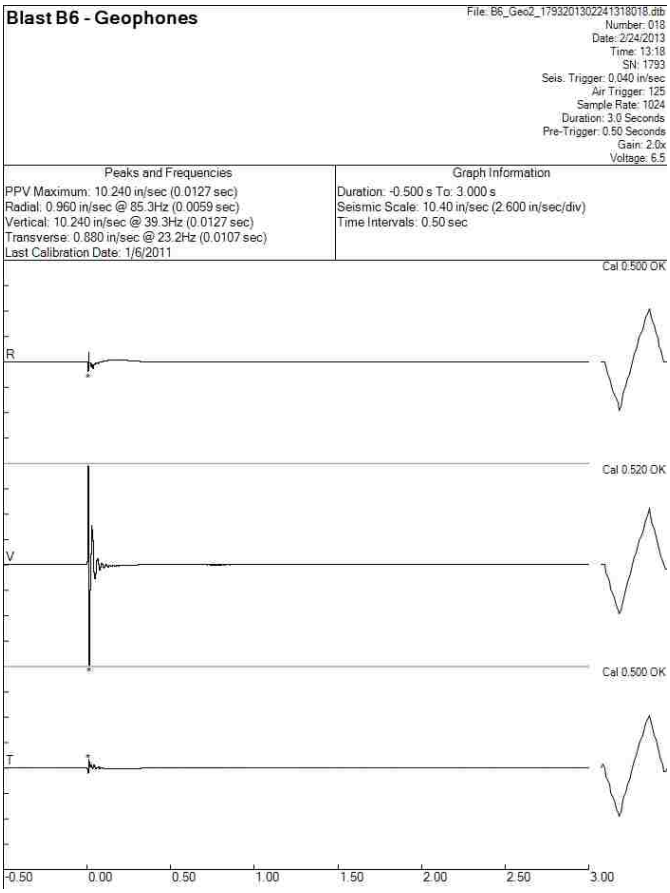

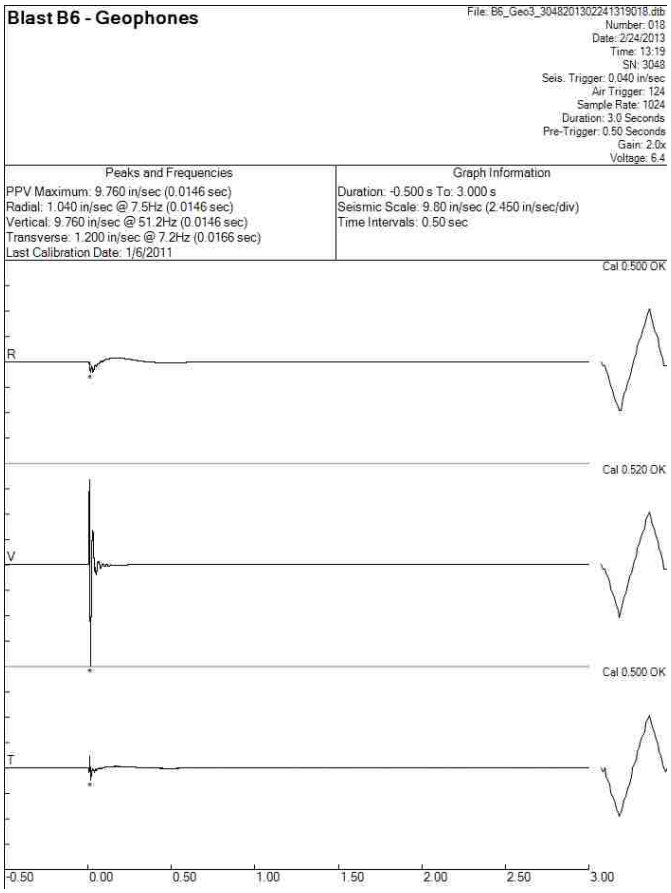

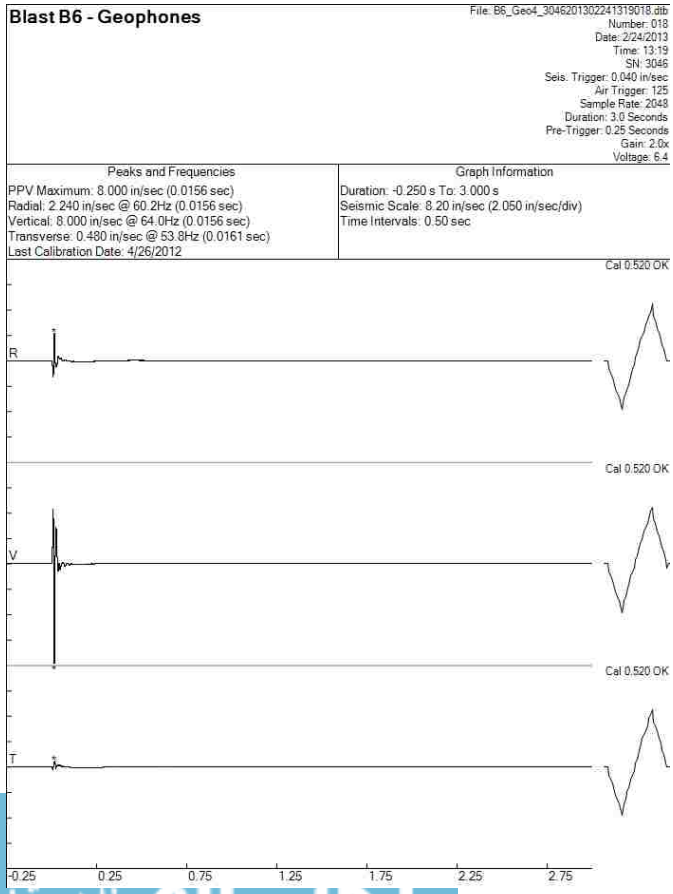

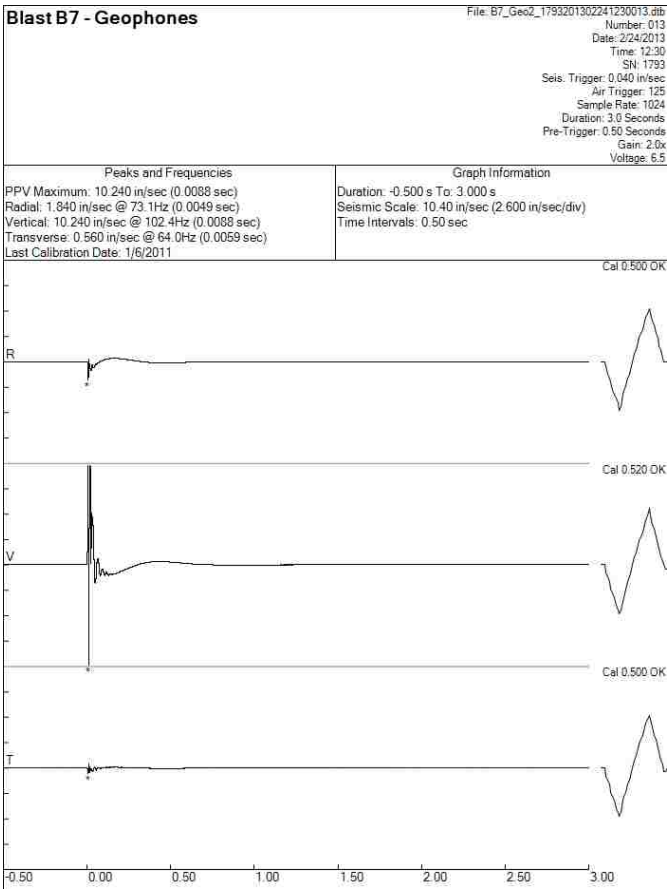

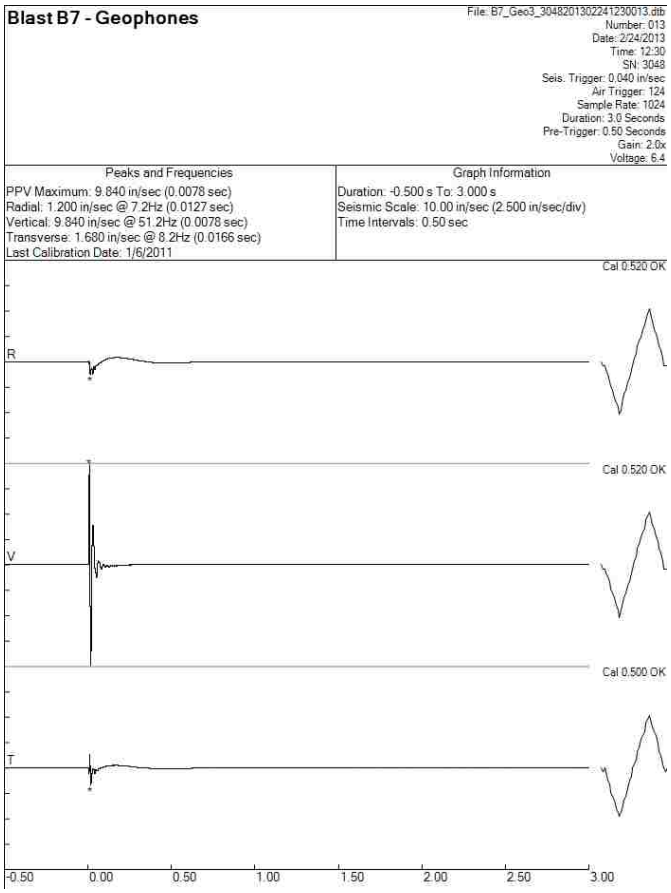

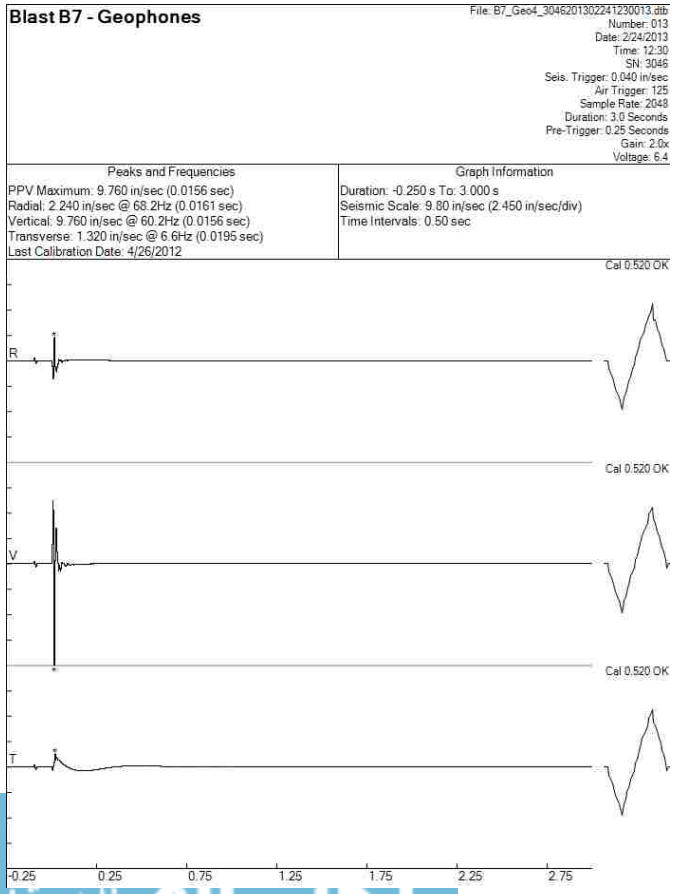

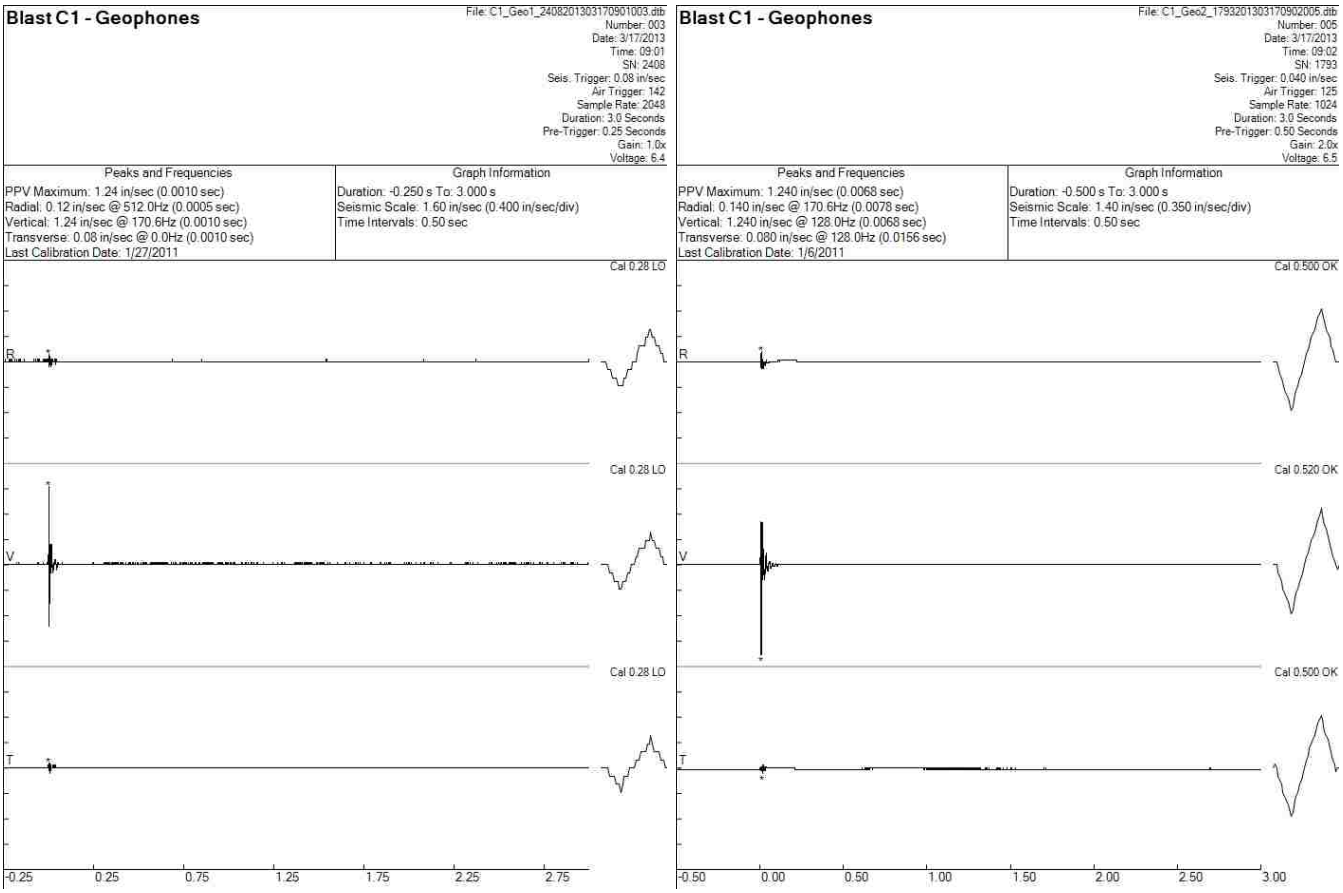

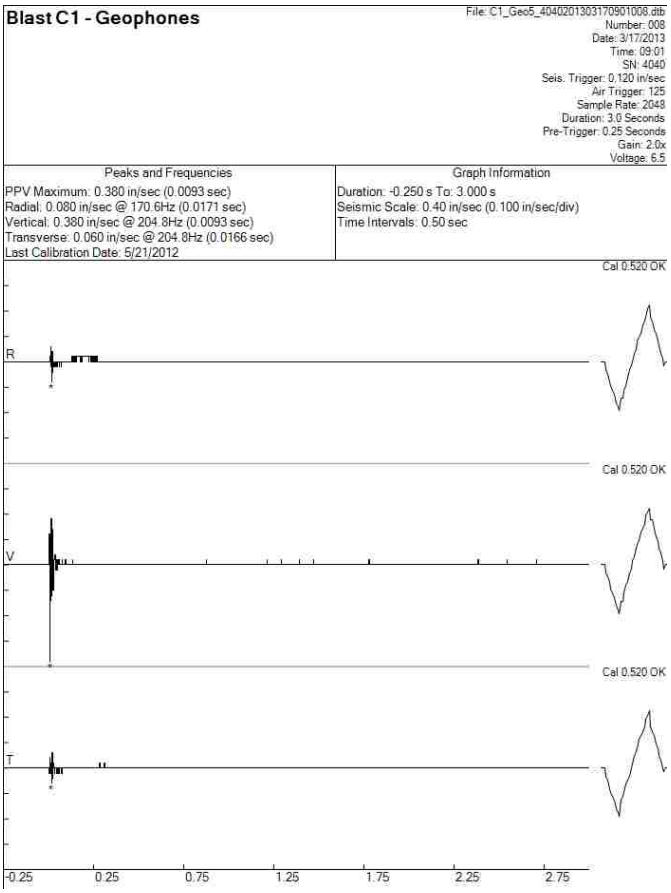

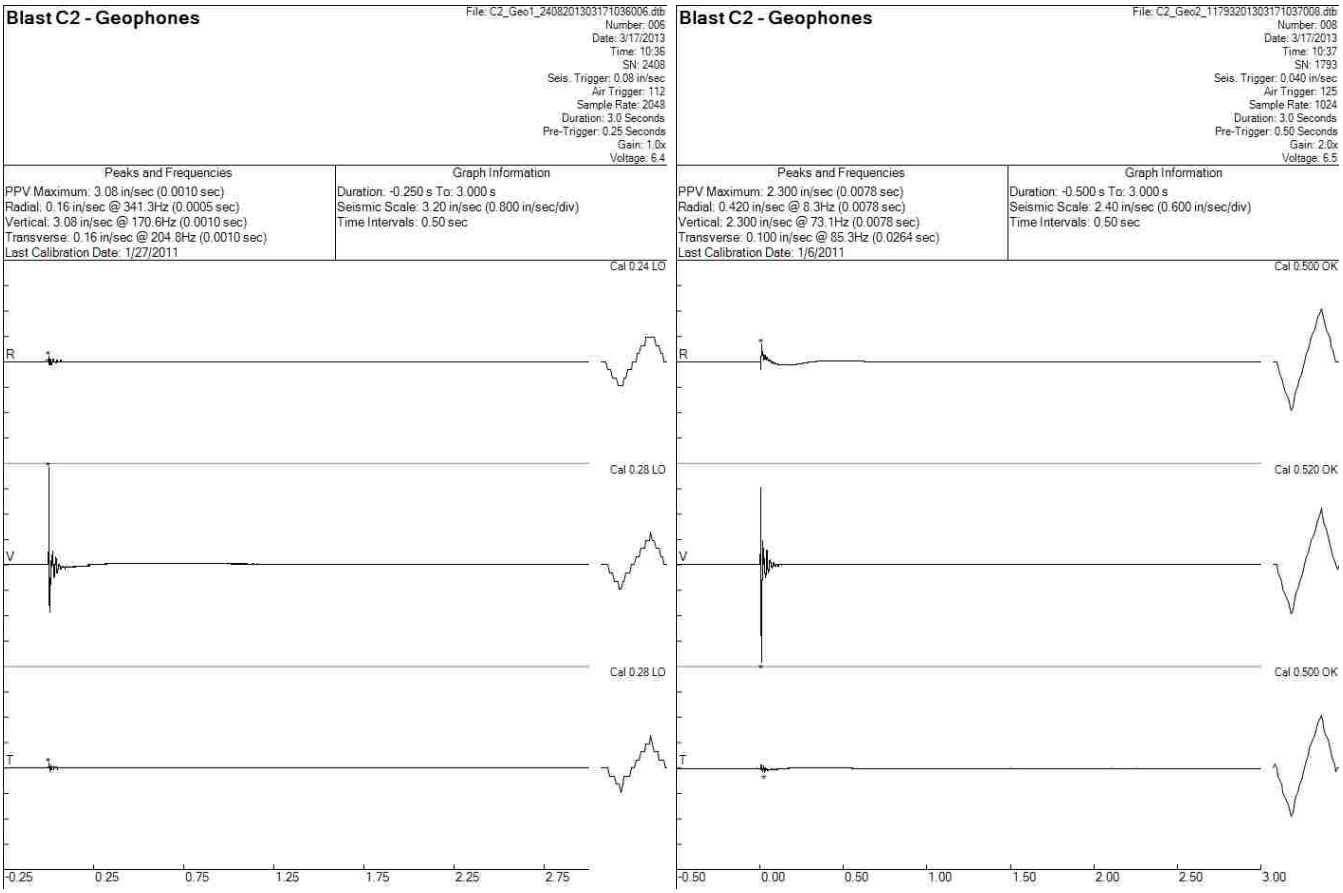

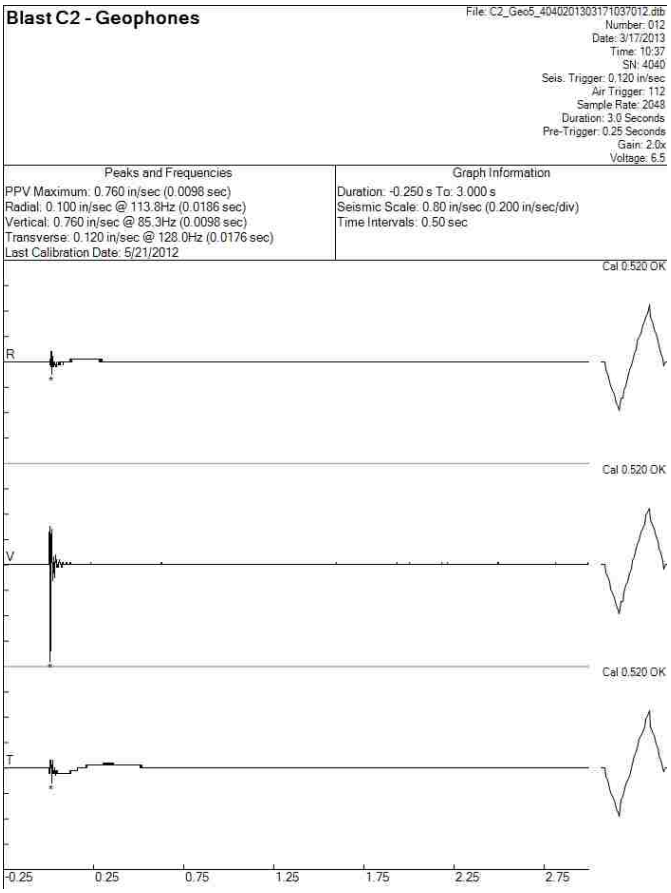

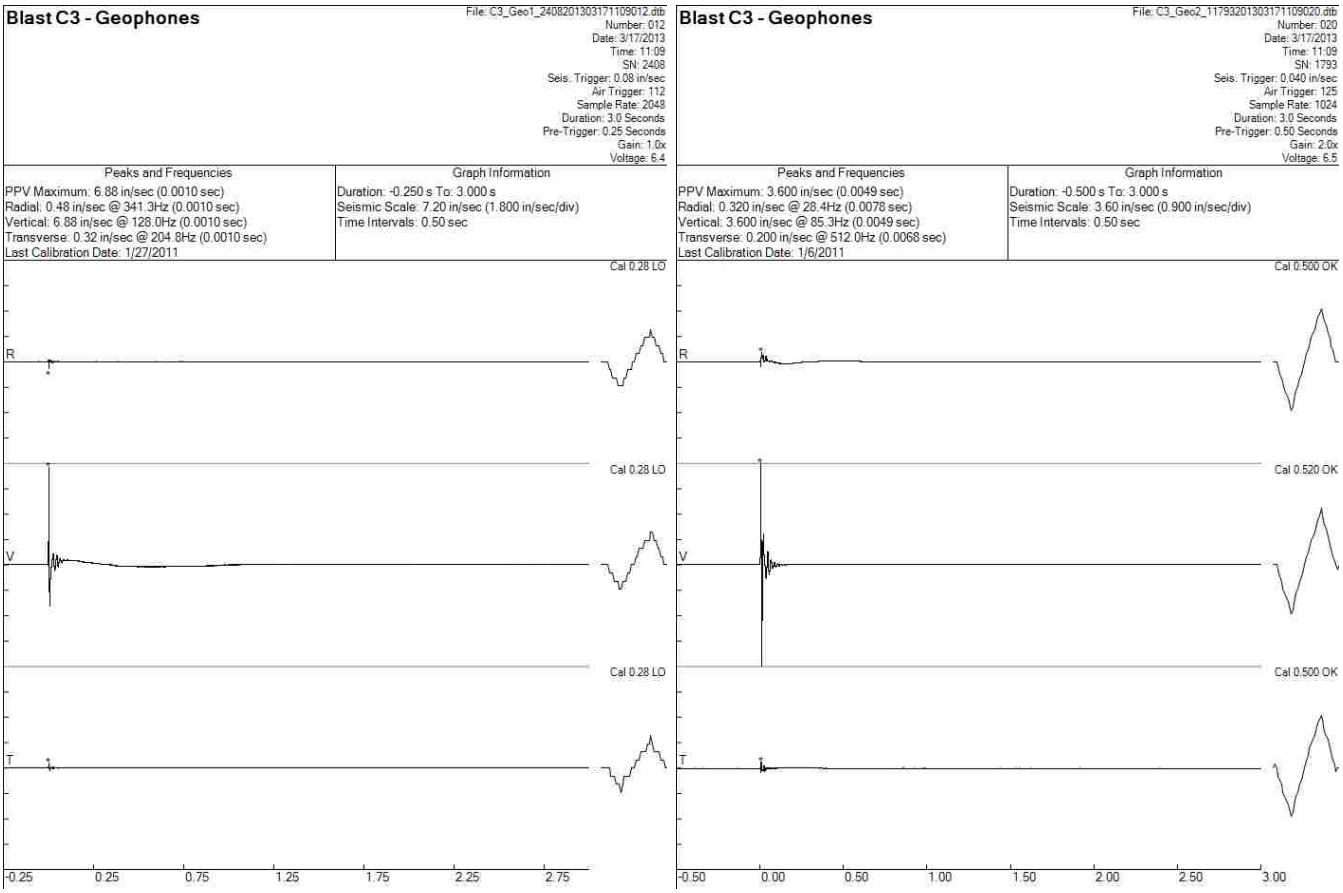

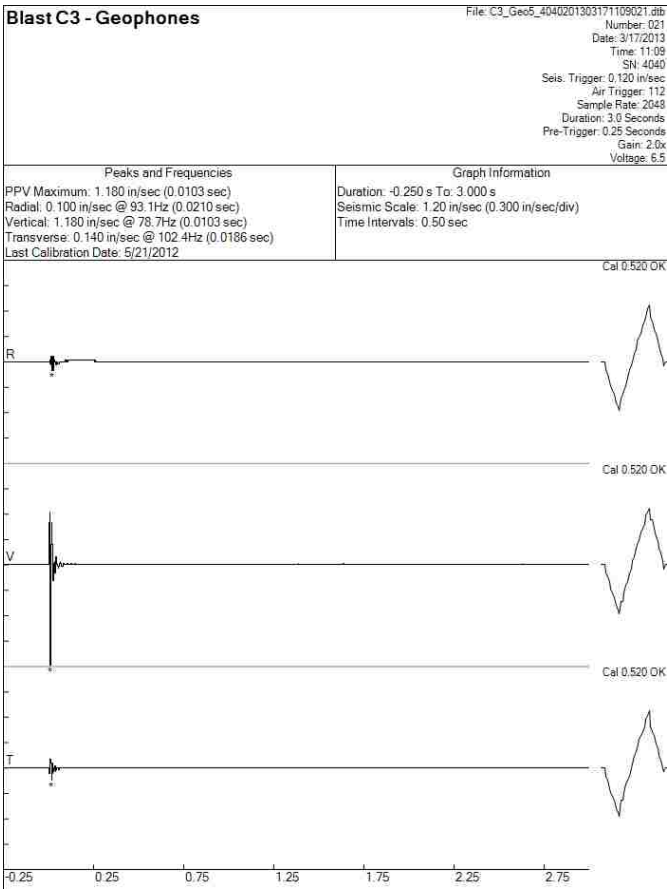

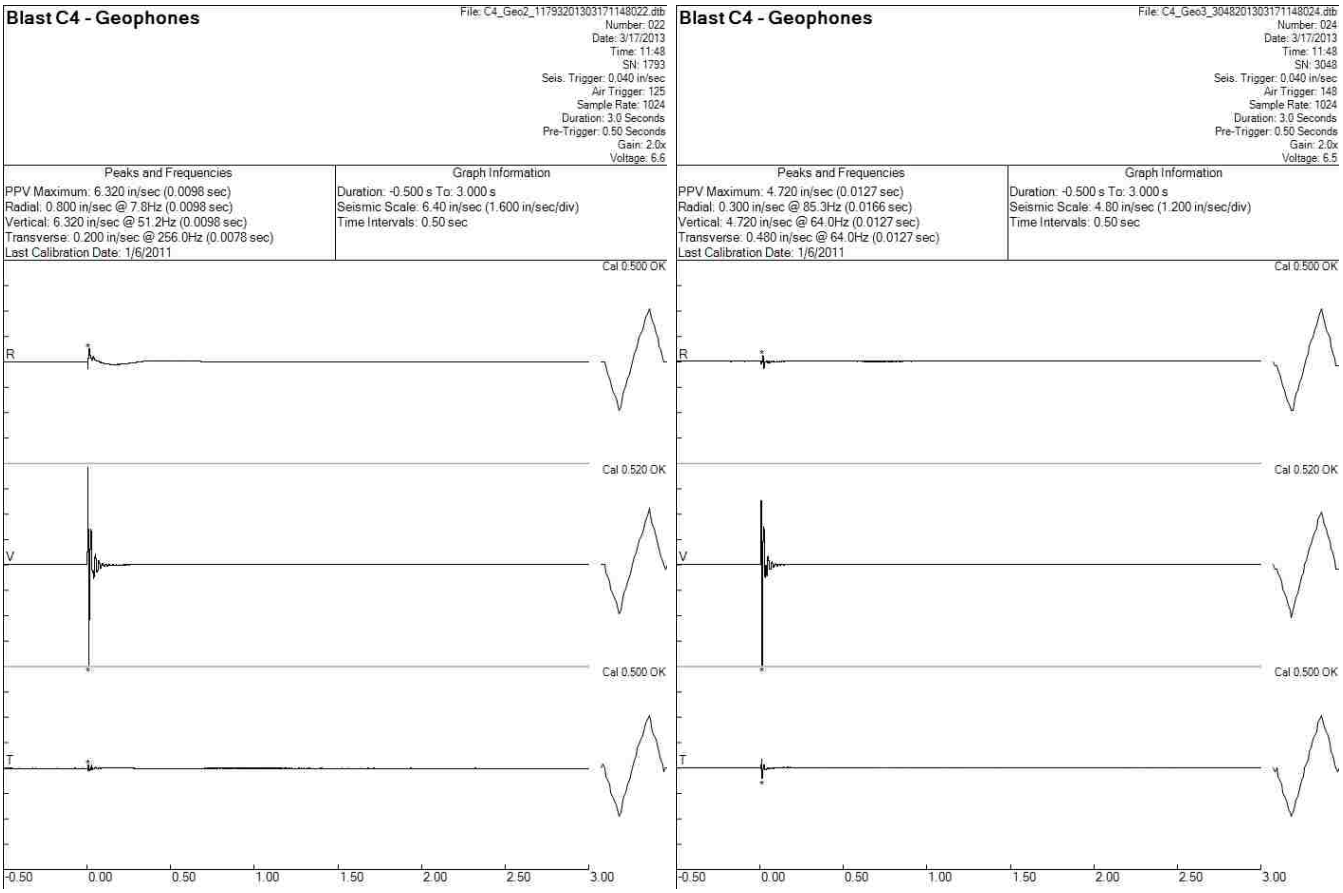

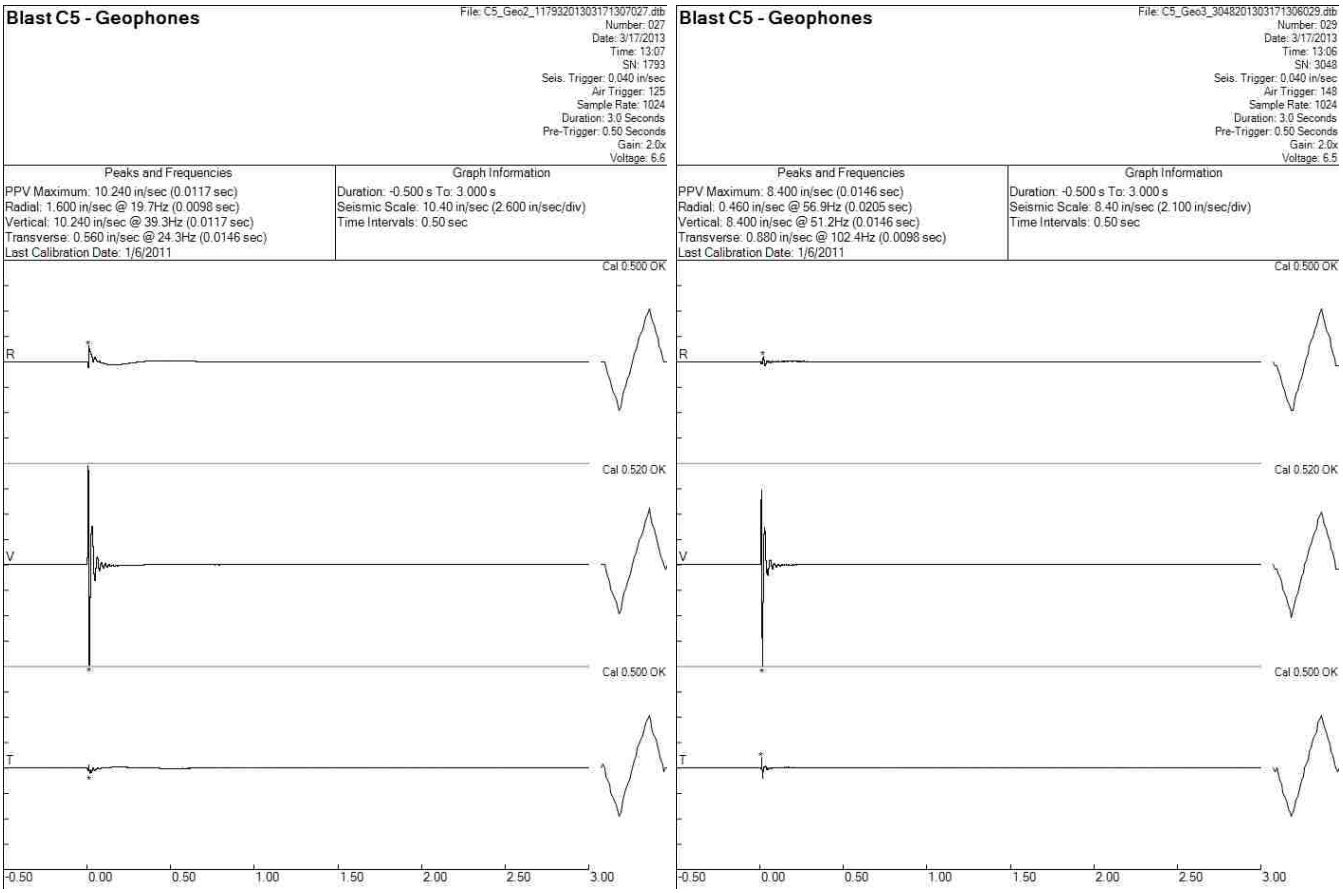

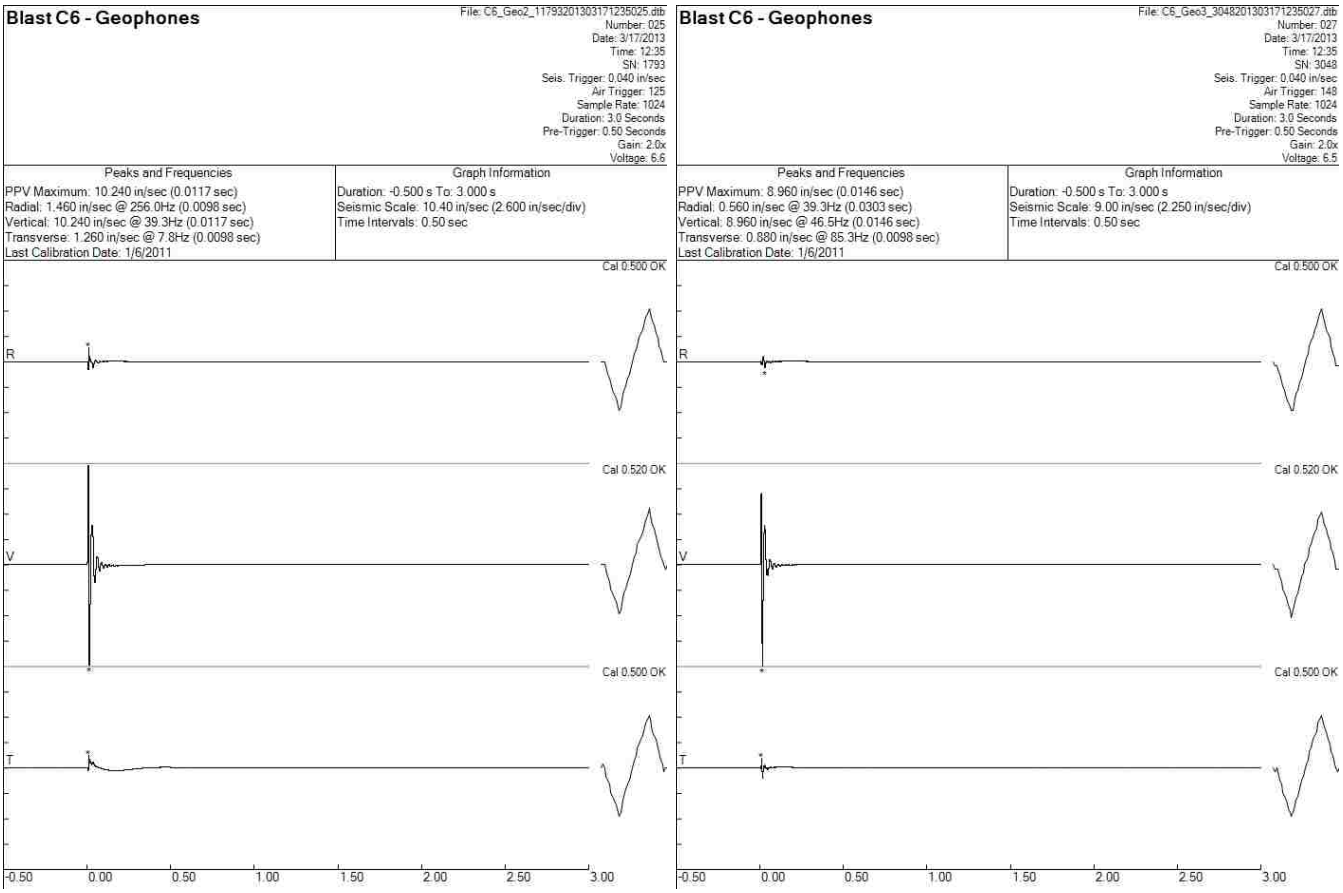

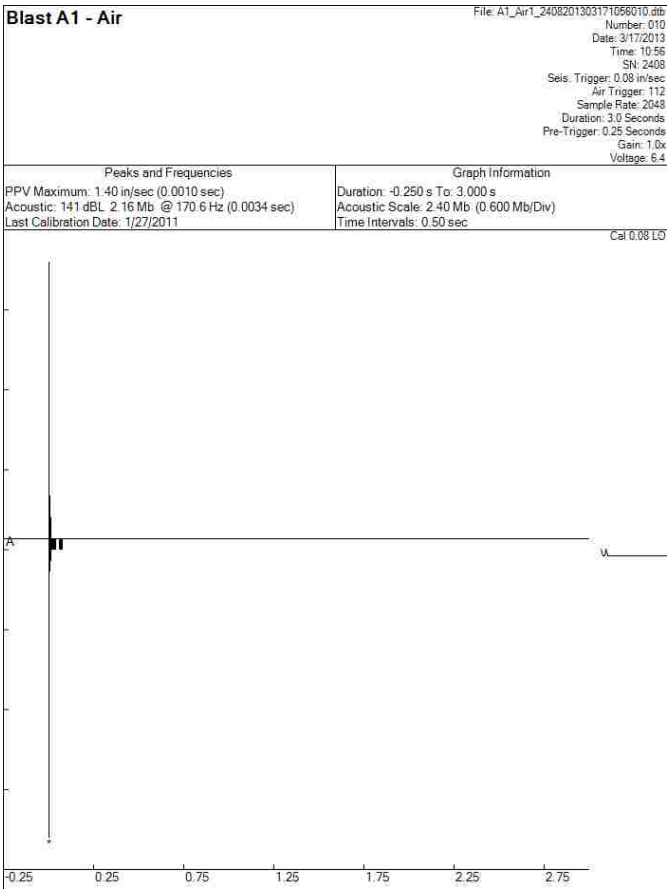

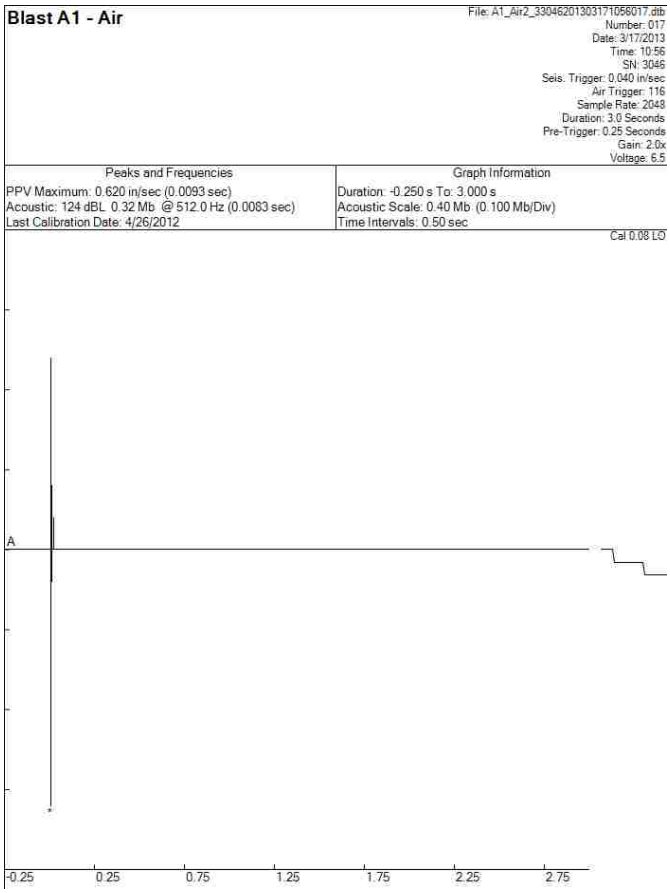

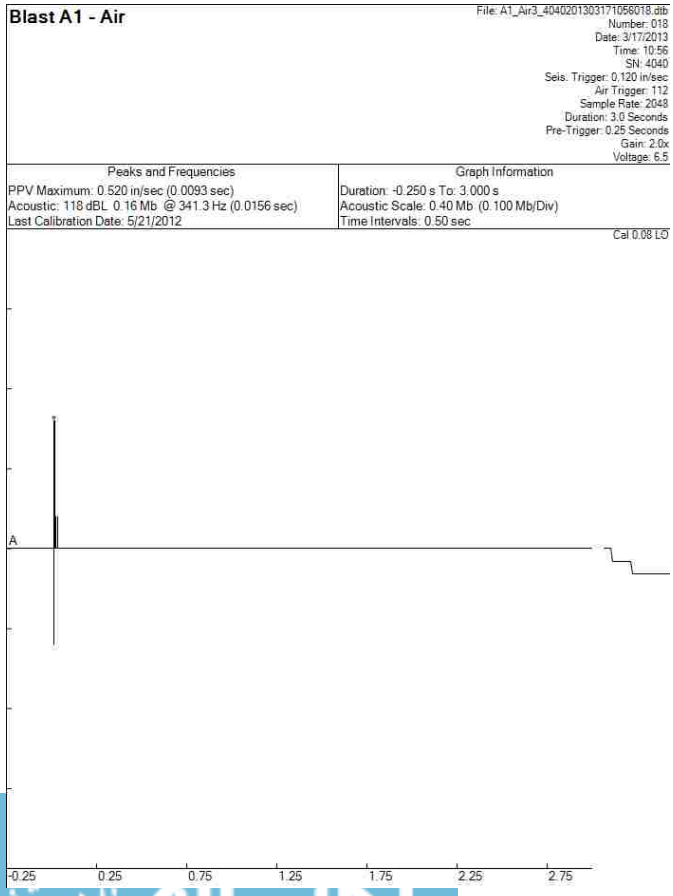

Blast A2 - Air

File: A2_Air1_5069201302231704067.dtb
Number: 067
Date: 2/23/2013
Time: 17:04
SN: 5069
Seis. Trigger: 0.030 in/sec
Air Trigger: 124
Sample Rate: 2048
Duration: 2.0 Seconds
Pre-Trigger: 0.25 Seconds
Gain: 2.0x
Voltage: 6.5

Peaks and Frequencies	Graph Information
PPV Maximum: 0.010 in/sec (0.0078 sec)	Duration: -0.250 s To: 2.000 s
Acoustic: 128 dBL 0.52 Mb @ 341.3 Hz (0.0078 sec)	Acoustic Scale: 0.80 Mb (0.200 Mb/Div)
Last Calibration Date: 11/6/2012	Time Intervals: 0.50 sec

Cal 0.00 LO

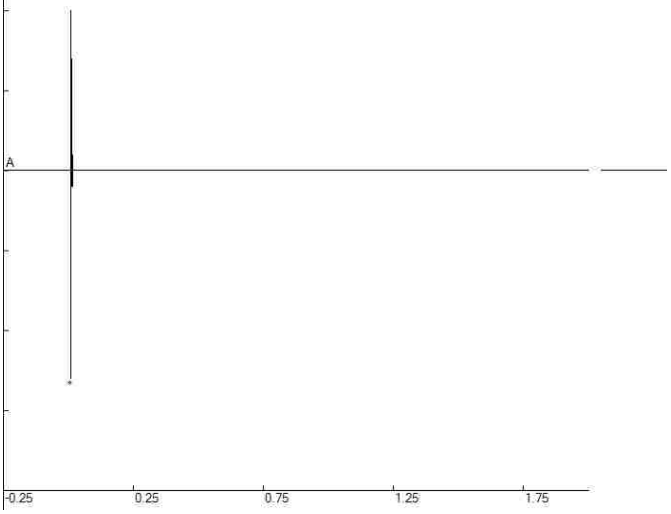

Blast A2 - Air

File: A2_Air2_5039201302231704067.dtb
Number: 067
Date: 2/23/2013
Time: 17:04
SN: 5039
Seis. Trigger: 0.0600 in/sec
Air Trigger: 124
Sample Rate: 2048
Duration: 2.0 Seconds
Pre-Trigger: 0.25 Seconds
Gain: 4.0x
Voltage: 6.4

Peaks and Frequencies	Graph Information
PPV Maximum: 0.0050 in/sec (0.0112 sec)	Duration: -0.250 s To: 2.000 s
Acoustic: 127 dBL 0.44 Mb @ 341.3 Hz (0.0127 sec)	Acoustic Scale: 0.80 Mb (0.200 Mb/Div)
Last Calibration Date: 7/9/2012	Time Intervals: 0.50 sec

Cal 0.00 LO

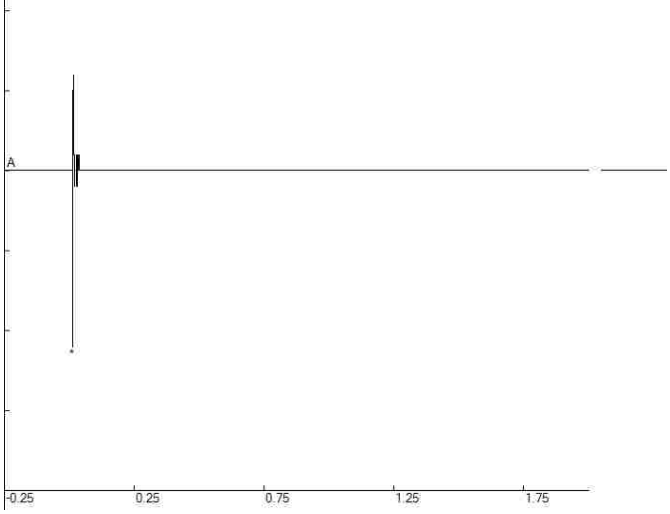

Blast A2 - Air

File: A2_Air3_7852013022317050 67.dtb
Number: 067
Date: 2/23/2013
Time: 17:05
SN: 0785
Seis. Trigger: 0.0300 in/sec
Air Trigger: 106
Sample Rate: 2048
Duration: 2.0 Seconds
Pre-Trigger: 0.25 Seconds
Gain: 4.0x
Voltage: 6.1

Peaks and Frequencies	Graph Information
PPV Maximum: 0.0025 in/sec (0.0210 sec)	Duration: -0.250 s To: 2.000 s
Acoustic: 123 dBL 0.28 Mb @ 3.9 Hz (0.0220 sec)	Acoustic Scale: 0.40 Mb (0.100 Mb/Div)
Last Calibration Date: 6/8/2012	Time Intervals: 0.50 sec

Cal 0.04 LO

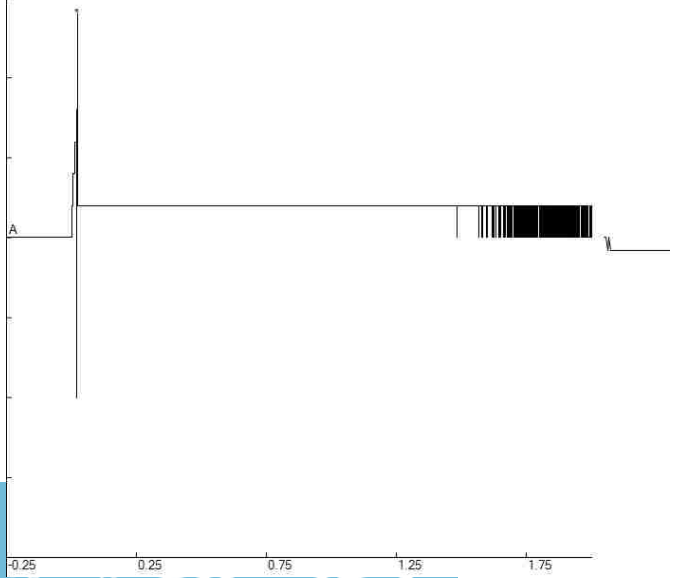

Blast A3 - Air

File: A3_Air1_3048201303171127023.dtb
Number: 023
Date: 3/17/2013
Time: 11:27
SN: 3048
Seis. Trigger: 0.040 in/sec
Air Trigger: 148
Sample Rate: 1024
Duration: 3.0 Seconds
Pre-Trigger: 0.50 Seconds
Gain: 2.0x
Voltage: 6.5

Peaks and Frequencies	Graph Information
PPV Maximum: 1.900 in/sec (0.0117 sec)	Duration: -0.500 s To: 3.000 s
Acoustic: 131 dBL 0.72 Mb @ 170.6 Hz (0.0049 sec)	Acoustic Scale: 0.80 Mb (0.200 Mb/Div)
Last Calibration Date: 1/6/2011	Time Intervals: 0.50 sec

Cal 0.12 LO

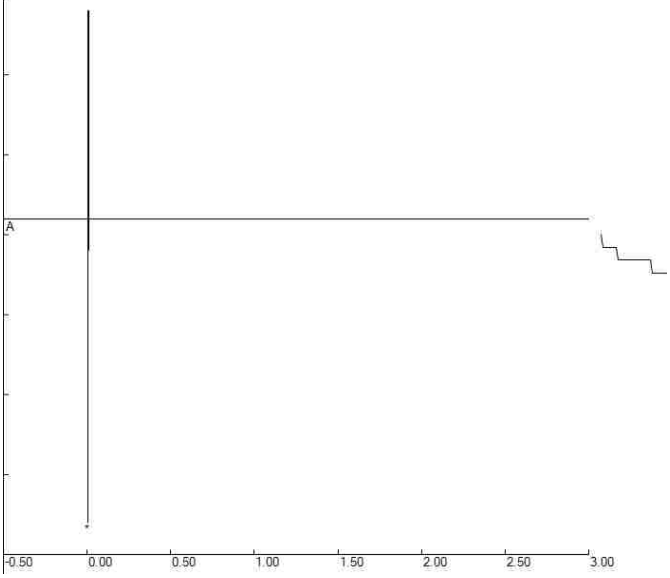

Blast A3 - Air

File: A3_Air2_3304620130317112702 1.dtb
Number: 021
Date: 3/17/2013
Time: 11:27
SN: 3046
Seis. Trigger: 0.040 in/sec
Air Trigger: 116
Sample Rate: 2048
Duration: 3.0 Seconds
Pre-Trigger: 0.25 Seconds
Gain: 2.0x
Voltage: 6.5

Peaks and Frequencies	Graph Information
PPV Maximum: 1.820 in/sec (0.0107 sec)	Duration: -0.250 s To: 3.000 s
Acoustic: 129 dBL 0.56 Mb @ 341.3 Hz (0.0078 sec)	Acoustic Scale: 0.80 Mb (0.200 Mb/Div)
Last Calibration Date: 4/26/2012	Time Intervals: 0.50 sec

Cal 0.08 LO

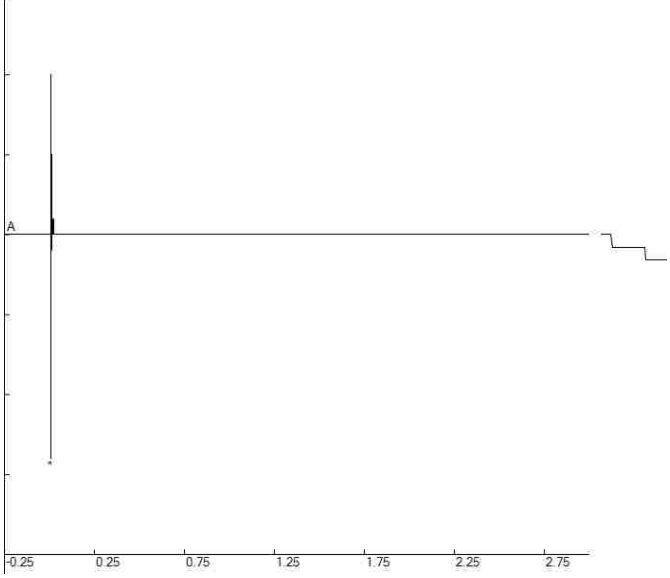

Blast A3 - Air

File: A3_Air3_4040201303171128022.dtb
Number: 022
Date: 3/17/2013
Time: 11:28
SN: 4040
Seis. Trigger: 0.120 in/sec
Air Trigger: 112
Sample Rate: 2048
Duration: 3.0 Seconds
Pre-Trigger: 0.25 Seconds
Gain: 2.0x
Voltage: 6.5

Peaks and Frequencies	Graph Information
PPV Maximum: 1.240 in/sec (0.0107 sec)	Duration: -0.250 s To: 3.000 s
Acoustic: 123 dBL 0.28 Mb @ 512.0 Hz (0.0142 sec)	Acoustic Scale: 0.40 Mb (0.100 Mb/Div)
Last Calibration Date: 5/21/2012	Time Intervals: 0.50 sec

Cal 0.08 LO

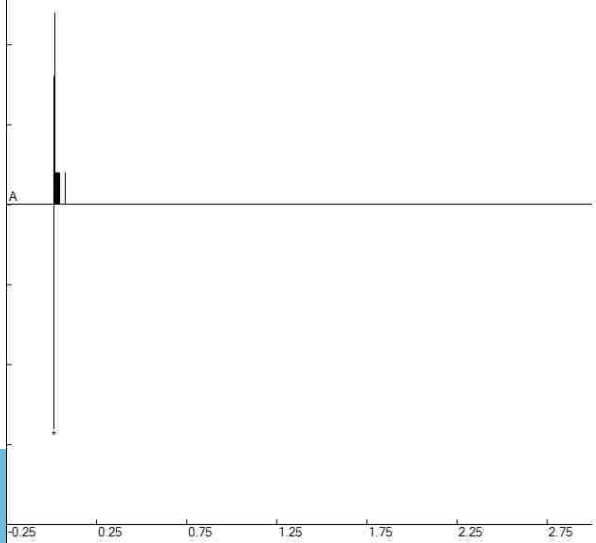

Blast A4 - Air

File: A4_Air1_5069201302231748073.dtb
Number: 073
Date: 2/23/2013
Time: 17:46
SN: 5069
Seis. Trigger: 0.030 in/sec
Air Trigger: 124
Sample Rate: 2048
Duration: 2.0 Seconds
Pre-Trigger: 0.25 Seconds
Gain: 2.0x
Voltage: 6.5

Peaks and Frequencies	Graph Information
PPV Maximum: 0.010 in/sec (0.0083 sec)	Duration: -0.250 s To: 2.000 s
Acoustic: 130 dBL 0.64 Mb @ 341.3 Hz (0.0088 sec)	Acoustic Scale: 0.80 Mb (0.200 Mb/Div)
Last Calibration Date: 11/6/2012	Time Intervals: 0.50 sec

Cal 0.00 LO

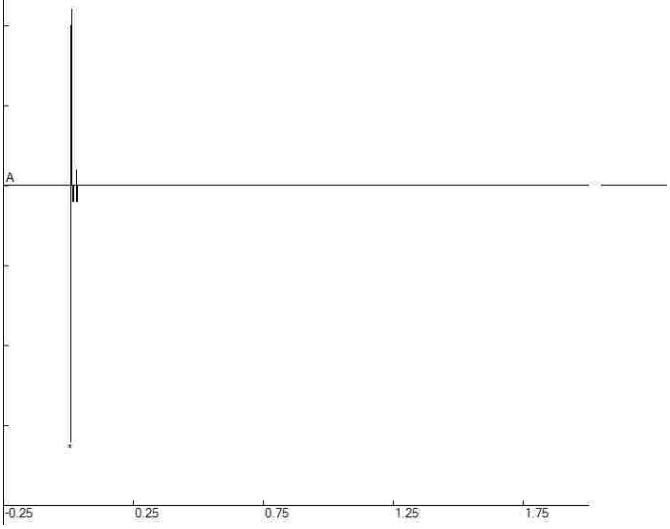

Blast A4 - Air

File: A4_Air2_5039201302231747073.dtb
Number: 073
Date: 2/23/2013
Time: 17:47
SN: 5039
Seis. Trigger: 0.0600 in/sec
Air Trigger: 124
Sample Rate: 2048
Duration: 2.0 Seconds
Pre-Trigger: 0.25 Seconds
Gain: 4.0x
Voltage: 6.4

Peaks and Frequencies	Graph Information
PPV Maximum: 0.0050 in/sec (0.0122 sec)	Duration: -0.250 s To: 2.000 s
Acoustic: 128 dBL 0.52 Mb @ 256.0 Hz (0.0127 sec)	Acoustic Scale: 0.80 Mb (0.200 Mb/Div)
Last Calibration Date: 7/9/2012	Time Intervals: 0.50 sec

Cal 0.00 LO

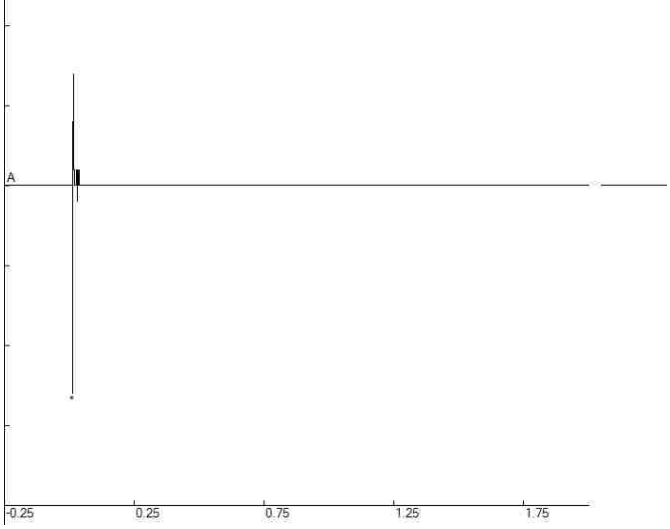

Blast A4 - Air

File: A4_Air3_7852013022317480 73.dtb
Number: 073
Date: 2/23/2013
Time: 17:48
SN: 0785
Seis. Trigger: 0.0300 in/sec
Air Trigger: 106
Sample Rate: 2048
Duration: 2.0 Seconds
Pre-Trigger: 0.25 Seconds
Gain: 4.0x
Voltage: 6.1

Peaks and Frequencies	Graph Information
PPV Maximum: 0.0025 in/sec (0.0210 sec)	Duration: -0.250 s To: 2.000 s
Acoustic: 125 dBL 0.36 Mb @ 146.2 Hz (0.0225 sec)	Acoustic Scale: 0.40 Mb (0.100 Mb/Div)
Last Calibration Date: 6/8/2012	Time Intervals: 0.50 sec

Cal 0.04 LO

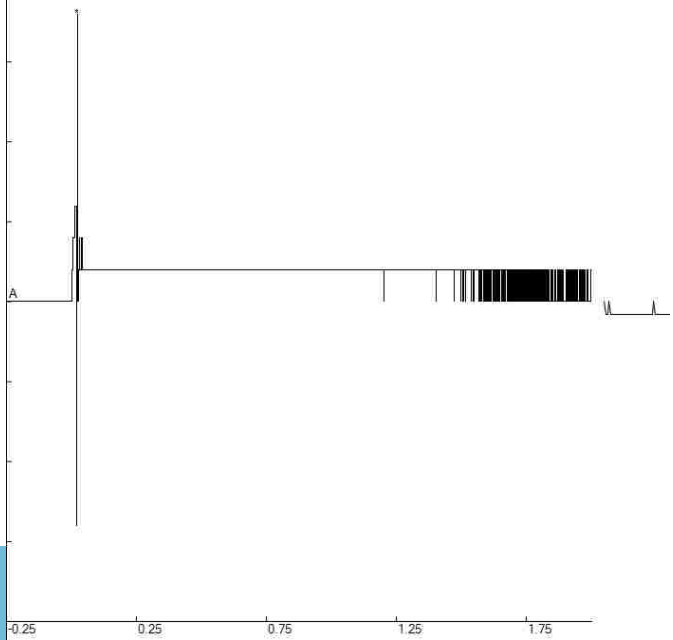

Blast A5 - Air

File: A5_Air1_5069201302231605055.dtb
Number: 055
Date: 2/23/2013
Time: 16:05
SN: 5069
Seis. Trigger: 0.030 in/sec
Air Trigger: 124
Sample Rate: 2048
Duration: 2.0 Seconds
Pre-Trigger: 0.25 Seconds
Gain: 2.0x
Voltage: 6.5

Peaks and Frequencies	Graph Information
PPV Maximum: 0.010 in/sec (0.0073 sec)	Duration: -0.250 s To: 2.000 s
Acoustic: 132 dBL 0.84 Mb @ 341.3 Hz (0.0078 sec)	Acoustic Scale: 1.20 Mb (0.300 Mb/Div)
Last Calibration Date: 11/6/2012	Time Intervals: 0.50 sec

Cal 0.00 LO

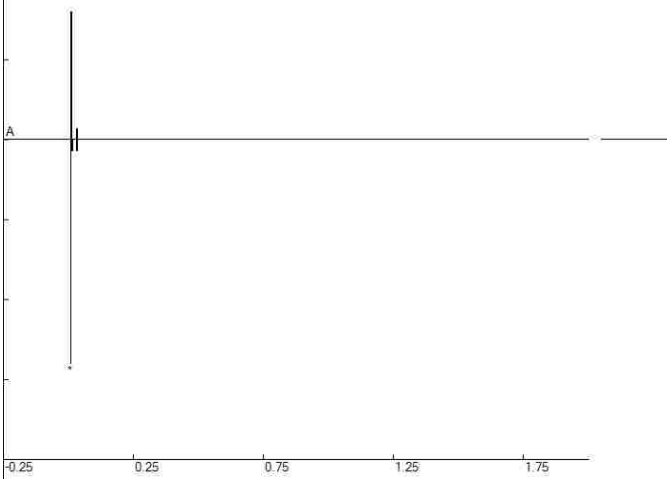

Blast A5 - Air

File: A5_Air2_5039201302231606055.dtb
Number: 055
Date: 2/23/2013
Time: 16:06
SN: 5039
Seis. Trigger: 0.0600 in/sec
Air Trigger: 124
Sample Rate: 2048
Duration: 2.0 Seconds
Pre-Trigger: 0.25 Seconds
Gain: 4.0x
Voltage: 6.4

Peaks and Frequencies	Graph Information
PPV Maximum: 0.0050 in/sec (0.0112 sec)	Duration: -0.250 s To: 2.000 s
Acoustic: 130 dBL 0.60 Mb @ 256.0 Hz (0.0122 sec)	Acoustic Scale: 0.80 Mb (0.200 Mb/Div)
Last Calibration Date: 7/9/2012	Time Intervals: 0.50 sec

Cal 0.00 LO

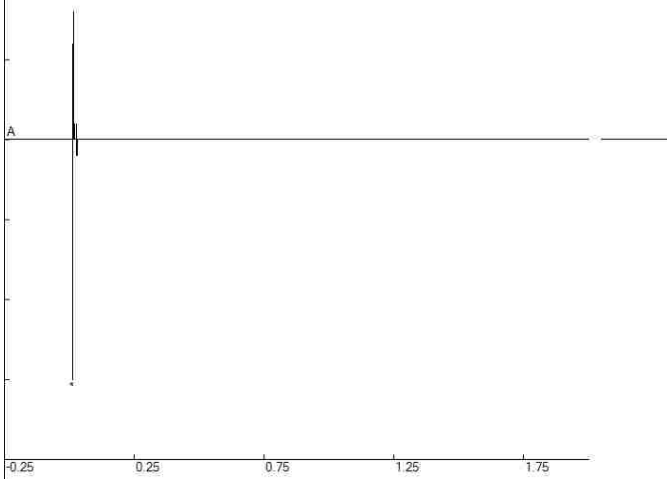

Blast A5 - Air

File: A5_Air3_7852013022316070 55.dtb
Number: 055
Date: 2/23/2013
Time: 16:07
SN: 0785
Seis. Trigger: 0.0300 in/sec
Air Trigger: 106
Sample Rate: 2048
Duration: 2.0 Seconds
Pre-Trigger: 0.25 Seconds
Gain: 4.0x
Voltage: 6.1

Peaks and Frequencies	Graph Information
PPV Maximum: 0.0025 in/sec (0.0205 sec)	Duration: -0.250 s To: 2.000 s
Acoustic: 125 dBL 0.36 Mb @ 3.9 Hz (0.0220 sec)	Acoustic Scale: 0.40 Mb (0.100 Mb/Div)
Last Calibration Date: 6/8/2012	Time Intervals: 0.50 sec

Cal 0.04 LO

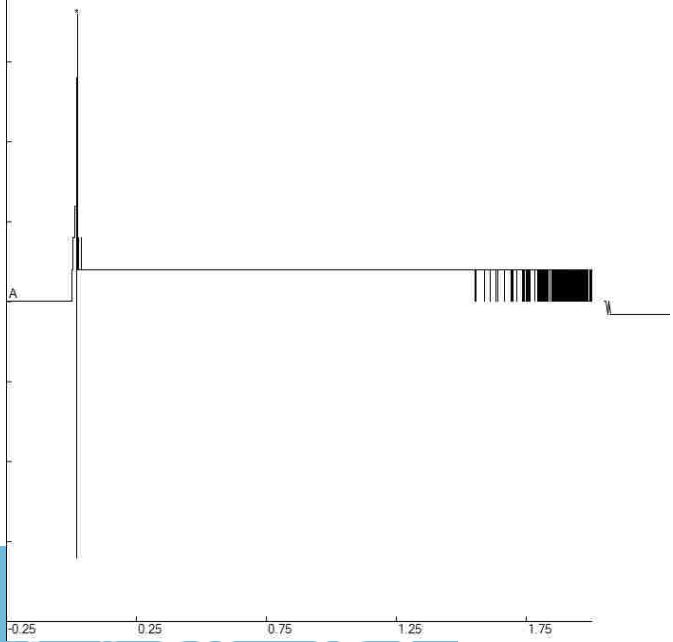

Blast A6 - Air

File: A6_Air1_5069201302231716069.dtb
Number: 069
Date: 2/23/2013
Time: 17:16
SN: 5069
Seis. Trigger: 0.030 in/sec
Air Trigger: 124
Sample Rate: 2048
Duration: 2.0 Seconds
Pre-Trigger: 0.25 Seconds
Gain: 2.0x
Voltage: 6.5

Peaks and Frequencies	Graph Information
PPV Maximum: 0.010 in/sec (0.0078 sec)	Duration: -0.250 s To: 2.000 s
Acoustic: 133 dBL 0.88 Mb @ 256.0 Hz (0.0078 sec)	Acoustic Scale: 1.20 Mb (0.300 Mb/Div)
Last Calibration Date: 11/6/2012	Time Intervals: 0.50 sec

Cal 0.00 LO

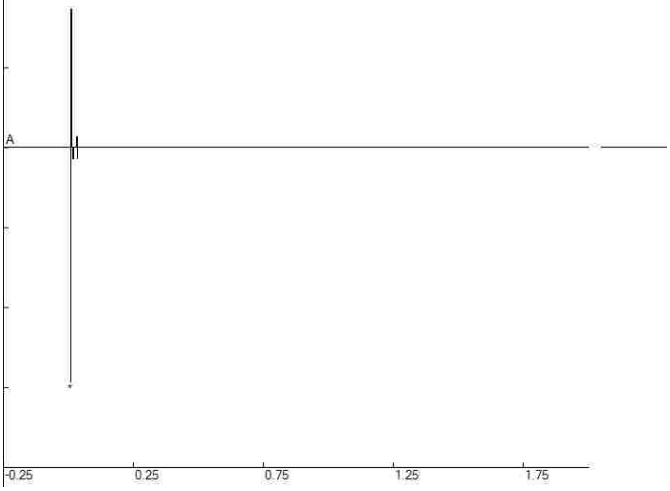

Blast A6 - Air

File: A6_Air2_5039201302231717069.dtb
Number: 069
Date: 2/23/2013
Time: 17:17
SN: 5039
Seis. Trigger: 0.0600 in/sec
Air Trigger: 124
Sample Rate: 2048
Duration: 2.0 Seconds
Pre-Trigger: 0.25 Seconds
Gain: 4.0x
Voltage: 6.4

Peaks and Frequencies	Graph Information
PPV Maximum: 0.0050 in/sec (0.0112 sec)	Duration: -0.250 s To: 2.000 s
Acoustic: 131 dBL 0.68 Mb @ 341.3 Hz (0.0122 sec)	Acoustic Scale: 0.80 Mb (0.200 Mb/Div)
Last Calibration Date: 7/9/2012	Time Intervals: 0.50 sec

Cal 0.00 LO

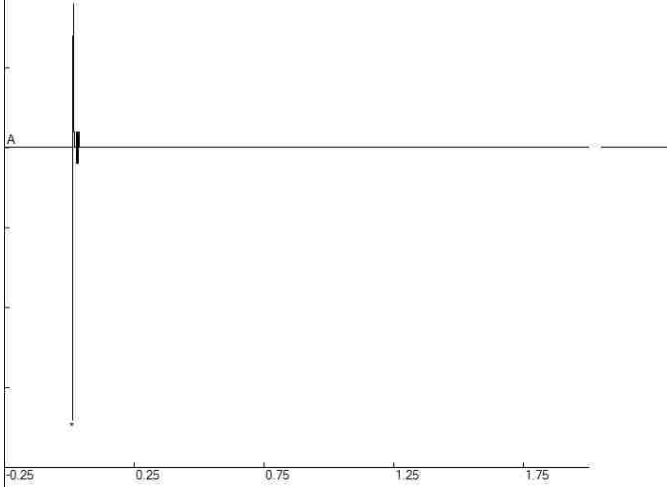

Blast A6 - Air

File: A6_Air3_7852013022317180 69.dtb
Number: 069
Date: 2/23/2013
Time: 17:18
SN: 0785
Seis. Trigger: 0.0300 in/sec
Air Trigger: 106
Sample Rate: 2048
Duration: 2.0 Seconds
Pre-Trigger: 0.25 Seconds
Gain: 4.0x
Voltage: 6.1

Peaks and Frequencies	Graph Information
PPV Maximum: 0.0025 in/sec (0.0205 sec)	Duration: -0.250 s To: 2.000 s
Acoustic: 125 dBL 0.36 Mb @ 3.9 Hz (0.0195 sec)	Acoustic Scale: 0.40 Mb (0.100 Mb/Div)
Last Calibration Date: 6/8/2012	Time Intervals: 0.50 sec

Cal 0.04 LO

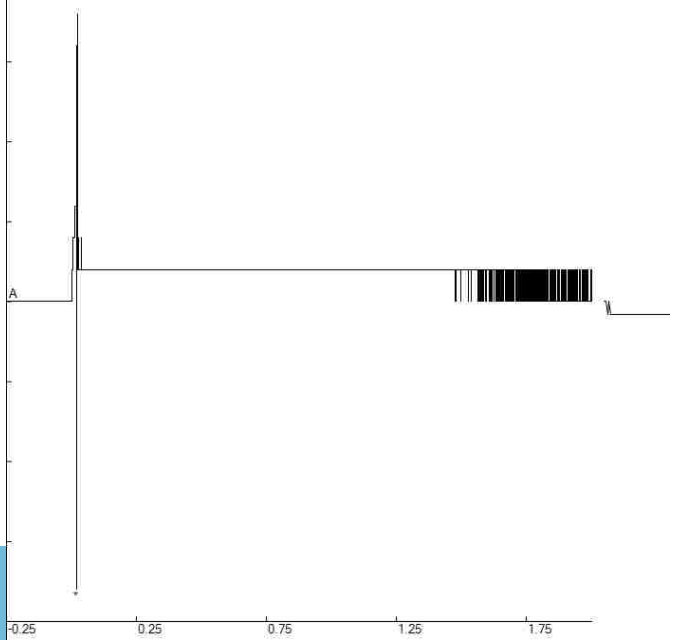

Blast A7 - Air

File: A7_Air1_5069201302231619060.dtb
Number: 060
Date: 2/23/2013
Time: 16:19
SN: 5069
Seis. Trigger: 0.030 in/sec
Air Trigger: 124
Sample Rate: 2048
Duration: 2.0 Seconds
Pre-Trigger: 0.25 Seconds
Gain: 2.0x
Voltage: 6.5

Peaks and Frequencies	Graph Information
PPV Maximum: 0.010 in/sec (0.0073 sec)	Duration: -0.250 s To: 2.000 s
Acoustic: 133 dBL 0.92 Mb @ 256.0 Hz (0.0078 sec)	Acoustic Scale: 1.20 Mb (0.300 Mb/Div)
Last Calibration Date: 11/6/2012	Time Intervals: 0.50 sec

Cal 0.00 LO

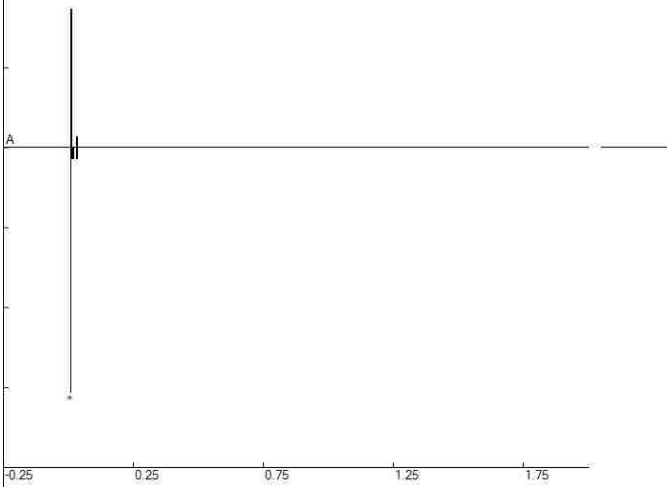

Blast A7 - Air

File: A7_Air2_5039201302231620060.dtb
Number: 060
Date: 2/23/2013
Time: 16:20
SN: 5039
Seis. Trigger: 0.0600 in/sec
Air Trigger: 124
Sample Rate: 2048
Duration: 2.0 Seconds
Pre-Trigger: 0.25 Seconds
Gain: 4.0x
Voltage: 6.4

Peaks and Frequencies	Graph Information
PPV Maximum: 0.0050 in/sec (0.0112 sec)	Duration: -0.250 s To: 2.000 s
Acoustic: 130 dBL 0.60 Mb @ 341.3 Hz (0.0127 sec)	Acoustic Scale: 0.80 Mb (0.200 Mb/Div)
Last Calibration Date: 7/9/2012	Time Intervals: 0.50 sec

Cal 0.00 LO

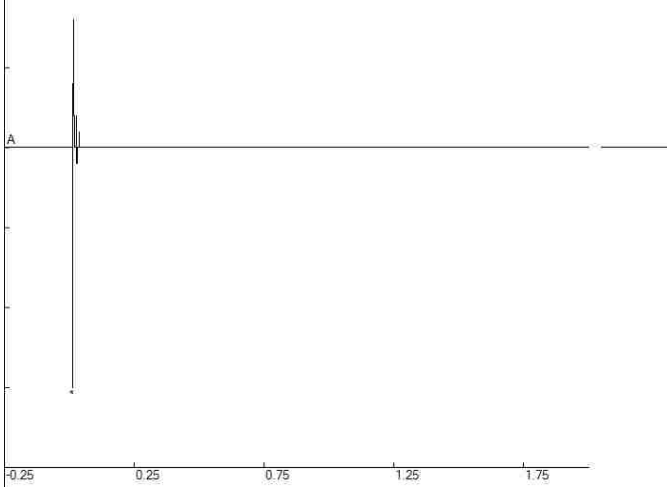

Blast A7 - Air

File: A7_Air3_7852013022316210 60.dtb
Number: 060
Date: 2/23/2013
Time: 16:21
SN: 0785
Seis. Trigger: 0.0300 in/sec
Air Trigger: 106
Sample Rate: 2048
Duration: 2.0 Seconds
Pre-Trigger: 0.25 Seconds
Gain: 4.0x
Voltage: 6.1

Peaks and Frequencies	Graph Information
PPV Maximum: 0.0025 in/sec (0.0205 sec)	Duration: -0.250 s To: 2.000 s
Acoustic: 125 dBL 0.36 Mb @ 28.4 Hz (0.0200 sec)	Acoustic Scale: 0.40 Mb (0.100 Mb/Div)
Last Calibration Date: 6/8/2012	Time Intervals: 0.50 sec

Cal 0.04 LO

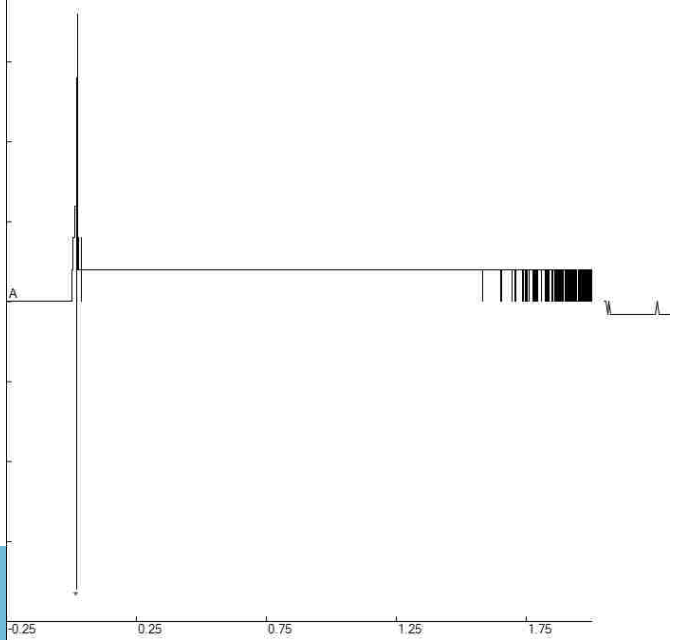

Blast A8 - Air

File: A8_Air1_5069201302231759075.dtb
Number: 075
Date: 2/23/2013
Time: 17:59
SN: 5069
Seis. Trigger: 0.030 in/sec
Air Trigger: 124
Sample Rate: 2048
Duration: 2.0 Seconds
Pre-Trigger: 0.25 Seconds
Gain: 2.0x
Voltage: 6.5

Peaks and Frequencies	Graph Information
PPV Maximum: 0.015 in/sec (0.0073 sec)	Duration: -0.250 s To: 2.000 s
Acoustic: 135 dBL 1.12 Mb @ 256.0 Hz (0.0078 sec)	Acoustic Scale: 1.20 Mb (0.300 Mb/Div)
Last Calibration Date: 11/6/2012	Time Intervals: 0.50 sec

Cal 0.00 LO

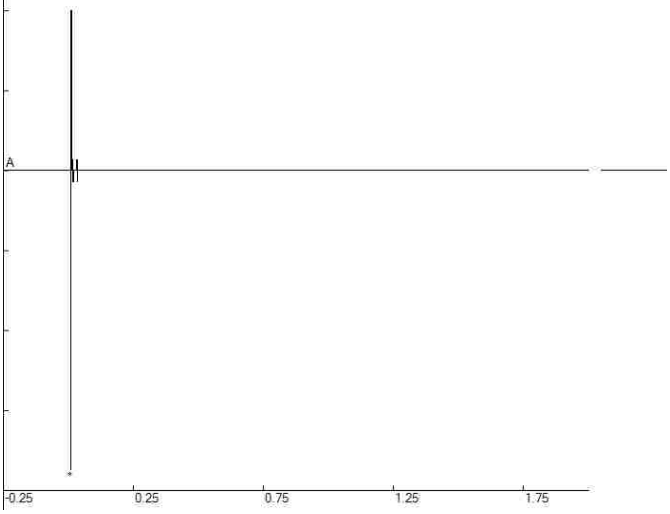

Blast A8 - Air

File: A8_Air2_5039201302231759075.dtb
Number: 075
Date: 2/23/2013
Time: 17:59
SN: 5039
Seis. Trigger: 0.0600 in/sec
Air Trigger: 124
Sample Rate: 2048
Duration: 2.0 Seconds
Pre-Trigger: 0.25 Seconds
Gain: 4.0x
Voltage: 6.4

Peaks and Frequencies	Graph Information
PPV Maximum: 0.0050 in/sec (0.0117 sec)	Duration: -0.250 s To: 2.000 s
Acoustic: 132 dBL 0.76 Mb @ 256.0 Hz (0.0117 sec)	Acoustic Scale: 0.80 Mb (0.200 Mb/Div)
Last Calibration Date: 7/9/2012	Time Intervals: 0.50 sec

Cal 0.00 LO

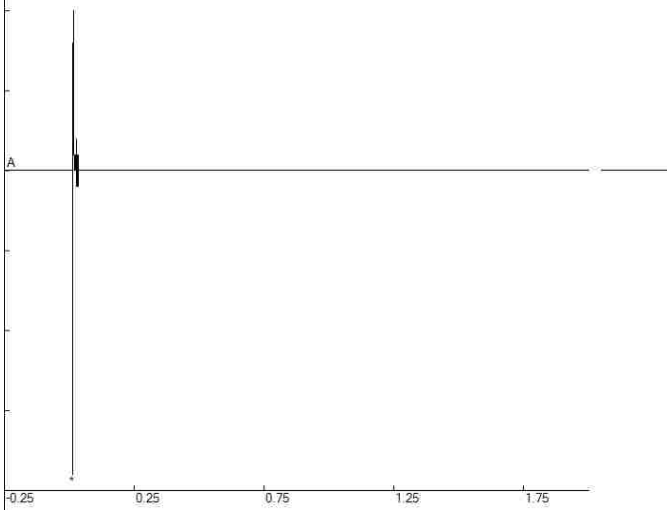

Blast A8 - Air

File: A8_Air3_7852013022318000075.dtb
Number: 075
Date: 2/23/2013
Time: 18:00
SN: 0785
Seis. Trigger: 0.0300 in/sec
Air Trigger: 106
Sample Rate: 2048
Duration: 2.0 Seconds
Pre-Trigger: 0.25 Seconds
Gain: 4.0x
Voltage: 6.1

Peaks and Frequencies	Graph Information
PPV Maximum: 0.0025 in/sec (0.0190 sec)	Duration: -0.250 s To: 2.000 s
Acoustic: 128 dBL 0.48 Mb @ 256.0 Hz (0.0195 sec)	Acoustic Scale: 0.80 Mb (0.200 Mb/Div)
Last Calibration Date: 6/8/2012	Time Intervals: 0.50 sec

Cal 0.04 LO

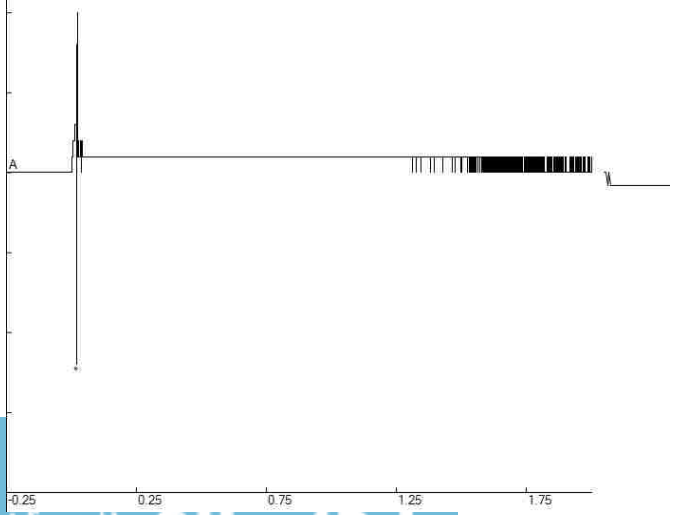

Blast A9 - Air

File: A9_Air1_5069201302231633062.dtb
Number: 062
Date: 2/23/2013
Time: 16:33
SN: 5069
Seis. Trigger: 0.030 in/sec
Air Trigger: 124
Sample Rate: 2048
Duration: 2.0 Seconds
Pre-Trigger: 0.25 Seconds
Gain: 2.0x
Voltage: 6.5

Peaks and Frequencies	Graph Information
PPV Maximum: 0.015 in/sec (0.0073 sec)	Duration: -0.250 s To: 2.000 s
Acoustic: 136 dBL 1.24 Mb @ 256.0 Hz (0.0073 sec)	Acoustic Scale: 1.60 Mb (0.400 Mb/Div)
Last Calibration Date: 11/6/2012	Time Intervals: 0.50 sec

Cal 0.00 LO

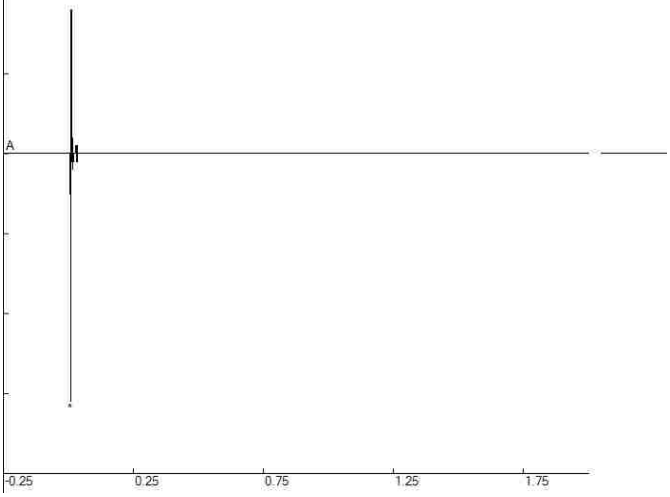

Blast A9 - Air

File: A9_Air2_5039201302231633062.dtb
Number: 062
Date: 2/23/2013
Time: 16:33
SN: 5039
Seis. Trigger: 0.0600 in/sec
Air Trigger: 124
Sample Rate: 2048
Duration: 2.0 Seconds
Pre-Trigger: 0.25 Seconds
Gain: 4.0x
Voltage: 6.4

Peaks and Frequencies	Graph Information
PPV Maximum: 0.0050 in/sec (0.0112 sec)	Duration: -0.250 s To: 2.000 s
Acoustic: 133 dBL 0.92 Mb @ 256.0 Hz (0.0117 sec)	Acoustic Scale: 1.20 Mb (0.300 Mb/Div)
Last Calibration Date: 7/9/2012	Time Intervals: 0.50 sec

Cal 0.00 LO

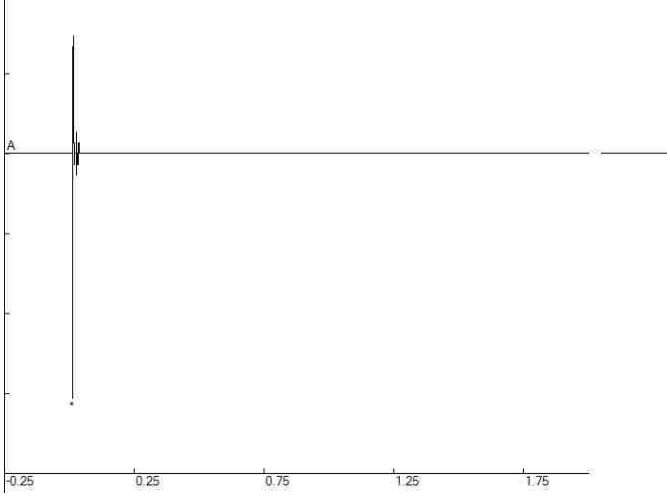

Blast A9 - Air

File: A9_Air3_7852013022316340 62.dtb
Number: 062
Date: 2/23/2013
Time: 16:34
SN: 0785
Seis. Trigger: 0.0300 in/sec
Air Trigger: 106
Sample Rate: 2048
Duration: 2.0 Seconds
Pre-Trigger: 0.25 Seconds
Gain: 4.0x
Voltage: 6.1

Peaks and Frequencies	Graph Information
PPV Maximum: 0.0025 in/sec (0.0190 sec)	Duration: -0.250 s To: 2.000 s
Acoustic: 129 dBL 0.56 Mb @ 341.3 Hz (0.0195 sec)	Acoustic Scale: 0.80 Mb (0.200 Mb/Div)
Last Calibration Date: 6/8/2012	Time Intervals: 0.50 sec

Cal 0.04 LO

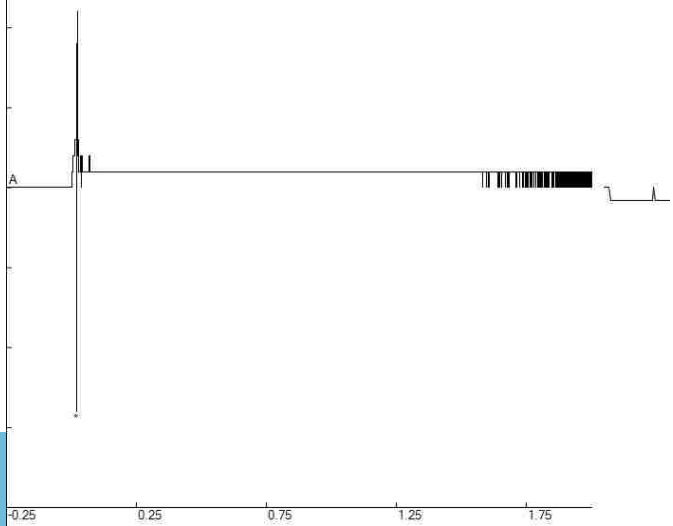

Blast A10 - Air

File: A10_Air1_5069201302231728070.dtb
Number: 070
Date: 2/23/2013
Time: 17:28
SN: 5069
Seis. Trigger: 0.030 in/sec
Air Trigger: 124
Sample Rate: 2048
Duration: 2.0 Seconds
Pre-Trigger: 0.25 Seconds
Gain: 2.0x
Voltage: 6.5

Peaks and Frequencies	Graph Information
PPV Maximum: 0.015 in/sec (0.0073 sec)	Duration: -0.250 s To: 2.000 s
Acoustic: 137 dBL 1.44 Mb @ 256.0 Hz (0.0078 sec)	Acoustic Scale: 1.60 Mb (0.400 Mb/Div)
Last Calibration Date: 11/6/2012	Time Intervals: 0.50 sec

Cal 0.00 LO

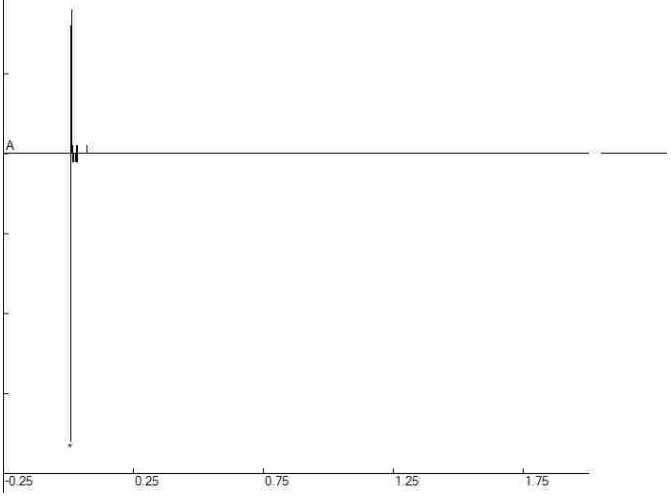

Blast A10 - Air

File: A10_Air2_5039201302231729070.dtb
Number: 070
Date: 2/23/2013
Time: 17:29
SN: 5039
Seis. Trigger: 0.0600 in/sec
Air Trigger: 124
Sample Rate: 2048
Duration: 2.0 Seconds
Pre-Trigger: 0.25 Seconds
Gain: 4.0x
Voltage: 6.4

Peaks and Frequencies	Graph Information
PPV Maximum: 0.0050 in/sec (0.0112 sec)	Duration: -0.250 s To: 2.000 s
Acoustic: 134 dBL 1.00 Mb @ 256.0 Hz (0.0122 sec)	Acoustic Scale: 1.20 Mb (0.300 Mb/Div)
Last Calibration Date: 7/9/2012	Time Intervals: 0.50 sec

Cal 0.00 LO

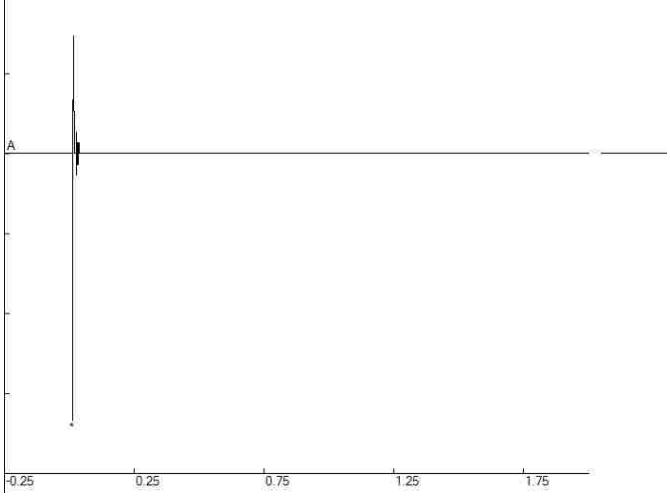

Blast A10 - Air

File: A10_Air3_7852013022317300 70.dtb
Number: 070
Date: 2/23/2013
Time: 17:30
SN: 0785
Seis. Trigger: 0.0300 in/sec
Air Trigger: 106
Sample Rate: 2048
Duration: 2.0 Seconds
Pre-Trigger: 0.25 Seconds
Gain: 4.0x
Voltage: 6.1

Peaks and Frequencies	Graph Information
PPV Maximum: 0.0050 in/sec (0.0205 sec)	Duration: -0.250 s To: 2.000 s
Acoustic: 130 dBL 0.60 Mb @ 256.0 Hz (0.0195 sec)	Acoustic Scale: 0.80 Mb (0.200 Mb/Div)
Last Calibration Date: 6/8/2012	Time Intervals: 0.50 sec

Cal 0.04 LO

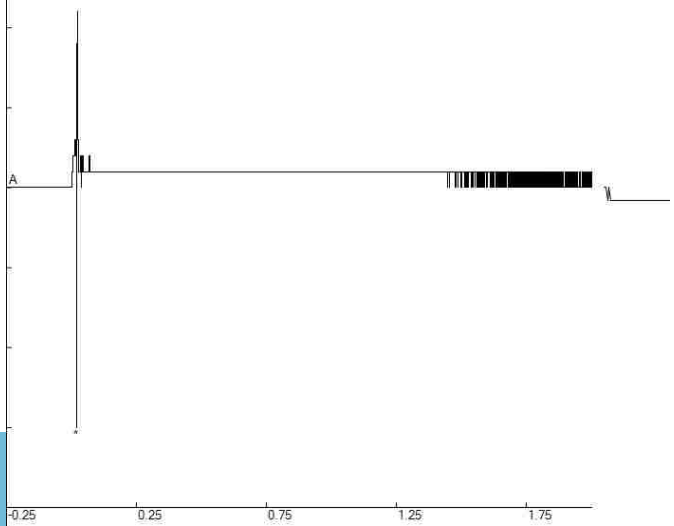

Blast A11 - Air

File: A11_Air1_5069201302231647063.dtb
Number: 063
Date: 2/23/2013
Time: 16:47
SN: 5069
Seis. Trigger: 0.030 in/sec
Air Trigger: 124
Sample Rate: 2048
Duration: 2.0 Seconds
Pre-Trigger: 0.25 Seconds
Gain: 2.0x
Voltage: 6.5

Peaks and Frequencies	Graph Information
PPV Maximum: 0.015 in/sec (0.0073 sec)	Duration: -0.250 s To: 2.000 s
Acoustic: 137 dBL 1.36 Mb @ 256.0 Hz (0.0073 sec)	Acoustic Scale: 1.60 Mb (0.400 Mb/Div)
Last Calibration Date: 11/6/2012	Time Intervals: 0.50 sec

Cal 0.00 LO

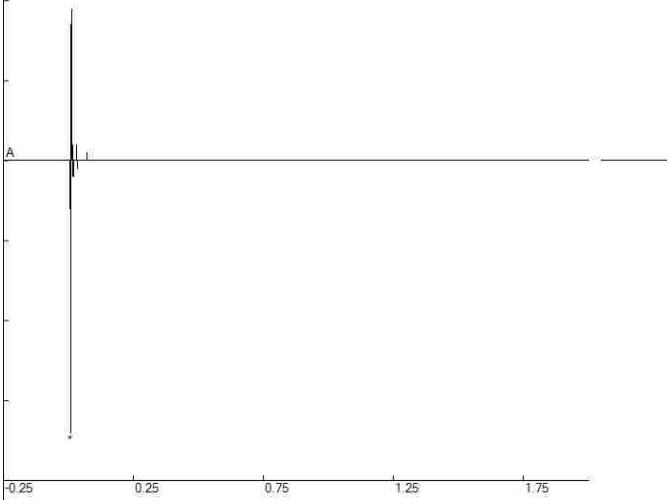

Blast A11 - Air

File: A11_Air2_5039201302231647063.dtb
Number: 063
Date: 2/23/2013
Time: 16:47
SN: 5039
Seis. Trigger: 0.0600 in/sec
Air Trigger: 124
Sample Rate: 2048
Duration: 2.0 Seconds
Pre-Trigger: 0.25 Seconds
Gain: 4.0x
Voltage: 6.4

Peaks and Frequencies	Graph Information
PPV Maximum: 0.0050 in/sec (0.0112 sec)	Duration: -0.250 s To: 2.000 s
Acoustic: 134 dBL 1.00 Mb @ 256.0 Hz (0.0117 sec)	Acoustic Scale: 1.20 Mb (0.300 Mb/Div)
Last Calibration Date: 7/9/2012	Time Intervals: 0.50 sec

Cal 0.00 LO

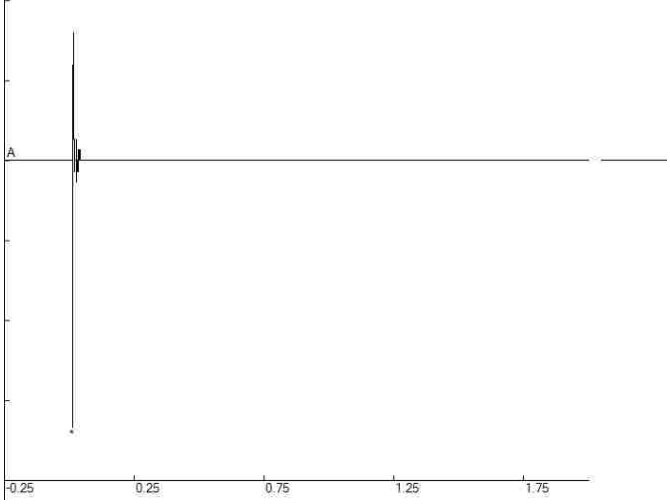

Blast A11 - Air

File: A11_Air3_7852013022316480 63.dtb
Number: 063
Date: 2/23/2013
Time: 16:48
SN: 0785
Seis. Trigger: 0.0300 in/sec
Air Trigger: 106
Sample Rate: 2048
Duration: 2.0 Seconds
Pre-Trigger: 0.25 Seconds
Gain: 4.0x
Voltage: 6.1

Peaks and Frequencies	Graph Information
PPV Maximum: 0.0025 in/sec (0.0186 sec)	Duration: -0.250 s To: 2.000 s
Acoustic: 130 dBL 0.64 Mb @ 256.0 Hz (0.0190 sec)	Acoustic Scale: 0.80 Mb (0.200 Mb/Div)
Last Calibration Date: 6/8/2012	Time Intervals: 0.50 sec

Cal 0.04 LO

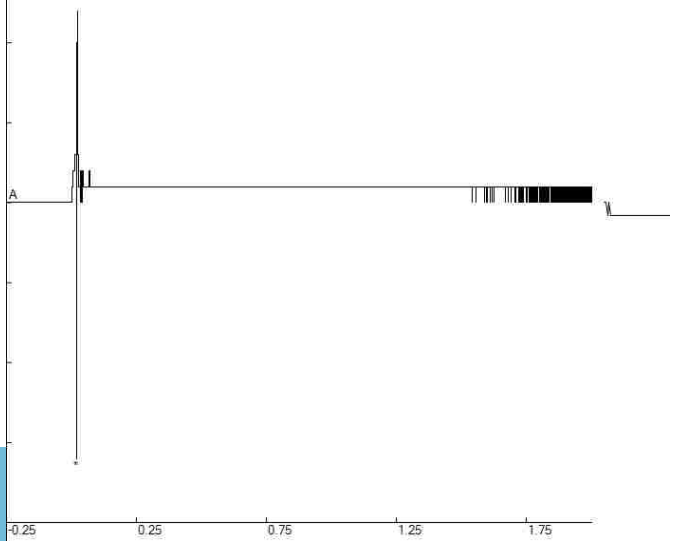

Blast B1 - Air

File: B1_Air1_506920130224104300 4.dtb
Number: 004
Date: 2/24/2013
Time: 10:43
SN: 5069
Seis. Trigger: 0.030 in/sec
Air Trigger: 124
Sample Rate: 2048
Duration: 2.0 Seconds
Pre-Trigger: 0.25 Seconds
Gain: 2.0x
Voltage: 6.4

Peaks and Frequencies	Graph Information
PPV Maximum: 0.005 in/sec (0.0010 sec)	Duration: -0.250 s To: 2.000 s
Acoustic: 122 dBL 0.24 Mb @ 341.3 Hz (0.0029 sec)	Acoustic Scale: 0.40 Mb (0.100 Mb/Div)
Last Calibration Date: 11/6/2012	Time Intervals: 0.50 sec

Cal 0.00 LO

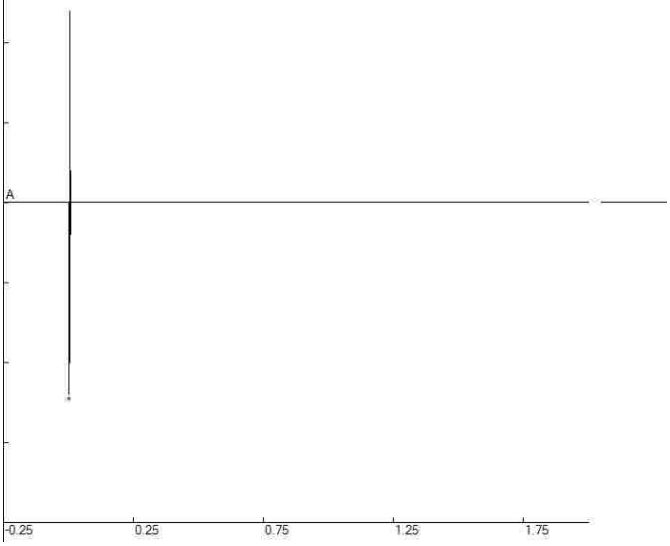

Blast B1 - Air

File: B1_Air2_785201302241045004.dtb
Number: 004
Date: 2/24/2013
Time: 10:45
SN: 0785
Seis. Trigger: 0.0300 in/sec
Air Trigger: 106
Sample Rate: 2048
Duration: 2.0 Seconds
Pre-Trigger: 0.25 Seconds
Gain: 4.0x
Voltage: 6.0

Peaks and Frequencies	Graph Information
PPV Maximum: 0.0025 in/sec (0.0103 sec)	Duration: -0.250 s To: 2.000 s
Acoustic: 120 dBL 0.20 Mb @ 3.9 Hz (0.0107 sec)	Acoustic Scale: 0.40 Mb (0.100 Mb/Div)
Last Calibration Date: 6/8/2012	Time Intervals: 0.50 sec

Cal 0.04 LO

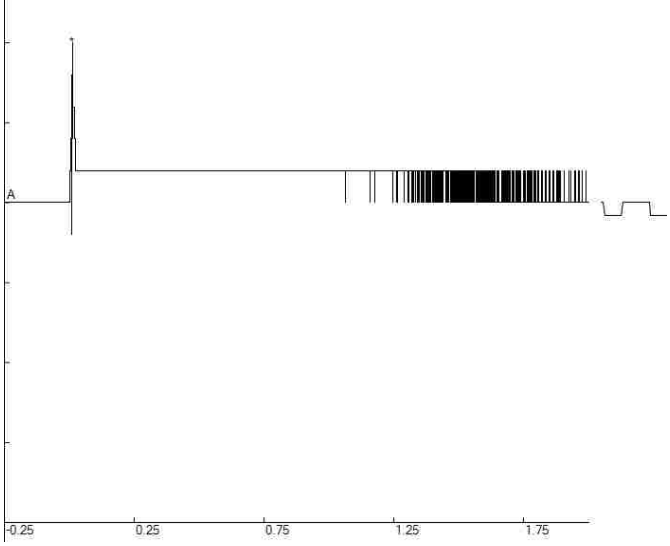

Blast B1 - Air

File: B1_Air3_503920130224104400 4.dtb
Number: 004
Date: 2/24/2013
Time: 10:44
SN: 5039
Seis. Trigger: 0.0600 in/sec
Air Trigger: 124
Sample Rate: 2048
Duration: 2.0 Seconds
Pre-Trigger: 0.25 Seconds
Gain: 4.0x
Voltage: 6.3

Peaks and Frequencies	Graph Information
PPV Maximum: 0.0050 in/sec (0.0112 sec)	Duration: -0.250 s To: 2.000 s
Acoustic: 112 dBL 0.08 Mb @ 0.0 Hz (0.0181 sec)	Acoustic Scale: 0.40 Mb (0.100 Mb/Div)
Last Calibration Date: 7/9/2012	Time Intervals: 0.50 sec

Cal 0.00 LO

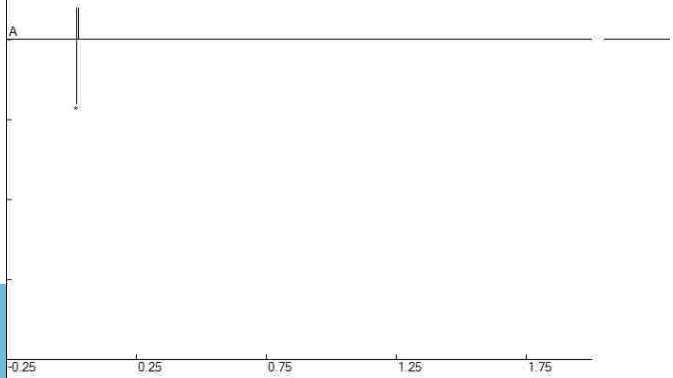

Blast B2 - Air

File: B2_Air1_506920130224110400 5.dtb
Number: 005
Date: 2/24/2013
Time: 11:04
SN: 5069
Seis. Trigger: 0.030 in/sec
Air Trigger: 124
Sample Rate: 2048
Duration: 2.0 Seconds
Pre-Trigger: 0.25 Seconds
Gain: 2.0x
Voltage: 6.4

Peaks and Frequencies	Graph Information
PPV Maximum: 0.010 in/sec (0.0024 sec)	Duration: -0.250 s To: 2.000 s
Acoustic: 128 dBL 0.52 Mb @ 512.0 Hz (0.0024 sec)	Acoustic Scale: 0.80 Mb (0.200 Mb/Div)
Last Calibration Date: 11/6/2012	Time Intervals: 0.50 sec

Cal 0.00 LO

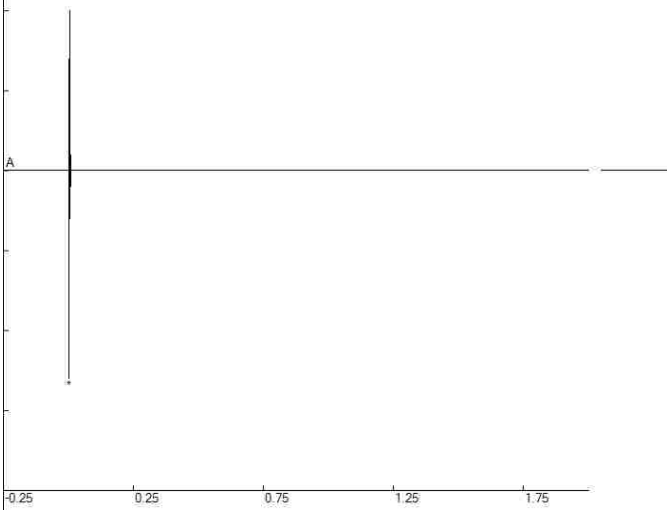

Blast B2 - Air

File: B2_Air2_785201302241106005.dtb
Number: 005
Date: 2/24/2013
Time: 11:06
SN: 0785
Seis. Trigger: 0.0300 in/sec
Air Trigger: 106
Sample Rate: 2048
Duration: 2.0 Seconds
Pre-Trigger: 0.25 Seconds
Gain: 4.0x
Voltage: 6.0

Peaks and Frequencies	Graph Information
PPV Maximum: 0.0025 in/sec (0.0098 sec)	Duration: -0.250 s To: 2.000 s
Acoustic: 123 dBL 0.28 Mb @ 3.9 Hz (0.0103 sec)	Acoustic Scale: 0.40 Mb (0.100 Mb/Div)
Last Calibration Date: 6/8/2012	Time Intervals: 0.50 sec

Cal 0.04 LO

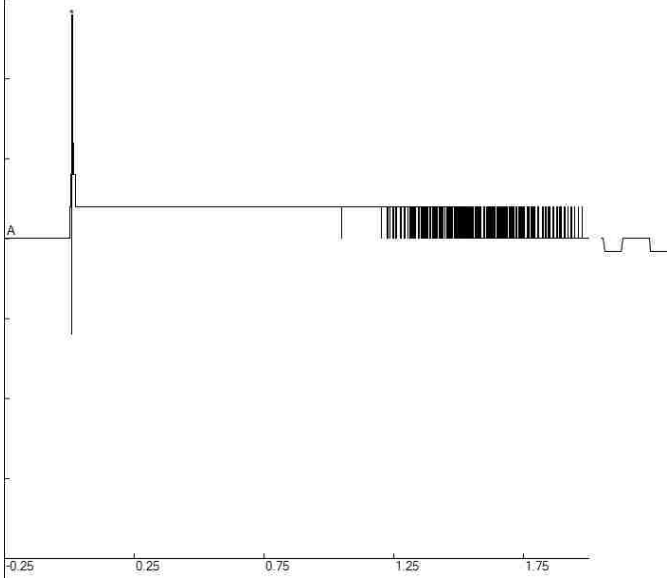

Blast B2 - Air

File: B2_Air3_503920130224110500 5.dtb
Number: 005
Date: 2/24/2013
Time: 11:05
SN: 5039
Seis. Trigger: 0.0600 in/sec
Air Trigger: 124
Sample Rate: 2048
Duration: 2.0 Seconds
Pre-Trigger: 0.25 Seconds
Gain: 4.0x
Voltage: 6.4

Peaks and Frequencies	Graph Information
PPV Maximum: 0.0050 in/sec (0.0112 sec)	Duration: -0.250 s To: 2.000 s
Acoustic: 112 dBL 0.08 Mb @ 0.0 Hz (0.0176 sec)	Acoustic Scale: 0.40 Mb (0.100 Mb/Div)
Last Calibration Date: 7/9/2012	Time Intervals: 0.50 sec

Cal 0.00 LO

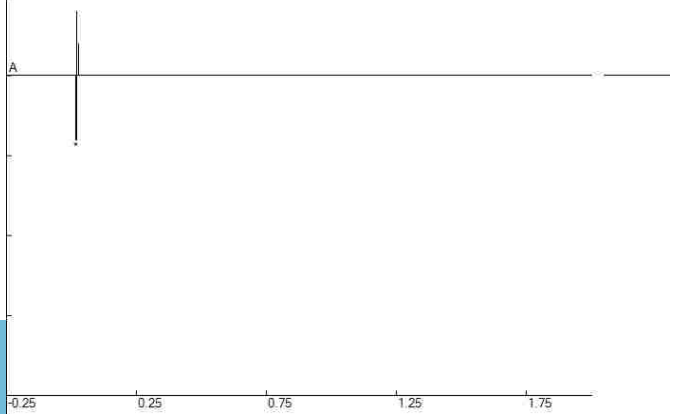

Blast B3 - Air

File: B3_Air1_506920130224112400 6.dtb
Number: 006
Date: 2/24/2013
Time: 11:24
SN: 5069
Seis. Trigger: 0.030 in/sec
Air Trigger: 124
Sample Rate: 2048
Duration: 2.0 Seconds
Pre-Trigger: 0.25 Seconds
Gain: 2.0x
Voltage: 6.4

Peaks and Frequencies	Graph Information
PPV Maximum: 0.005 in/sec (0.0000 sec)	Duration: -0.250 s To: 2.000 s
Acoustic: 130 dBL 0.64 Mb @ 341.3 Hz (0.0029 sec)	Acoustic Scale: 0.80 Mb (0.200 Mb/Div)
Last Calibration Date: 11/6/2012	Time Intervals: 0.50 sec

Cal 0.00 LO

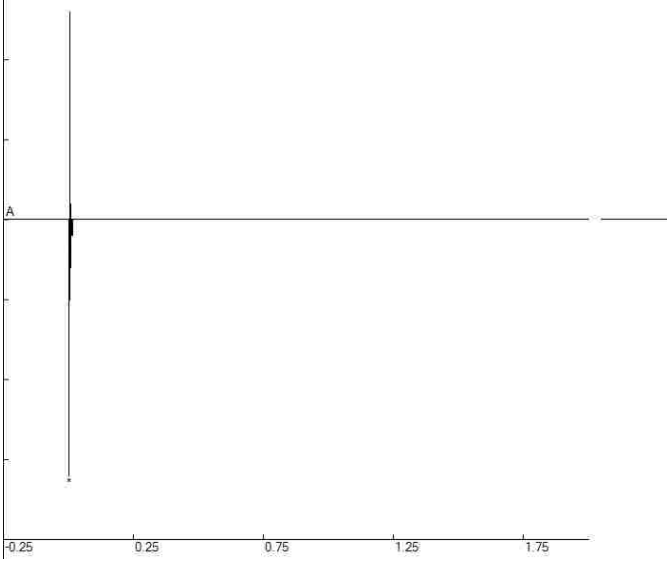

Blast B3 - Air

File: B3_Air2_785201302241125006.dtb
Number: 006
Date: 2/24/2013
Time: 11:25
SN: 0785
Seis. Trigger: 0.0300 in/sec
Air Trigger: 106
Sample Rate: 2048
Duration: 2.0 Seconds
Pre-Trigger: 0.25 Seconds
Gain: 4.0x
Voltage: 6.0

Peaks and Frequencies	Graph Information
PPV Maximum: 0.0025 in/sec (0.0098 sec)	Duration: -0.250 s To: 2.000 s
Acoustic: 124 dBL 0.32 Mb @ 3.9 Hz (0.0107 sec)	Acoustic Scale: 0.40 Mb (0.100 Mb/Div)
Last Calibration Date: 6/8/2012	Time Intervals: 0.50 sec

Cal 0.04 LO

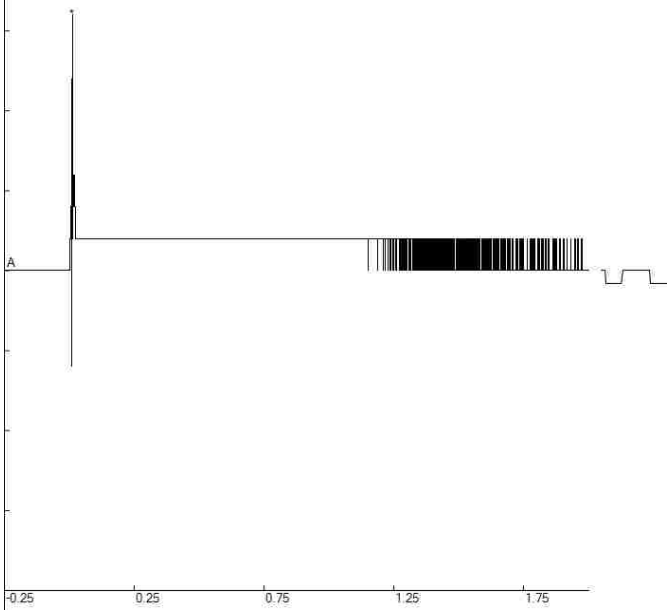

Blast B3 - Air

File: B3_Air3_503920130224112400 6.dtb
Number: 006
Date: 2/24/2013
Time: 11:24
SN: 5039
Seis. Trigger: 0.0600 in/sec
Air Trigger: 124
Sample Rate: 2048
Duration: 2.0 Seconds
Pre-Trigger: 0.25 Seconds
Gain: 4.0x
Voltage: 6.3

Peaks and Frequencies	Graph Information
PPV Maximum: 0.0050 in/sec (0.0127 sec)	Duration: -0.250 s To: 2.000 s
Acoustic: 112 dBL 0.08 Mb @ 0.0 Hz (0.0176 sec)	Acoustic Scale: 0.40 Mb (0.100 Mb/Div)
Last Calibration Date: 7/9/2012	Time Intervals: 0.50 sec

Cal 0.00 LO

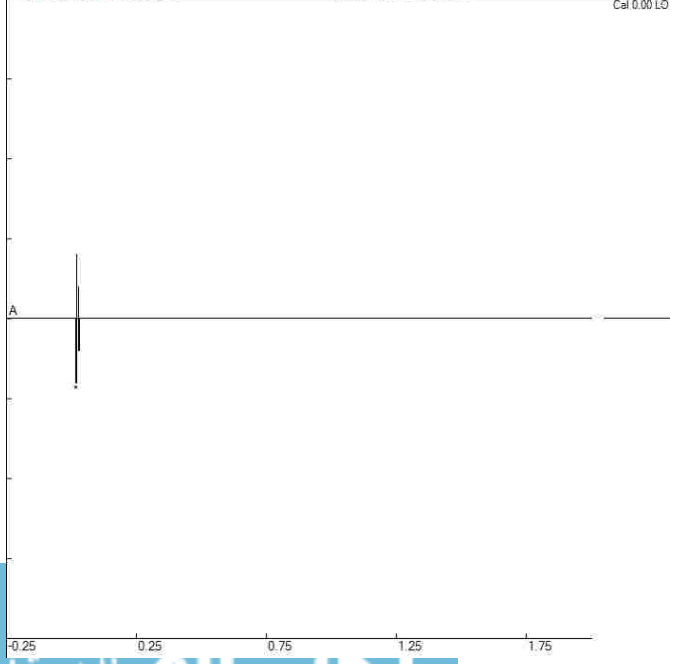

Blast B4 - Air

File: B4_Air1_506920130224114900 7.dtb
Number: 007
Date: 2/24/2013
Time: 11:49
SN: 5069
Seis. Trigger: 0.030 in/sec
Air Trigger: 124
Sample Rate: 2048
Duration: 2.0 Seconds
Pre-Trigger: 0.25 Seconds
Gain: 2.0x
Voltage: 6.4

Peaks and Frequencies	Graph Information
PPV Maximum: 0.015 in/sec (0.0024 sec)	Duration: -0.250 s To: 2.000 s
Acoustic: 134 dBL 1.00 Mb @ 341.3 Hz (0.0029 sec)	Acoustic Scale: 1.20 Mb (0.300 Mb/Div)
Last Calibration Date: 11/6/2012	Time Intervals: 0.50 sec

Cal 0.00 LO

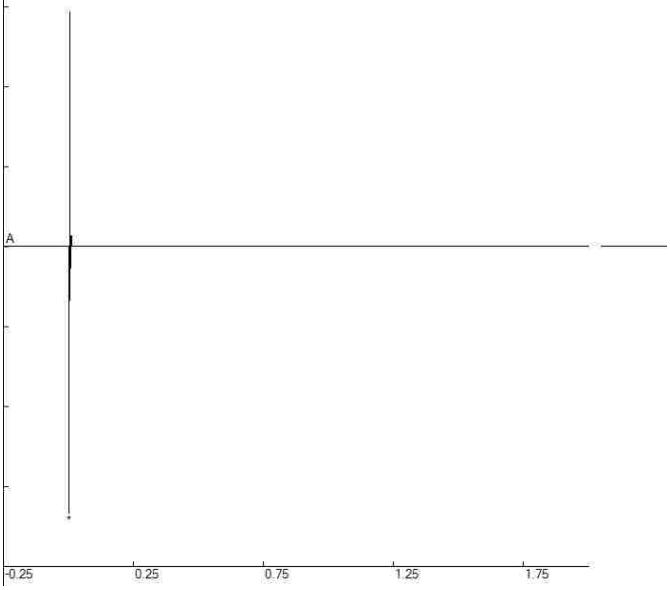

Blast B4 - Air

File: B4_Air2_785201302241151007.dtb
Number: 007
Date: 2/24/2013
Time: 11:51
SN: 0785
Seis. Trigger: 0.0300 in/sec
Air Trigger: 106
Sample Rate: 2048
Duration: 2.0 Seconds
Pre-Trigger: 0.25 Seconds
Gain: 4.0x
Voltage: 6.0

Peaks and Frequencies	Graph Information
PPV Maximum: 0.0025 in/sec (0.0083 sec)	Duration: -0.250 s To: 2.000 s
Acoustic: 128 dBL 0.48 Mb @ 3.9 Hz (0.0107 sec)	Acoustic Scale: 0.80 Mb (0.200 Mb/Div)
Last Calibration Date: 6/8/2012	Time Intervals: 0.50 sec

Cal 0.04 LO

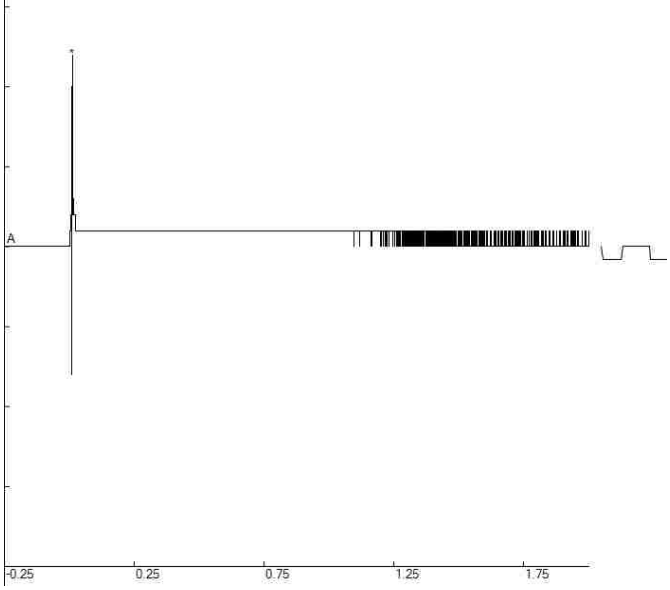

Blast B4 - Air

File: B4_Air3_503920130224115000 7.dtb
Number: 007
Date: 2/24/2013
Time: 11:50
SN: 5039
Seis. Trigger: 0.0600 in/sec
Air Trigger: 124
Sample Rate: 2048
Duration: 2.0 Seconds
Pre-Trigger: 0.25 Seconds
Gain: 4.0x
Voltage: 6.3

Peaks and Frequencies	Graph Information
PPV Maximum: 0.0050 in/sec (0.0112 sec)	Duration: -0.250 s To: 2.000 s
Acoustic: 118 dBL 0.16 Mb @ 204.8 Hz (0.0181 sec)	Acoustic Scale: 0.40 Mb (0.100 Mb/Div)
Last Calibration Date: 7/9/2012	Time Intervals: 0.50 sec

Cal 0.00 LO

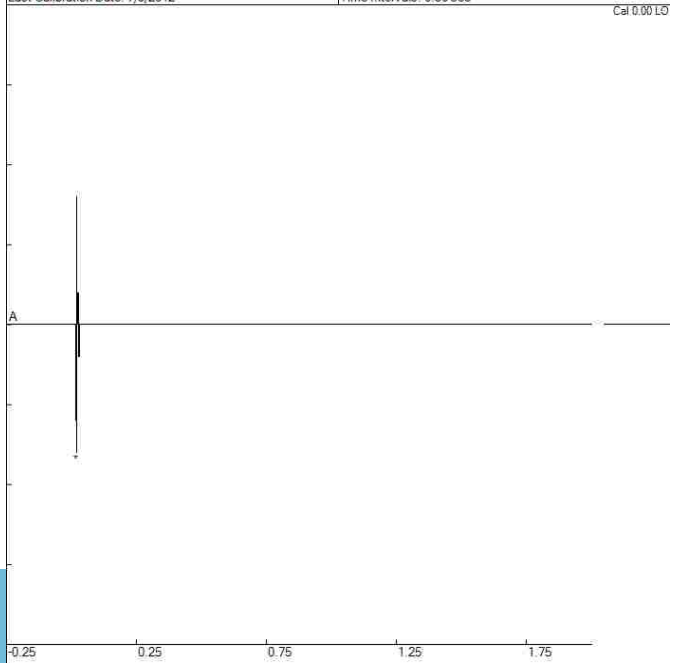

Blast B5 - Air

File: B5_Air1_5069201302241209008.dtb
Number: 008
Date: 2/24/2013
Time: 12:09
SN: 5069
Seis. Trigger: 0.030 in/sec
Air Trigger: 124
Sample Rate: 2048
Duration: 2.0 Seconds
Pre-Trigger: 0.25 Seconds
Gain: 2.0x
Voltage: 6.4

Peaks and Frequencies	Graph Information
PPV Maximum: 0.020 in/sec (0.0024 sec)	Duration: -0.250 s To: 2.000 s
Acoustic: 136 dBL 1.24 Mb @ 341.3 Hz (0.0029 sec)	Acoustic Scale: 1.60 Mb (0.400 Mb/Div)
Last Calibration Date: 11/6/2012	Time Intervals: 0.50 sec

Cal 0.00 LO

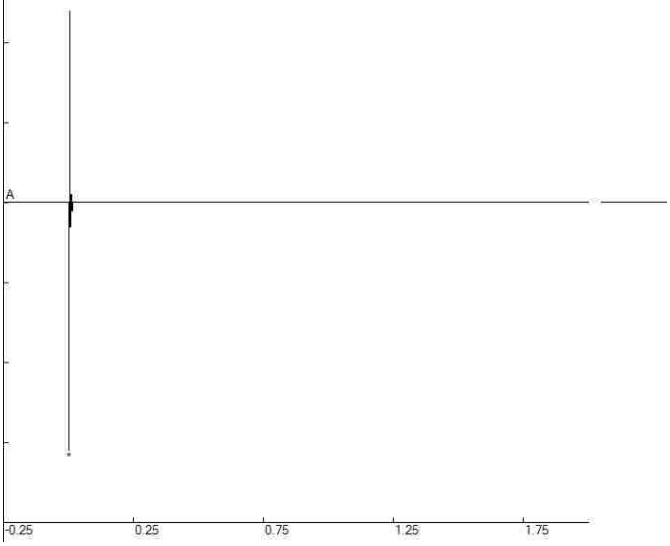

Blast B5 - Air

File: B5_Air2_7852013022412100008.dtb
Number: 008
Date: 2/24/2013
Time: 12:10
SN: 0785
Seis. Trigger: 0.0300 in/sec
Air Trigger: 106
Sample Rate: 2048
Duration: 2.0 Seconds
Pre-Trigger: 0.25 Seconds
Gain: 4.0x
Voltage: 6.0

Peaks and Frequencies	Graph Information
PPV Maximum: 0.0025 in/sec (0.0078 sec)	Duration: -0.250 s To: 2.000 s
Acoustic: 129 dBL 0.56 Mb @ 3.9 Hz (0.0107 sec)	Acoustic Scale: 0.80 Mb (0.200 Mb/Div)
Last Calibration Date: 6/8/2012	Time Intervals: 0.50 sec

Cal 0.04 LO

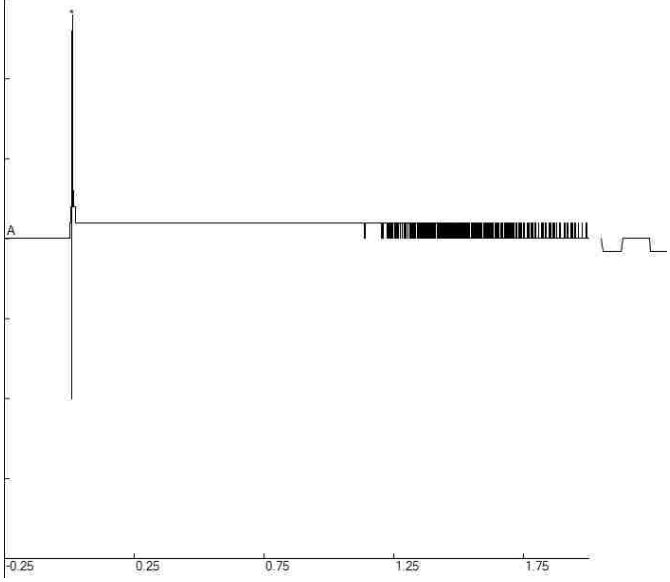

Blast B5 - Air

File: B5_Air3_5039201302241210008.dtb
Number: 008
Date: 2/24/2013
Time: 12:10
SN: 5039
Seis. Trigger: 0.0600 in/sec
Air Trigger: 124
Sample Rate: 2048
Duration: 2.0 Seconds
Pre-Trigger: 0.25 Seconds
Gain: 4.0x
Voltage: 6.3

Peaks and Frequencies	Graph Information
PPV Maximum: 0.0050 in/sec (0.0122 sec)	Duration: -0.250 s To: 2.000 s
Acoustic: 120 dBL 0.20 Mb @ 204.8 Hz (0.0176 sec)	Acoustic Scale: 0.40 Mb (0.100 Mb/Div)
Last Calibration Date: 7/9/2012	Time Intervals: 0.50 sec

Cal 0.00 LO

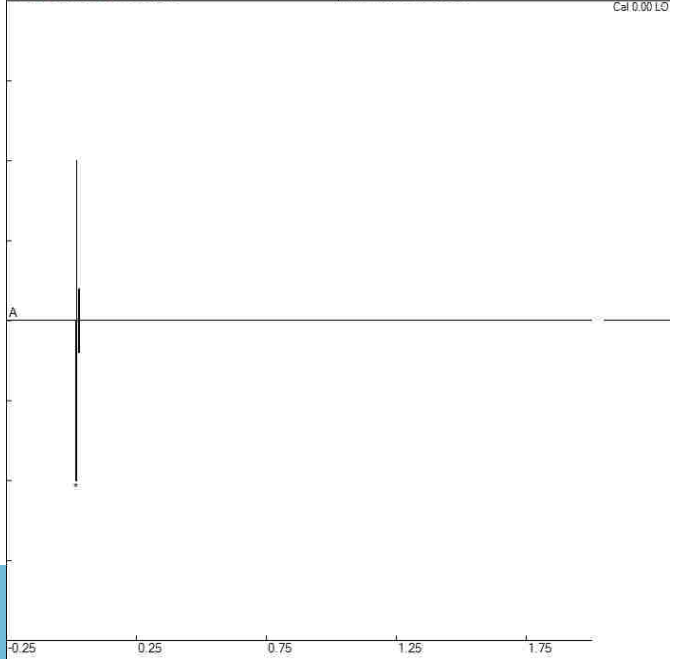

Blast B6 - Air

File: B6_Air1_5069201302241318014.dtb
Number: 014
Date: 2/24/2013
Time: 13:18
SN: 5069
Seis. Trigger: 0.030 in/sec
Air Trigger: 124
Sample Rate: 2048
Duration: 2.0 Seconds
Pre-Trigger: 0.25 Seconds
Gain: 2.0x
Voltage: 6.4

Peaks and Frequencies	Graph Information
PPV Maximum: 0.015 in/sec (0.0020 sec)	Duration: -0.250 s To: 2.000 s
Acoustic: 139 dBL 1.88 Mb @ 341.3 Hz (0.0024 sec)	Acoustic Scale: 2.00 Mb (0.500 Mb/Div)
Last Calibration Date: 11/6/2012	Time Intervals: 0.50 sec

Cal 0.00 LO

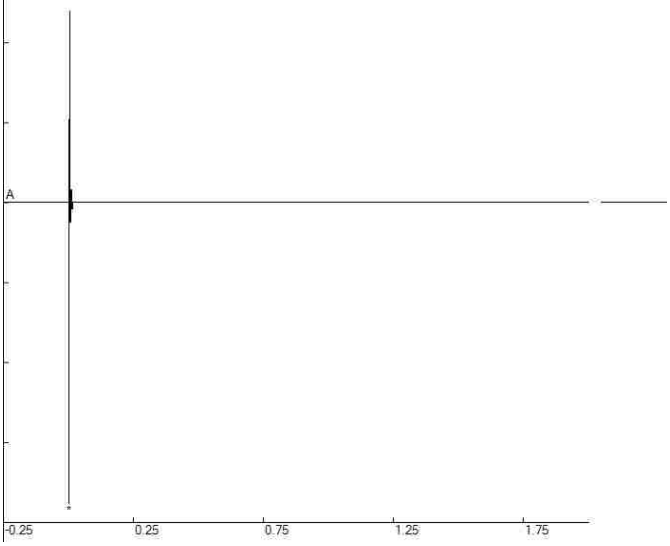

Blast B6 - Air

File: B6_Air2_7852013022413190l4.dtb
Number: 014
Date: 2/24/2013
Time: 13:19
SN: 0785
Seis. Trigger: 0.0300 in/sec
Air Trigger: 106
Sample Rate: 2048
Duration: 2.0 Seconds
Pre-Trigger: 0.25 Seconds
Gain: 4.0x
Voltage: 6.0

Peaks and Frequencies	Graph Information
PPV Maximum: 0.0025 in/sec (0.0083 sec)	Duration: -0.250 s To: 2.000 s
Acoustic: 130 dBL 0.64 Mb @ 3.9 Hz (0.0112 sec)	Acoustic Scale: 0.80 Mb (0.200 Mb/Div)
Last Calibration Date: 6/8/2012	Time Intervals: 0.50 sec

Cal 0.04 LO

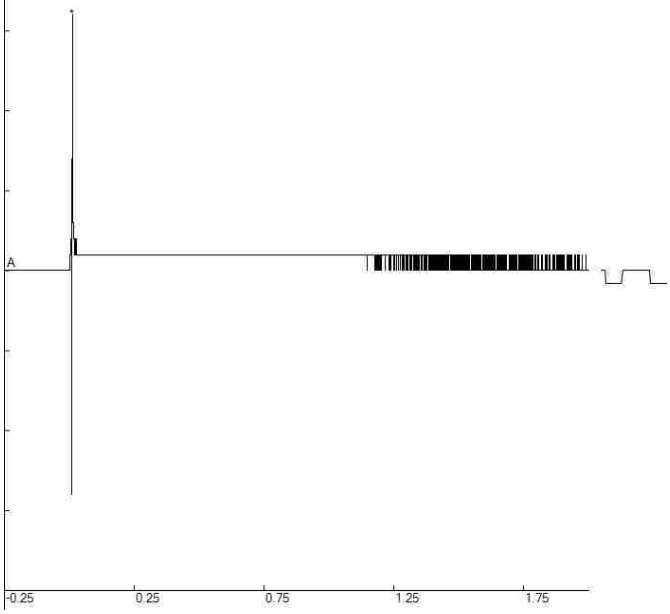

Blast B6 - Air

File: B6_Air3_5039201302241318014.dtb
Number: 014
Date: 2/24/2013
Time: 13:18
SN: 5039
Seis. Trigger: 0.0600 in/sec
Air Trigger: 124
Sample Rate: 2048
Duration: 2.0 Seconds
Pre-Trigger: 0.25 Seconds
Gain: 4.0x
Voltage: 6.3

Peaks and Frequencies	Graph Information
PPV Maximum: 0.0050 in/sec (0.0000 sec)	Duration: -0.250 s To: 2.000 s
Acoustic: 122 dBL 0.24 Mb @ 146.2 Hz (0.0176 sec)	Acoustic Scale: 0.40 Mb (0.100 Mb/Div)
Last Calibration Date: 7/9/2012	Time Intervals: 0.50 sec

Cal 0.00 LO

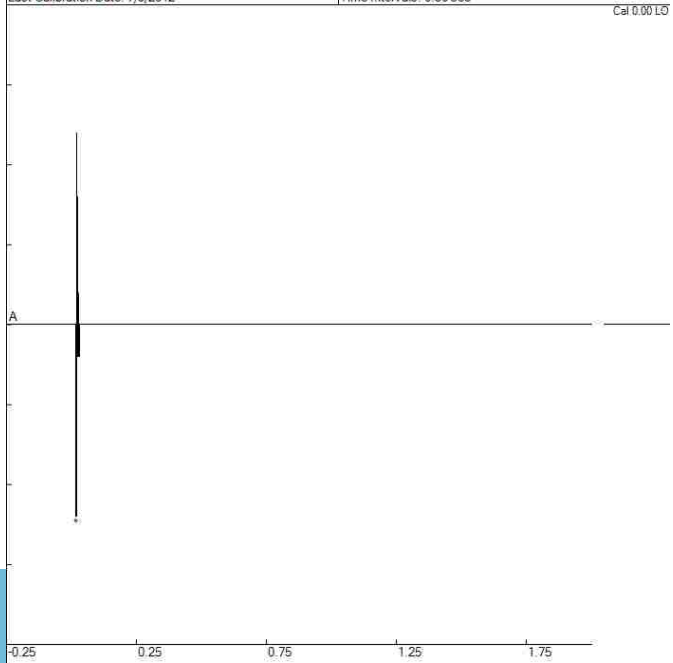

Blast B7 - Air

File: B7_Air1_5069201302241229009.dtb
Number: 009
Date: 2/24/2013
Time: 12:29
SN: 5069
Seis. Trigger: 0.030 in/sec
Air Trigger: 124
Sample Rate: 2048
Duration: 2.0 Seconds
Pre-Trigger: 0.25 Seconds
Gain: 2.0x
Voltage: 6.4

Peaks and Frequencies	Graph Information
PPV Maximum: 0.025 in/sec (0.0015 sec)	Duration: -0.250 s To: 2.000 s
Acoustic: 142 dBL 2.64 Mb @ 341.3 Hz (0.0020 sec)	Acoustic Scale: 2.80 Mb (0.700 Mb/Div)
Last Calibration Date: 11/6/2012	Time Intervals: 0.50 sec

Cal 0.00 LO

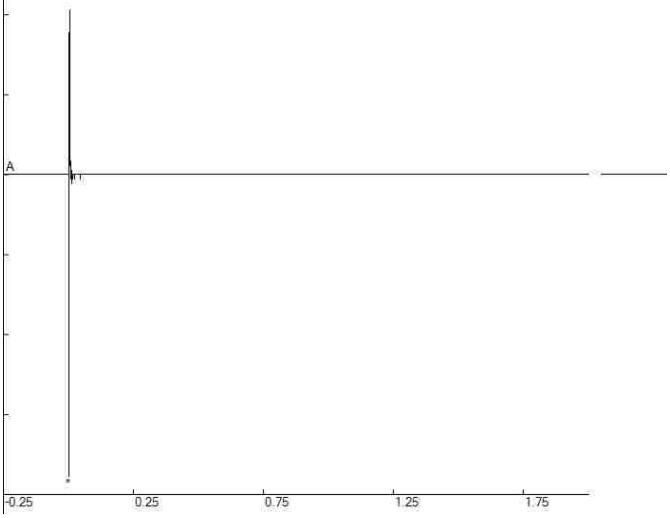

Blast B7 - Air

File: B7_Air2_7852013022412310008.dtb
Number: 009
Date: 2/24/2013
Time: 12:31
SN: 0785
Seis. Trigger: 0.0300 in/sec
Air Trigger: 106
Sample Rate: 2048
Duration: 2.0 Seconds
Pre-Trigger: 0.25 Seconds
Gain: 4.0x
Voltage: 6.0

Peaks and Frequencies	Graph Information
PPV Maximum: 0.0050 in/sec (0.0093 sec)	Duration: -0.250 s To: 2.000 s
Acoustic: 132 dBL 0.84 Mb @ 341.3 Hz (0.0083 sec)	Acoustic Scale: 1.20 Mb (0.300 Mb/Div)
Last Calibration Date: 6/8/2012	Time Intervals: 0.50 sec

Cal 0.04 LO

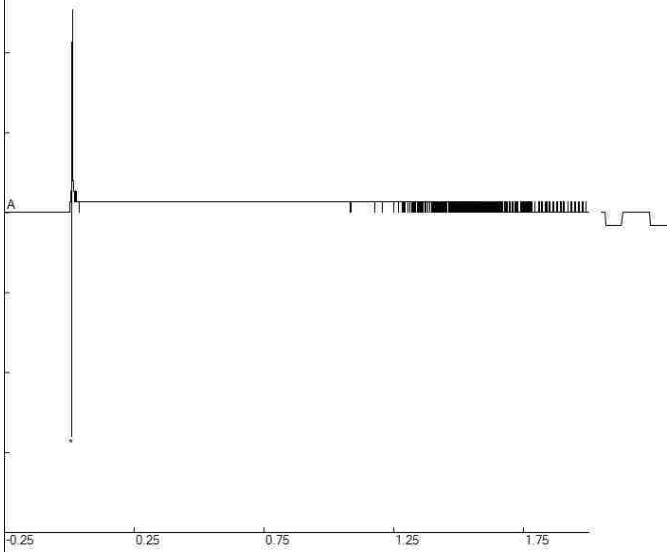

Blast B7 - Air

File: B7_Air3_5039201302241230009.dtb
Number: 009
Date: 2/24/2013
Time: 12:30
SN: 5039
Seis. Trigger: 0.0600 in/sec
Air Trigger: 124
Sample Rate: 2048
Duration: 2.0 Seconds
Pre-Trigger: 0.25 Seconds
Gain: 4.0x
Voltage: 6.3

Peaks and Frequencies	Graph Information
PPV Maximum: 0.0050 in/sec (0.0166 sec)	Duration: -0.250 s To: 2.000 s
Acoustic: 125 dBL 0.36 Mb @ 204.8 Hz (0.0171 sec)	Acoustic Scale: 0.40 Mb (0.100 Mb/Div)
Last Calibration Date: 7/9/2012	Time Intervals: 0.50 sec

Cal 0.00 LO

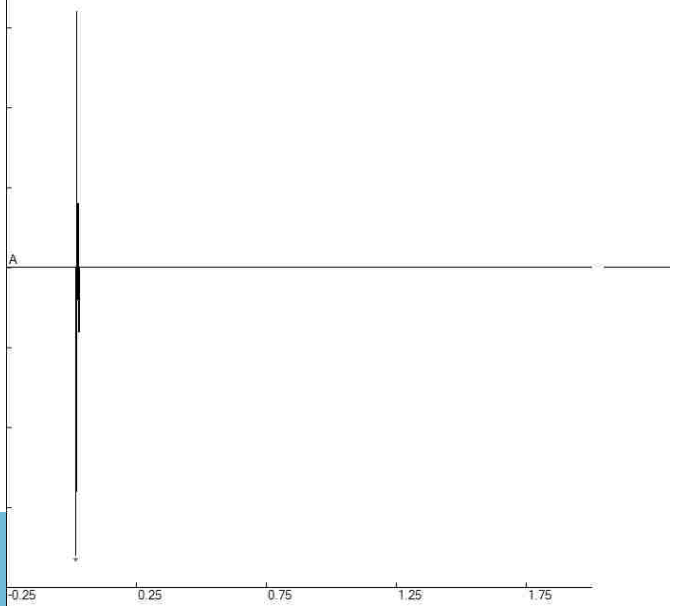

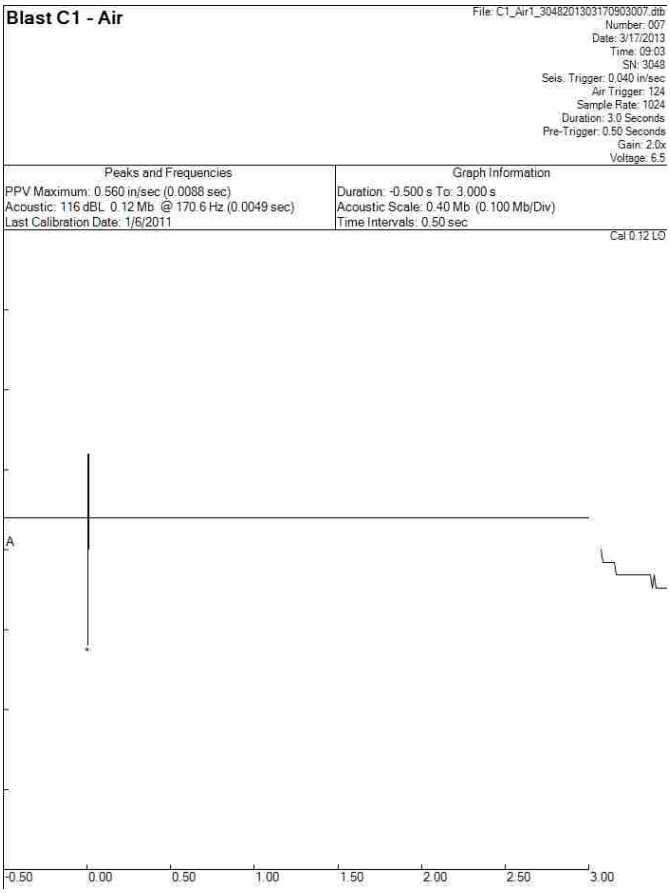

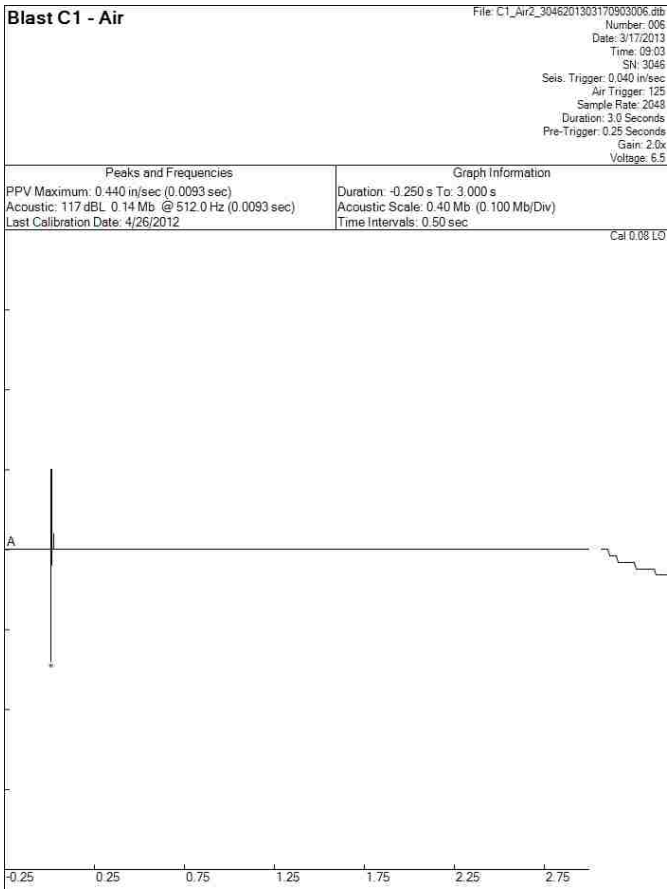

Blast C2 - Air

File: C2_Air1_2408201303171038006.dtb
Number: 006
Date: 3/17/2013
Time: 10:36
SN: 2408
Seis. Trigger: 0.08 in/sec
Air Trigger: 112
Sample Rate: 2048
Duration: 3.0 Seconds
Pre-Trigger: 0.25 Seconds
Gain: 1.0x
Voltage: 6.4

Peaks and Frequencies	Graph Information
PPV Maximum: 3.08 in/sec (0.0010 sec)	Duration: -0.250 s To: 3.000 s
Acoustic: 144 dBL 3.04 Mb @ 341.3 Hz (0.0039 sec)	Acoustic Scale: 3.20 Mb (0.800 Mb/Div)
Last Calibration Date: 1/27/2011	Time Intervals: 0.50 sec

Cal 0.08 LO

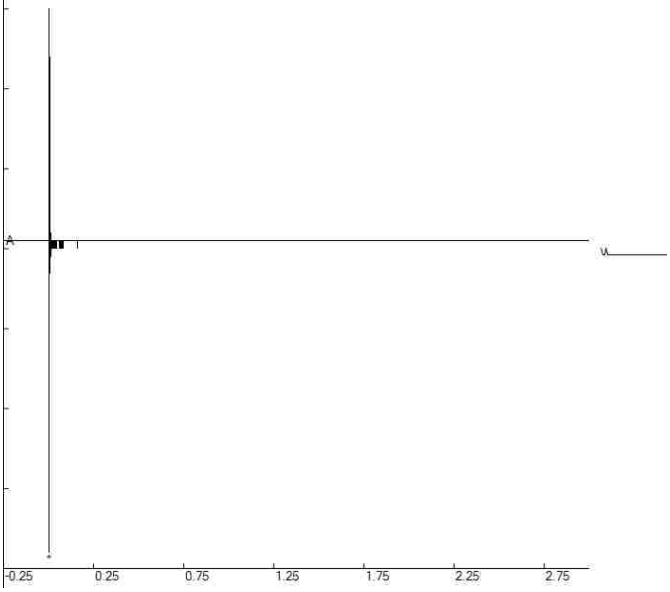

Blast C2 - Air

File: C2_Air2_3304620130317103601 1.dtb
Number: 011
Date: 3/17/2013
Time: 10:36
SN: 3046
Seis. Trigger: 0.040 in/sec
Air Trigger: 116
Sample Rate: 2048
Duration: 3.0 Seconds
Pre-Trigger: 0.25 Seconds
Gain: 2.0x
Voltage: 6.5

Peaks and Frequencies	Graph Information
PPV Maximum: 1.040 in/sec (0.0103 sec)	Duration: -0.250 s To: 3.000 s
Acoustic: 124 dBL 0.32 Mb @ 341.3 Hz (0.0088 sec)	Acoustic Scale: 0.40 Mb (0.100 Mb/Div)
Last Calibration Date: 4/26/2012	Time Intervals: 0.50 sec

Cal 0.08 LO

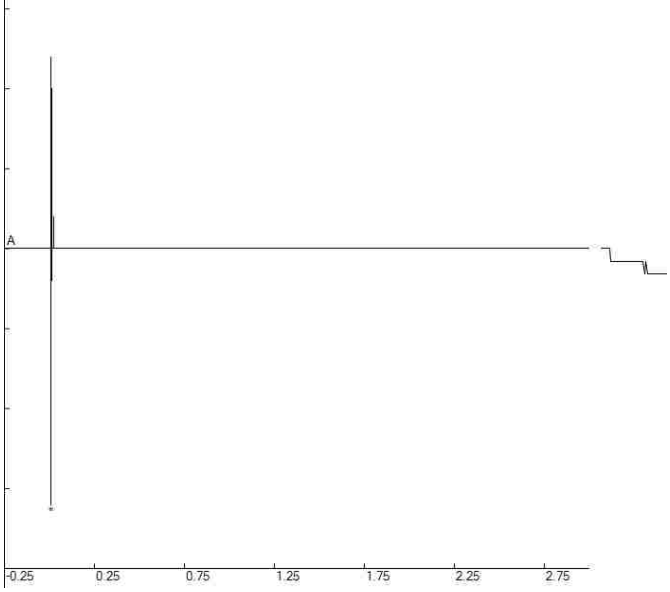

Blast C2 - Air

File: C2_Air3_4040201303171037012.dtb
Number: 012
Date: 3/17/2013
Time: 10:37
SN: 4040
Seis. Trigger: 0.120 in/sec
Air Trigger: 112
Sample Rate: 2048
Duration: 3.0 Seconds
Pre-Trigger: 0.25 Seconds
Gain: 2.0x
Voltage: 6.5

Peaks and Frequencies	Graph Information
PPV Maximum: 0.760 in/sec (0.0098 sec)	Duration: -0.250 s To: 3.000 s
Acoustic: 118 dBL 0.16 Mb @ 170.6 Hz (0.0146 sec)	Acoustic Scale: 0.40 Mb (0.100 Mb/Div)
Last Calibration Date: 5/21/2012	Time Intervals: 0.50 sec

Cal 0.08 LO

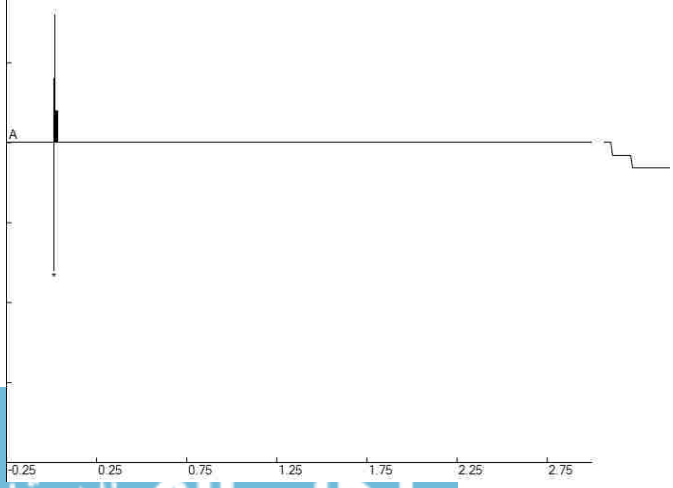

Blast C3 - Air

File: C3_Air1_304820130317109022.dtb
Number: 022
Date: 3/17/2013
Time: 11:09
SN: 3048
Seis. Trigger: 0.040 in/sec
Air Trigger: 148
Sample Rate: 1024
Duration: 3.0 Seconds
Pre-Trigger: 0.50 Seconds
Gain: 2.0x
Voltage: 6.5

Peaks and Frequencies	Graph Information
PPV Maximum: 2.340 in/sec (0.0107 sec)	Duration: -0.500 s To: 3.000 s
Acoustic: 130 dBL 0.64 Mb @ 170.6 Hz (0.0059 sec)	Acoustic Scale: 0.80 Mb (0.200 Mb/Div)
Last Calibration Date: 1/6/2011	Time Intervals: 0.50 sec

Cal 0.12 LO

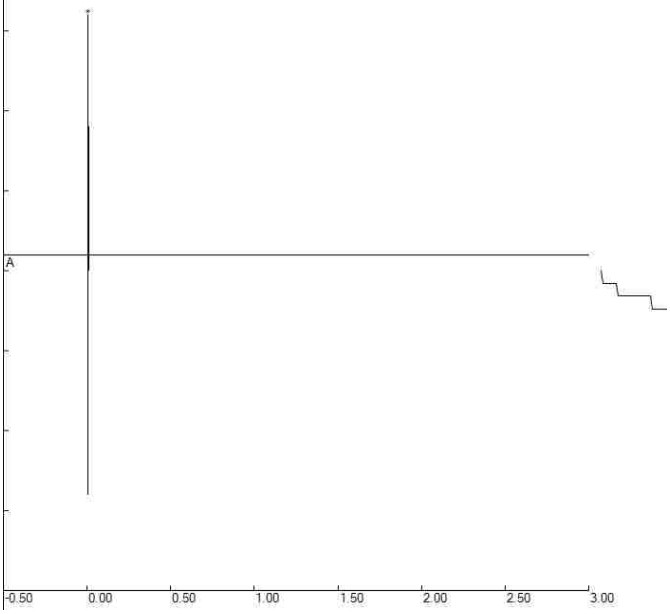

Blast C3 - Air

File: C3_Air2_330462013031711090 20.dtb
Number: 020
Date: 3/17/2013
Time: 11:09
SN: 3046
Seis. Trigger: 0.040 in/sec
Air Trigger: 116
Sample Rate: 2048
Duration: 3.0 Seconds
Pre-Trigger: 0.25 Seconds
Gain: 2.0x
Voltage: 6.5

Peaks and Frequencies	Graph Information
PPV Maximum: 1.980 in/sec (0.0107 sec)	Duration: -0.250 s To: 3.000 s
Acoustic: 128 dBL 0.48 Mb @ 341.3 Hz (0.0078 sec)	Acoustic Scale: 0.80 Mb (0.200 Mb/Div)
Last Calibration Date: 4/26/2012	Time Intervals: 0.50 sec

Cal 0.08 LO

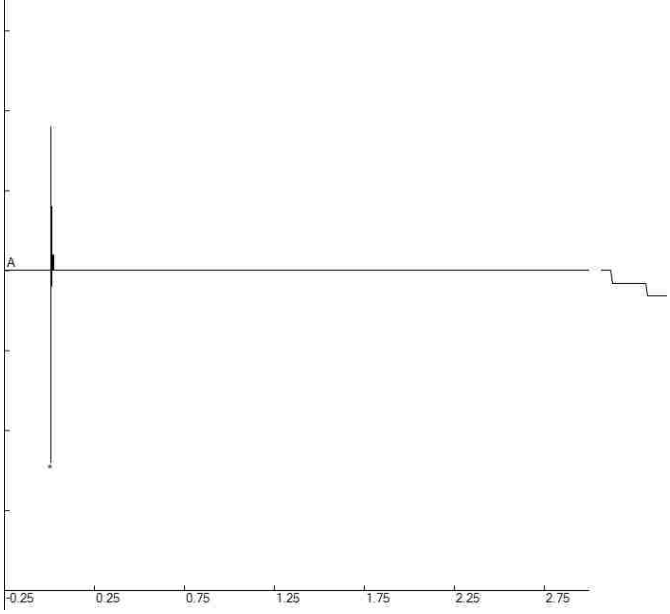

Blast C3 - Air

File: C3_Air3_404020130317109021.dtb
Number: 021
Date: 3/17/2013
Time: 11:09
SN: 4040
Seis. Trigger: 0.120 in/sec
Air Trigger: 112
Sample Rate: 2048
Duration: 3.0 Seconds
Pre-Trigger: 0.25 Seconds
Gain: 2.0x
Voltage: 6.5

Peaks and Frequencies	Graph Information
PPV Maximum: 1.180 in/sec (0.0103 sec)	Duration: -0.250 s To: 3.000 s
Acoustic: 122 dBL 0.24 Mb @ 341.3 Hz (0.0142 sec)	Acoustic Scale: 0.40 Mb (0.100 Mb/Div)
Last Calibration Date: 5/21/2012	Time Intervals: 0.50 sec

Cal 0.08 LO

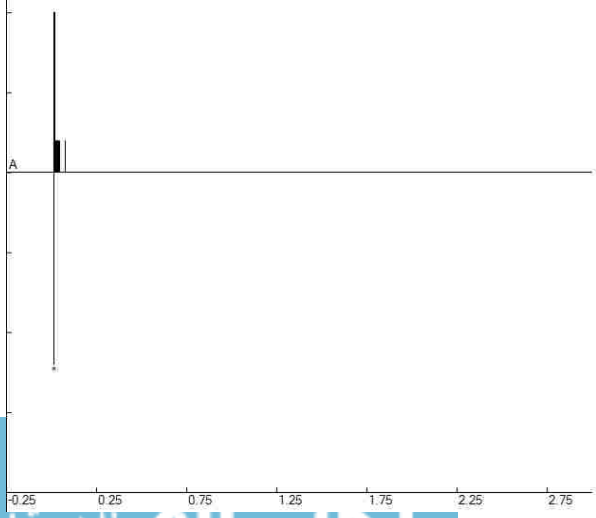

Blast C4 - Air

File: C4_Air1_3048201303171148024.dtb
Number: 024
Date: 3/17/2013
Time: 11:48
SN: 3048
Seis. Trigger: 0.040 in/sec
Air Trigger: 148
Sample Rate: 1024
Duration: 3.0 Seconds
Pre-Trigger: 0.50 Seconds
Gain: 2.0x
Voltage: 6.5

Peaks and Frequencies	Graph Information
PPV Maximum: 4.720 in/sec (0.0127 sec)	Duration: -0.500 s To: 3.000 s
Acoustic: 130 dBL 0.64 Mb @ 170.6 Hz (0.0059 sec)	Acoustic Scale: 0.80 Mb (0.200 Mb/Div)
Last Calibration Date: 1/6/2011	Time Intervals: 0.50 sec

Cal 0.12 LO

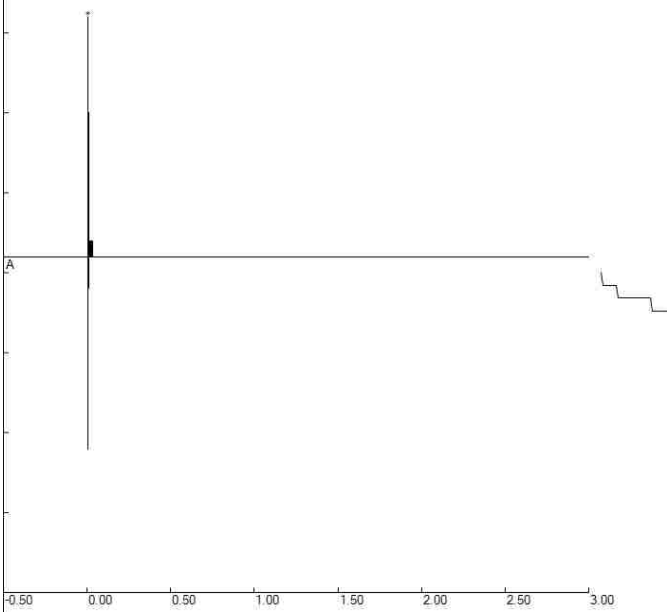

Blast C4 - Air

File: C4_Air2_3304620130317114802 2.dtb
Number: 022
Date: 3/17/2013
Time: 11:48
SN: 3046
Seis. Trigger: 0.040 in/sec
Air Trigger: 116
Sample Rate: 2048
Duration: 3.0 Seconds
Pre-Trigger: 0.25 Seconds
Gain: 2.0x
Voltage: 6.5

Peaks and Frequencies	Graph Information
PPV Maximum: 3.360 in/sec (0.0122 sec)	Duration: -0.250 s To: 3.000 s
Acoustic: 128 dBL 0.52 Mb @ 512.0 Hz (0.0083 sec)	Acoustic Scale: 0.80 Mb (0.200 Mb/Div)
Last Calibration Date: 4/26/2012	Time Intervals: 0.50 sec

Cal 0.08 LO

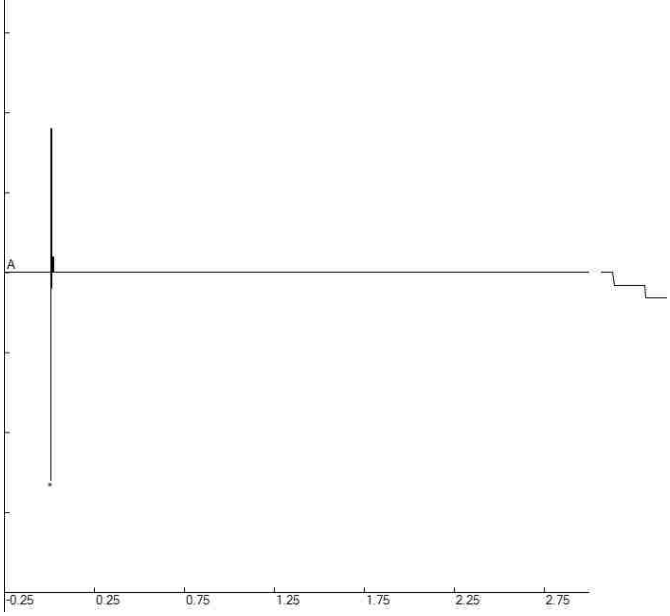

Blast C4 - Air

File: C4_Air3_4040201303171148023.dtb
Number: 023
Date: 3/17/2013
Time: 11:48
SN: 4040
Seis. Trigger: 0.120 in/sec
Air Trigger: 112
Sample Rate: 2048
Duration: 3.0 Seconds
Pre-Trigger: 0.25 Seconds
Gain: 2.0x
Voltage: 6.5

Peaks and Frequencies	Graph Information
PPV Maximum: 1.620 in/sec (0.0117 sec)	Duration: -0.250 s To: 3.000 s
Acoustic: 122 dBL 0.24 Mb @ 341.3 Hz (0.0146 sec)	Acoustic Scale: 0.40 Mb (0.100 Mb/Div)
Last Calibration Date: 5/21/2012	Time Intervals: 0.50 sec

Cal 0.08 LO

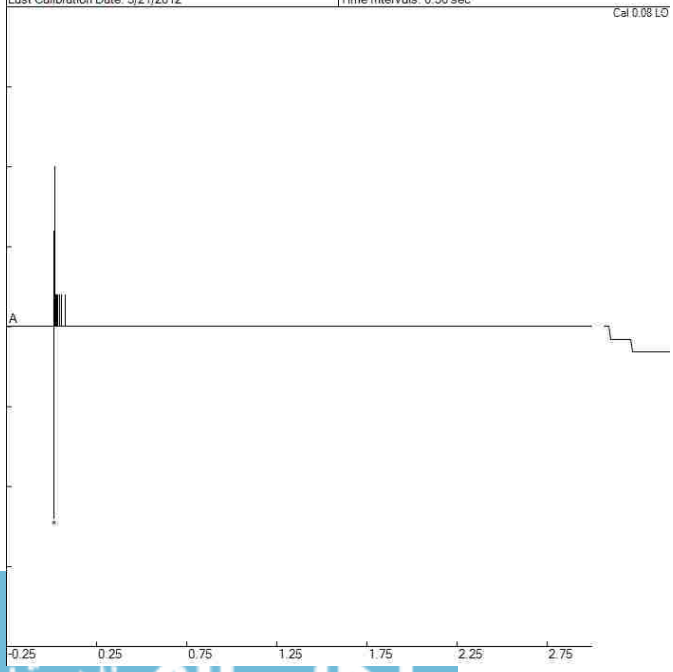

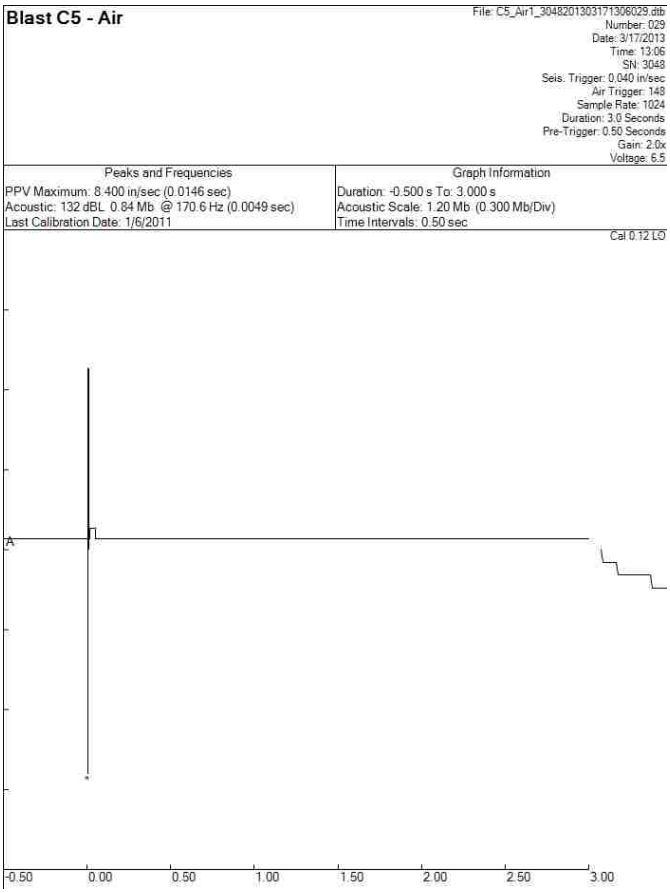

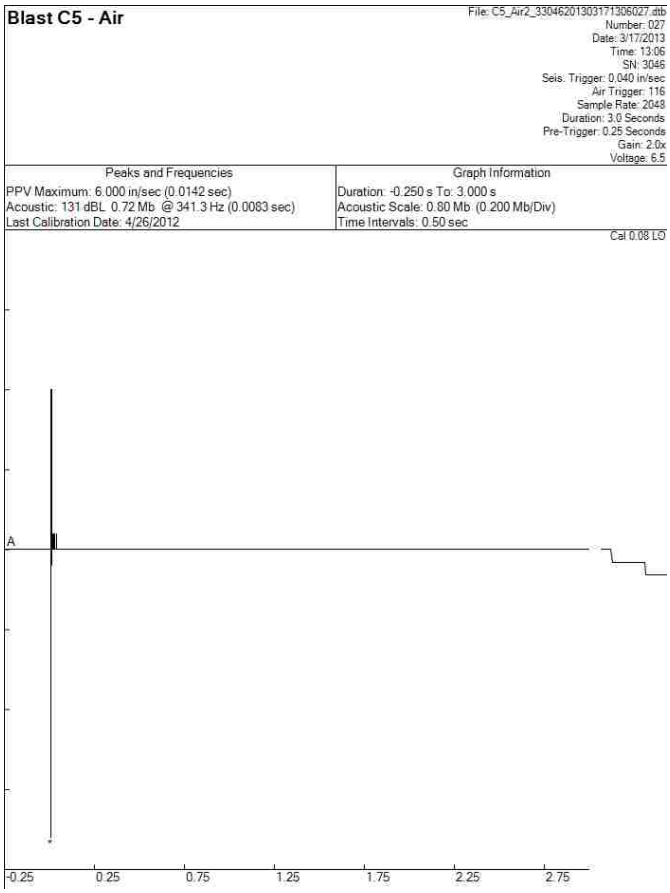

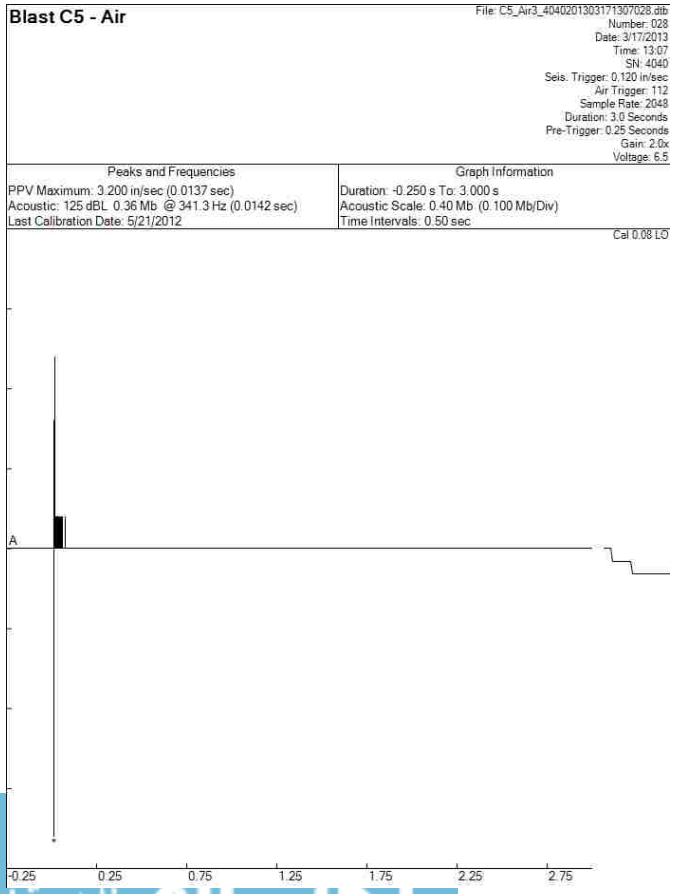

Blast C6 - Air

File: C6_Air1_3048201303171235027.dtb
Number: 027
Date: 3/17/2013
Time: 12:35
SN: 3048
Seis. Trigger: 0.040 in/sec
Air Trigger: 148
Sample Rate: 1024
Duration: 3.0 Seconds
Pre-Trigger: 0.50 Seconds
Gain: 2.0x
Voltage: 6.5

Peaks and Frequencies	Graph Information
PPV Maximum: 8.960 in/sec (0.0146 sec)	Duration: -0.500 s To: 3.000 s
Acoustic: 134 dBL 1.00 Mb @ 256.0 Hz (0.0039 sec)	Acoustic Scale: 1.20 Mb (0.300 Mb/Div)
Last Calibration Date: 1/6/2011	Time Intervals: 0.50 sec

Cal 0.12 LO

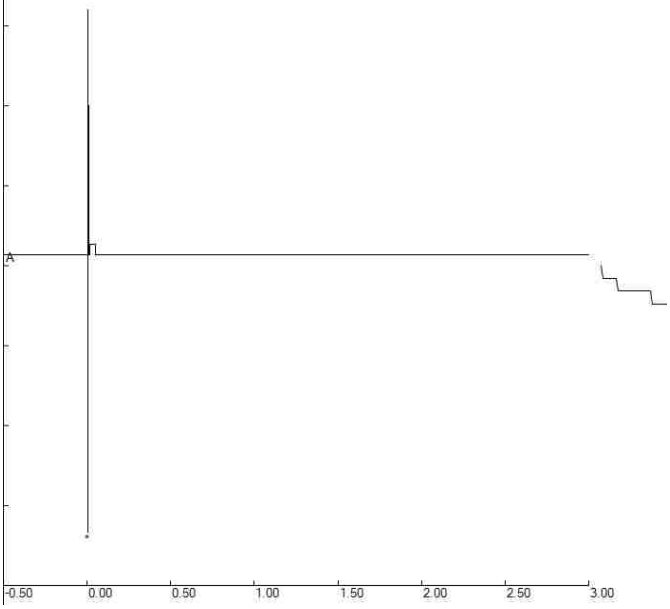

Blast C6 - Air

File: C6_Air2_3304620130317123502 5.dtb
Number: 025
Date: 3/17/2013
Time: 12:35
SN: 3046
Seis. Trigger: 0.040 in/sec
Air Trigger: 116
Sample Rate: 2048
Duration: 3.0 Seconds
Pre-Trigger: 0.25 Seconds
Gain: 2.0x
Voltage: 6.5

Peaks and Frequencies	Graph Information
PPV Maximum: 6.000 in/sec (0.0146 sec)	Duration: -0.250 s To: 3.000 s
Acoustic: 132 dBL 0.76 Mb @ 341.3 Hz (0.0088 sec)	Acoustic Scale: 0.80 Mb (0.200 Mb/Div)
Last Calibration Date: 4/26/2012	Time Intervals: 0.50 sec

Cal 0.08 LO

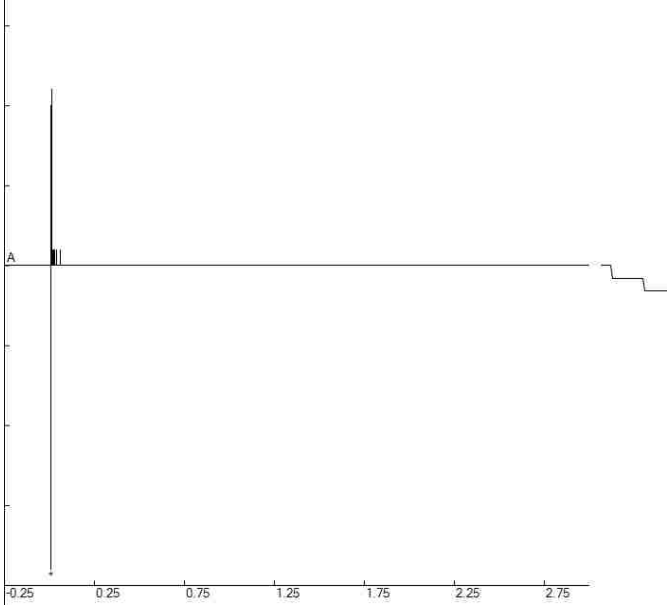

Blast C6 - Air

File: C6_Air3_4040201303171235026.dtb
Number: 026
Date: 3/17/2013
Time: 12:35
SN: 4040
Seis. Trigger: 0.120 in/sec
Air Trigger: 112
Sample Rate: 2048
Duration: 3.0 Seconds
Pre-Trigger: 0.25 Seconds
Gain: 2.0x
Voltage: 6.5

Peaks and Frequencies	Graph Information
PPV Maximum: 3.120 in/sec (0.0146 sec)	Duration: -0.250 s To: 3.000 s
Acoustic: 126 dBL 0.40 Mb @ 256.0 Hz (0.0142 sec)	Acoustic Scale: 0.80 Mb (0.200 Mb/Div)
Last Calibration Date: 5/21/2012	Time Intervals: 0.50 sec

Cal 0.08 LO

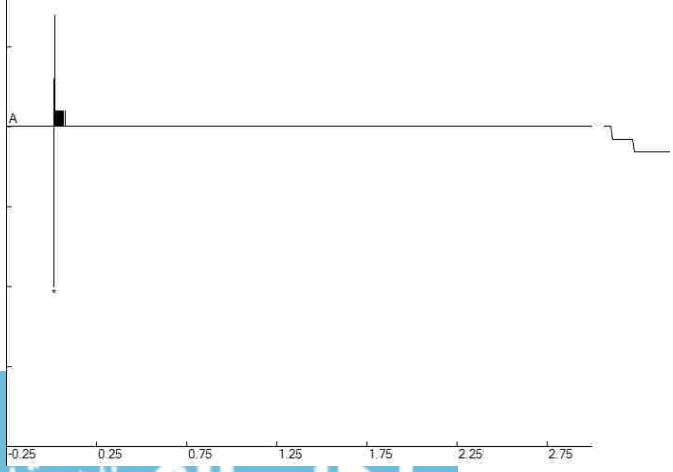

APPENDIX D EMBANKMENT DAM SEEPAGE AND SLOPE STABILITY RESULTS

Appendix D provides the results of the seepage and slope stability analyses of an earthen embankment dam under blast loading. Analyses were performed determined using the numerical seepage modeling software SEEP/W and the numerical stability modeling software SLOPE/W (GEO-SLOPE International Ltd. 2015a). Results for varying reservoir levels and explosive masses are presented.